Karlsruher Institut für Technologie

Global fits of sub-GeV dark matter models

Zur Erlangung des akademischen Grades eines

DOKTORS DER NATURWISSENSCHAFTEN (DR. RER. NAT.)

von der KIT-Fakultät für Physik
des Karlsruher Instituts für Technologie (KIT)

genehmigte

DISSERTATION

von

MSc Sri Sankari alias Sowmiya Balan

aus Puducherry, India

Referent:	Prof. Dr. Felix Kahlhöfer
Korreferent:	Prof. Dr. Thomas Schwetz-Mangold

Tag der mündlichen Prüfung: 07 November 2025

Eidesstattliche Versicherung gemäß § 13 Absatz 2 Ziffer 3 der Promotionsordnung des Karlsruher Instituts für Technologie (KIT) für die KIT-Fakultät für Physik:

1. Bei der eingereichten Dissertation zu dem Thema

   Global fits of sub-GeV dark matter models

   handelt es sich um meine eigenständig erbrachte Leistung.

2. Ich habe nur die angegebenen Quellen und Hilfsmittel benutzt und mich keiner unzulässigen Hilfe Dritter bedient. Insbesondere habe ich wörtlich oder sinngemäß aus anderen Werken übernommene Inhalte als solche kenntlich gemacht.

3. Die Arbeit oder Teile davon habe ich bislang nicht an einer Hochschule des In- oder Auslands als Bestandteil einer Prüfungs- oder Qualifikationsleistung vorgelegt.

4. Die Richtigkeit der vorstehenden Erklärungen bestätige ich.

5. Die Bedeutung der eidesstattlichen Versicherung und die strafrechtlichen Folgen einer unrichtigen oder unvollständigen eidesstattlichen Versicherung sind mir bekannt.

Ich versichere an Eides statt, dass ich nach bestem Wissen die reine Wahrheit erklärt und nichts verschwiegen habe.

Karlsruhe,

. . . . . .

(Sri Sankari alias Sowmiya Balan)

To my dad, who would have been the most proud person to see me achieve this.

Abstract

We have seen enormous success in building the Standard Model of particle physics for the visible sector using the frameworks of gauge theories and quantum field theory. It has been challenging to translate this success to dark matter, because unlike the visible sector, dark matter has so far only been unambiguously observed through its gravitational consequences. This allows for a degeneracy in models that can fit data from current dark matter searches. Due to the lack of complementary dark matter signals in experiments that can break the degeneracy, the current strategy to find the dark matter model closest to the truth is by means of exclusion. Formally, this is done through rigorous statistical fits of dark matter models against all available experimental data – called *global fits* – and through model comparisons. In the first part of the thesis, we extend and employ the code `GAMBIT` to perform global fits of a well motivated class of dark matter models. In the second part, we present `GAMBIT UTILISeD`, a tool developed to interactively visualise global fit results obtained using `GAMBIT`.

We perform global fits of models with thermal sub-GeV dark matter candidates coupled to a dark photon mediator that undergoes kinetic mixing with the standard model photon. Direct detection bounds on dark matter scattering are relatively weaker for sub-GeV dark matter compared to the traditional GeV-TeV scale weakly interacting massive particles (WIMPs). Sub-GeV dark matter is thus a particularly well-motivated alternative to traditional WIMPs. However, for s-wave annihilating fermionic sub-GeV dark matter, the strong constraints from indirect detection and the cosmic microwave background (CMB) can significantly restrict the model parameter space that reproduces the correct dark matter relic abundance. We explore different ways in which these constraints can be evaded for fermionic dark matter and also study the p-wave annihilating complex scalar dark matter candidate, which is free from the CMB constraint. These models additionally face new bounds from laboratory experiments and we thus perform global fits to determine their current status. We also study an extension of this model class which includes a dark Higgs that gives rise to the dark matter and dark photon masses. The first-order phase transition of such a dark Higgs in a sub-GeV dark sector can produce nano-Hertz gravitational waves. This is particularly interesting in the context of the nano-Hertz stochastic gravitational wave background (SGWB), recently observed by various pulsar timing arrays. The statistical fit of the leading astrophysical explanation of this signal – gravitational waves from merging super-massive black hole (SMBH) binaries – leaves room for contribution from exotic sources, such as the first-order phase transition in our sub-GeV dark sector. We thus study the viability of this model to explain the gravitational wave background (in addition to the contribution from SMBH binaries) and simultaneously reproduce the correct dark matter relic abundance, while satisfying constraints imposed by laboratory, astrophysical and cosmological data.

Zusammenfassung

Unter Verwendung von Eichtheorien und Quantenfeldtheorie haben wir enorme Erfolge beim Aufbau des Standardmodells der Teilchenphysik für den sichtbaren Sektor erzielt. Es ist jedoch eine große Herausforderung, diesen Erfolg auf Dunkle Materie zu übertragen, da diese - im Gegensatz zum sichtbaren Sektor - bislang ausschließlich über ihre gravitativen Konsequenzen eindeutig nachgewiesen werden konnte. Dies führt zu einer Vielfalt von Modellen, die derzeitigen Daten aus Suchen nach Dunkler Materie gleichermaßen beschreiben können. Aufgrund fehlender komplementärer experimenteller Signale, die diese Entartung aufheben könnten, besteht die derzeitige Strategie zur Identifikation des Modells Dunkler Materie, das der Realität am nächsten kommt, aus dem Ausschlussverfahren. Formal geschieht dies durch

strenge statistische Anpassungen von Modellen an sämtlichen verfügbaren experimentellen Daten - sogenannte globale Fits - sowie durch Modellvergleiche. Im ersten Teil der Arbeit verwenden und erweitern wir den Code `GAMBIT`, um globale Fits einer gut motivierten Klasse von Modellen von Dunkler Materie durchzuführen. Im zweiten Teil stellen wir `GAMBIT UTILISeD` vor, ein Werkzeug zur interaktiven Visualisierung der mit `GAMBIT` gewonnenen globalen Fit-Ergebnisse.

Wir führen globale Fits von Modellen mit thermischen sub-GeV Kandidaten für Dunkle Materie durch, die über einen Dunklen Photonenvermittler koppeln, welcher kinetisch mit dem Photon des Standard modells mischt. Beschränkungen an Streuprozesse durch direkte Nachweise sind im sub-GeV-Bereich vergleichsweise schwächer als für die herkömmlichen Weakly Interacting Massive Particles (WIMPs) im GeV-TeV Bereich. Sub-GeV Dunkle Materie stellt daher eine besonders gut motivierte Alternative zu traditionellen WIMPs dar. Für s-Wellen-annihilierende fermionische sub-GeV Dunkle Materie können jedoch indirekte Nachweise sowie die kosmische Hintergrundstrahlung (CMB) den Parameterraum, der die richtige Dunkle Materie Reliktdichte reproduziert, erheblich einschränken. Wir untersuchen verschiedene Mechanismen, mit denen diese Einschränkungen im fermionischen Fall umgangen werden können, und analysieren zudem den p-Wellen-annihilierenden komplex-skalaren Kandidaten, der die CMB Beschränkung umgeht. Diese Modelle unterliegen zusätzlich neuen Laborgrenzen, weshalb wir globale Fits durchführen, um ihren aktuellen Status zu bestimmen.

Darüber hinaus betrachten wir eine Erweiterung dieser Modellklasse, die ein Dunkles Higgs-Feld einschließt, das der Masse von Dunkler Materie und Dunklen Photonen ihren Ursprung verleiht. Der Phasenübergang erster Ordnung eines solchen Dunklen Higgs im sub-GeV Dunklen Sektor kann Gravitationswellen im Nanohertz-Bereich erzeugen. Dies ist insbesondere im Kontext des jüngst von verschiedenen Pulsartiming-Arrays beobachteten Nanohertz-stochastischen Gravitationswellenhintergrunds (SGWB) von großem Interesse. Der statistische Fit der führenden astrophysikalischen Erklärung dieses Signals - Gravitationswellen aus der Verschmelzung von Binärsystemen von supermassereichen Schwarzen Löchern - lässt Raum für Beiträge exotischer Quellen, wie etwa dem Phasenübergang erster Ordnung in unserem sub-GeV Dunkle Sektor. Wir untersuchen daher die Tragfähigkeit dieses Modells, um den beobachteten Gravitationswellenhintergrund (zusätzlich zu den Beiträgen durch SMBH-Binärsysteme) zu erklären und gleichzeitig die korrekte Dunkle Materie Reliktdichte zu reproduzieren, unter Beachtung der Beschränkungen durch astrophysikalische, kosmologische und Labordaten.

Publication list

Part of the work presented in this thesis has been published in the following articles.

Journal publications

- S. Balan *et al.*, "Resonant or asymmetric: the status of sub-GeV dark matter", *JCAP* **01** (2025) 053, arXiv:2405.17548 [hep-ph].
- S. Balan, T. Bringmann, F. Kahlhoefer, J. Matuszak, and C. Tasillo, "Sub-GeV dark matter and nano-Hertz gravitational waves from a classically conformal dark sector", *JCAP* **08** (2025) 062, arXiv:2502.19478 [hep-ph].

Publications not discussed in the thesis

- S. Balan, F. Kahlhoefer, M. Korsmeier, S. Manconi, and K. Nippel, "Fast and accurate AMS-02 antiproton likelihoods for global dark matter fits," *JCAP* **08** (2023) 052, arXiv:2303.07362 [hep-ph].

Under preparation

- S. Balan, "`GAMBIT UTILISeD`: Utility for interactive visualisation of high-dimensional global fits results from `GAMBIT`", (2025).

Conference proceedings

- S. Balan, "Global fits of sub-GeV dark matter models with `GAMBIT`" in Proceedings of 59th Rencontres de Moriond on Gravitation" (2025).
- S. Balan, "Global fits of sub-GeV dark matter models with `GAMBIT`" in Proceddings of 59th Rencontres de Moriond on QCD" (2025).

Contents

CHAPTER 1

Introduction to dark matter

Astronomers have long evoked the existence of dark stars, planets, meteoric matter and cold gas to explain missing masses, implied by the deviation of astrophysical systems from Newtonian dynamics. This unobserved, non-luminous, baryonic matter had been called *dark matter* (DM). In the 20th century, with the advent of modern astronomy and cosmology, we began observing missing masses across length scales from that of galaxies to the universe. With these observations, particularly, the flattening of rotation curves in spiral galaxies, gravitational lensing of galaxy clusters, the cosmic microwave background (CMB), and large scale structures, it became evident that the baryonic content of the universe is insufficient to fully explain the missing mass. We still refer to this phenomenon as "dark matter", while we now know that it is neither dark, nor matter in the traditional sense, i.e., baryonic matter.

In this thesis, we will investigate new elementary particles as candidates for DM. Specifically, we are interested in particles with sub-GeV masses that can be produced as a thermal relics. We will begin this chapter by discussing the experimental observations that lead us to the current interpretation of DM in section 1.1. We will discuss the current concordance model of cosmology in section 1.2, which will serve as the backdrop for our study of various DM models. In section 1.3, we get back to DM and introduce some DM candidates. We will then turn our focus to weakly interacting massive particles (WIMPs) in section 1.4 and also present the status of their searches. In section 1.5, we will talk about strategies to extend the vanilla WIMP DM models to be consistent with current WIMP searches and conclude with a case for sub-GeV DM.

1.1. A brief history of dark matter

With the discovery of the universe extending beyond the Milky Way in the 1930s, astronomers began to make estimates of masses of galaxies and galaxy clusters based on arguments of dynamics. The virial theorem was applied to relaxed clusters to calculate their mass and consequently the mass-to-light ratios (MLR) [1,2]. Assuming that the clusters are isolated and virialized, the virial mass $M_{\rm vir}$ can be obtained once the virial radius $r_{\rm vir}$ and velocity dispersion of galaxies $\langle v^2 \rangle$ are known, $M_{\rm vir} \sim r_{\rm vir}\langle v^2 \rangle / G$. MLRs obtained from such virial masses were found to be orders of magnitude larger than that in the solar neighbourhood.

While assuming circular orbits, the mass of spiral galaxies can be calculated by measuring the rotational velocity at the outermost orbits, $M(r) \sim v_{\rm rot}^2 r/G$. Similar to clusters, the MLRs from these masses were also abnormally large [3]. The missing mass indicated by these observations was, at the time, largely considered to be speculative. This changed in the 1970s when Rubin and Ford [4] published their spectroscopic observations of the Andromeda galaxy. They observed rotational velocities that remained constant at large distances from the galactic center. This was in contradiction with the expectation from Newtonian physics for spiral galaxies, $v_{\rm rot}(r) \propto r^{-1/2}$. It thus became the first direct and robust evidence to undisputably establish the missing mass problem.

1.1.1. Cosmological evidence for non-baryonic matter

Alongside the developments in astronomy, we had made huge strides in understanding the cosmology of the universe. By the 1980s, the theoretical frameworks of big bang nucleosynthesis (BBN), baryon acoustic oscillations (BAO), and the hot big bang cosmological model had been established. The successful observation of their predictions, namely that of the primordial light element abundances produced in BBN and BAO features in both the CMB and large scale structure (LSS) surveys, provided robust estimates of the total baryonic content of the universe. These constraints implied that the majority of the matter required to explain structure formation could not be baryonic. Thus, it was cosmological evidence that ultimately played the decisive role in identifying DM as a non-baryonic.

BBN describes the production of light elements in the early universe from a primordial baryon-photon plasma. As the universe cooled to temperatures below the binding energies of light nuclei, light elements could form in significant quantities without being immediately dissociated by energetic photons. The abundance of light elements, hence, depends sensitively on the ratio of baryon to photon abundance $\eta_{\rm B}$. By measuring the primordial light element abundance and photon abundance, one could estimate the total baryonic abundance in the universe. Since there aren't many other astrophysical processes that produce deuterium in the universe, the deuterium abundance measured in the interstellar medium is considered to represent the primordial deuterium abundance. Using the deuterium abundance measurements available at the time, along with the photon abundance derived from the CMB temperature, the baryonic abundance was estimated to be about 3% [5]. On the other hand, a simple estimate of the total matter abundance could be obtained from cluster MLRs given the average luminosity density of the universe, $\Omega_{\rm m} \sim (M/L)(\rho_L/\rho_{\rm crit})$. Although such estimates were already available (e.g. [6]) showing that $\Omega_{\rm m} > \Omega_{\rm b}$, it took another two decades of studies of gas distributions, gravitational lensing, galaxy surveys and CMB experiments for the scientific community to be convinced that the DM in galaxies and galaxy clusters is *weakly-interacting, non-baryonic, invisible matter*.

The CMB is a flux of relic photons that decoupled from the primordial plasma and started free-streaming through the universe. At high temperatures, photons were kept in thermal equilibrium with the plasma via frequent scattering off free electrons. Once the universe cooled to temperatures well below the ionization energies of the hydrogen atom (~ 13.6 eV), electrons and protons combined to form neutral hydrogen, making the universe transparent. The free-streaming photons that we observe today, thus, follow a thermal black body spectrum with the temperature $T \approx 2.7$ K. More interesting is the angular power spectrum of correlations in the CMB temperature fluctuations shown in Figure 1.1, because BAO leaves imprints on the angular power spectrum that are sensitive to both the total matter and baryonic abundances.

Density perturbations in the early universe cause baryons to collapse and fall into potential wells. This is counteracted by photon pressure, setting up acoustic oscillations in the baryon-photon fluid as a result. The system oscillates between states of maximum compression

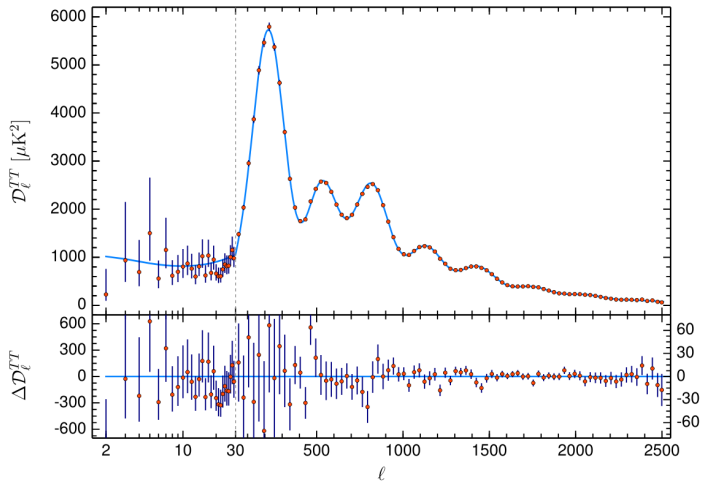

Figure 1.1.: Angular power spectrum of correlations in CMB temperature fluctuations as measured by Planck 2018 [7].

and rarefaction until photon decoupling, and the CMB is essentially a frozen picture of this epoch. The effect of BAO on CMB can be understood with linear perturbation theory. In linear perturbation theory, we consider the density perturbations to be small and study the evolution of each Fourier mode separately. Not all modes can oscillate, only those with wavelengths smaller than the *causal horizon* - maximum distance over which information could have travelled since the big bang - can oscillate. The fundamental mode of the baryon-photon oscillation has a wavelength $\lambda \approx r_s/2$. Here r_s is the sound horizon at recombination. This mode would have reached a state of maximum compression by recombination and would have a maximum positive temperature fluctuation. This gives rise to the first peak at $l \approx 200$ that we see in Figure 1.1. The peaks at higher multipoles correspond to higher harmonics of the acoustic oscillations.

The total matter and baryonic abundances affect the angular power spectrum in a multitude of ways. The baryonic abundance affects the relative heights of peaks corresponding to compressions and rarefactions. Baryons falling into potential wells deepen the potential wells, and cause more pronounced positive temperature fluctuations (compression) compared to negative fluctuations (rarefactions). Thus, increased baryonic abundance enhances the compression peaks (odd peaks) and suppresses the rarefaction peaks (even peaks). The total matter abundance, on the other hand, determines when the matter-radiation equality occurs and hence the size of the sound horizon at recombination. Increasing the total matter abundance shifts all peaks to larger angular scales (smaller multipoles), and also decreases the ratio of heights of the first peak relative to the third (and successive peaks) [8]. These effects, among others, allow us to determine the total matter and baryonic abundance from the CMB. It wasn't until the early 2000s, when data sensitive enough to resolve the acoustic peaks were published by BOOMERANG [9] and MAXIMA [10], which were later refine by the Wilkinson Microwave Anisotropy Probe (WMAP) experiment [11]. Today, we have the most precise measurements of the abundance parameters from the latest CMB mission, Planck 2018 [7],

$$\Omega_{\rm DM}h^2 = 0.120 \pm 0.001, \quad \Omega_{\rm b}h^2 = 0.0224 \pm 0.0001 \ , \tag{1.1}$$

where $h = H_0/(100$ km/s/Mpc) is the dimensionless Hubble parameter and H_0 is the current day Hubble rate.

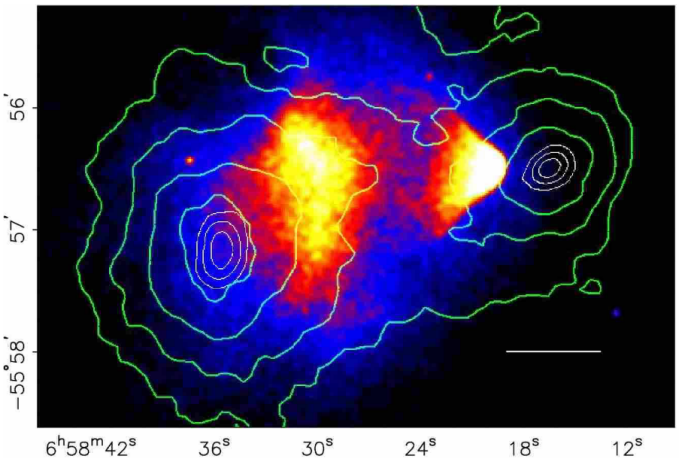

Figure 1.2.: X-ray and weak lensing image of the bullet cluster. The green contours show the weak lensing mass reconstruction, while the colored regions trace the hot plasma. From [17].

Another product of linear perturbation theory is the linear matter power spectrum. Like the CMB angular power spectrum, the matter power spectrum describes the correlations in density perturbations and tracks the clustering of matter on different length scales. BAO leave imprints on the matter power spectrum as well, leading to wiggles that are sensitive to the abundance parameters. The matter power spectrum is measured using galaxy surveys where galaxies are used as tracers to study the clustering of matter. The first estimates of abundance parameters from galaxy surveys came in the early 2000s and were broadly consistent with CMB measurements [12]. The most recent results are from a much larger galaxy survey by the Dark Energy Spectroscopic Instrument (DESI), with early data released in 2025 [13].

1.1.2. Evidence for collisionless particle dark matter

Cluster 1E0657-56 was first identified in 1998 as a contender for the hottest known cluster [14] using optical and X-ray observations. Subsequent higher quality X-ray data of the cluster from Chandra X-ray Observatory helped clearly identify a bow shock in the cluster. This indicated that a smaller subcluster had recently passed through the main cluster's central region [15], and thus the system came to be known as the *bullet cluster*. In 2004, Clowe et al. [16] studied weak lensing mass reconstruction for the Bullet cluster. They, for the first time, identified that the X-ray peak of the main cluster was offset from the mass peak at $3.4\,\sigma$ significance. A later analysis with Hubble Space Telescope data [17], increased the significance of the spatial offset of the total mass peak from the baryonic mass peak to $8\,\sigma$ and produced the iconic bullet cluster image shown in Figure 1.2. This implied that the majority of the mass in the cluster remains unseen and separated from the baryonic mass, and thus cannot be explained with an alteration of the Newtonian gravitational force law. The bullet cluster, therefore, came to be called a *direct empirical proof of the existence of dark matter* and earned its reputation as one of the most widely cited evidence of collisionless DM.

Constraints on the self-interaction cross-section can be derived in a number of ways from the observation of the bullet cluster. The leading constraint comes from the survival of the subcluster passing through the main cluster, $\sigma/m_{\mathrm{DM}} < 1\,\mathrm{cm}^2/\mathrm{g}$. A larger cross-section would have lead to expulsion of a large number of particles from the subcluster due to self-interactions, leading to a subcluster mass smaller than what we observe. We discuss the bullet cluster constraints in more detail in subsection 2.6.1.

1.2. The ΛCDM Model

In the previous century, before the precise measurements from CMB, the exact details of our cosmology were unclear. But from different observations, we built up a standard model of cosmology. We began with the cosmological principle which states that the universe is homogenous and isotropic along with the observation that the universe is expanding [18]. The *Friedmann-Lemaitre-Robertson-Walker* (FLRW) metric is the most general solution to the Einstein's field equation for such a universe,

$$\mathrm{d}s^2 = -c^2\mathrm{d}t^2 + a(t)^2\left[\frac{\mathrm{d}r^2}{1-kr^2} + r^2(\mathrm{d}\theta^2 + \sin^2\theta\mathrm{d}\phi^2)\right] , \tag{1.2}$$

where k is the curvature and the scale factor $a(t)$ gives the scaling between physical distance and coordinate distance (comoving distance). The Hubble rate, $H(t) = \dot{a}(t)/a(t)$ describes the expansion of the universe and its evolution is given by the Friedmann equation obtained from Einstein's field equation for the FLRW metric,

$$H^2 = \frac{8\pi G}{3}\rho_{\mathrm{tot}} - \frac{k}{a^2} , \tag{1.3}$$

where ρ_{tot} is the total energy density of matter and radiation in the universe. By the 1960s, it was already established that the universe started in an era where radiation dominated the energy density of the universe and hence controlled its evolution. This era, called radiation domination era, was expected to be followed by a matter domination era, where the energy density of the universe would be dominated by *cold*, i.e. non-relativistic particles with negligible pressure density, that cluster and form structures efficiently.

Following the discussion in the previous section, the baryonic matter density was understood to be insufficient to drive structure formation and hence the need for the electrically neutral, non-baryonic, *cold dark matter* (CDM) component [19]. Furthermore, from other observations [20, 21], it was also deduced that the universe is currently in a state of accelerated expansion which can only be achieved by a constant energy density, unlike matter or radiation that gets diluted with expansion. Thus, the Friedmann equation gets an additional contribution involving a non-zero cosmological constant Λ attributed to a *dark energy* component, was introduced to our cosmological model, hence the name "ΛCDM". With the curvature measured to be zero [22], the Friedmann equation can be rewritten as,

$$\Omega_{\mathrm{rad}} + \Omega_{\mathrm{DM}} + \Omega_{\mathrm{b}} + \Omega_{\Lambda} = 1 \tag{1.4}$$

where the abundance parameters $\Omega_{\mathrm{x}} = \rho_{\mathrm{x},0}/\rho_{\mathrm{crit},0}$ give the ratio of the current energy density of a species to the *critical density* - the total energy density of a flat universe, $\rho_{\mathrm{crit},0} = 3H_0^2/8\pi G$. The subscript X_0 indicates the values of various cosmological quantities *today*. The evolution of the homogenous universe in the ΛCDM model can thus be described by the set of parameters $\{\Omega_{\mathrm{rad}}, \Omega_{\mathrm{DM}}, \Omega_{\mathrm{b}}, \Omega_{\Lambda}, H_0\}$. [1]

1.2.1. Challenges of ΛCDM

The agreement between cosmological parameters inferred from observations across a time scale of billions of years – BBN, CMB and LSS – is the biggest success of the ΛCDM model. Apart from BAO features in the matter power spectrum, there are many observables of small and large scale structures in the current universe that are sensitive to cosmology. These are, for instance, halo mass function, galaxy clustering statistics, and weak lensing statistics. These observables can test the success of ΛCDM and infer the parameters of the model.

[1] Parameterization in terms of the physical density parameter $\omega = \Omega h^2$, as well as the precise measurement of Ω_{rad} through the CMB temperature, allow us to reduce the required set of free parameters to $\{\omega_b, \omega_{\mathrm{DM}}, \Omega_{\Lambda}\}$.

N-body simulations are indispensable in these tests, as they form the bridge between predictions of ΛCDM from linear perturbation theory and non-linear structures that we observe today. A notable outcome of cosmological N-body simulations is the prediction of universal DM density profiles across scales of galaxies to galaxy clusters. One such profile that provides a good fit to halos in cosmological CDM-only simulations was proposed by Navarro, Frenk and White [23], called the NFW profile,

$$\rho(r) = \frac{\rho_s}{r/r_s(1 + r/r_s)^2} \tag{1.5}$$

with two free parameters, the scale radius r_s and the scale density ρ_s. Subsequent higher resolution simulations revealed more cuspy inner profiles with significant halo-to-halo scatter. Thus, other empirical profiles with an extra free parameter for the central slope have also been used in fitting haloes from CDM-only simulations. Although these profiles have global properties that are broadly consistent with observations, there exist discrepancies between simulations and observations at small scales ($\lesssim 1$ Mpc). For a detailed review on small-scale challenges, see [24]. Observations have identified galactic haloes with diverse inner slopes ranging from cored to cuspy central regions, while CDM-only simulations consistently predict cuspy central regions. This is the so-called *diversity problem* [25]. We also observe fewer satellite galaxies and massive subhaloes with luminous counterparts, than that predicted in CDM-only simulations. These are called the *missing satellite* [2] [27]and *too-big-to-fail* problems [28], respectively. As of yet, it is unclear whether more precise observations and inclusion of baryonic physics in simulations can fully resolve the small scale challenges.

Self-interacting DM (SIDM) was first proposed as a solution to small scale challenges by David and Spergel [29] requiring self-interaction cross-sections in range $0.5 - 10\,\mathrm{cm}^2/\mathrm{g}$ to solve these problems. But tight constraints from galaxy clusters indicate that SIDM cross-sections have to be velocity-dependent to simultaneously satisfy stringent constraints and alleviate small scale problems. Such non-gravitational DM self-scatterings can lead to testable predictions on a wide range of length scales and is an active area of research today [30]. Other alternatives to CDM – warm DM and fuzzy DM – have also been explored as solutions in the literature [24].

An unrelated, bigger challenge to ΛCDM is the H_0 tension which was first identified a little over a decade ago. This is the 4σ to 6σ tension between the late universe and early universe measurements of the Hubble constant, depending on the datasets considered. The late universe measurement comes from observing objects located deep in the Hubble flow (velocities of these objects are dominated by expansion of the universe, rather than the effect of the local environment), and is based on the distance-ladder calibration [31]. The early universe measurement comes from a fit of parameters to CMB data [7]. Extensive studies of systematics in local universe measurements have only increased the significance of the tension [32] and a number of different solutions have been explored with no common consensus in the community yet, see review [33].

For a review of other challenges, albeit with lesser statistical significance, see [34]. Thus, it remains to be seen whether new and improved data from different experiments in the near future will absolve ΛCDM of its current issues or reveal a more fundamental problem within the model.

1.2.2. Interlude: Theories of modified gravity

The dearth of observations accumulated over the last century leading to the unsettling implication that the universe is almost completely filled with a new forms of matter and energy

[2] With the recent identification of a number of new satellite galaxies, this isn't considered to be as big a problem anymore,e.g. [26].

have been based on Newtonian and Einstein's gravity. It is thus reasonable to question the validity of these theories and explore modifications of gravity as a solution to these problems. There are many classes of modified gravity theories that are pursued as alternatives to the ΛCDM model, see review [35]. Most of these aim to explain late-time accelerated expansion of the universe without a cosmological constant. These models still require a particle CDM component and won't be discussed here. Since the focus of the thesis is on DM, we will mention the class of theories that try to explain observations without introducing CDM – TeVeS (Tensor-Vector-Scalar) theories [36–38].

Most of these theories add new fields that modify gravity and add their own contribution to the stress-energy tensor. The modification to gravity leads to modified newtonian dynamics (MOND) in the non-relativistic limit, while their density perturbations provide the non-decaying deep potential wells for structures to grow in. MOND introduces a critical length scale below which acceleration would be the usual Newtonian gravitational acceleration $\vec{a}$ and above this scale, the acceleration would be $\vec{a}^2/a_0$. Thus a system would deviate from Newtonian dynamics for accelerations smaller than $a_0 \sim 10^{-8}\,\mathrm{cm\,s^{-2}}$. MOND is successful in reproducing observations on the galactic scales, while the relativistic extension with new fields that behave like dust, seem to allow for enough structure formation. This is achieved by choosing the right form for the function that enters in the non-canonical kinetic term of the scalar field lagrangian [39]. It is this functional freedom that reduces the predictive power of these theories. Thus, in a bayesian model comparison, one could argue that the Occam's penalty would disfavour these theories compared to the much simpler ΛCDM model. But since the nature of DM and dark energy remain unknown, such parallel lines of investigation are crucial in arriving at the ultimate truth.

1.3. DM candidates

Despite the above mentioned challenges faced by ΛCDM, its enormous success in explaining observations across cosmic time and length scales implies that any viable alternative must reproduce its predictions in some appropriate limit. With this context, let us examine the properties of a DM candidate required to successfully reproduce the formation of structures observed today.

DM needs to cluster efficiently, unlike baryons that experience photon pressure. They should thus possess effectively no interactions with the SM particles. However, photon pressure isn't the only thing that suppresses growth of density perturbations, but also random thermal motion. Depending on when and how they are produced, DM particles with large kinetic energies can evade gravitational capture. But with the expansion of the universe, their momenta redshift and can eventually fall into potential wells if they had slowed down enough by the time of matter-radiation equality. Density perturbation with potential wells too shallow to capture even the slowest DM particles, thus, do not grow with time and get suppressed. This effect is quantified by the *free-streaming length*, defined as the comoving distance travelled by the DM particle since production until matter-radiation equality,

$$\lambda_{\mathrm{fs}} = \int_{t_{\mathrm{prod}}}^{t_{\mathrm{EQ}}} \frac{v(t)\mathrm{d}t}{a(t)} \tag{1.6}$$

Thus, structures on length scales below λ_{fs} get suppressed. This naturally leads to a classification of DM particles as *cold*, *warm* and *hot*. Particles that were non-relativistic at production would have negligible λ_{fs}. If such particles followed a thermal velocity distribution at production with a temperature T, they would have $T \ll m_{\mathrm{DM}}$ and hence the name *cold dark matter*. Similarly, particles with intermediate and relativistic velocities at production and are called warm and hot DM, respectively. These particles would have large free-streaming

lengths and lead to suppression of structures on different length scales. But for the smallest gravitationally bound structures that we observe today to have survived, the free-streaming length should be $\lambda_{\rm fs} \lesssim 0.1$ Mpc [40]. This bound severely constrains hot DM and places a lower bound on DM mass for thermally produced warm DM, $m_{\rm DM} \gtrsim 3\,{\rm keV}$ [40].

Having discussed the classification of DM based on macroscopic observations, let us now turn to the microphysics. From a particle physics perspective, DM can be broadly classified as particle and wave-like DM. Today, we have a plethora of DM candidates with different combinations of the macroscopic and microscopic properties that we just mentioned, addressing different problems. But historically, physicists, being economical as always, nominated new particles, proposed to solve problems in the standard model of particle physics, as DM candidates.

Weakly-interacting massive particles (WIMPs) arose in supersymmetric theories that aimed to address the hierarchy problem. They rose to fame due to the *WIMP miracle*, wherein GeV-TeV mass scale particles that interact weakly reproduce the correct DM abundance. This happens if they are produced in a process called *freeze-out*, and particles produced by this mechanism are called thermal relics. In this process, DM undergoes chemical decoupling from the thermal plasma once its interaction rates drop below the Hubble rate, and thereafter its abundance remains stable. They are non-relativistic at production, and thus form a cold particle DM candidate. *QCD axions* were proposed to solve the strong CP problem and are produced through the misalignment mechanism. They are non-relativistic at production, with macroscopic de Broglie wavelengths, making them a cold wave-like DM candidate. *Sterile neutrinos* were proposed to explain non-zero neutrino masses implied by neutrino oscillations. They are produced from oscillations of active neutrinos and form a warm particle DM candidate.

All three candidates as they were originally proposed are severely constrained today by different observations. But, their definitions have now expanded: WIMPs include any massive, thermally produced cold DM candidate with weak-scale interactions with the SM (see [41] for a review); axions have been generalized to axion-like-particles (ALPs) that include any pseudoscalar bosons with a wider range of masses and couplings to SM photons (for a review, see [42]). More complex production mechanisms of sterile neutrinos have now been explored and have opened up regions of parameter space where sterile neutrinos can make up all of dark matter, e.g. see [43, 44].

In this thesis, we focus on WIMPs and we will now briefly introduce them before discussing the status of their searches.

1.4. WIMP Dark Matter

In the simplest scenario, the CDM component added to fit observations needs to be a dust-like fluid evolving purely gravitationally. This means that they have to be stable and collisionless, apart from being cold and weakly-interacting as discussed earlier. At the least, this should be the characteristic of the particle during and after BBN. Of course, one can assume that such DM particles were produced in some exotic way in the very early universe through a mechanism that was completely independent of the SM particle production. But it is more pleasing to have a testable, falsifiable theory than to have the most general self-consistent theory that cannot be tested. This is why WIMPs have been one of the most popular DM candidates. Traditional WIMPs were hypothesised to be GeV-TeV mass scale DM particles with weak-scale interactions between DM and SM. These interactions affects its evolution in the very hot and dense early universe before BBN, allowing us to formulate DM production mechanisms. The same interactions also enable us to design experiments that can look for them.

The afore-mentioned requirements for a CDM candidate and weak DM-SM interactions lead to an elegant production mechanism for DM: *thermal freeze-out*. Non-negligible DM-SM interactions in the early universe establishes thermal and chemical equilibrium between DM and the SM plasma. DM would thus follow a thermal distribution specified by its temperature. Once it becomes non-relativistic, the number density gets Boltzmann suppressed due to efficient annihilations. But as the universe expands and cools, the annihilation rates eventually drop below the Hubble rate and the DM abundance "freezes out". This process is known as the freeze-out mechanism, which will be discussed in more detail in the next chapter, section 2.2.

These same interactions between DM and SM, either through a coupling to an existing mediator or a new mediator, also create multiple avenues to look for DM. Such a coupling would allow DM-SM scatterings, DM production in SM collisions, and SM production in DM annihilation. These three types of interactions lead to a three-pronged search for DM.

Collider searches look for DM particles produced in energetic particle collisions. Since DM is weakly-interacting, these particles would escape the detector and lead to missing energies in these events. In *indirect searches*, we look for SM particles that can be produced in DM annihilations in DM dense structures in the sky. In *direct detection*, DM particles from the halo could pass through deep underground detectors filled with inert material, occasionally scattering off target nuclei. This could lead to recoil signatures in the target material through which we can look for DM. Recently, gravitational wave astronomy has enabled a completely new way to look for DM. Dark sectors that involve a first order phase transition can produce gravitational waves, as well as contain a thermal relic DM candidate. This will be the focus of chapter 4.

We will discuss the status of searches for GeV-TeV scale WIMPs in the following subsections.

1.4.1. Direct detection

Direct detection experiments look for galactic halo DM scattering off target nuclei or bound electrons in low-background underground detectors. The energy deposited can lead to scintillation, ionisation or phonon emission which can be detected with appropriate detector design. For a DM mass m_{DM} and speed v, the expected differential event rate is given by,

$$\frac{\mathrm{d}R\left(E_R,t\right)}{\mathrm{d}E_R} = N_T \frac{\rho_\odot}{m_{\mathrm{DM}}} \int_{v>v_{\mathrm{min}}} v f\left(\vec{v}+\vec{v}_E(t)\right) \frac{\mathrm{d}\sigma\left(E_R,v\right)}{\mathrm{d}E_R} \mathrm{d}^3 v. \tag{1.7}$$

Here, N_T is the number of target nuclei, σ is the nuclear scattering cross-section and v_{min} is the minimum velocity required to produce a recoil energy E_R. The local DM density $\rho_\odot$ and the DM velocity distribution $f\left(\vec{v}+\vec{v}_E(t)\right)$ enter as inputs from astrophysical observations. The observation or non-observation of signals constrain σ for a given m_{DM}. Despite the large experimental effort in designing, building and operating such experiments over nearly 4 decades, we haven't found DM so far, leaving us with upper-limits on the scattering cross-section. Recently, LZ collaboration set the most stringent constraint to-date on the spin-independent (SI) and spin-dependent (SD) WIMP-nucleon scattering cross-sections in the GeV-TeV mass range [45].

Shown in Figure 1.3 is the upper limit on σ_{SI} for different m_{DM} from various experiments. By tracking the motion of stars in our local neighbourhood, the local DM density has been measured to be $\rho_\odot \approx 0.5\,\mathrm{GeV\,cm^{-3}}$. Thus, large DM masses mean lower DM flux and lower event rates compared to smaller masses. The sensitivity therefore increases towards smaller masses. Similar to $\rho_\odot$, the local DM velocity has been determined to peak around $200\,\mathrm{km\,s^{-1}}$.

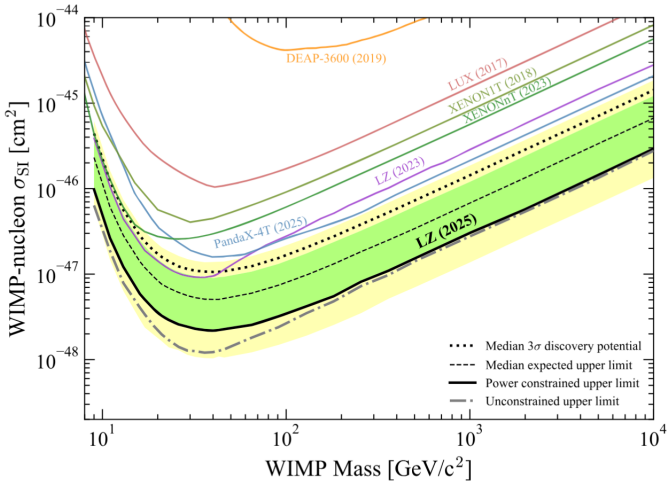

Figure 1.3.: World leading spin independent WIMP-nucleon cross-section constraint from the LZ experiment. Taken from [45].

Thus for very small masses, the kinetic energy available for transfer to the target material decreases and detection of very small recoil energies becomes increasingly difficult. The sensitivity hence decreases towards very small masses below about 10 GeV. This gives rise to the characteristic shape of direct detection upper-limits. For many generic WIMP models, with heavy DM and portals to SM through existing mediators, such a strong constraint on the WIMP-nucleon scattering cross-section excludes most part of the model parameter space that can correctly reproduce the observed DM relic abundance.

Electrons, being much lighter than nuclei, allow for relatively larger momentum transfer from galactic DM. Hence, detectors with sufficiently low energy thresholds can be sensitive to sub-GeV DM via electron recoils. Moreover, ionisation electrons produced in nuclear recoils through the *Migdal effect* [46] can increase sensitivity to sub-GeV DM. These bounds on sub-GeV DM scattering will be relevant for the models we will study later in the thesis, see subsection 3.2.3.

1.4.2. Indirect detection

In the current universe, we have plenty of DM dense structures in the sky. DM in these regions could annihilate into SM particles. Such annihilation products would lead to an excess above the expected flux from astrophysical backgrounds. Annihilation into most SM final states leads, directly or indirectly, to photon production. On the other hand, DM annihilations can produce SM anti-particles that are otherwise rare compared to SM particles. Thus, an excess in γ-rays or anti-particles would be a good candidate for a DM signal. Moreover, complementary excesses in several of these messengers would be a smoking-gun signal of DM.

Over the years, we have observed excesses in both anti-particles and γ-rays. Examples include the galactic center γ-ray excess (GCE) observed by Fermi-LAT [47], positron excess observed by PAMELA [48] and the antiproton excess reported in AMS-02 [49]. While the source of the galactic center excess is still a topic of intense debate [50], it has been shown that correct modelling of systematics leads to very low statistical significance for the antiproton excess [51, 52]. Moreover, the antiproton excess seemed to prefer slightly heavier DM masses than that required to fit the galactic center γ-ray excess, with a small overlap in the preferred regions [53]. But the common DM interpretation is very sensitive to background and signal modelling. Thus, such excesses in several of these messengers is more an indication of the highly complex astrophysical backgrounds and signal modelling, rather than an underlying DM model.

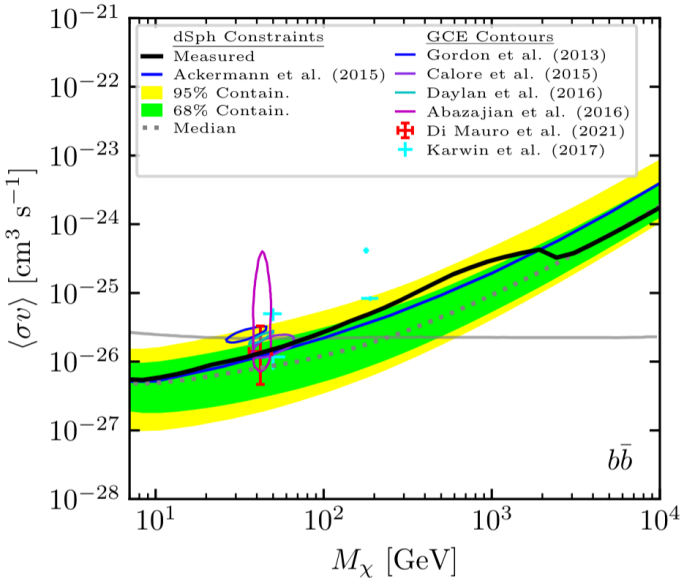

Figure 1.4.: Constraints on annihilation into bottom quarks from analysis of 14 year Fermi-LAT data of Milky Way dwarf spheroidal galaxies, taken from [54].

Currently, the most robust and stringent constraint on DM annihilation comes from the 14-year Fermi-LAT data of Milky Way dwarf spheroidal galaxies [54]. They are DM-dominated with low astrophysical backgrounds, making them perfect for indirect detection studies. Constraints on annihilation into bottom quarks are shown in Figure 1.4. Like in direct detection, the number density of DM particles in a gravitationally bound astrophysical object decreases with larger DM masses, hence we see decrease in sensitivity with increasing masses. The constraint on the total annihilation cross-section of a DM model is obtained by rescaling the published constraint on annihilation into a specific channel by the corresponding branching ratio. These constraints once again severely limit the model parameter space allowed for the generic WIMP DM.

1.4.3. Collider searches

DM can be produced in colliders in SM particle collisions. Such DM produced in colliders would escape the detectors undetected due to their feebly-interacting nature. This would lead to events with missing energies, which constitutes the DM signal. Such events can be identified if they are accompanied by visible particles and are hence called *mono-X* signals. But these aren't the only channels through which we can look for DM. If DM is coupled to one of the existing heavier SM bosons, then DM can be produced in their decays. One can then look for invisible decays of these SM mediators to constrain DM. If the DM model instead involves a new mediator, depending on the mediator mass and coupling to SM and DM, a variety of different collider signals can be produced. Thus, maximally utilizing the different ways in which DM can be constrained with colliders often requires full specification of the new physics relevant for DM phenomenology at colliders. The collider searches are hence, inherently model-dependent and depend sensitively on the DM and mediator properties. As a result, constraints are usually presented for certain benchmark models called simplified models. These models consist of a DM and a mediator with different choices of spins and couplings for both.

As an example, we show in Figure 1.5, the constraints on a model with a Dirac DM coupled to a vector mediator, from various searches performed by the CMS collaboration [55]. For the given couplings, the colored regions are excluded at 95% confidence level by various

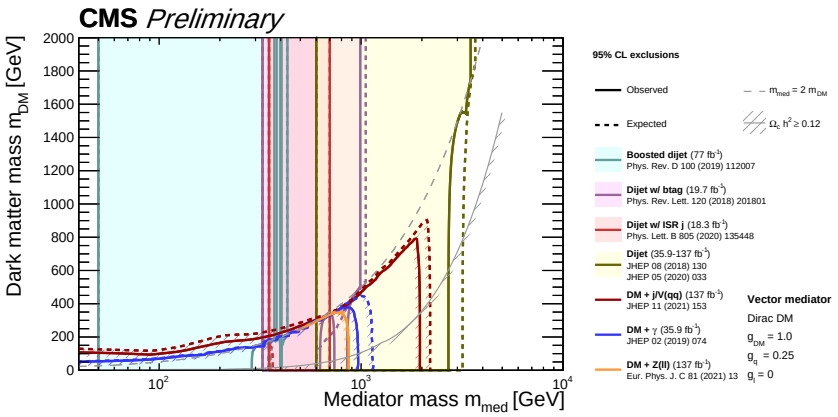

Figure 1.5.: Exclusion bounds on the plane of DM mass vs. mediator mass, from different searches performed by the CMS collaboration. From [55]

searches; the grey hashed line corresponds to parameter values that reproduce the DM relic abundance. We observe viable regions only above a few TeV. Over the years, the CMS and ATLAS collaborations have performed many such DM searches, notably placing stringent bounds on a number of WIMP candidates.

1.5. Pathways to a new landscape: Beyond conventional WIMPs

As summarized in the previous section, the decades long searches for conventional WIMPs – GeV-TeV scale DM particles with weak-scale interactions with the SM, produced by thermal freeze-out mechanism – have heavily constrained the allowed parameter space that can reproduce the correct relic abundance in most cases [41]. Furthermore, many of the experiments that currently place stringent constraints are still running, with constraints only expected to get stronger with increased exposure, unless we find unambiguous complementary DM signals across different searches.

Current direct detection experiments like PandaX-4T and LZ are pushing sensitivities toward the so-called "neutrino floor," where backgrounds from coherent elastic neutrino-nucleus scatterings (CEνNS) begin to dominate. Notably, at the IDM 2024 conference in L'Aquila, the XENONnT collaboration announced the first-ever observation of a CEνNS event from a solar neutrino using a Xe target [56]. With proof that such observations are now possible, direct detection experiments are expected to penetrate the neutrino-floor and turn it into a "neutrino-fog", which will allow us to keep looking for DM [57]. Upcoming experiments like PandaX-xT [58], XLZD [59] will probe DM-nucleon scatterings down to very weak couplings and improve the current constraints further. In indirect detection, with more γ-ray and cosmic-ray data from Fermi-LAT and AMS-02, constraints are expected to get stronger, but would require better control of astrophysical backgrounds for significant gains in sensitivity. The upcoming Cherenkov Telescope Array (CTA) [60] will further enhance the sensitivity to multi-TeV-scale DM, especially via searches for very high-energy gamma-ray signatures.

In response to these developments, theoretical explorations of scenarios beyond the vanilla models of WIMP DM became a need of the hour. These explorations in DM model building are informed and shaped by current experimental constraints. Therefore, any plausible DM model proposed today, apart from fitting the cosmological DM bill, has to also be able to *evade* constraints from DM searches so far. Several promising directions have emerged.

Non-thermal production: Alternate production mechanisms like *freeze-in* production [61], make it possible to produce the correct DM abundance even for very small couplings while

evading constraints. It does so by beginning with a negligible out-of-equilibrium DM population and is produced by inverse decays or annihilations of SM particles in the thermal bath. Once these interactions drop out as they become inefficient compared to the expansion rate of the universe, the production stops and the abundance becomes constant.
Multi-component DM: A different solution is to consider that the WIMP DM model makes up only a fraction of DM [62], thus evading direct and indirect detection constraints. Although a plausible scenario, this is an unsatisfactory solution as it simply changes the problem to a new one - what is the rest of DM made of?

Here, we want to focus on WIMP DM produced through thermal freeze-out, so we look for ways to produce the correct relic abundance in the early universe, while suppressing the DM-nucleon scatterings and DM-DM annihilations in the current universe. Different models have been studied that manage to evade either direct or indirect detection constraints or sometimes, both. We mention some of them here.

Asymmetric DM: Another possibility is to introduce an asymmetry between DM particles and antiparticles similar to the baryon asymmetry. Such an asymmetry would suppress indirect detection constraints and the new physics that produces the DM asymmetry might make testable predictions, see review [63].
Secluded DM: The relic density is set by DM annihilations dominantly into dark sector states that later decay away. Direct constraints can be evaded through very small couplings to SM, while still reproducing the correct DM relic abundance [64].
Co-annihilations and inelastic DM: In dark sectors with additional nearly mass-degenerate unstable particles χ_i', apart from the stable DM particle χ, the correct DM relic abundance can be set by self-annihilations and co-annihilations ($\chi+\chi_i' \to \mathrm{SM}+\mathrm{SM}$) [65]. If the relic density is mainly set by co-annihilations, the self-annihilation ($\chi+\chi \to \mathrm{SM}+\mathrm{SM}$) cross-section is unconstrained by the relic density requirement and can be tiny enough to evade indirect detection constraints. Additionally, if scattering with SM is always inelastic ($\chi + \mathrm{SM} \to \chi_i' + \mathrm{SM}$), the direct detection constraints can be evaded through kinematic suppression of the inelastic scattering cross-section in the late universe [66].
Resonant annihilations: The annihilation cross-section is resonantly enhanced at early times close to freeze-out, but becomes suppressed at later times, evading indirect detection constraints.
Forbidden annihilations: Forbidden annihilations to heavier final states can be accessible in the early universe to set the correct DM relic abundance, while becoming kinematically forbidden in the late universe.
Furthermore, more exotic scenarios exist, such as late-time entropy injection (e.g., from decaying particles [67]) or modified cosmological histories (e.g., early matter domination [68] or late-time inflation [69]), which can dilute an initially overproduced DM abundance or change the freeze-out dynamics.

In this thesis, we will choose the strategy of going to sub-GeV DM masses to evade direct detection constraints. In the first two chapters, we will collect different model-building guidelines that come from DM searches in callout boxes, as shown below.

Model-building guide

1. DD constraints can be evaded by going to sub-GeV masses.

These guidelines will later help us build viable DM models. Coming back to sub-GeV DM, they can reproduce the correct relic abundance with the introduction of a new mediator. The indirect detection constraints can be evaded by using one or more of the above-mentioned

strategies. The mediators in these models can be probed with beam-dump experiments at accelerators. Such a rich predictive phenomenology and a well-established theoretical framework make sub-GeV DM models attractive candidates.

One of the two main outputs of this thesis, is global fits of sub-GeV DM models with `GAMBIT` [70]. Global fits is a statistical method to constrain models with more than two free parameters, with data from different experiments. `GAMBIT`, which stands for *Global And Modular BSM Inference Tool*, is a code specializing in performing beyond-the-Standard Model (BSM) global fits. The other main output is the tool `GUtilized`, developed as a part of this thesis for the visualization of global fit results. In chapter 2, we will present the cosmological and astrophysical constraints relevant to sub-GeV DM that guide us in building viable DM models. In chapter 3 and chapter 4, we will study specific sub-GeV DM models, relevant constraints, and present the results from their global fits with `GAMBIT`. In chapter 5, we will examine the statistical methods used in this thesis and present the usage and features of `GUtilized`.

CHAPTER 2

Cosmological and astrophysical constraints

In this chapter, I first review the existing astrophysical and cosmological constraints on dark matter in the literature. As part of the work leading to the first publication (discussed in chapter 3), I constructed and implemented an improved version of the bullet cluster likelihood, which is presented in subsection 2.6.2.

In this chapter we study the relevant astrophysical and cosmological constraints on sub-GeV thermal DM. We begin the chapter by making arguments for how the evolution of the universe should have approximately played out based on the glimpses we have of its timeline in section 2.1. Before discussing constraints, we study DM production through freeze-out in section 2.2, which should explain the only unambiguous signal we have of DM so far, its relic abundance measured by the CMB. We then start with the earliest observable, primordial light elements produced in BBN. In section 2.3, we will present how BBN proceeds in standard cosmology, how to make precise predictions for light element abundances and then various ways in which dark sector particles affect BBN. We then move on to the next interesting event in the cosmic timeline, the production of CMB photons. In section 2.4, we start with a brief description of the events that lead to photon decoupling, and then discuss various ways to constrain dark sector particles using CMB. Moving to even later times, the current universe, we present indirect detection constraints on sub-GeV DM in section 2.5. We summarize the various constraints on annihilating and decaying DM from BBN, CMB and indirect detection in section 2.5. Finally, in section 2.6, we mention various ways of constraining DM self-interactions before presenting an improved version of the bullet cluster constraint.

2.1. The big picture

The investigation of microphysics of the early universe is greatly simplified thanks to the works of a few great minds. If there are interactions that can establish local thermal equilibrium, the phase space distributions are known and described by two thermodynamic quantities, temperature T and chemical potential μ. The thermal distribution for relativistic particles is given by,

$$f(t,E) = \frac{g}{(2\pi)^3} \frac{1}{1 \pm \exp\left(\frac{E-\mu(t)}{T(t)}\right)} \ , \tag{2.1}$$

where g is the number of internal degrees of freedom, the positive sign in the denominator is for fermions (*Fermi-Dirac* distribution) and the negative sign is for bosons (*Bose-Einstein* distribution). For a dilute non-relativistic gas for which $m \gg T$ and $(m-\mu) \gg T$, the thermal distributions for both bosons and fermions reduce to the *Maxwell-Boltzmann* distribution ,

$$f(t,p) = \frac{g}{(2\pi)^3} \exp\left(\frac{\mu(t)-m}{T(t)}\right) \exp\left(-\frac{p^2}{2mT(t)}\right) . \tag{2.2}$$

The number, energy and pressure densities can be determined from these thermal distributions. Using these distributions, we also find that $T \gg m$ corresponds to a relativistic species with $\langle p^2 \rangle \gg m^2$, and $T \ll m$ to a non-relativistic species.

Armed with thermal distributions, let us now examine when DM freeze-out can happen without contradicting observations. In freeze-out production, DM is initially kept in thermodynamic (chemical and kinetic) equilibrium with the SM through some DM-SM interactions. As the universe expands and cools down, the number densities dilute, decreasing the interaction rate that maintains chemical equilibrium between DM and SM. Once this interaction rate drops below the Hubble rate, the co-moving DM number density stays constant. If one assumes instantaneous decoupling, the number density at freeze-out would be approximately given by the equilibrium number density,

$$n_{\rm DM}(T_{\rm f}) \approx n^{\rm eq}_{\rm DM}(T_{\rm f}) . \tag{2.3}$$

The energy density after freeze-out would then simply redshift as $\rho_{\rm DM} \propto a^{-4}$ if it is relativistic and $\rho_{\rm DM} \propto a^{-3}$ if non-relativistic.

For a non-relativistic freeze-out, a simple argument can tell us the suitable range of values for the ratio between the DM mass ($m_{\rm DM}$) and the freeze-out temperature ($T_{\rm f}$), $x_{\rm f} = m_{\rm DM}/T_{\rm f}$. A useful quantity in studying DM freeze-out is the yield, $Y_{\rm DM} = n_{\rm DM}/s$. Here, s is the total entropy density of the SM thermal bath. In the absence of entropy injection, the co-moving entropy density of the SM plasma is always conserved, as so is the co-moving DM number density after freeze-out. The yield, therefore, stays constant after freeze-out. The observed yield can be calculated from the abundance as,

$$Y_{\rm DM,obs} = \frac{\rho_{\rm c,0}\ \Omega_{\rm DM}}{s_0\ m_{\rm DM}}$$

One can then calculate the values of $x_{\rm f}$ that reproduce the observed yield for different values of $m_{\rm DM}$.

The results are shown in Figure 2.1. For thermal DM mass range bounded by the warm DM constraint from below and unitarity bound from above, $m_{\rm DM} \in [3\,{\rm keV}, 100\,{\rm TeV}]$, we see that the observed DM yield can be achieved with $x_{\rm f} \approx 10 - 30$. This result implies that DM has to freeze-out soon after the temperature becomes comparable to its mass. This is because, the number density of non-relativistic DM with a negligible chemical potential consists of an exponential factor, $n_{\rm DM} \propto \exp(-m_{\rm DM}/T)$ called the Boltzmann suppression. Hence, it has to freeze-out quick enough after turning non-relativistic to avoid getting completely depleted by the Boltzmann suppression.

Let us now make arguments based on BBN and CMB observations for if and when relativistic and non-relativistic DM freeze-out can occur. From the perfect match between predictions and observations of light element abundances, we know that, at the beginning of BBN, the energy density of the universe was dominated by the SM relativistic species which consisted of mainly photons and neutrinos[3],

$$\rho_{\rm tot}(T_{\rm BBN}) \approx \rho_{\rm rad}(T_{\rm BBN}) \approx \rho_\gamma(T_{\rm BBN}) + \rho_\nu(T_{\rm BBN}) . \tag{2.4}$$

[3]Here, we neglect $e^\pm$ which only changes $\rho_{\rm rad}$ by a factor of $\mathcal{O}(1)$.

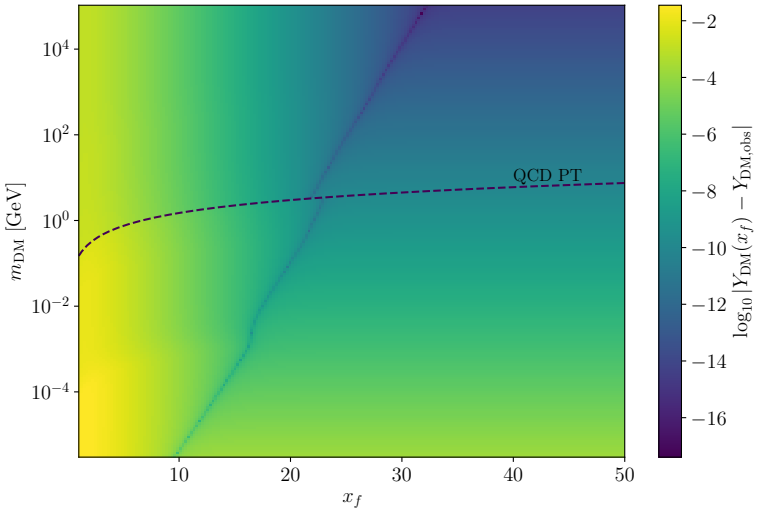

Figure 2.1.: Difference between yield at freeze-out and observed yield for different values of $x_{\rm f} = m_{\rm DM}/T_{\rm f}$ and $m_{\rm DM}$.

Based on this observation, we can deduce that DM should freeze-out before BBN and after turning non-relativistic. Let's discuss why other scenarios are in contradiction with Equation 2.4.

DM that is relativistic and in chemical equilibrium with the SM thermal bath would have $\rho_{\rm DM}(T_{\rm BBN}) \sim \rho_\gamma(T_{\rm BBN})$. Therefore, DM freeze-out, has to happen before BBN. DM that underwent a relativistic freeze-out before BBN and is still relativistic during BBN, in the absence of new physics that changes the temperature of DM, would have redshifted with $T_{\rm DM} = T_{\rm SM}$ and hence would also have $\rho_{\rm DM}(T_{\rm BBN}) \sim \rho_\gamma(T_{\rm BBN})$.

For DM that underwent a relativistic freeze-out before BBN, even if it had become non-relativistic by the time of BBN, i.e. $m_{\rm DM} > T_{\rm BBN}$, it is still in contradiction with Equation 2.4. To see why, let us calculate the ratio of DM and SM radiation energy densities at the start of BBN (denoted by subscript BBN). If DM underwent freeze-out when it was relativistic, at decoupling it has an energy density of the same order of magnitude as the SM radiation energy density, $\rho_{\rm DM,dec} \sim \rho_{\rm rad,dec}$. After decoupling, it will redshift as a^{-4} until it turns non-relativistic, at which point, it will start decreasing as a^{-3}. We have,

$$\begin{aligned} \rho_{\rm DM,dec}\ a_{\rm dec}^4 &\approx \rho_{\rm DM,NR}\ a_{\rm NR}^4\ , \\ \rho_{\rm DM,NR}\ a_{\rm NR}^3 &\approx \rho_{\rm DM,BBN}\ a_{\rm BBN}^3\ , \end{aligned} \tag{2.5}$$

where the subscript NR indicates the quantities at a time when DM turns non-relativistic, i.e. at $T_{\rm NR} \sim m_{\rm DM}$. Using these equations, we can calculate the DM energy density at the start of BBN as,

$$\rho_{\rm DM,BBN} \approx \rho_{\rm DM,dec} \left(\frac{a_{\rm dec}}{a_{\rm NR}}\right)^4 \left(\frac{a_{\rm NR}}{a_{\rm BBN}}\right)^3 . \tag{2.6}$$

Since the SM radiation energy density redshifts as a^{-4}, we have $\rho_{\rm rad,dec}\, a_{\rm dec}^4 = \rho_{\rm rad,BBN}\, a_{\rm BBN}^4$. We can then calculate the ratio of DM and radiation energy densities at the beginning of BBN as,

$$\begin{aligned}\frac{\rho_{\rm DM,BBN}}{\rho_{\rm rad,BBN}} &\approx \left(\frac{a_{\rm BBN}}{a_{\rm dec}}\right)^4 \left(\frac{a_{\rm dec}}{a_{\rm NR}}\right)^4 \left(\frac{a_{\rm dec}}{a_{\rm NR}}\right)^4 \approx \frac{a_{\rm BBN}}{a_{\rm NR}} \\ &\approx \frac{T_{\rm NR}}{T_{\rm BBN}} \sim \frac{m_{\rm DM}}{T_{\rm BBN}} \gtrsim 1 \ . \end{aligned} \tag{2.7}$$

In the above calculation, we have used $aT =$ constant implied by entropy conservation. This is only true as long as g_*, the effective entropy degrees of freedom of the SM plasma, remains constant. But, even when including it's variation with temperature, the result doesn't change because $g_*(T_{\rm BBN}) < g_*(T_{\rm NR})$. Therefore, to be consistent with BBN observations, DM cannot freeze-out while it is still relativistic.

For DM that decoupled before BBN, when it was non-relativistic, one can calculate the ratio of DM and radiation energy densities at the beginning of BBN, that is consistent with the current day DM and radiation abundances as measured by the CMB. The energy densities at $T = 10\,\text{MeV}$ can be related to their current day energy densities as,

$$\begin{aligned}\rho_{\rm DM}(10\,\text{MeV}) =& \rho_{\rm DM,0} \left(\frac{a_0}{a(10\,\text{MeV})}\right)^3 \ , \\ \rho_{\rm rad}(10\,\text{MeV}) =& \rho_{\rm rad,0} \left(\frac{a_0}{a(10\,\text{MeV})}\right)^4 \ . \end{aligned}$$

Neglecting the brief change in g_* due to $e^\pm$ annihilation, and rewriting in terms of quantities measured by the CMB, we get,

$$\begin{aligned}\frac{\rho_{\rm DM}}{\rho_{\rm rad}}(10\,\text{MeV}) \approx& \frac{\Omega_{\rm DM}}{\Omega_{\rm rad}} \left(\frac{T_0}{10\,\text{MeV}}\right) \\ \approx& \frac{\Omega_{\rm DM}}{\frac{8\pi G}{3H_0^2}\frac{\pi^2}{30}\left(2 + \frac{7}{8} 2 N_{\rm eff} \left(\frac{4}{11}\right)^{4/3}\right) T_0^4} \left(\frac{T_0}{10\,\text{MeV}}\right) \end{aligned}$$

For $\Omega_{\rm DM} \approx 0.24$, $H_0 \approx 70\,\text{km/Mpc/s}$, $N_{\rm eff} \approx 3$, $T_0 \approx 0.2\,\text{meV}$, we get

$$\frac{\rho_{\rm DM}}{\rho_{\rm rad}}(10\,\text{MeV}) \sim \mathcal{O}(10^{-7})$$

Thus, to be consistent with both BBN and CMB observations, DM should freeze-out once it turns non-relativistic and the freeze-out should happen before BBN, such that the DM energy density at the start of BBN is already negligible compared to that of the radiation energy density. An exception here is if one can find a way to avoid Boltzmann suppression while being non-relativistic, in which case freeze-out can happen even after BBN. This will be the case in one of the models we study in this thesis, discussed in chapter 4.

In case our model has other thermal dark sector particles, their energy densities should also be negligible at the time of BBN. For relativistic particles, this can be achieved by having a temperature smaller than that of the SM thermal bath. For a non-relativistic species in chemical equilibrium with the SM plasma, negligible chemical potentials can lead to exponentially suppressed number densities. For decoupled particles, the solution is to deplete their energy densities by decays or annihilations to SM particles. We will see in subsection 2.3.2 and subsection 2.4.1 how such scenarios can be constrained by BBN and CMB.

2.2. Freeze-out

The picture of DM freeze-out presented so far makes multiple assumptions, most importantly, that DM decoupled instantaneously. This allowed us to make the approximation in Equation 2.3. But, of course, decoupling is not instantaneous and occurs over a range of temperatures such that $T_{\rm f}$ is not well defined. Therefore, DM freeze-out should be studied using Boltzmann equations for every new particle that contributes to the the DM relic abundance.

In all DM models studied in this thesis, we only consider one DM species that is not self-conjugate. In this section, we will thus focus on the freeze-out of a DM model with a single particle DM candidate χ which is different from its anti-particle $\bar{\chi}$. The Boltzmann equation describes the out-of-equilibrium evolution of the DM phase-space distribution $f_{\chi(\bar{\chi})}(\mathbf{x}, \mathbf{p}, t)$,

$$\hat{L}[f_{\chi(\bar{\chi})}(\mathbf{x}, \mathbf{p}, t)] = \hat{C}[f_{\chi(\bar{\chi})}(\mathbf{x}, \mathbf{p}, t)], \tag{2.8}$$

where the Liouville operator $\hat{L}$ involves partial derivatives of the phase-space distribution and the collision operator involves multiple integrals. Solving such an integro-differential equation can be highly challenging. We will make a series of arguments and reasonable assumptions to reduce the above complex Boltzmann equation to a simpler and solvable form. The LHS in the above equation can be simplified by considering the fact that the adiabatic perturbations were small in the radiation-dominated early universe. We can thus assume homogeneity and isotropy,

$$f_{\chi(\bar{\chi})}(\mathbf{x}, \mathbf{p}, t) = f_{\chi(\bar{\chi})}(E, t)$$

which simplifies the Liouville operator to $\dfrac{\mathrm{d}f_{\chi(\bar{\chi})}}{\mathrm{d}t}$. For non-negligible perturbations caused by exotic physics, the acoustic oscillations of the plasma can potentially cause freeze-out to progress inhomogeneously, thus affecting the average DM relic abundance [71]. In this thesis, we stick to the simpler case with negligible adiabatic perturbations during DM freeze out. To simplify the RHS, we need to make assumptions on the microscopic properties of particles and interactions, as discussed below.

First, a vast simplification of the collision operator is achieved by assuming efficient DM number-conserving elastic scatterings that can establish thermal equilibrium between DM and the SM thermal bath in the early universe. This allows us to work with the known thermal distributions. Assuming that kinetic equilibrium holds until the end of freeze-out, we can integrate out the momenta on both sides of the Boltzmann equation,

$$\frac{\mathrm{d}n_{\chi(\bar{\chi})}}{\mathrm{d}t} + 3Hn_{\chi(\bar{\chi})} = g\int \frac{\mathrm{d}^3p}{(2\pi)^3}\hat{C}[f_{\chi(\bar{\chi})}], \tag{2.9}$$

where g is the number of internal degrees of freedom of the DM particle. Secondly, for a *non-relativistic* DM freeze-out, the more fundamental requirement is DM participation in number-changing interactions with *lighter* SM particles. These interactions establish chemical equilibrium between DM and SM in the early universe. Such interactions can include annihilations and decays, as well as their inverse processes. For a DM model with the only number-changing process being $\chi\ \bar{\chi} \leftrightarrow$ SM SM, the collision integral becomes,

$$g\int \frac{\mathrm{d}^3p}{(2\pi)^3}\hat{C}[f_{\chi(\bar{\chi})}] = n_{\chi}^{(0)}n_{\bar{\chi}}^{(0)}\langle\sigma_{\rm ann}v\rangle\left[\frac{(n_{\rm SM}^{(\rm eq)})^2}{(n_{\rm SM}^{(0)})^2} - \frac{n_{\chi}n_{\bar{\chi}}}{n_{\chi}^{(0)}n_{\bar{\chi}}^{(0)}}\right], \tag{2.10}$$

where $n_X^{(0)}$ denotes number density of the species X with zero chemical potential, $n_X^{(0)} = n_X(T, \mu_X = 0)$. Note that this need not be equal to the equilibrium number density. For

instance, asymmetric species have non-zero chemical potentials in chemical equilibrium. Here, $\langle\sigma_{\rm ann}v\rangle$ is the thermal average of the product of the total annihilation cross-section times the relative velocity of the annihilating particles.

Moreover, SM bosons have no conserved number and hence $\mu_{\rm bosons} = 0$ and SM fermions are observed to have a very small asymmetry, such that in the early universe, when they are relativistic, $\mu_{\rm fermions}/T \ll 1$. Thus, for annihilations predominantly into either SM bosons or relativistic SM fermions, we can assume $n^{\rm eq}_{\rm SM} = n^{(0)}_{\rm SM}$ [4]. Using this approximation, we arrive at the standard Boltzmann equation for non-relativistic freeze-out,

$$\frac{{\rm d}n_{\chi(\bar{\chi})}}{{\rm d}t} + 3Hn_{\chi(\bar{\chi})} = -\langle\sigma_{\rm ann}v\rangle(n_\chi n_{\bar{\chi}} - n^{(0)}_\chi n^{(0)}_{\bar{\chi}}). \tag{2.11}$$

One would then have to numerically integrate the above equation until today to get the present day DM number density, from which we can obtain the relic abundance. But a more suitable form of the Boltzmann equation for numerical integration can be written in terms of the DM yield, $Y_{\chi(\bar{\chi})} = n_{\chi(\bar{\chi})}/s$ [65]. Now, all terms in the equation are known as an explicit function of temperature, hence we switch to $x = m_\chi/T$ as the integration variable,

$$\frac{{\rm d}Y_{\chi(\bar{\chi})}}{{\rm d}x} = -\frac{m}{x^2}\frac{1}{3H}\frac{{\rm d}s}{{\rm d}T}\langle\sigma_{\rm ann}v\rangle(Y_\chi Y_{\bar{\chi}} - Y^{(0)}_\chi Y^{(0)}_{\bar{\chi}}), \tag{2.12}$$

where we used

$$\frac{{\rm d}T}{{\rm d}t} = -3Hs\frac{{\rm d}T}{{\rm d}s},$$

which comes from entropy conservation of the SM thermal bath. We use the standard relations for quantities in radiation domination,

$$H^2 = \frac{8\pi G}{3}\rho, \quad \rho = g_{\rm eff}(T)\frac{\pi^2}{30}T^4, \quad s = h_{\rm eff}(T)\frac{2\pi^2}{45}T^3, \tag{2.13}$$

where $g_{\rm eff}$ and $h_{\rm eff}$ are the effective energy and entropy degrees of freedom respectively. For the yield $Y^{(0)}_{\chi(\bar{\chi})}$, we use,

$$Y^{(0)}_{\chi(\bar{\chi})} = \frac{n^{(0)}_{\chi(\bar{\chi})}}{s} = \frac{1}{s}\left(g\left(\frac{m_\chi T}{2\pi}\right)^{3/2}\exp\left(\frac{-m_\chi}{T}\right)\right) . \tag{2.14}$$

We can then numerically integrate Equation 2.12 using these relations, from $x = 0$ to $x = m_\chi/T_0$, where $T_0 = 2.726\,{\rm K}$ is the current day photon temperature. The DM density parameter is then obtained from the current day DM yield $Y_{\chi(\bar{\chi}),0}$ as,

$$\Omega_{\rm DM}h^2 = 2.755\times10^8\left(\frac{m_\chi}{1{\rm GeV}}\right)(Y_{\chi,0} + Y_{\bar{\chi},0}). \tag{2.15}$$

Following [72], one can also obtain a rough analytic estimate of the abundance as,

$$\Omega_{\rm DM}h^2 = 0.1\ \frac{x_{\rm f}(m_\chi)}{20}\ \left(\frac{g_*(m_\chi)}{100}\right)^{1/2}\ \frac{2\times10^{-26}\,{\rm cm}^3\,{\rm s}^{-1}}{\langle\sigma_{\rm ann}v\rangle}\ . \tag{2.16}$$

Model-building guide

2. MeV-scale DM can reproduce the correct relic abundance with $\langle\sigma_{\rm ann}v\rangle \sim 10^{-27} - 10^{-26}\,{\rm cm}^3\,{\rm s}^{-1}$ $(10^{-10} - 10^{-9}\,{\rm GeV}^{-2})$.

[4] In the case where such an approximation is not possible, eg. annihilation into other dark sector states, one would have to solve the coupled Boltzmann equations, with non-zero chemical potentials, for the initial and final states involved in the DM number-changing process that sets the DM relic abundance. See chapter 4.

It is important to stress here that the Planck 2018 measurement [7] (TT,TE,EE+lowE+lensing) gives the DM density parameter with percent-level precision,

$$\Omega_{\rm DM}h^2 = 0.1200 \pm 0.0012 \ . \tag{2.17}$$

Hence, we must understand the level and sources of uncertainties in our theoretical prediction.

One non-trivial task involved in solving Equation 2.12 is the computation of $\langle\sigma_{\rm ann}v\rangle$. Following [73], it is calculated calculated as[5],

$$\langle\sigma_{\rm ann}v_{\rm M\o l}\rangle = \frac{1}{8m_\chi^4 T K_2^2(m_\chi/T)}\int_{4m_\chi^2}^{\infty}\sigma_{\rm ann}\left(s-4m_\chi^2\right)\sqrt{s}K_1(\sqrt{s}/T)\mathrm{d}s. \tag{2.18}$$

using Bessel functions of the first and second kind, K_1 and K_2 and Maxwell-Boltzmann statistics, instead of relativistic thermal distributions, which can contribute to $\sim 1\%$ errors. Ignoring higher-order corrections to relevant cross-sections can also introduce uncertainties. Poor numerical treatment of $\langle\sigma_{\rm ann}v_{\rm M\o l}\rangle$ when effects such as resonances and thresholds are involved can further introduce significant uncertainties. Uncertainties can also enter from predictions of background SM processes, most notably the QCD phase transition [74]. Differences in such theoretical and numerical considerations often result in a few % discrepancy between different sophisticated codes like `DarkSUSY 6` [75] and `micrOMEGAs` [76]. We can thus safely assume that most often, the uncertainties in theoretical predictions are larger than that in observation.

To conclude, let us summarize this section with a physical picture of the stages of evolution for a generic WIMP-like DM particle:

- DM starts in chemical and kinetic equilibrium with the SM plasma. DM follows the equilibrium number density, $n^{\rm eq}_{\chi(\bar{\chi})}(T)$. While DM is still relativistic, the comoving number density is conserved as annihilations and pair productions balance each other. The DM temperature evolves due to the expansion of the universe and its relation to time or scale factor is governed by conservation of the total entropy of the thermal bath.
- As soon as DM turns non-relativistic, pair production becomes inefficient and number densities fall, $n^{\rm eq}_{\chi(\bar{\chi})} \propto \exp\left(-m_\chi/T\right)$.
- *Chemical decoupling*: Annihilations become inefficient compared to the universe expansion, thus comoving number densities once again become constant. This means the number density deviates from the equilibrium density, $n_{\chi(\bar{\chi})} \neq n^{\rm eq}_{\chi(\bar{\chi})}$, and the chemical potential now evolves to compensate for the Boltzmann suppression, $n_{\chi(\bar{\chi})} \propto \exp\left((\mu_{\chi(\bar{\chi})} - m_\chi)/T\right)$.
- *Kinetic decoupling*: Scatterings become inefficient. But the distribution can still be parametrised in terms of an effective temperature. This is because DM had a thermal distribution when it decoupled. After decoupling, the momentum of each decoupled DM particle decreases as $p \propto a^{-1}$. So, the shape of the distribution is maintained close to the thermal Maxwell-Boltzmann distribution, while being simply redshifted to lower temperatures. For non-relativistic DM, the temperature falls faster as $T_{\rm DM} \propto a^{-2}$, compared to that of the SM plasma in radiation domination, which goes as $T_{\rm SM} \propto a^{-1}$.

2.3. BBN

BBN is a theory that puts together all the existing and new tools that became available to 19th century physicists - nuclear physics, particle physics, statistical mechanics and cosmology. The unification of concepts from such different fields to make predictions about the

[5] In the absence of complications like resonances, thresholds or co-annihilations, for a non-relativistic gas, $\langle\sigma_{\rm ann}v\rangle$ can be approximated by an expansion in powers of x^{-1} by using $s = 4m_\chi^2 + 4m_\chi^2 v^2$.

early universe is in itself a great theoretical feat [77]. But an even more spectacular success is the precise agreement between predictions and observations of primordial light element abundances.

In this section, we review how BBN proceeds in standard cosmology, here on referred to as standard BBN (SBBN) and then in the subsections that follow, we will explore how BBN can constrain new physics, in particular, decaying and annihilating dark sector particles.

We start with an approximate analytic treatment of BBN, where we assume that various events occur when the relevant processes are in chemical equilibrium. This assumption lets us make use of the Saha equation, which will help us determine the order in which events occur. This assumption is incorrect and an accurate study of BBN involves following out-of-equilibrium processes with Boltzmann equations, which is discussed in subsection 2.3.1.

The formation of light elements occurs through a chain of nuclear reactions such as,

$$\begin{aligned} p + n &\to \mathrm{D} + \gamma \\ \mathrm{D} + \mathrm{D} &\to {}^3\mathrm{He} + n \\ {}^3\mathrm{He} + \mathrm{D} &\to {}^4\mathrm{He} + p \\ &\dots \end{aligned} \tag{2.19}$$

The number densities of these light elements build up considerably only at temperatures smaller than the binding energy of nuclei, otherwise they are immediately dissociated by energetic photons in the thermal bath. For the lightest stable nucleus, deuterium D, the binding energy is $B_D = 2.22\,\mathrm{MeV}$ and is smaller than that of the helium isotopes, $B_\mathrm{D} < B_{^3\mathrm{He}} < B_{^4\mathrm{He}}$. Even though the binding energies of helium isotopes are larger and can avoid photo-dissociation at $B_{3(4)He} > T > B_\mathrm{D}$, since the reaction chain starts with deuterium formation, formation of helium isotopes is also delayed until $T < B_\mathrm{D}$. This is the so-called *deuterium bottleneck*.

The temperatures relevant to BBN are, thus, $\mathcal{O}(1)\,\mathrm{MeV}$. In order to determine the initial conditions for BBN, let us examine the contents of the universe at 10 MeV. At these temperatures, SM particles in thermal equilibrium are:

- non-relativistic baryons (protons and neutrons). Due to a pre-existing asymmetry between baryons and antibaryons, the anti-baryons have been completely depleted by annihilations at this point, and we are left with just baryons. At these temperatures and below, the number density of baryons (n_b) is equal to that of the baryon number (n_B), which is conserved, $(n_b)a^3 = (n_B)a^3 = \text{const}$. This implies that for $n_B a^3$ to be conserved, protons ($m_p = 0.938\,\mathrm{GeV},\ g_p = 2$) and neutrons ($m_n = 0.939\,\mathrm{GeV},\ g_n = 2$) should have non-zero chemical potentials. Their number densities are then given by,

$$n_{n(p)}(T, \mu_{n(p)}) = g_{n(p)} \left(\frac{m_{n(p)} T}{2\pi}\right)^{3/2} \exp\left(\frac{\mu_{n(p)} - m_{n(p)}}{T}\right). \tag{2.20}$$

- relativistic electrons and positrons ($m_{e^\pm} = 0.5\,\mathrm{MeV},\ g_{e^\pm} = 2$) with negligible chemical potentials,
- three species of relativistic left-handed neutrinos and anti-neutrinos ($m_\nu = m_{\bar\nu} \approx 0,\ g_\nu = g_{\bar\nu} = 1$), with negligible chemical potentials,
- photons ($m_\gamma = 0,\ g_\gamma = 2$).

The universe is radiation dominated at these temperatures with,

$$H^2 = \frac{8\pi G}{3}\rho_{\rm rad} \ , \tag{2.21}$$

$$\rho_{\rm rad} = \frac{\pi^2}{30} g_* T^4 \ , \tag{2.22}$$

where g_* is the number of relativistic degrees of freedom. For these temperatures, g_* counts contributions from photons, electrons, positrons and three species of neutrinos and antineutrinos,

$$g_*(10\,{\rm MeV}) \approx g_\gamma + \frac{7}{8}(g_{e^-} + g_{e^+} + 3g_\nu + 3g_{\bar\nu}) = 10.75 \ . \tag{2.23}$$

Neutrons and protons are kept in chemical equilibrium by the processes,

$$p + e^- \leftrightarrow n + \nu_e, \quad p + \bar\nu_e \leftrightarrow n + e^+ \tag{2.24}$$

such that,

$$\mu_p + \mu_{\bar\nu_e} = \mu_n + \mu_{e^+}.$$

For negligible chemical potentials for electrons and electron neutrinos, we get $\mu_p = \mu_n$. Therefore, even without the exact knowledge of the value of chemical potentials, we can calculate the ratio of neutron-to-proton number densities as a function of just the temperature until they remain in chemical equilibrium,

$$\frac{n_n}{n_p}(T) = \left(\frac{m_n}{m_p}\right)^{3/2} \exp\left(\frac{-\Delta m}{T}\right). \tag{2.25}$$

where $\Delta m = m_n - m_p = 1.3\,{\rm MeV}$. Hence, at $T > 1.3\,{\rm MeV}$, we have $n_n/n_p \approx 1$. So, if protons and neutrons are maintained in chemical equilibrium until temperatures well below Δm, all neutrons would be converted to protons by the weak-interaction process in Equation 2.24. We would then be left with just protons, i.e. hydrogen nuclei and no heavier elements. But in reality, the weak interactions become inefficient before the neutron abundance is significantly depleted and the ratio n_n/n_p "freezes-out" and is reduced further only by neutron decays.

The temperature $T^{\rm f}_{np}$ at which n_n/n_p freezes-out can be approximated as the temperature at which the interaction rate for the above processes equals the Hubble rate,

$$\Gamma(T^{\rm f}_{np}) \approx \frac{1.66\sqrt{g_*(T)}}{M_{\rm Pl}}(T^{\rm f}_{np})^2 \ , \tag{2.26}$$

where $\Gamma(T) \approx 1.2 G_F^2 T^5$ for the p-n conversions through scattering off relativistic partners, and we have used the relation for the Hubble rate in radiation domination. Note that the relativistic degrees of freedom is a function of temperature and the above equation would have to be solved numerically. But we observe that, $\Gamma(10\,{\rm MeV}) > H(10\,{\rm MeV})$, while $\Gamma(0.5\,{\rm MeV}) < H(0.5\,{\rm MeV})$ and thus Equation 2.26 is satisfied somewhen between 10 MeV and 0.5 MeV. In this temperature range, $g_* \approx 10.75$. Using this value in Equation 2.26, we find $T^{\rm f}_{np} = 1.4\,{\rm MeV}$. It then follows from Equation 2.25 that $n_n/n_p(T^{\rm f}_{np}) \approx 0.4$. At this point, $T^{\rm f}_{np} < B_{\rm D}$ but deuterium hasn't started accumulating yet because they are still quickly dissociated by the high energy tail of the photon distribution in the process,

$$p + n \leftrightarrow D + \gamma \ . \tag{2.27}$$

From the Saha condition for chemical equilibrium of the process above, we can calculate the following quantity without the knowledge of their chemical potentials,

$$\frac{n_{\rm D}}{n_n n_p} = \frac{3}{4}\left(\frac{2\pi m_{\rm D}}{m_n m_p T}\right)^{3/2} e^{B_{\rm D}/T} \ . \tag{2.28}$$

Let us introduce the parameter n_B/s, which is the ratio of number density of baryon number (n_B) to the total entropy density of the SM plasma (s). Both $n_B a^3$ and sa^3 are conserved in SBBN, and hence n_B/s is constant after baryogenesis. In practice, we use the baryon-to-photon ratio, $\eta = n_B/n_\gamma$ which is also conserved except during electron-positron annihilation. We thus have $n_B \approx n_p(1+n_n/n_p) \approx 1.4 n_p$ which implies $n_p \approx \eta n_\gamma$. Therefore, Equation 2.28 now reduces to,

$$\frac{n_{\rm D}}{n_B} \approx \eta\ T^{3/2}\ e^{B_{\rm D}/T}\ . \tag{2.29}$$

At $T = 1\,\text{MeV}$, $n_{\rm D}/n_p \sim \eta \sim 10^{-10}$. Thus, due to the very small value of η, deuterium starts accumulating only after the freeze-out of the neutron-to-proton ratio, when $T \ll B_D$. Note that, neutron decays will lower n_n/n_p to a value lower than $n_n/n_p(T^{\rm f}_{np})$, until neutrons get trapped in nuclei.

Numerically solving Equation 2.29 for $n_{\rm D}/n_B \sim 1$, we find that deuterium formation starts at temperatures below 0.07 MeV. As soon as D production starts, ^{4}He is also quickly formed and freezes-out soon after. Other light elements, namely, ^{3}H, ^{3}He,^{7}Be, ^{6}Li and ^{7}Li are also produced in trace amounts. Heavier elements are not produced because the number densities are already very dilute at this point and the rate for their formation through 2-body reactions is highly suppressed.

Similar to the calculation for deuterium, with the knowledge of nuclear reaction rates and using the Saha equation, one can approximate the freeze-out value of other nuclides, $n_{^A{\rm X}}/n_B$. Results are usually quoted in terms of yields defined as,

$$Y_{n(p)} = \frac{n_{n(p)}}{n_B}, \quad Y(^A{\rm X}) = \frac{A n_{^A{\rm X}}}{n_B}\ , \tag{2.30}$$

where $Y(^A{\rm X})$ is the yield of the element ^{A}X. From the approximate analytic treatment in this section, we get $Y_n(T^{\rm f}_{np}) \approx 0.3$ and since all neutrons end up in ^{4}He, $Y(^4{\rm He}) \approx 2X_n(T^{\rm f}_{np}) \approx 0.6$. These values are a factor of 3 larger than those obtained from a more accurate numerical treatment, discussed in the next subsection.

2.3.1. Precise numerical treatment

From the above discussion, it follows that the calculation of light element abundances can be done in two steps: tracking the evolution of neutrons and protons until the processes that inter-convert them freezes-out, followed by the evolution of light elements until the end of BBN, when the thermonuclear reactions freeze-out. Several inputs from theory, particle physics experiments and cosmological experiments go into these steps in BBN calculations. We will elaborate on them when appropriated. The numerical recipe for the prediction of light element abundances from BBN discussed in this section closely follows the treatment in [78] and [79].

We first determine the neutron and proton at freeze-out by numerically solving the Boltzmann equations for their yields,

$$\begin{aligned} \frac{{\rm d}Y_n}{{\rm d}t} + 3HY_n &= Y_p\Gamma_{p\to n} - Y_n\Gamma_{n\to p}\ , \\ \frac{{\rm d}Y_p}{{\rm d}t} + 3HY_p &= Y_n\Gamma_{n\to p} - Y_p\Gamma_{p\to n}\ , \end{aligned} \tag{2.31}$$

where the rates involve all relevant n-p interconversion processes. The current state-of-the-art calculation of weak rates takes into account radiative corrections, finite-temperature corrections, finite mass corrections and weak magnetism corrections [80]. The rates are then nor-

malized to τ_n^{-1}, the inverse free neutron decay lifetime, which is treated as an experimentally determined nuisance parameter[6].

A bit before n-p inter-conversions become inefficient, neutrinos decouple from the thermal bath at $T_\nu^{\rm dec} \approx 2\,{\rm MeV}$ ($t_\nu^{\rm dec} \approx 0.2\,{\rm s}$) and start redshifting with a temperature T_ν. An accurate treatment of neutrino decoupling including non-instantaneous decoupling, finite temperature QED corrections and flavour oscillations lead to non-negligible effects on cosmology, i.e., BBN and CMB and can be absorbed into a parameter called the effective number of neutrino species, $N_{\rm eff}$. Using this parametrisation, the total radiation energy density after neutrino decoupling is given by,

$$\rho_{\rm rad} = \begin{cases} \rho_\gamma \left(1 + \dfrac{7}{4} + \dfrac{7}{8} N_{\rm eff}\right), & \text{before } e^+e^- \text{annihilation,} \\ \rho_\gamma \left(1 + \dfrac{7}{8} N_{\rm eff} \left(\dfrac{4}{11}\right)^{4/3}\right), & \text{after } e^+e^- \text{annihilation.} \end{cases} \tag{2.32}$$

Currently, the most precise prediction for $N_{\rm eff}$ at the end of BBN gives $N_{\rm eff}(T < \mathcal{O}({\rm keV})) = 3.044$ [82–84].

The final ingredient to solving equations 2.31 is the evolution of the SM plasma temperature T and neutrino temperature T_ν with time. This can be obtained by solving their momentum-integrated Boltzmann equations [78],

$$\begin{aligned} \frac{{\rm d}\left(\rho_\gamma + \rho_{e^\pm}\right)}{{\rm d}T} \frac{dT}{dt} &= -4H\rho_\gamma - 3H\left(\rho_{e^\pm} + p_{e^\pm}\right) + \delta C_{e^\pm}, \\ \frac{{\rm d}\rho_\nu}{{\rm d}T} \frac{dT_\nu}{dt} &= -4H\rho_\nu + \delta C_\nu, \end{aligned} \tag{2.33}$$

with the momentum-integrated collision terms being equal, $\delta C_{e^\pm} = -\delta C_\nu$ as imposed by total energy conservation. The collision term δC_ν has been evaluated in [85, 86]. Here, $p_{e^\pm}$ is the pressure density of electrons and positrons. We can numerically solve the equations 2.33 to obtain $T(t)$ and $T_\nu(t)$, which can then be used to solve equations 2.31. The neutrons and protons are found to freeze-out with $n_n/n_p \approx 1/6$ which can be associated with a freeze-out temperature, $T_{np}^{\rm f} \approx 0.7\,{\rm MeV}$ ($t_{np}^{\rm f} \approx 1.5\,{\rm s}$).

In the second step, the evolution of light elements is tracked with the Boltzmann equations for their yields, involving all processes in the thermonuclear network, until the end of BBN. Photo-dissociation of deuterium gets inefficient at $T_\gamma^{\rm D} \approx 0.073\,{\rm MeV}$ ($t_\gamma^{\rm D} \approx 241\,{\rm s}$). All relevant reactions that affect light nuclei yields freeze-out at $T_{\rm BBN,end} \sim \mathcal{O}(10)\,{\rm keV}$ temperatures ($t_{\rm BBN,end} \sim 10^4\,{\rm s}$), and we are left with a universe in which $\sim 75\%$ of the baryonic energy density is in the form of hydrogen and $\sim 25\%$ predominantly in the form of ^{4}He.

In literature, different complete sets of thermonuclear networks exist with different parametrisation of the cross-sections, for e.g. those compiled in `PRIMAT` [80], `PArthENoPE` [87] and NACRE II database [88]. `PArthENoPE` and NACRE II give BBN predictions that agree better with observations, while NACRE II leads to large uncertainties [79]. See [89–91] for a discussion on this topic based on updated nuclear cross-section measurements by the LUNA collaboration [92].

Once we have made a choice on the network, the calculation of reaction rates requires n_B as a function of time. We exploit baryon number conservation and determine n_B as a function of the scale-factor, $n_B \propto 1/a^3$. Thus we also need to solve for $a(t)$. This can be

[6] Two different measurements of neutron lifetime result in values varying by about 1%, the so-called *neutron-lifetime puzzle*. The effects of varying τ_n on BBN have been studied in [81].

obtained by solving either the equation for the Hubble rate or the plasma entropy density (s) conservation,

$$\frac{\mathrm{d}\ln a}{\mathrm{d}t} = \left(\frac{8\pi G}{3}\rho_{\rm rad}(t)\right)^{1/2}, \quad \frac{1}{a^3}\frac{\mathrm{d}\left(sa^3\right)}{\mathrm{d}\ln a} = \frac{\delta C_{e^\pm}}{HT}. \tag{2.34}$$

Finally, the initial conditions for all these Boltzmann equations are obtained assuming that they all start in chemical equilibrium with yields given similar to Equation 2.29, which depends on the baryon-to-photon ratio η. In SBBN case, nothing happens between BBN and CMB that can change the value[7] of η and hence, $\eta_{\rm BBN} = \eta_{\rm CMB}$. Thus, in practice, the precise Planck (TT,TE,EE+lowE+lensing) measurement, $\eta_{\rm CMB} = 6.104 \pm 0.058 \times 10^{-10}$ [93], is used as an input to BBN, making SBBN a "parameter-free" theory.

2.3.2. Effects of dark sector particles on BBN

As discussed in section 2.1, an MeV-scale DM would have to freeze-out before or during BBN in order to reproduce the correct relic abundance. The kinematically allowed final states for such an MeV-scale DM would be electro-magnetic (EM) particles (γ and $e^\pm$) and neutrinos. When it undergoes freeze-out, energy would be injected into EM sector and/or neutrino sector. Such energy injections will affect BBN predictions depending on the the time of freeze-out and the branching ratios, through various effects that we will discuss in this subsection. But, for very small masses, regardless of the branching ratios, the relic abundance requirement implies that DM is in equilibrium with the SM bath during BBN, while being semi-relativistic. It would then have a non-negligible energy density compared to SM radiation and contribute to an increased Hubble rate.

Model-building guide

3. BBN thus places an almost model-independent lower bound on mass of thermal DM [94–96], $m_{\rm DM} \gtrsim \mathcal{O}(1)\,\mathrm{MeV}$.

In the rest of the section, we deal with changes to BBN due to thermal DM with $m_{\rm DM} \gtrsim \mathcal{O}(1)\,\mathrm{MeV}$ and decaying dark sector particles. To be consistent with CMB measurement of DM abundance, the energy density in dark sector particles that are not DM, have to be depleted before CMB. This can be achieved by decay or annihilations into SM or dark radiation, which injects entropy into the universe. On the other hand, residual annihilations of decoupled DM can also inject energy into the SM thermal bath. Depending on the time of the entropy/energy injection, different quantities get affected.

Let us first consider the case where the dark sector particles only deplete their energy close to CMB. In this case, we have relevant energy injection constraints from CMB, discussed in subsection 2.4.1. These particles are essentially stable during BBN, and only affect BBN through its additional contribution to the Hubble rate,

$$H^2 = \frac{8\pi G}{3}(\rho_{\rm rad} + \rho_{\rm dark}) \ , \tag{2.35}$$

where the energy density in the dark sector, $\rho_{\rm dark}$, should be tracked with appropriate Boltzmann equations. An increased expansion rate causes earlier freeze-out of weak-interactions and modifies the temperature at which other thermonuclear reactions freeze-out. An earlier neutrino decoupling can slightly decrease $N_{\rm eff}$ from its standard model value of 3.044, since energy from $e^\pm$ annihilation is even less probable to be shared with the neutrino sector. The earlier neutrino decoupling also leads to a larger value of n_n/n_p at freeze-out. Since η is

[7] Except for the small change during $e^\pm$ annihilation, η is fixed throughout BBN.

undisturbed, nucleosynthesis effectively begins at the same temperature as SBBN. Provided neutron decays don't compensate for the increased $n_n/n_p(T^{\rm f}_{np})$, this leads to a larger ^{4}He yield.

Decays into dark radiation before BBN results in a larger value of $N_{\rm eff}$ measured by BBN and CMB, while decays after BBN results in an increase in an increase in $N_{\rm eff}$, such that $N_{\rm eff}(T_{\rm BBN}) < N_{\rm eff}(T_{\rm CMB})$. These cases can be constrained by the Planck $N_{\rm eff}$ likelihood as well as an independent BBN constraint on $N_{\rm eff}$ [97]. The effect of MeV-scale thermal relics that decay into dark radiation during BBN cannot be encapsulated in a single value of $N_{\rm eff}$ that enters BBN calculation. They have to be studied by following the Boltzmann equations of the decaying particle and dark radiation, whose energy densities enter the Hubble rate. Constraints on such MeV-scale unstable thermal relics, by comparing predictions to observations of light element abundances, have been placed by [98].

We now move on to constraints on energy injection into the SM thermal bath. Depending on the specific model, DM can annihilate into quarks, charged leptons, neutrinos, photons, $W^{\pm}/Z$ bosons or Higgs bosons. These final states can then induce particle cascades, undergo hadronisation or decay further. Thus, most often some fraction of energy from DM annihilations ends up in the form of energetic electrons, positrons, photons and neutrinos. Similarly, decays of dark sector particles can also inject EM particles.

If energy is injected into the SM bath[8] through annihilations or decays into EM particles, the energy conservation now implies,

$$\delta C_{e^{\pm}} = -\delta C_{\nu} - \dot{q}_{\rm dark} \ , \tag{2.36}$$

where the additional term $\dot{q}_{\rm dark}$ is the volume heating rate due to energy injection from the dark sector. If it happens well before neutrino decoupling ($\tau \lesssim 0.02\,{\rm s},\ T(\tau) \gtrsim 5\,{\rm MeV}$), energy is quickly thermalised with the plasma and is shared with both the EM and the neutrino sector. This would cause an increase in the initial temperature of the SM plasma and results in a shift of the overall cosmic timeline, but leaves no imprints on observable quantities. If energy injection happens after neutrino decoupling ($\tau \gtrsim 0.2\,{\rm s},\ T(\tau) \lesssim 2\,{\rm MeV}$), it heats up the SM bath and not the neutrino bath. This will thus reduce both $N_{\rm eff}$ and η. The resulting light element yields then non-trivially depend on all the above changes to the background cosmology induced by the dark sector. Latest studies of BBN constraints on EM decays of MeV-scale relic dark sector particles have been performed in [99, 100]. Energy injection between the temperatures $5\,{\rm MeV} \gtrsim T \gtrsim 2\,{\rm MeV}$, when neutrino is partially decoupled from the EM plasma, can introduce neutrino spectral distortions and have to be studied by solving their full Boltzmann equations [101].

If the dark sector instead injects energy directly into the neutrino sector, the most consistent way to study the resulting non-standard evolution of neutrinos is to solve their full Boltzmann equations at the phase-space level, with $\delta C_{\nu} = -\delta C_{e^{\pm}} - \dot{q}_{\rm dark}$, following the non-thermal distributions. Energy injection well after neutrino decoupling, would increase $N_{\rm eff}$. But as before, energy injection close to neutrino decoupling is non-trivial and depending on the energy of the injected neutrinos can increase ($E_{\nu} \simeq 3T$) or decrease ($E_{\nu} \gg 3T$) the value of $N_{\rm eff}$ [101,102]. Such models of decaying dark sector particles, when kinematically allowed, can also involve decays to mesons. Effect of meson-driven n-p inter-conversions on BBN have been studied in [101,103,104]. These are results for energy injection into an already existing thermal plasma. Such neutrino thermalisation arguments can also constrain low reheating scenarios, where the plasma is populated from the decays of an electro-weak scale massive particle that

[8]For any energy injected into EM particles before recombination, EM scatterings are efficient enough to quickly thermalize the injected particles with the SM bath.

dominates the energy density of the universe prior to decays. In this case, low reheating always decreases $N_{\rm eff}$ and constrains the reheating temperature to $T_{\rm reh} \gtrsim 3\,\text{MeV}$ [105, 106].

Finally, if energy injection occurs after BBN, into any of the channels described before, it can lead to disintegration of the light nuclei by photons or hadrons called photo- or hadrodisintegration. For injection into EM sector, if the energy of the injected photons is below the threshold for pair-production from scattering off a thermal photon, the injected photons can be end up dissociating light nuclei that are formed in BBN. The threshold energy for pair-production $E^{\rm th}_{e^+e^-} \simeq m_e^2/(22T)$ [107], increases with decreasing temperature of the thermal photon, and falls below the lowest binding energy which is that of Beryllium ($E^{\rm th}_{^7\text{Be}} \approx 1.59\,\text{MeV}$) at around 7.48 keV. Thus photodisintegration becomes relevant only after the end of BBN. Hence the study of photodisintegration factorizes from that of light nuclei production in BBN. Constraints on energy injection in this scenario have been well-studied in the literature, see [94, 99, 108]. Similarly, high energy neutrino injections can result in EM and hadronic showers from final state radiation, non-thermal high energy neutrino scatterings and scattering off thermal neutrinos. The resulting photons and hadrons can contribute to photo- and hadrodisintegration. Unlike photons, neutrons experience negligible energy loss through other mechanisms only for $t > 10^2\,\text{s}$ [109], and hence can disintegrate light nuclei before photodisintegration becomes efficient. Hence, the study of BBN constraints from neutrino injection is more involved as all effects – changes to η and $N_{\rm eff}$, photo- and hadrodisintegration have to be studied simultaneously. But this scenario provides constraints that are stronger than pure EM injection [110]. For a detailed review of BBN constraints on other non-standard cosmologies, see [111].

2.4. CMB

In standard cosmology, after BBN ends around $\mathcal{O}(10)\,\text{keV}$, the SM thermal bath contains photons, and non-relativistic electrons, positrons, protons, helium nuclei and tiny amounts of other light nuclei. The next most interesting event that happens in the universe is the formation of neutral hydrogen in a process called *recombination*. Recombination occurs at approximately the temperature when dissociation of neutral hydrogen by the energetic tail of the thermal photon distribution,

$$\text{H} + \gamma \to p + e^- \ , \tag{2.37}$$

becomes inefficient. Let us assume that the rate of this process falls below the Hubble rate when chemical equilibrium is still maintained. Then, using charge neutrality of the universe, i.e. $n_p = n_e$ and baryon number conservation, one can arrive at the Saha equation for the yield of neutral hydrogen [112],

$$X_{\rm H} = \frac{2\zeta(3)}{\pi^2} 0.75 \eta_B \left(\frac{2\pi T}{m_e}\right)^{3/2} X_p^2 e^{\frac{\Delta_{\rm H}}{T}} \tag{2.38}$$

where $\Delta_{\rm H} = 13.6\,\text{eV}$ is the binding energy of hydrogen, η_B is the baryon-to-photon ratio and X_p is the proton yield. Similar to deuterium formation, hydrogen formation is delayed until $T \ll \Delta_{\rm H}$ owing to the small value of η_B and since electrons are non-relativistic at these temperatures. Recombination thus happens at about $T_{\rm rec} \approx 0.3\,\text{eV}$ ($t_{\rm rec} \approx 10^{13}\,\text{s}$, $z_{\rm rec} \approx 1100$).

The capture of free electrons in neutral hydrogen during recombination results in a sharp decrease in free electron density, making the universe essentially transparent to photons, leading to *photon decoupling*. Note that, recombination is not instantaneous and the decrease in free electron density occurs in finite time. This gives rise to a finite width in redshift for the last scattering surface of photons.

Matter-radiation equality occurs a bit earlier at $T_{\rm eq} \approx 0.8\,\text{eV}$ ($t_{\rm eq} \approx 10^{12}\,\text{s},\ z_{\rm eq} \approx 3300$). Recombination and photon decoupling thus occur in the era of matter domination. An accurate study of these events hence involves tracking the evolution of both the background and the perturbations in the photon-baryon-CDM fluid. Codes like `HyRec-2` [113] can perform a precise numerical study of recombination and follow the ionization history of the *homogeneous* universe. Boltzmann codes like `camb` [114] and `class` [115] take the ionization history as input, solve the coupled Boltzmann equations for perturbations and finally, give precise predictions for CMB spectra.

2.4.1. Constraints on dark sectors

Apart from the measurement of the DM relic abundance which serves as the holy grail for DM model building, the CMB constrains energy injection from DM residual annihilations and extra dark sector particles. The extra source of energy density in dark sector particles can change the redshift of matter-radiation. If the energy density is (non-)relativistic, it can shift the equality to later(earlier) times, which can push the first peak to high(low)-l. Such an effect can only be studied by a complete analysis of CMB power spectra that requires running Boltzmann codes like `class`.

In some cases, the effects of extra dark particles can be captured by changes to $N_{\rm eff}$ measured by the CMB. The presence of relativistic ($m_\chi < 0.1\,\text{eV}$) dark particles at recombination, can increase $N_{\rm eff}$ measured by the CMB. A decrease in $N_{\rm eff}$ can be caused by EM energy injection, from decays or annihilations in the dark sector, after neutrino decoupling. In the absence of other new physics phenomena that increases $N_{\rm eff}$ between BBN and photon decoupling, CMB can be sensitive to such energy injections during BBN. Dark radiation and energy injections during BBN can thus be constrained solely by $N_{\rm eff}$. The CMB constraint on $N_{\rm eff}$ from Planck 2018 (TT,TE,EE+lowE+lensing +BAO) [7] is,

$$N_{\rm eff} = 2.99 \pm 0.17\ , \tag{2.39}$$

which is close to the SM prediction of $N_{\rm eff} = 3.044$, leaving very little room for dark radiation.

At later times, $z \lesssim 10^6$ ($t \gtrsim 10^7\,\text{s},\ T \lesssim 0.2\,\text{keV}$), when thermalisation becomes inefficient, EM energy injected can distort the CMB energy spectrum away from that of a perfect blackbody. At the present, constraints from COBE FIRAS [116] are quite weak and are thus not included in any of the global analyses in later chapters; future experiments like PIXIE [117] are expected to bring substantial improvement in sensitivity and hence can place much stronger constraints. Energy injection after recombination, $z \lesssim 10^3$ ($t \gtrsim 10^{13}\,\text{s},\ T \lesssim 0.3\,\text{eV}$) can end up ionizing neutral hydrogen and broadening the last scattering surface. This can suppress the correlations in small scales in temperature and polarization spectra. In literature, effects of energy injection from residual DM annihilations after recombination are parametrised in terms of the rate of energy injected per unit volume [118],

$$p_{\rm ann} = f_{\rm DM} f_{\rm eff} \frac{(\sigma_{\rm ann} v)_0}{m_{\rm DM}}\ , \tag{2.40}$$

where the subscript 0 indicates the zero velocity limit, $f_{\rm DM}$ is the fraction of observed DM that our model accounts for, and $f_{\rm eff}$ is the fraction of energy deposited in the plasma which depends on the DM mass and the final states of decay or annihilations. From Planck 2018 (TT,TE,EE+lowE+lensing) [7], we have the following constraint:

$$p_{\rm ann} < 3.3 \cdot 10^{-28}\,\text{cm}^3\,\text{s}^{-1}\,\text{GeV}^{-1}\ . \tag{2.41}$$

Model-building guide

4. The CMB energy injection constraint for residual annihilations of MeV-scale thermal DM implies,

$$(\sigma_{\rm ann} v)(T^{\rm f}_{\rm DM}) \gg (\sigma_{\rm ann} v)(T_{\rm CMB})$$

Improved measurements of the CMB power spectra in small scales from upcoming experiments like CMB-S4 [119], will further strengthen the CMB constraints on a dark sector.

2.5. Indirect detection constraints

Annihilations of sub-GeV DM in the current universe in DM dense structures can produce three kinds of signals: prompt and secondary emission of photons, and emission of charged cosmic rays. MeV-GeV photons can be produced from prompt emission - production of photons at the site of DM annihilation through direct annihilation ($\chi\bar{\chi} \to \gamma\gamma$); final state radiation (FSR) from charged final states (e.g. $\chi\bar{\chi} \to e^+e^-\gamma$); or from decays of unstable annihilation products. The observation of MeV-scale photons is hindered by the lack of telescopes with large sensitivity in this energy range, the so-called *MeV gap* [120]. The best γ-ray telescope we have, Fermi-LAT, loses sensitivity below a 100 MeV and the X-ray telescopes INTEGRAL and CHANDRA lose sensitivity above a few MeV. Currently, the only data available in this MeV gap is from the relatively old experiment, COMPTEL. Constraints have been derived on DM decays and annihilations to $e^\pm$, based on X-rays and soft γ-rays produced as FSR, using data from HEAO-1, INTEGRAL, COMPTEL, EGRET and FERMI in [121]. With many experiments proposed to fill the MeV gap, data and hence constraints are expected to improve [122].

Sub-GeV DM can annihilate directly to charged particles with sub-GeV energies. Observation of such MeV-scale charged particles is hindered by powerful solar magnetic fields in the heliosphere. The magnetic fields deflect these incoming charged cosmic rays away from the earth and hence from the powerful AMS-02 experiment located in the earth's orbit. But, the experiments VOYAGER-1 and VOYAGER-2 have left the region of influence of heliosphere and can thus observe MeV-scale charged cosmic rays from sub-GeV DM annihilations. Constraints on DM annihilation and decays through different channels using combined AMS-02 and VOYAGER-1 data were derived in [123].

Sub-GeV DM can produce keV-scale X-rays from secondary emission of charged cosmic rays from DM annihilations and decays. The charged annihilation or decay products can inverse Compton scatter off of star light or CMB photons, or emit synchrotron radiation, and end up producing keV-scale X-rays. Telescopes such as XMM-NEWTON, INTEGRAL, NUSTAR and SUZAKU operate in this energy range. Currently, the strongest constraints on DM annihilation based on secondary emission comes from INTEGRAL, and that on decays comes from NUSTAR data [124].

Unlike CMB and BBN constraints, indirect detection constraints are affected by uncertainties in signal and background modelling. Astrophysical inputs such as DM density profile, galactic magnetic fields, cosmic ray sources, modelling of cosmic ray transport introduce uncertainties in the constraints.

Finally, we point out the anomalous 511 keV signal that can be explained with annihilating sub-GeV DM in DM spikes [125]. Several X-rays satellites and balloon experiments have observed a bright 511 keV line in and around the galactic center, since the 1970's [126]. The signal matches that from e^+e^- annihilations via positronium and cannot be explained with positron injection solely from cosmic ray interactions with the interstellar medium. If these

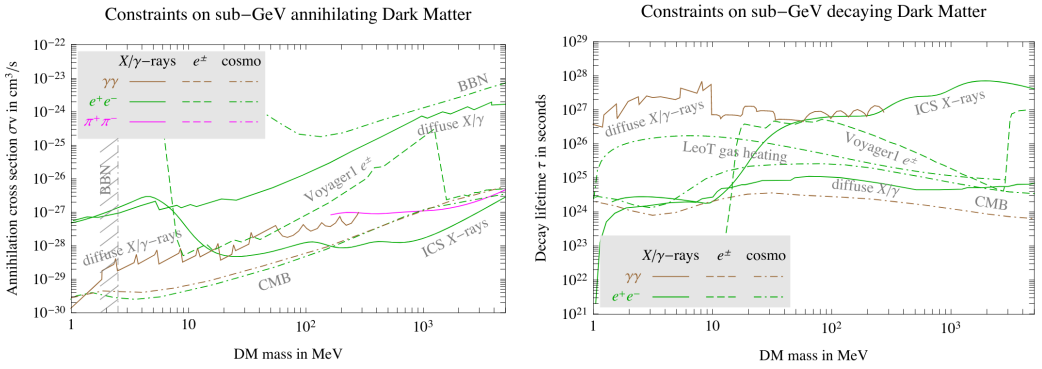

Figure 2.2.: Cosmological and indirect detection constraints on annihilating (left) and decaying (right) sub-GeV DM, from [128].

positrons are injected by DM annihilations, the morphology of the signal would be correlated with DM distribution. After accounting for positron propagation, the incompatibility of the 511 keV line morphology with that of annihilating sub-GeV DM has been used to place the most stringent constraint on annihilations [127]. But, these constraints are very sensitive the the model of cosmic ray propagation used and hence we refrain from using this constraint in our analysis.

Summary of constraints on sub-GeV dark sector

Current constraints on annihilating and decaying sub-GeV dark sector particles are shown in Figure 2.2. In the left panel, we see BBN, CMB as well as current indirect detection constraints on the s-wave annihilation cross-section times the relative velocity, $\sigma_{\rm ann} v$ as a function of DM mass, $m_{\rm DM}$. We see that regardless of the annihilation cross-section, BBN constrains masses below a few MeV. In the rest of the mass range, the strongest constraints on annihilating DM comes from the CMB energy injection constraint derived in [129]. Note that the constraint from secondary emission shown in this figure is outdated. It has been revised and is found to be weaker compared to CMB in the entire mass range for s-wave annihilation [124].

For decaying sub-GeV particles with lifetimes, $\tau > t_{\rm rec} \sim 10^{13}\,$s, the strongest constraint in the entire MeV mass range, comes from CMB energy injection constraint [130]. Lifetimes between BBN and recombination, $10^4\,{\rm s} \leq \tau \leq 10^{12}\,{\rm s}$ are constrained by photo- and hadro-disintegration of light nuclei from BBN and CMB spectral distortions, while decays during BBN, $10^{-2}\,{\rm s} \leq \tau \leq 10^4\,{\rm s}$, are constrained by BBN element abundance likelihoods and CMB $N_{\rm eff}$ likelihood (see subsection 2.3.2 and subsection 2.4.1).

2.6. Constraints on self-interaction cross-section

So far, we focused on probes of interactions between dark sector particles and the SM. But, as we will see, many models of sub-GeV DM involve new dark mediators that give rise to DM self-interactions, which opens more avenues to look for DM. On a different note, self-interacting DM (SIDM) had been proposed as a solution to problems arising from a mismatch between small scale observations and CDM-only N-body simulations. Hence, comprehensive studies of SIDM – particle physics modelling, identifying robust observables and comparing theory to observations – are an important step in understanding the nature of DM.

DM self-interactions, limited exclusively to the dark sector, can still be studied owing to the imprints they leave on the dynamics and evolution of astrophysical systems, and on structure

formation. Concretely, self-interactions allow for energy and momentum transfer between different parts of a DM density distribution, which would not occur in the case of collisionless DM. This can lead to intermediate core formation in DM haloes, resulting in central density profiles that are shallower than NFW profiles. But ultimately, in a process called gravo-thermal collapse, SIDM haloes can end up being cuspier than NFW haloes. Such non-trivial evolution of SIDM haloes can hence explain the observed diversity in rotation curves of galaxies and subhaloes [131]. Apart from this characteristic feature of SIDM, a number of other possible observables have been identified in literature, for instance, it can reduce the dynamical friction experienced by subhaloes and enhance their tidal disruption [132]; it can mildly affect halo shapes [133, 134]; it can contribute to drag experienced by dark matter in galaxy cluster mergers [135, 136]; it can affect structure formation in the early universe and hence cause changes to the matter power spectrum and the CMB [137]; it may stabilize SIDM spikes around super-massive black holes that source the dynamical friction experienced by the secondary black holes and thus potentially solve the so-called *final-parsec problem* [138, 139]; can potentially explain "Little Red Dots", the population of high-redshift, obscured quasars identified by JWST [140].

Based on such observables, several analyses have published self-interaction cross-sections and upper limits that are consistent with data. In the smallest scales, [141] has found $\sigma/m_{\rm DM} > 30\,{\rm cm}^2/{\rm g}$ to be favoured by the observed central densities of Milky-Way dwarf spheroidals. On galactic scales, cross-sections in the range $3-10\,{\rm cm}^2/{\rm g}$ are able to reproduce the diverse rotation curves in the SPARC dataset. Based on observation of core sizes and central densities , [142] places an upper limit of $\sigma/m_{\rm DM} < 0.35\,{\rm cm}^2/{\rm g}$ (95% CL) on cluster scales and $\sigma/m_{\rm DM} < 1.1\,{\rm cm}^2/{\rm g}$ on group scales. Such increasingly strong constraints towards systems with larger velocity dispersion have motivated the study of velocity-dependent self-interactions, while in this thesis, we will only encounter isotropic and velocity-independent self-interactions in the non-relativistic limit. In small scale systems, it is usually difficult to disentangle the effects of baryonic physics from that of SIDM and hence they are more challenging subjects from which to derive robust constraints. On the other hand, clusters are DM dominated and in general less sensitive to complicated baryonic physics and in principle make for good targets to study self-interactions. While a huge amount of theoretical and observational efforts go into studying systems at all scales, historically, the first stringent SIDM constraints came from cluster mergers and thus, they remain attractive candidates for SIDM studies.

2.6.1. Constraints from merging clusters

Self-scatterings between DM in merging galaxy clusters can cause the DM component to experience drag as it passes through the companion cluster. This can result in the DM component lagging behind the collisionless galaxy distribution, whereas the highly collisional gas component collides, heats up and stalls behind the DM component. Additionally, in galaxy mergers, the smaller subcluster can lose a part of its mass from particle ejection, due to energy transferred from the main cluster to the subcluster particles in DM self-interactions. Clusters with DM-galaxy offsets of $\mathcal{O}(10^2)\,{\rm kpc}$ have been observed [143]. But, it has been shown that such large offsets are inconsistent with simulations of mergers that predict DM-galaxy offsets $\lesssim 20\,{\rm kpc}$ for $\sigma/m_{\rm DM} = 1\,{\rm cm}^2/{\rm g}$. It was shown by [144] that the presence of intracluster medium can lead to larger offsets in the later evolutionary stages of mergers. Regardless, if we believe these observed offsets are due to complex merger histories, geometries or other reasons, we can still constrain SIDM cross-sections from other clusters that do not exhibit such DM-galaxy offsets. Based on the non-detection of DM-galaxy offsets in an ensemble of 72 observed cluster mergers, [145] placed a stringent constraint, $\sigma/m_{\rm DM} = 0.47\,{\rm cm}^2/{\rm g}$ (95% CL). But, a later study [146] found errors in their offset measurements with subsequent corrections relaxing the bound to $\sigma/m_{\rm DM} = 2\,{\rm cm}^2/{\rm g}$.

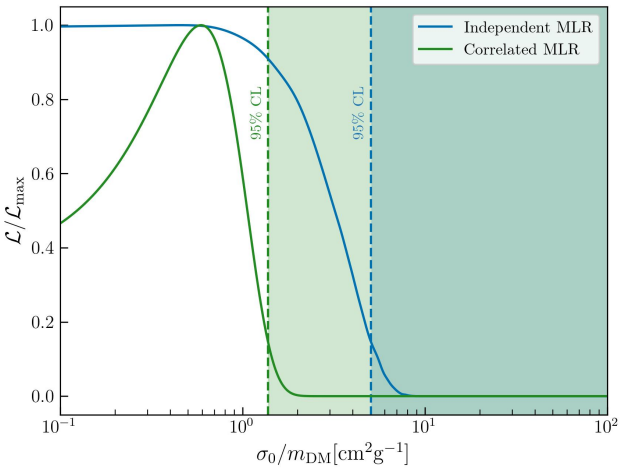

Figure 2.3.: Constraint from bullet cluster on an isotropic, velocity-independent self-interaction cross-section. Shown is the likelihood for final subcluster MLR, marginalized over initial subcluster MLR, using a gaussian prior (green) that assumes correlated initial MLRs for subcluster and main cluster; and log-normal prior (blue) that makes no assumption on correlation of initial MLRs.

In this context, the *Bullet cluster* is very popular owing to its favourable geometry and clean merger. Consequently, it has received much more observation time compared to other merging clusters and has exceptional X-ray and optical observations. It consists of clusters with a mass ratio of $1:10$, with the subcluster that has passed through the main cluster's central region, $0.1-0.2\,{\rm Gyr}$ ago, along the plane of the sky. Chandra X-ray data shows a clear bow shock in front of the bullet-like gas cloud [147]. This observation has enabled the determination of merger velocity to be $\sim 4000\,{\rm km/s}$. Later lensing and X-ray studies [16, 17, 148] found gas and mass peaks offset from each other at $\sim 100\,{\rm kpc}$, and hence constitutes an empirical proof for the existence of DM.

First constraints on the self-interaction cross-section came from [149]. Constraints derived using simple analytic methods were based on (*i*) non-negligible gas-DM offset which warrants small scattering depth for dark matter ($\sigma/m_{\rm DM} < 5\,{\rm cm}^2/{\rm g}$) (*ii*) high subcluster velocity which points to small deceleration/friction ($\sigma/m_{\rm DM} < 7\,{\rm cm}^2/{\rm g}$) (*iii*) small subcluster mass loss ($\sigma/m_{\rm DM} < 1\,{\rm cm}^2/{\rm g}$). Later, Randall et al. [150] used the non-observation of offset between DM and galaxy centroids to derive the constraint $\sigma/m_{\rm DM} < 1.25\,{\rm cm}^2/{\rm g}$ (68%CL) and subcluster survival to derive $\sigma/m_{\rm DM} < 0.7\,{\rm cm}^2/{\rm g}$. Both these constraints are subject to systematics. It has been pointed out by [151] that the DM-galaxy centroid separation is sensitive to the methods used to determine the separation, and can lead to false detection of offsets. Constraints based on mass loss have so far been derived from observed mass-to-light ratios (MLRs) under the assumption that the subcluster and main cluster start out with similar initial MLRs. MLRs have been observed to slowly increase with cluster mass [152] and more importantly, significant scatter in the mass-luminosity relationship has been observed [153–155].

2.6.2. Improved bullet cluster constraint

Constraints based on offsets require expensive numerical simulations, whereas *evaporation* rate of the subcluster can be analytically estimated [156]. Hence, we choose to constrain the self-interaction cross-section using subcluster survival in the bullet cluster. The analytic prescription in [156] has been extended to models with DM particles that make up only

a fraction $f_{\rm DM}$ of DM and asymmetric DM. See appendix A.1 for calculation. Using the predicted fractional mass lost $\Delta_{\rm M}$, and the initial subcluster MLR $\gamma_{\rm i}^{\rm sub}$, the prediction for the final subcluster MLR is given by, $\gamma_{\rm f}^{\rm sub} = \gamma_{\rm i}^{\rm sub}(1-\Delta_{\rm M})$. We then compare the theoretical prediction $\gamma_{\rm f}^{\rm sub}$, to the observed subcluster MLR $\gamma_{\rm obs}^{\rm sub}$. We use measurements of MLR within 150 kpc of the total mass peak using photometric i-band data, taken from [150], $\gamma_{\rm obs}^{\rm sub} = 179\pm11$ and $\gamma_{\rm obs}^{\rm main} = 214 \pm 13$. We choose to use MLRs rather than direct mass measurements for reasons explained appendix A.2.

An important improvement in our constraint is that we treat the initial subcluster MLR $\gamma_{\rm i}^{\rm sub}$ as a nuisance parameter. The constraint on SIDM cross-section is then obtained from a likelihood for $\gamma_{\rm f}^{\rm sub}$ marginalized over $\gamma_{\rm i}^{\rm sub}$,

$$\begin{aligned}\log \mathcal{P} &\propto \int {\rm d}\gamma_{\rm i}^{\rm sub}\ \mathcal{L}(\gamma_{\rm f}^{\rm sub})\ \Pi(\gamma_{\rm i}^{\rm sub}) \\ &\propto \log \sum_n \exp\left(-\frac{1}{2}\frac{(\gamma_{\rm obs}^{\rm sub} - \gamma_{\rm i,n}^{\rm sub}(1-\Delta_{\rm M}))^2}{(\sigma_{\rm obs}^{\rm sub})^2 + \sigma_{\rm theory}^2}\right)\ . \end{aligned} \tag{2.42}$$

We consider two different priors for the subcluster MLR. The first is a prior that matches the previous treatment in literature where the subcluster and main cluster are assumed to start with similar MLRs. The main cluster is 10 times as heavy as the subcluster, we can thus reasonably assume that it underwent negligible mass loss during the collision, $\gamma_{\rm i}^{\rm sub} = \gamma_{\rm i}^{\rm main} = \gamma_{\rm obs}^{\rm main}$. We then consider a gaussian prior for $\gamma_{\rm i}^{\rm sub}$ centred around $\gamma_{\rm obs}^{\rm main}$. The other prior is based on a log-normal distribution fitted to the observed MLRs of a sample of clusters in [154] using the i-band data. Compared to the large scatter for observed MLRs in this sample, the main cluster and subcluster are observed to have values quite close to each other. Hence the gaussian prior gives a stronger constraint, compared to the log-normal prior.

The marginalized likelihood for an isotropic, velocity-independent self-interaction cross-section, $\sigma_0/m_{\rm DM}$, is shown in Figure 2.3. The likelihood marginalized over the gaussian prior gives a constraint $\sigma_0/m_{\rm DM} < 1.4\,{\rm cm}^2/{\rm g}$ ($\Delta\chi^2 < 3.84$), consistent with [149]. The more conservative log-normal prior gives a limit $\sigma_0/m_{\rm DM} < 5.0\,{\rm cm}^2/{\rm g}$ ($\Delta\chi^2 < 3.84$). This likelihood with gaussian prior shows a slight preference for non-zero self-interaction cross section, with a best-fit value around $\sigma_0/m_{\rm DM} < 0.5\,{\rm cm}^2/{\rm g}$. However, this cross-section is consistent with collisional DM at 1σ level.

Part I.

Global fits of Sub-GeV Dark Matter

CHAPTER 3

Resonant or asymmetric

This chapter is based on the publication [157]. My contributions to this work were constructing and implementing an improved bullet cluster likelihood to constrain the self-interaction cross-section. I performed all the frequentist global analyses required for this work, as well as produced all the plots presenting the frequentist global fit results.

Currently, an important part of theoretical efforts in DM research is an exercise in phenomenology, where we aim to build models of DM that are not already excluded by current observations and are preferably discoverable in upcoming experiments. Global analyses are a crucial ingredient in this process as they guide theoretical efforts by testing viability of DM models given relevant constraints and guide future experiments by identifying target parameter regions.

Using such global fits, DM candidates that are charged under the SM gauge group have been found to be heavily constrained by current data (for e.g., see [158]). New physics searches at colliders thus targeted hypothetical new SM singlets. There is only one lowest-dimensional renormalisable operator each, for singlets of spin-$0, 1$ and $1/2$, that couple them to the SM, making them discoverable in laboratory experiments. These singlets can themselves be dark matter candidates: scalar singlet DM [52, 159], dark photon DM [160] and sterile neutrinos [161]. If instead, they act as mediators of interactions between a DM candidate and SM, they are called *portals*. Models of GeV-scale thermal DM with scalar, vector and neutrino portals have been extensively studied before (e.g. [162–165]). While a few studies of sub-GeV DM models with vector portals do exist [166, 167], comprehensive global fits including all available constraints while varying all model parameters freely, were still lacking. With bounds on sub-GeV DM getting continuously stronger, identifying viable sub-GeV DM models became a need of the hour.

In our first publication [157] (hereafter referred to as B24), we aimed to fill this gap in literature, by performing frequentist and Bayesian global fits of two different sub-GeV thermal DM models with a vector portal. The current chapter is based on this publication. We begin by building the thermal DM models of interest in section 3.1, using constraints encountered in the previous chapters as guidelines. In section 3.2, we mention further constraints that are relevant for the models considered. We present the results of global fits of these DM

models performed with GAMBIT in section 3.3. In section 3.4, we discuss the implication of our results for future DM searches and also briefly comment on the effects of new bounds (that were published after our publication) on our results. We finally summarize our findings and conclude in section 3.5.

3.1. Model building

The goal of this section is to build a model of thermal DM that is viable under existing constraints. To this end, we will make use of the model-building guidelines that we've collected based on the constraints discussed in this thesis so far. Let's build the model by going through the guidelines one by one.

Model-building guide

1. DD constraints can be evaded by going to sub-GeV masses.

The energy threshold for current direct detection experiments is at a few keV. For halo DM with $v/c \sim 10^{-3}$, the energy available for transfer to the target depends on the DM mass, $E_{\rm recoil} \sim m_{\rm DM} v^2$. For sub-GeV DM, the average recoil energy falls below the threshold of current direct detection experiments, $E_{\rm recoil} \lesssim$ keV. Sub-GeV DM are thus less severely constrained compared to GeV-TeV scale DM. We will therefore consider sub-GeV masses for DM in our models.

Model-building guide

2. MeV-scale DM can reproduce the correct relic abundance with $\langle \sigma_{\rm ann} v \rangle \sim 10^{-27} - 10^{-26}\,{\rm cm}^3\,{\rm s}^{-1}$ $(10^{-10} - 10^{-9}\,{\rm GeV}^{-2})$.

Similar to conventional WIMPs, if we consider sub-GeV DM to undergo SM weak interactions, the annihilation cross-section would be given by $\sigma_{\rm ann} v \sim 10^{-5} g^4 m_{\rm DM}^2 / m_W^4$, where $m_W \approx 80\,{\rm GeV}$ is the W-boson mass. For $\mathcal{O}(1)$ coupling and sub-GeV DM mass, the annihilation cross-section would be $\sim 10^{-13}\,{\rm GeV}^{-2}$, which is much smaller than that which reproduces the correct relic abundance. We can overcome this obstacle if we move beyond the conventional WIMP picture and assume that DM interacts with the SM through a new force. This would introduce the following free parameters in the theory: the mediator mass, and it's couplings to SM and DM. The extra parameters can then provide the freedom to achieve the correct annihilation cross-section that hits the target relic abundance.

In this thesis, we choose to work with the dark photon A'_μ that couples to both DM and electrically charged SM particles. We will discuss the dark photon in detail in subsection 3.1.1.

Model-building guide

3. BBN places an almost model-independent lower bound on the mass of thermal DM [94], $m_{\rm DM} \gtrsim \mathcal{O}(1)\,{\rm MeV}$.

We will study both a complex scalar Φ and Dirac fermion ψ DM that couple to dark photon. In order to be consistent with BBN bound mentioned above, we will restrict ourselves to DM masses above an MeV. The Lagrangians for the DM particles are given by

$$\mathcal{L}_\Phi = |\partial_\mu \Phi|^2 - m_{\rm DM}^2 |\Phi|^2 + i g_{\rm DM} A'^\mu \left[\Phi^* (\partial_\mu \Phi) - (\partial_\mu \Phi^*)\Phi\right] - g_{\rm DM}^2 A'_\mu A'^\mu |\Phi|^2 \,, \tag{3.1}$$

$$\mathcal{L}_\psi = \bar{\psi}(i\partial\!\!\!/ - m_{\rm DM})\psi + g_{\rm DM} A'^\mu \bar{\psi}\gamma_\mu \psi \,. \tag{3.2}$$

Model-building guide

4. The CMB energy injection constraint for residual annihilations of MeV-scale thermal DM implies,

$$(\sigma_{\rm ann} v)(T^{\rm f}_{\rm DM}) \gg (\sigma_{\rm ann} v)(T_{\rm CMB})$$

In order to produce the correct relic abundance through freeze-out in the early universe, and be consistent with CMB and X-ray constraints on annihilations in the late universe, the annihilation cross-section in the late universe should be suppressed with respect to that in the early universe. We can exploit the colder temperatures of the late universe to suppress the annihilation cross-section by making it velocity-dependent. The complex scalar DM Φ coupled to the dark photon undergoes annihilation that proceeds via p-wave. It can hence possibly achieve the correct relic abundance while evading constraints on annihilation in the late universe.

For the Dirac fermion DM ψ, annihilation proceeds via a velocity-independent cross-section, i.e. *s-wave* and can still be made viable, by considering the same strategies used in GeV-scale DM models to evade indirect detection constraints, which were discussed in section 1.5. We choose to study three different strategies to avoid constraints on late universe annihilation. By restricting our model parameter space to remain in the vicinity of resonance, $m_{A'} \approx m_{\rm DM}/2$, DM annihilation can be resonantly enhanced in the early universe, while keeping it suppressed in the late universe, see subsection 3.1.2. Introducing an asymmetry between DM particle and antiparticle ($n_\psi > n_{\bar{\psi}}$) can result in strong depletion of antiparticles, such that there are not enough particle-antiparticle pairs in the current universe to produce strong annihilation signals. We discuss asymmetric DM in subsection 3.1.3. Finally, we also consider the case where our DM candidate makes up only a fraction of the observed DM (also discussed in subsection 3.1.3).

3.1.1. Dark Photon

We consider a new $U(1)'$ gauge symmetry in the dark sector, whose gauge boson is the *dark photon*, A'. The vector portal between the dark sector and the SM, arises from the kinetic mixing term of the gauge bosons of the SM hypercharge $U(1)$ and the new $U(1)'$ symmetries [168],

$$\mathcal{L} \supset -\frac{\kappa}{2\cos\theta_w} F'_{\mu\nu} B^{\mu\nu} \ ,$$

where $F'_{\mu\nu}$ and $B^{\mu\nu}$ are the field strength tensors of the dark photon and SM hypercharge boson respectively, κ is the dimensionless kinetic-mixing parameter and θ_w is the weak mixing angle. In the massless dark photon case, the fields can be freely redefined to diagonalise the kinetic terms. After diagonalising the kinetic terms with the appropriate choice of field redefinition, one can, in addition to couplings of the gauge bosons to particles in the corresponding sectors, couple them to the particles of the other sector. One of these cases, where the dark photon only couples to the vector current in the dark sector, while the SM hypercharge boson couples to currents in both the SM and the dark sector, gives rise to milli-charged dark matter. This case is heavily constrained by a combination of astrophysical, cosmological and laboratory constraints [169, 170].

The dark photon can also be given an explicit mass that arises from Stueckelberg mechanism [171] or through the spontaneous $U(1)'$ breaking resulting from a dark Higgs mechanism. In this chapter, we assume that the dark photon acquires mass through the Stueckelberg mechanism and postpone the study of the dark Higgs mechanism to chapter 4. Such a dark photon mass term limits the freedom to arbitrarily redefine the fields, when mixing with the massless SM hypercharge boson. In this case, for dark photon masses $m_{A'} \ll m_Z$, after electroweak

symmetry breaking and diagonalising the kinetic terms, the dark photon Lagrangian in terms of its mass eigenstate is written as

$$\mathcal{L}_{\rm int} = -\frac{1}{2}m_{A'}^2 A'_\mu A'^\mu - \frac{1}{4}A'_{\mu\nu}A'^{\mu\nu} - \kappa e A'_\mu \sum_f q_f \bar{f}\gamma^\mu f \ , \tag{3.3}$$

where the dark photon acquires an effective coupling of strength $\kappa q_f e$ to SM particles with electric charge $q_f e$. We thus choose to work with this setup, where the DM interacts with SM only through the dark photon. Additionally, we can choose between a vanishingly small or light dark photon masses. But fermionic DM coupled to ultra-light dark photons are also constrained by strong self-interaction and CMB constraints [169]. Hence, we choose to work with massive dark photons.

3.1.2. Enhancing early universe annihilation

In our model, to reproduce the correct DM relic density while satisfying the strong constraints on late universe annihilation, one can either enhance the early universe annihilation cross-section or suppress that of the late universe. In this subsection, we discuss the resonant enhancement of annihilations in the early universe. The Dirac fermion ψ receives a resonant enhancement of its annihilation cross-section,

$$\sigma_{\rm ann} v \propto \frac{m_{A'}\Gamma_{A'}}{(s-m_{A'}^2)^2 + m_{A'}^2\Gamma_{A'}^2}$$

when $s \approx m_{A'}^2$. In the non-relativistic limit, $s = 4m_{\rm DM}^2(1+v^2)$. For a given $m_{A'}$, the resonance enhancement depends on the temperature and mass of DM. Conversely, with the appropriate choice of $m_{\rm DM}$ and $m_{A'}$, the annihilation cross-section can be resonantly enhanced close to freeze-out temperatures, while it remains small in the late universe.

For a non-relativistic Boltzmann gas, which is how we approximate the behaviour of DM close to freeze-out, the temperature is related to the velocity dispersion as $\langle v^2 \rangle = 3T_{\rm f}/m_{\rm DM} = 3/x_{\rm f}$. We saw in section 2.1 that for sub-GeV DM, the typical values of $x_{\rm f}$ that give the correct relic density is in the range $10-30$. This implies that close to freeze-out DM has $v^2 \sim 0.1$, whereas today, $v^2 \sim 0$. Therefore, resonance occurs close to freeze-out when the resonance parameter ϵ_R, defined as

$$\epsilon_R = \frac{m_{A'}^2 - 4m_{\rm DM}^2}{4m_{\rm DM}^2} \tag{3.4}$$

takes the value, $\epsilon_R \approx 0.1$. When $\epsilon_R \ll 1$, the resonance moves to lower temperatures and the annihilation in the late universe becomes large, boosting indirect detection signals. The opposite limit, $\epsilon \gg 1$ implies $m_{A'} \gg m_{\rm DM}$ and annihilation can be enhanced for very large temperatures in the early universe.

3.1.3. Suppressing late universe annihilation

The DM candidate in our theory is not self-conjugate and the relic abundance is given by,

$$\Omega_{\rm DM}h^2 = \Omega_\chi h^2 + \Omega_{\bar{\chi}}h^2$$

where $\chi = \Phi, \psi$. In this work, we allow two cases, one where the abundance in χ and $\bar{\chi}$ saturate the observed DM abundance, i.e. $f_{\rm DM} = \Omega_{\rm DM}h^2/\Omega_{\rm DM,obs}h^2 = 1$, and the other where it accounts for only a part of it, $f_{\rm DM} \leq 1$. In this case, the DM density entering calculation of signal rates in direct, indirect and CMB constraints is suppressed by $f_{\rm DM}$. Thus constraints on the annihilation cross-section can be weakened when $f_{\rm DM} \leq 1$.

The second solution to suppress constraints on the annihilation cross-section is to consider an asymmetry between DM particles and antiparticles. Taking the DM particle to be the dominant species ($n_\chi > n_{\bar{\chi}}$), we define the asymmetry parameter as

$$\eta_{\rm DM} = \frac{n_\chi - n_{\bar{\chi}}}{s} \ ,$$

where s is the total entropy density of the universe. In our model, since the dark $U(1)'$ charge is conserved, the asymmetry stays constant once generated and in the absence of entropy injection, $\eta_{\rm DM}$ remains constant throughout the history of the universe. We can define the fraction of DM that is symmetric as,

$$f_{\rm sym} = \frac{2\Omega_{\bar{\chi}}h^2}{\Omega_{\rm DM,obs}h^2} = f_{\rm DM} - \eta_{\rm DM} m_{\rm DM} \frac{s_0}{\rho_{\rm DM,obs}} \ . \tag{3.5}$$

Only this fraction of DM can annihilate, while the rest is safe from getting depleted by annihilation. Thus the indirect detection signal gets suppressed by a factor $\xi_{\rm asym}$ compared to symmetric DM,

$$\xi_{\rm asym} = \frac{n_\chi n_{\bar{\chi}}}{\frac{1}{4}(n_\chi + n_{\bar{\chi}})^2} = \frac{f_{\rm sym}}{f_{\rm DM}} \left(2 - \frac{f_{\rm sym}}{f_{\rm DM}}\right) \tag{3.6}$$

The value of $\eta_{\rm DM}$ where the asymmetric component alone saturates the relic abundance, i.e. $f_{\rm sym} = 0$ can be obtained from Equation 3.5 as,

$$\eta_{\rm asym} = \frac{4.33 \times 10^{-10}\,{\rm GeV}}{m_{\rm DM}} \ . \tag{3.7}$$

This value serves as the upper bound for asymmetry, $\eta_{\rm DM} \leq \eta_{\rm asym}$.

3.1.4. Parameters and priors

We have constructed two models of DM, a complex scalar Φ and a Dirac fermion ψ coupled to a dark photon A' that undergoes kinetic mixing with the SM photon. Lagrangians are given in equations 3.1, 3.2 and 3.3. In order to simultaneously satisfy the relic density as well as the CMB and X-ray constraints on the annihilation cross-section, we consider resonant annihilation; introduce an asymmetry between DM particles and antiparticles; and allow for our DM candidate to make up only a part of the observed DM relic abundance. Thus we have 5 free model parameters: $m_{\rm DM}$, $m_{A'}$, $g_{\rm DM}$, κ, and $\eta_{\rm DM}$.

In order to explore the parameter space close to resonance efficiently, we introduced the resonance parameter ϵ_R. Similarly, since $\eta_{\rm DM} m_{\rm DM}$ enters the relic density calculation directly, we choose to vary this product rather than $\eta_{\rm DM}$ in the scans. This way we can restrict the range for $\eta_{\rm DM} m_{\rm DM}$ by requiring $\Omega_{\rm DM}h^2 < 0.275$. The model parameters and their ranges are summarized in Table 3.1. For details on the choice of priors used and nuisance parameters included in the scan, refer to Sec. 2.2 in B24.

3.2. Constraints

In this section, we discuss constraints from different DM searches that are relevant for our sub-GeV DM models. We already discussed astrophysical and cosmological constraints relevant to sub-GeV DM in chapter 2. In subsection 3.2.1, we briefly mention the exact astrophysical and cosmological likelihoods that are included in the global fits of our sub-GeV DM candidates. In subsection 3.2.2, we discuss the relevant constraints from fixed-target and collider experiments. Finally, in subsection 3.2.3, we discuss constraints from direct detection experiments.

Table 3.1.: List of model parameters and their ranges. For frequentist scans, the prior is only used to determine the sampling strategy.

Parameter name	Symbol	Unit	Range	Prior
Kinetic mixing	κ	–	$[10^{-8}, 10^{-2}]$	logarithmic
Dark sector coupling	$g_{\rm DM}$	–	$[10^{-2}, \sqrt{4\pi}]$	logarithmic
Asymmetry parameter	$\eta_{\rm DM}$	–	$[0, 10^{-9}\,{\rm GeV}/m_{\rm DM}]$	linear
Dark matter mass	$m_{\rm DM}$	MeV	[1,1000]	logarithmic
Dark photon mass	$m_{A'}$	MeV	[2,6000] with $m_{A'} \geq 2m_{\rm DM}$	logarithmic
or				
Resonance parameter	ϵ_R	–	$[10^{-3}$,8]	logarithmic

3.2.1. Cosmological and astrophysical constraints

Relic density

The DM relic density is calculated by solving the standard Boltzmann equation as discussed in section 2.2. We use the `GAMBIT` interface to `DarkSUSY` v6.4 [75] to perform this calculation. We perform global scans for both cases where our candidate makes up all and part of the observed DM relic abundance, i.e. $f_{\rm DM} = 1$ and $f_{\rm DM} \leq 1$, respectively. To impose the first case, we use a Gaussian likelihood centred around the Planck measurement in Equation 2.17. For the second case, we use a one-sided likelihood which penalizes parameter points with $f_{\rm DM} > 1$, but not those with $f_{\rm DM} < 1$. We include an uncertainty of 10% on the theoretical estimate of $\Omega_{\rm DM}h^2$.

It should be noted that in models with resonant annihilation, kinetic decoupling can in fact occur close to chemical decoupling. In this case, the relic density estimate obtained by solving the standard Boltzmann equation can be an order of magnitude different from the true value obtained by solving the Boltzmann equation at the phase-space level [172]. This uncertainty is much larger than the one included as a theoretical uncertainty in the scan. But in the context of global fits, it is more important to have computationally efficient calculation with reasonable accuracy. This is because, even though an accurate $\Omega_{\rm DM}h^2$ might lead to a different distribution of allowed parameter points in the full 5-dimensional model parameter space, the changes would be minimal when projecting them onto 2-dimensional parameter spaces by profiling. Therefore, we argue that given the models are not fine-tuned, the qualitative results would remain unaffected when performing a more accurate relic density calculation.

BBN and CMB constraints

For the parameter ranges considered, the dark photon is very short-lived in our models, $\tau_{A'} \ll 1\,{\rm s}$. Hence, there are no relevant constraints on dark photons decays from BBN and CMB. Instead, as discussed in subsection 2.3.2 and subsection 2.4.1, BBN and CMB constrain energy injection from DM annihilations. The effect of DM annihilations on light element abundances is calculated using the `GAMBIT` interface to `AlterBBN` v2.2 [173]. We use the likelihoods implemented for ^{4}He and D abundances, as described in [174, 175]. `AlterBBN` also returns the neutrino temperature at the end of BBN, which might be different from the standard value because DM was semi-relativistic and in equilibrium with SM during BBN

or because of energy injection from DM annihilations when it freezes out. The non-standard value of N_{eff} is calculated from the neutrino temperature and is then fed to the Gaussian likelihood centred around the Planck measurement of N_{eff} given in Equation 2.39.

The constraint on DM annihilations close to recombination are parametrized in terms of p_{ann} as discussed in subsection 2.4.1. To apply the constraint in Equation 2.41, the fraction of energy deposited in the plasma needs to be calculated. This calculation is performed by `DarkAges` [176] which takes as input yields of injected γ-rays and positrons. These spectra are available in tabulated form in `DarkSUSY` and are obtained from `Hazma` v2.0 [177,178]. For details on likelihood implementation of p_{ann}, see [179].

Astrophysical constraints

For the indirect detection constraints, we include the strongest constraint from X-rays, which comes from DM annihilation into e^+e^- in our analysis. The X-ray likelihood for annihilation to this channel, provided by the authors of [124], was implemented in `GAMBIT`. We also include the improved constraint on the self-interaction cross-section from the Bullet cluster, discussed in subsection 2.6.2.

3.2.2. Accelerator constraints

For the chosen parameter ranges, we have $m_{A'} > 2m_{\text{DM}}$ and $g_{\text{DM}} > \kappa$. Thus dark photon predominantly decays into DM particles. Even close to resonance, the branching fraction into visible SM final states is small and so is the decay length. Therefore, collider experiments and searches for long-lived dark photons, looking for visible decays are insensitive. Hence, we only include constraints on invisibly decaying dark photons from LSND [180,181], MiniBooNE [182], NA64 [183] and BaBar [184].

LSND and MiniBooNE experiments are analogous to direct detection experiments that look for DM-electron or DM-nucleon scattering events. The only difference is that, instead of waiting for galactic DM to scatter off target material in detectors, these experiments aim to produce a relativistic flux of DM from dark photon decays. Dark photons can be produced in decays of mesons which come from interactions between a proton beam and nucleons in a dense target. For a given parameter point, the number of signal events, $s \propto \kappa^4 g_{\text{DM}}^2$, is predicted using a Monte Carlo simulation software for beam-dump experiments, `BdNMC` [181]. The observed data is modelled as a Poisson distribution and likelihood is calculated for a predicted number of signal events, given the total number of observed and background events. The recent MiniBooNE results from [185] are difficult to reinterpret and are not included in the analysis.

NA64 is also a beam-dump experiment that collides an electron beam with a fixed target, which can potentially produce dark photons via dark bremsstrahlung. This experiment looks for missing energy events arising from invisible decays of dark photons. The data is once again modelled as a Poisson distribution, which is used to calculate the likelihood for a predicted number of signal events, $s \propto \kappa^2$.

BaBar looks for invisibly decaying dark photons produced along with mono-energetic photons in e^+e^- collisions. We use a likelihood function that reproduces limits from [184] on the kinetic mixing parameter as a function of the dark photon mass. BaBar excludes $\kappa > 10^{-3}$ in the entire dark photon mass range considered. For $m_{A'} < 300\,\text{MeV}$, NA64 strongly constrains κ. For $g_{\text{DM}} < 1$, constraints from LSND and MiniBooNE are found to be subleading.

3.2.3. Direct detection constraints

Even though we chose to deal with sub-GeV DM precisely to evade direct detection constraints, this mass range is not completely unconstrained. In particular, sensitivity of direct detection experiments for sub-GeV DM has been extended by considering electron recoils as well as production of electrons in nuclear recoils in the so-called *Migdal effect*.

Strong constraints on electron recoils come from XENON1T [186], SENSEI [187], DarkSide50 [188], PandaX-4T [189], DAMIC-M [190] and SuperCDMS HV [191]. We have left out the recent results of LZ [192] from our analysis due to difficult reinterpretation of the results. Atomic response functions are calculated using the `GAMBIT` interface to `obscura` [193]. We then calculate a binned Poisson likelihood for a given value of background expectation and signal prediction, by comparing it against observed number of events. The leading constraints come from SENSEI and PandaX-4T.

Strong constraints on nuclear recoils come from CRESST-III [194] calculated using `DDCalc` [195]. Exploiting the Migdal effect, even stronger constraints are obtained. To this end, we use `obscura` and the electron-recoil data to calculate the likelihoods for DarkSide50, XENON1T and PandaX-4T. Of these, PandaX-4T gives the strongest constraint.

3.3. Results

To test the viability of scalar and fermionic sub-GeV DM models in light of all constraints discussed in the previous section, we perform global fits with `GAMBIT`. As mentioned earlier, for both models, we consider two cases: one where the DM candidate is required to saturate the observed relic abundance, $\Omega_{\rm DM}h^2 = 0.12$ and the other where it is allowed to make up only a part of it, $\Omega_{\rm DM}h^2 \leq 0.12$. Furthermore, for the fermionic DM model, we study two more cases when $\Omega_{\rm DM}h^2 = 0.12$: one where we consider DM to be symmetric, $\eta_{\rm DM} = 0$ and the other where we let the asymmetry parameter to vary freely in the parameter scan. For the scalar DM model, since the indirect detection constraints are weak, we only study the symmetric case. In total, we have run 4 parameter scans for the fermionic DM model and 2 scans for scalar DM model under different assumptions on DM relic density and asymmetry.

We perform both frequentist and Bayesian analysis of the DM models. For the frequentist analysis, we explore the parameter space with `Diver` [196] using a population size of 38000 and a convergence threshold of 10^{-6}. We use `pippi` v2.1 [197] to make the 2-D profiled likelihood plots. For the Bayesian analysis, we use `Polchord` [198] for parameter exploration with 1000 live points and a tolerance of 10^{-10}. We plot the results from the Bayesian scans with `anesthetic` [199]. The results of the global fits and example plotting scripts are available on Zenodo [200].

3.3.1. Symmetric fermionic DM

Frequentist results

The frequentist results are presented as plots showing the contours of the allowed regions as well as the likelihoods within these regions. We show the results in planes of pairs of model parameters or derived quantities, $\{x_A,\ x_B\}$. The colored area in blue with black contours represent the confidence regions corresponding to 68% and 95% confidence levels. The regions in white are excluded at 95% confidence level. The shading within the confidence regions shows the profiled likelihood relative to the maximum likelihood. Profiling here refers to maximizing the likelihood in each bin of the $x_A - x_B$ plane with respect to rest of the parameters not shown in the plots. The white star indicates the parameter point with the

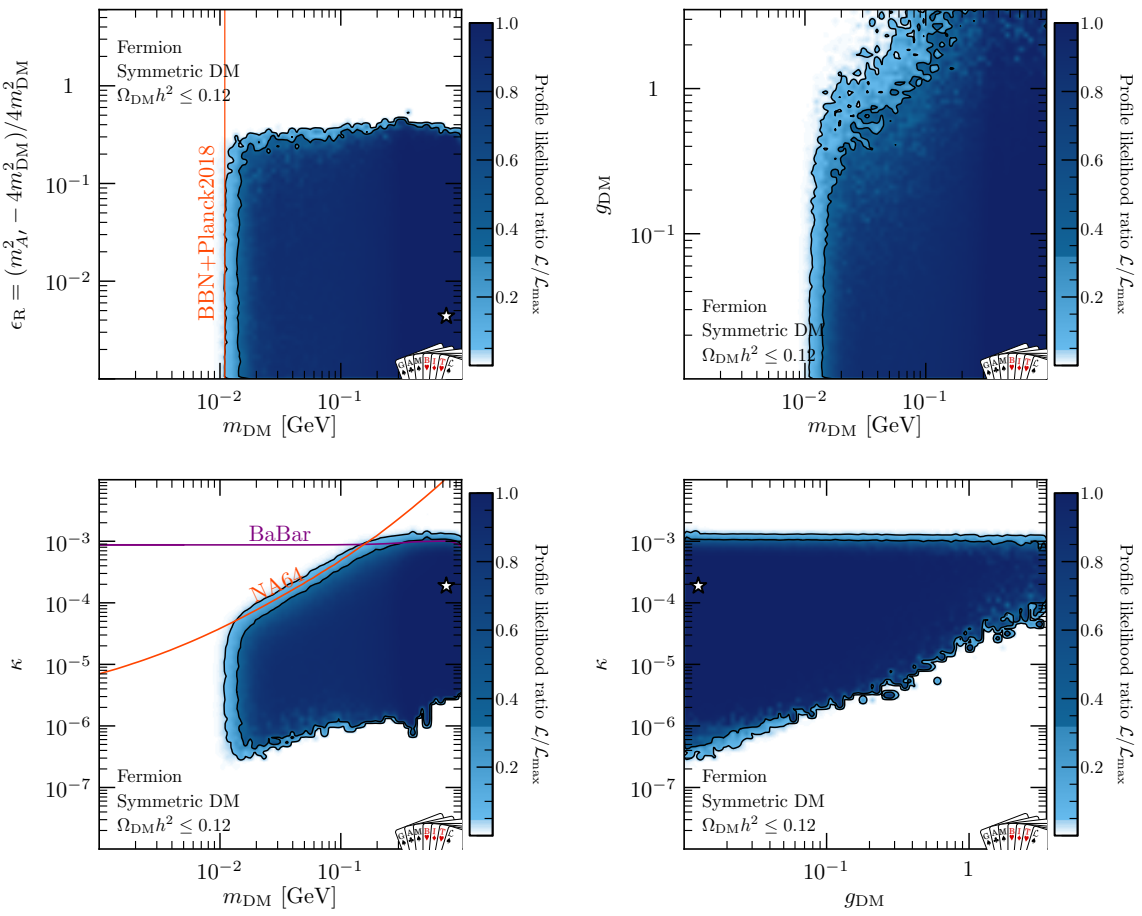

Figure 3.1.: Allowed parameter regions for symmetric fermionic dark matter with $\Omega_{\rm DM}h^2 \leq 0.12$ for different model parameters. For description see beginning of text in section 3.3.1.

maximum likelihood, called the *best-fit* point. In addition, we also show individual likelihoods from the constraints discussed in the previous section in parameter planes where appropriate.

We first discuss the results of the symmetric fermionic DM with $\Omega_{\rm DM}h^2 \leq 0.12$. The results are shown in Figure 3.1. In three panels showing the DM mass, we see that masses below $\mathcal{O}(10)$ MeV are excluded by the BBN and Planck $N_{\rm eff}$ constraints. In the $\epsilon_R - m_{\rm DM}$ plot, we see that the smallest values of the resonance parameter are allowed by all likelihoods while $\epsilon \gtrsim 0.4$ is excluded. The resonance parameter mainly affects annihilation and hence is constrained by the relic density and indirect detection constraints. Small values of the resonance parameter corresponds to large values of the annihilation cross-section. Since there is no incentive from any of the involved likelihoods to make $f_{\rm DM}$ large, large values of annihilation cross-section that lead to underproduction of dark matter are accepted. These small values of $f_{\rm DM}$ would in turn suppress indirect detection signals. Hence, even when small values of resonance parameter push the resonance to lower temperatures, the indirect detection constraints are still satisfied. Thus, small ϵ_R are allowed by both the relic density and indirect detection constraints. But large values of ϵ_R lead to small annihilation cross-sections close to freeze-out. If not compensated by a corresponding increase in κ, these parameter points can lead to overproduction of DM and hence would be excluded. This implies that for $\epsilon_R > 0.4$, the largest allowed values of κ are not enough to compensate for ϵ_R to avoid DM overproduction.

In the $\kappa - m_{\rm DM}$ plane, we see small values of κ excluded by the relic density constraint again due to DM overproduction, while large values are excluded by NA64 and BaBar. The

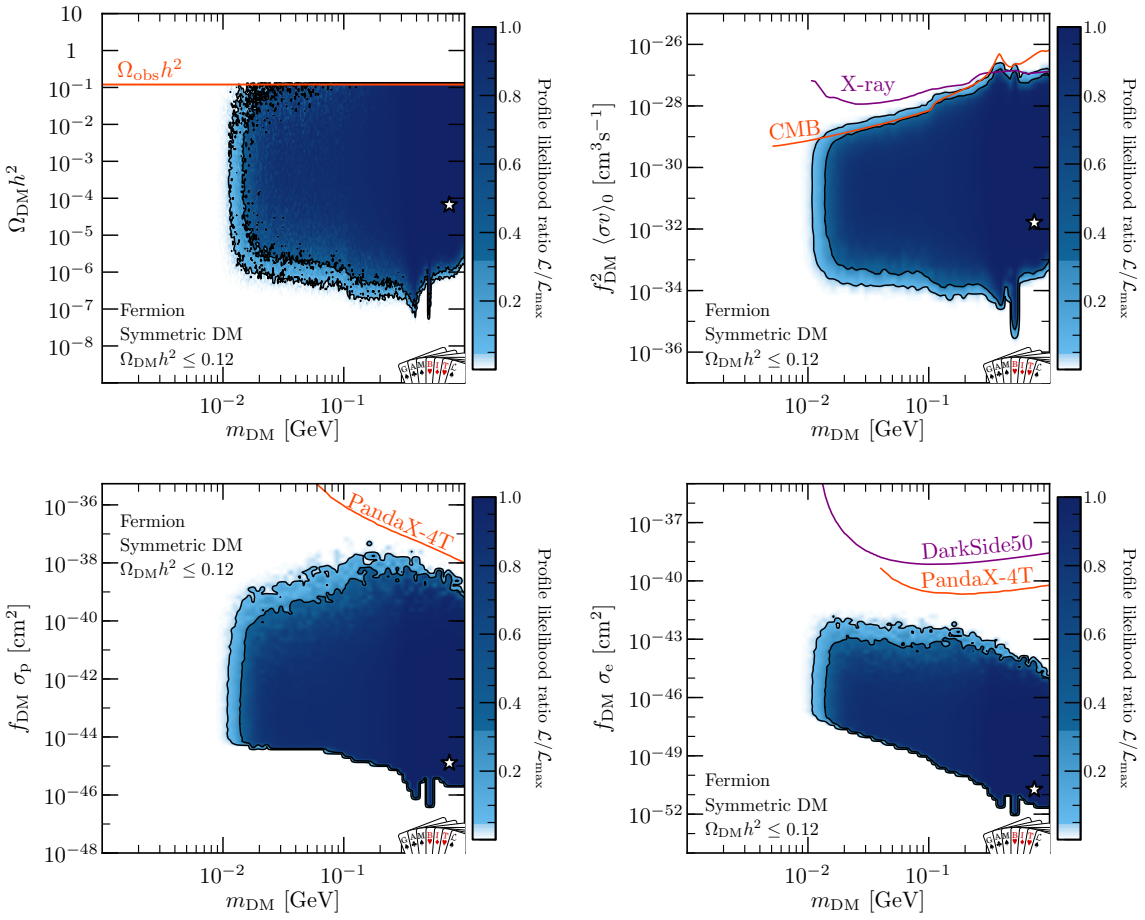

Figure 3.2.: Allowed parameter regions for symmetric fermionic dark matter with $\Omega_{\rm DM}h^2 \leq 0.12$ for various observables as a function of the DM mass.

$g_{\rm DM} - m_{\rm DM}$ plot shows that large values of $g_{\rm DM}$ up to the the perturbativity bound are allowed for large $m_{\rm DM}$. For smaller masses, the accelerator experiments require $g_{\rm DM} \lesssim 1$, because of the lower limit on κ from the relic density constraint. Without this lower bound, one can in principle compensate for increase in $g_{\rm DM}$ by decreasing κ to stay below the accelerator constraints. Finally, in the $\kappa - g_{\rm DM}$ plot, we see that the region with large $g_{\rm DM}$ and small κ are excluded as they would lead to DM overproduction. This is because large $g_{\rm DM}$ corresponds to a large dark photon decay width which leads to less resonant enhancement even for small ϵ_R.

In Figure 3.2, we show the profiled likelihoods in plots of useful observables vs. $m_{\rm DM}$. In the top left panel, we see that in the bulk of the confidence region, we have points with $f_{\rm DM} \leq 1$. But throughout the allowed DM mass range, there exist parameter points that reproduce the observed DM relic abundance. Regions close to these points with $f_{\rm DM} \approx 1$ have unsuppressed annihilation cross-sections and are hence constrained by the indirect detection and CMB constraints, as seen in the top right panel. Similarly, nuclear scattering cross-sections are also constrained by current experiments. But in the entire confidence region, the electron scattering cross-sections are below the reach of current experiments. In all these plots, the features at DM mass close to 400 MeV and 500 MeV come from hadronic resonances of ω and ϕ mesons, respectively.

Next, we discuss the results of global fits of symmetric fermionic DM with $\Omega_{\rm DM}h^2 = 0.12$, shown in Figure 3.4. The results are presented as profiled likelihood plots of confidence

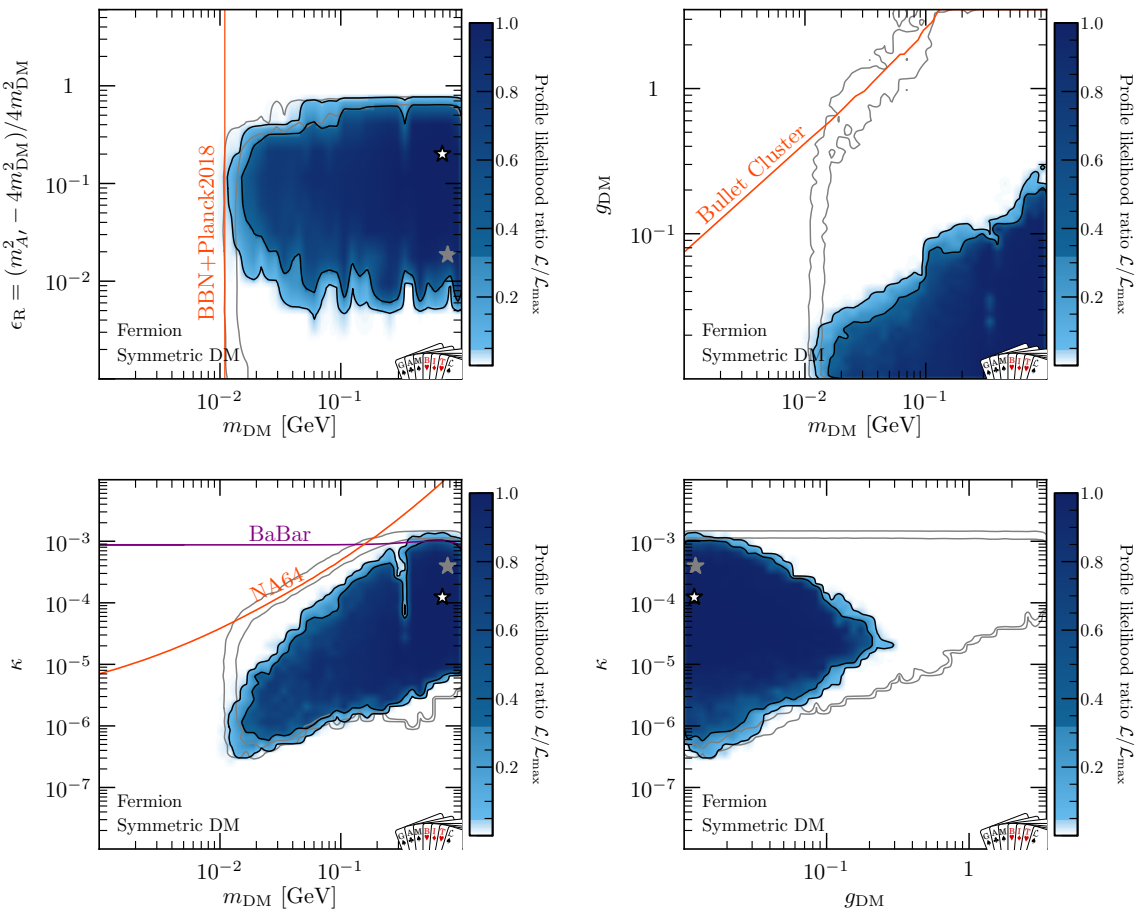

Figure 3.3.: Allowed parameter regions for symmetric fermionic dark matter, when requiring that the observed DM relic abundance is saturated ($\Omega_{\rm DM}h^2 \approx 0.12$). For comparison, we indicate with gray lines the allowed parameter regions for a sub-dominant DM component and with a gray star the corresponding best-fit point.

regions, like before. For comparison, we also show the 68% and 95% confidence level contours of the previous global scans with $\Omega_{\rm DM}h^2 \leq 0.12$ as grey lines and the corresponding best-fit is indicated by the grey star. As expected, the confidence regions shrink considerably due to the extra requirement that DM relic abundance needs to be saturated. Thus the difference in the confidence regions in both cases come mainly from the relic density and indirect detection constraints. The excluded regions that are common to both the previous and the current scan are excluded by a combination of relic density constraint (due to DM overproduction) and indirect detection constraint (relevant to regions with $f_{\rm DM} \approx 1$). In the current scan, parameters with large annihilation cross-sections that lead to DM underproduction as well as enhanced annihilation signals in the late universe are additionally excluded. This excludes the combination of small ϵ_R, and large κ and $g_{\rm DM}$ as seen in the different panels.

In both cases, the likelihood surrounding the best-fit point is quite flat and the preference comes from small numerical fluctuations. Thus, the best-fit likelihoods in both cases are similar and the difference is found to be insignificant, $-2\Delta \log \mathcal{L} = -0.9$.

In the entirety of the parameter space the DM-proton and DM-electron scattering cross sections are orders of magnitude below current limits, and predicted DM signals in the beam-dump experiments that we consider is much smaller than unity. The only laboratory ex-

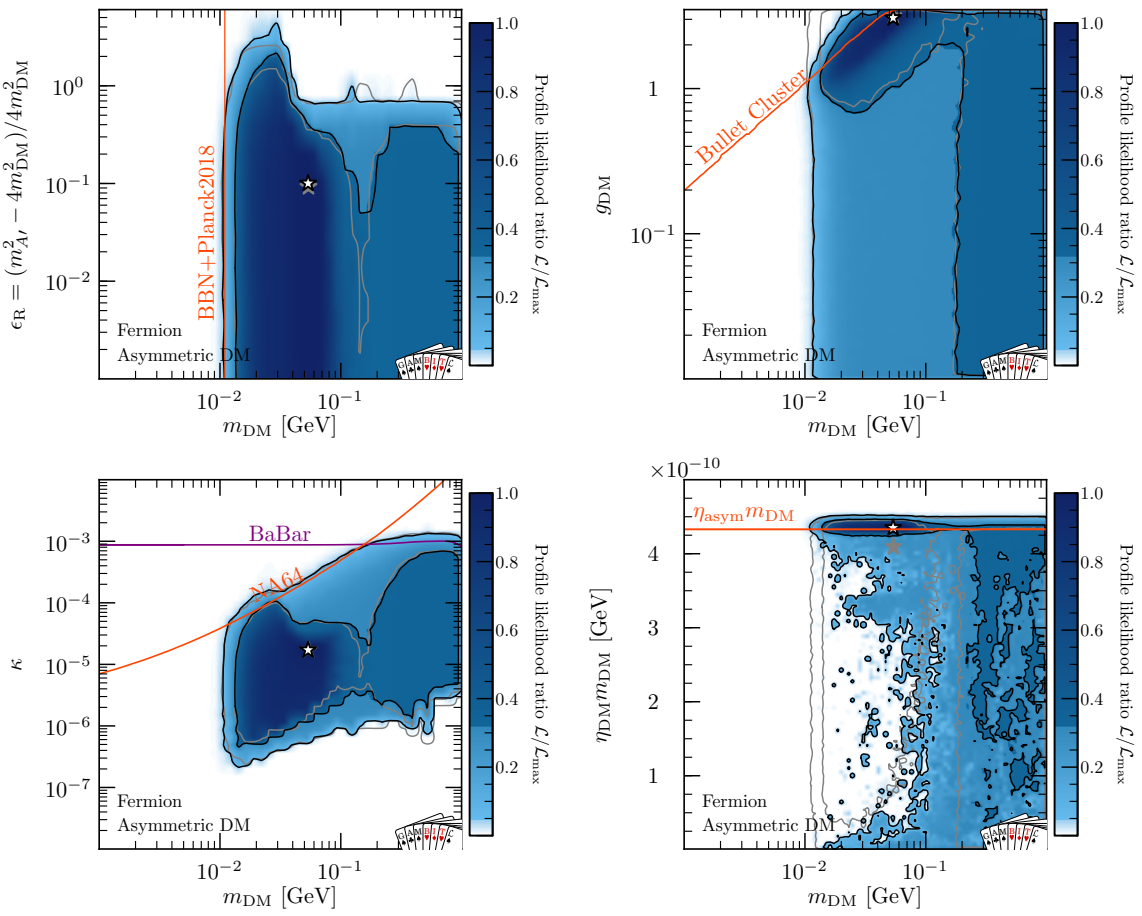

Figure 3.4.: Allowed parameter regions for asymmetric fermionic dark matter with $\Omega_{\rm DM}h^2 \approx 0.12$. As in figure 3.3, we indicate with grey lines the allowed parameter regions for a sub-dominant DM component and with a grey star the corresponding best-fit point. The red line in the bottom-right panel indicates the value of $\eta_{\rm DM}m_{\rm DM}$ that gives $\Omega_{\rm DM}h^2 = 0.12$ for the case of a negligible symmetric component.

periment that places relevant constraints on the parameter space is the BaBar single-photon search that excludes $\kappa > 10^{-3}$.

Now we turn to the case where we allow $\eta_{\rm DM}m_{\rm DM}$ to vary freely. The results are shown in Figure 3.4. Like before, we show the contours and best-fit corresponding to the case $\Omega_{\rm DM}h^2 \leq 0.12$ in grey. The contours corresponding to the case $\Omega_{\rm DM}h^2 = 0.12$ are shown in black, the best-fit is represented by the white star and the corresponding profiled likelihood is indicated by the blue shading. The confidence regions for both cases are pretty similar implying that throughout the parameter space, asymmetry is efficient in avoiding indirect detection constraint while satisfying the relic density requirement.

In the bottom right panel, we see a slight preference for $\eta_{\rm DM}m_{\rm DM} \approx 4 \times 10^{-10}\,\text{GeV}$, which corresponds to the case where DM is highly asymmetric. Thus, large values of $g_{\rm DM}$ and κ are allowed. In this case, the constraint from Bullet cluster on the self-interaction becomes relevant. In the case where $\Omega_{\rm DM}h^2 \approx 0.12$, it excludes very large $g_{\rm DM}$ at small $m_{\rm DM}$, while introducing a small preference for parameters corresponding to a self-interaction cross-section of $0.5\,\text{cm}^2\,\text{g}^{-1}$, as seen in Figure 2.3. This leads to a preference for small $m_{\rm DM}$and large $g_{\rm DM}$. This preference drives the best-fit in both cases, hence the white and grey stars lie on top

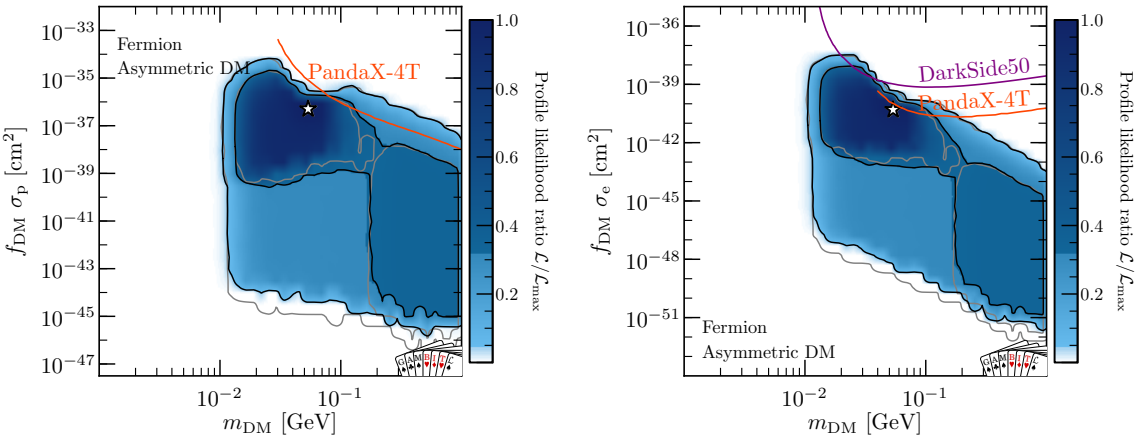

Figure 3.5.: Allowed parameter regions for asymmetric fermionic dark matter with $\Omega_{\rm DM}h^2 \approx 0.12$ in terms of various observables as a function of the DM mass.

of each other. In the case where $\Omega_{\rm DM}h^2 \leq 0.12$, the bullet cluster constraint is successfully evaded and hence we see that $g_{\rm DM}$ is essentially unconstrained throughout the $m_{\rm DM}$ range.

Compared to the case of symmetric DM with $\Omega_{\rm DM}h^2 \approx 0.12$, the asymmetric case has slightly enlarged parameter space, because large asymmetry can accommodate smaller annihilation cross-sections without overproducing DM. The likelihood of the asymmetric case is also slightly larger, $-2\Delta \log \mathcal{L} = 2.2$, but is insignificant at just 1σ level.

We also show the DM-proton and DM-electron scattering cross-sections for the asymmetric fermion in Figure 3.5. As expected from large $g_{\rm DM}$ and κ, these scattering cross-sections are large enough to be constrained by current direct detection experiments. Note that published bounds shown here correspond to 90% confidence level and, do not include uncertainties in the local DM density and velocity distribution. The best-fit is only slightly below the current exclusion bounds and within reach of future experiments.

Bayesian results

We repeat the scans (symmetric DM with $\Omega_{\rm DM}h^2 \leq 0.12$ and $\Omega_{\rm DM}h^2 \approx 0.12$ and asymmetric DM with $\Omega_{\rm DM}h^2 \approx 0.12$) in the Bayesian framework. The Bayesian results are presented as 2-D posteriors and scatter plots in all possible $x_A - x_B$ planes for the given set of model parameters included in the scan. The plots on the diagonal show histograms of the 1D posterior (orange) and prior (blue) for each model parameter marginalized over the other parameters. Marginalization here refers to integration of likelihood with respect to the other model parameters. The plots below the diagonal show the 2D marginalized priors (blue) and posteriors (orange). The regions in dark and light orange correspond to the regions with 68% and 95% credible levels, i.e. regions with the highest probability accounting for 68% and 95% of the posterior volume, respectively. The dotted lines and the crosses indicate the best-fit points in the 1-D and 2-D posteriors, respectively. The scatter plots above the diagonal show a representative sample of parameter points resulting from the scan.

Shown in Figure 3.6 are the results from the global fit of symmetric DM with $\Omega_{\rm DM}h^2 \leq 0.12$. Note that in all the Bayesian scans, we use $m_{A'}$ as the free parameter in contrast to ϵ_R used in the frequentist scan. The reason for this is that ϵ_R is not a fundamental parameter and hence it is difficult to choose an unbiased prior. Hence, we vary $m_{A'}$ between 2 MeV and 6 GeV and impose the requirement that $m_{A'} > 2m_{\rm DM}$ at prior level. For ease of comparison with the frequentist results, we still plot the posteriors and priors in terms of ϵ_R and therefore

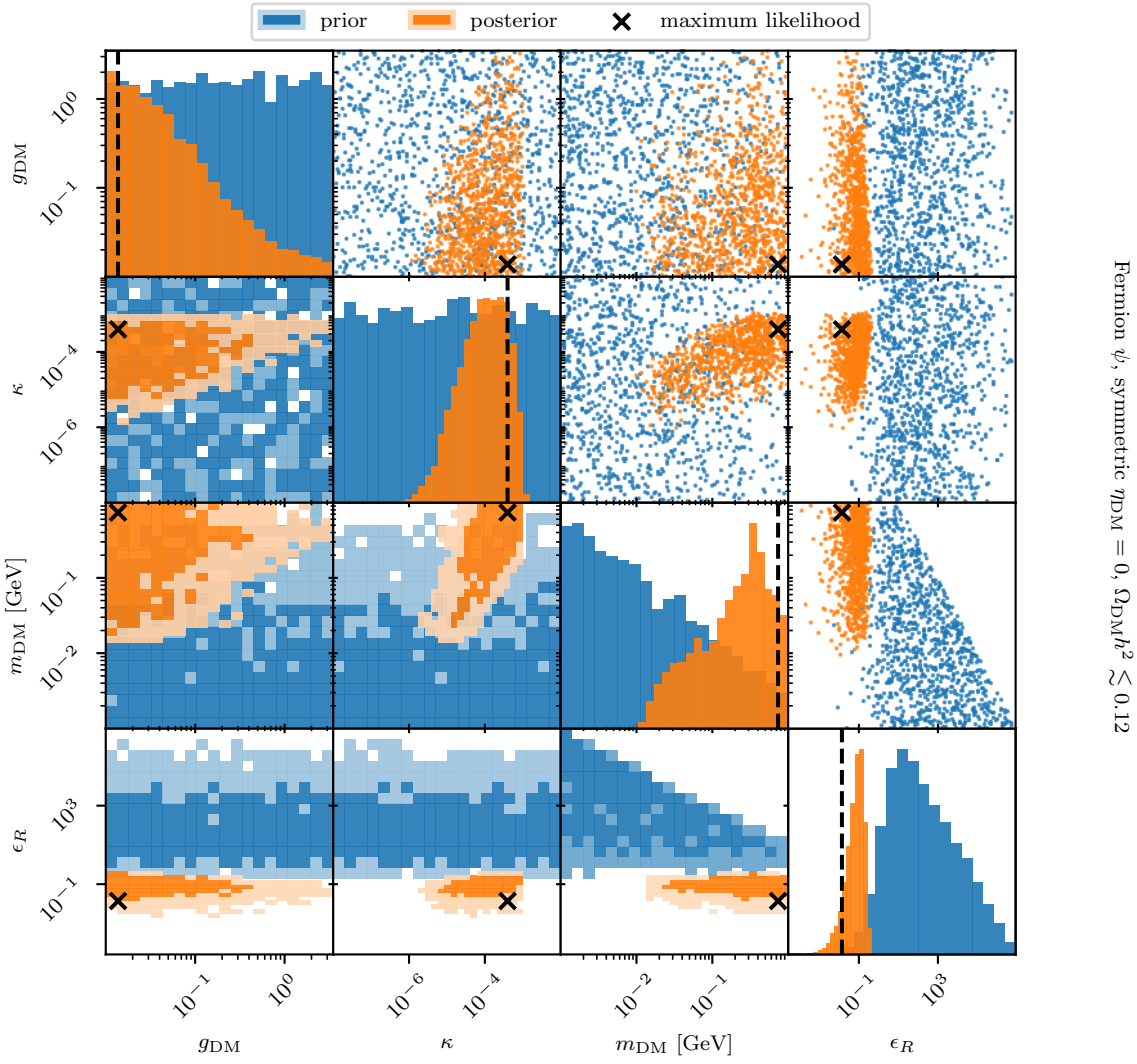

Figure 3.6.: Prior (blue) and posterior (orange) probabilities for the symmetric fermionic DM model with $\Omega_{\rm DM}h^2 \leq 0.12$. For description, see beginning of text in section 3.3.1.

see priors that are not flat for $m_{\rm DM}$ and ϵ_R. The shape of the allowed regions and the best-fit point match that found in the frequentist scans. We see large posterior probability for large κ, large $m_{\rm DM}$, small $g_{\rm DM}$ and $\epsilon_R \approx 0.1$. These preferences arise from the fine-tuning penalty in Bayesian approach. In particular, $\epsilon_R < 0.1$ requires fine-tuning between $m_{A'}$ and $m_{\rm DM}$. For these values of ϵ_R, $g_{\rm DM}$ and κ have to be fine-tuned to satisfy the relic density requirement, $\Omega_{\rm DM}h^2 \leq 0.12$.

In Figure 3.7, we show the results for symmetric fermionic DM with $\Omega_{\rm DM}h^2 \approx 0.12$. As in the frequentist scan, the credible regions shrink compared to the case of under-abundant DM, excluding $g_{\rm DM} \gtrsim 0.2$, $\epsilon_R \lesssim 10^{-2}$ and a small region towards large κ. As expected from the discussion in subsection 3.1.2, the posterior in ϵ_R peaks at ~ 0.1. This requires more fine-tuning in the other parameters, compared to the previous case, to satisfy the indirect detection constraints. The posteriors are thus more peaked towards small $g_{\rm DM}$ and large $m_{\rm DM}$ while the peak in κ shifts towards smaller values, all of which reduce the annihilation

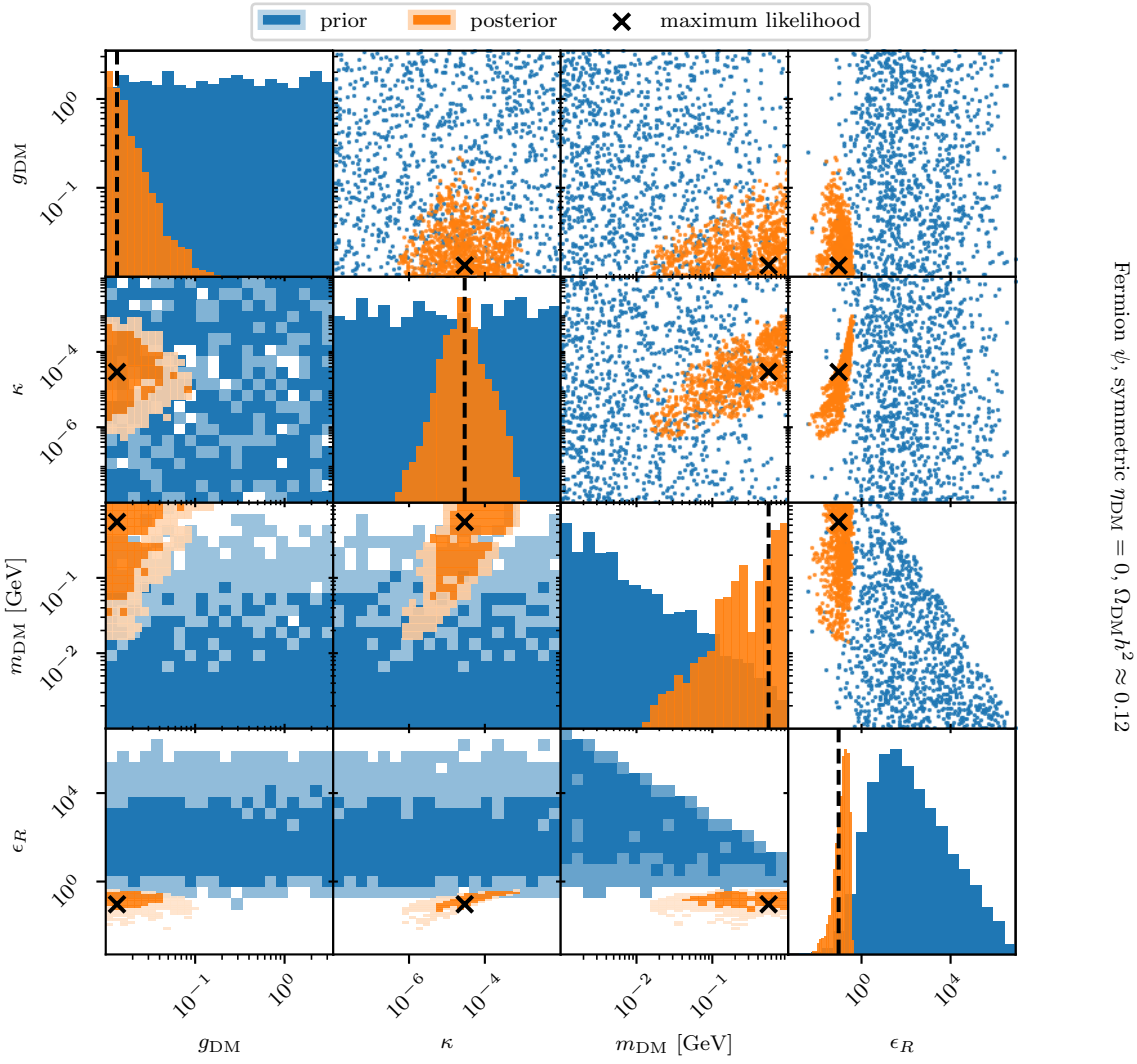

Figure 3.7.: Same as figure 3.6, but for the symmetric fermionic DM model with $\Omega_{\rm DM}h^2 \approx 0.12$.

cross-section in the late universe. The position of the best-fit once again agrees with the one found in the frequentist scan.

We next show the results for the asymmetric DM with $\Omega_{\rm DM}h^2 \approx 0.12$ in Figure 3.8. Introducing asymmetry, gives more freedom to fit data over a wide range of other parameters and hence the posteriors in $g_{\rm DM}$, $m_{\rm DM}$, and κ become broad again. The posterior for $\eta_{\rm DM}m_{\rm DM}$ is heavily constrained although it starts with a uniform flat prior. The (equal-tailed) credible interval for $\eta_{\rm DM}m_{\rm DM}$ is $[4.28, 4.35]\cdot10^{-10}$ GeV at 68% confidence level ($[3.78, 4.41]\cdot10^{-10}$ GeV at 95% confidence level). When we allow for under-abundant DM, the credible intervals broaden significantly to $[0.12, 4.30]\cdot10^{-10}$ GeV at 95% confidence level. In the entirety of the parameter space, the DM is maximally asymmetric and efficiently evades indirect detection constraints. This allows very large couplings such that the best-fit is now driven by the preference for a self-interaction cross-section of $0.5\,\mathrm{cm}^2\,\mathrm{g}^{-1}$ from the bullet cluster likelihood. The best-fit is correspondingly located at small $m_{\rm DM}$ and large $g_{\rm DM}$, away from the posterior

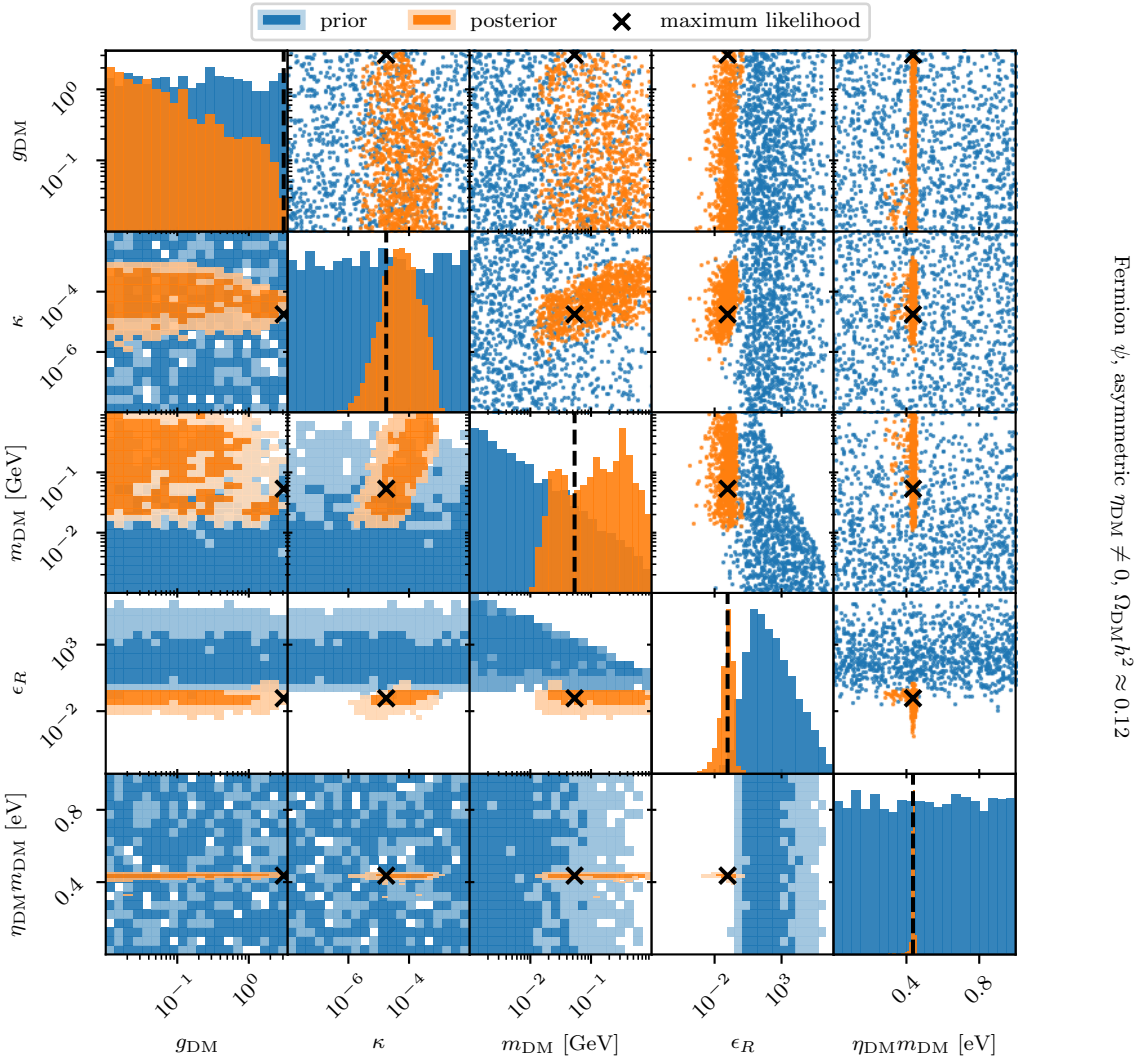

Figure 3.8.: Same as figure 3.6, but for the *asymmetric* fermionic DM model with $\Omega_{\rm DM} h^2 \approx 0.12$.

maxima. The confidence regions in Figure 3.4 which are driven by the best-fit are hence slightly different from the credible regions shown in Figure 3.8.

We perform Bayesian model comparison by decomposing the Bayesian evidence $\mathcal{Z}$ into the sum of posterior weighted log-likelihood $\langle \log \mathcal{L} \rangle_{\mathcal{P}}$ and the Kullback-Leibler divergence of the prior and posterior $\mathcal{D}_{\rm KL}$. When posterior regions fit the data quite well and have large likelihoods, $\langle \log \mathcal{L} \rangle_{\mathcal{P}}$ is large and boosts the Bayesian evidence. When fine-tuning is required to fit data well, such that the Kullback-Leibler divergence is large between the posterior and the prior, the Bayesian evidence gets a penalty from $\mathcal{D}_{\rm KL}$. Model comparison between symmetric and asymmetric fermionic DM models, where they are required to saturate the relic density, shows preference for the asymmetric fermionic model with a Bayes factor,

$$\frac{\mathcal{Z}_{\rm asym}}{\mathcal{Z}_{\rm sym}} = 15.6 \tag{3.8}$$

which corresponds to "strong" preference for the asymmetric DM model according to the Jeffrey's scale. While both models have similar best-fit likelihoods and thus similar $\langle \log \mathcal{L} \rangle_{\mathcal{P}}$,

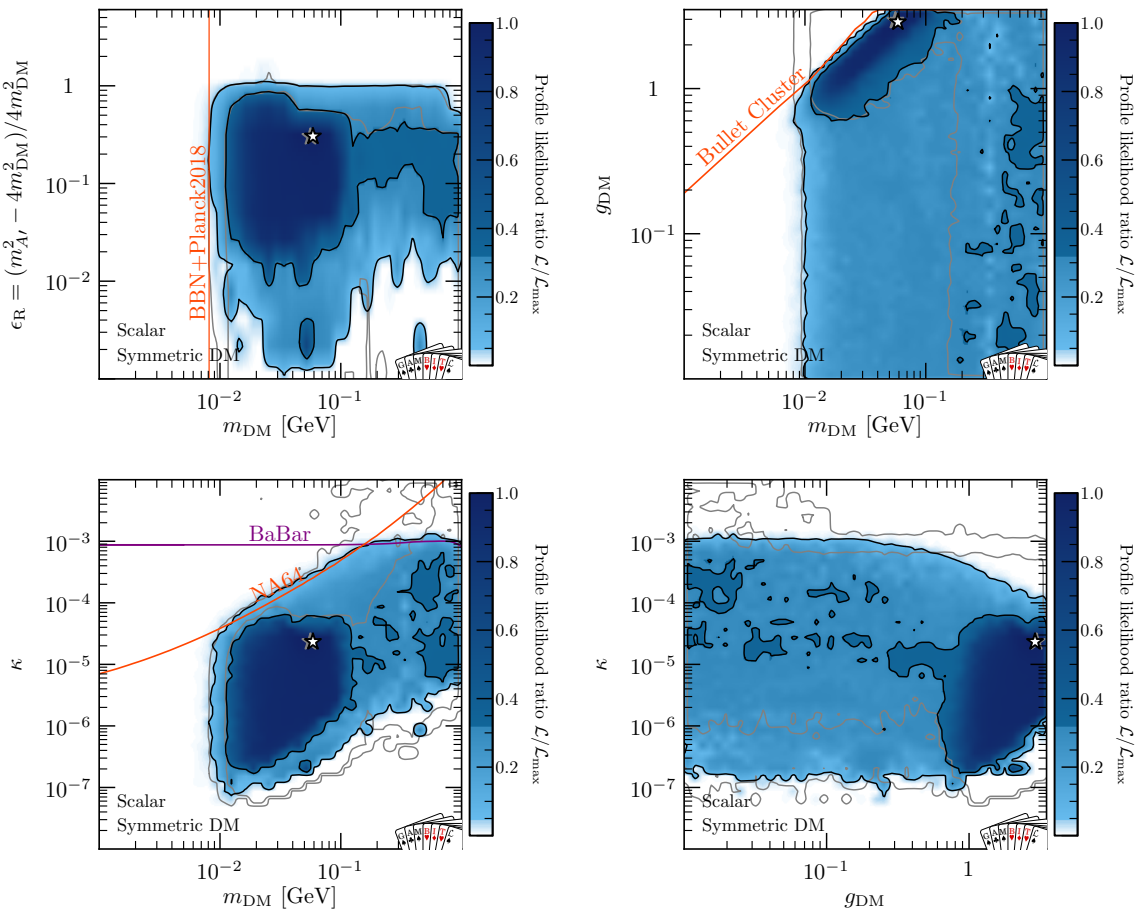

Figure 3.9.: Allowed parameter regions for symmetric scalar dark matter with $\Omega_{\rm DM}h^2 \approx 0.12$. See beginning of text in section 3.3.1 for description of plotting style.

the symmetric model requires fine-tuning in all parameters to fit data and gets a larger penalty from $\mathcal{D}_{\rm KL}$. But note that the Bayes factor depends on the choice of prior. Logarithmic prior on $\eta_{\rm DM}$ in the range $[10^{-13}, 10^{-6}]$ instead of a linear prior on $\eta_{\rm DM} m_{\rm DM}$ gives a Bayes factor of 2.9 which corresponds to a model preference that is "barely worth mentioning" according to the Jeffrey's scale.

3.3.2. Scalar DM

In this section, we present the results of frequentist and Bayesian global fits of scalar DM. Since its annihilation is p-wave suppressed, the model successfully evades indirect detection constraints without the need for asymmetry. So, we only show the results for symmetric scalar DM, but towards the end of the section give the Bayesian evidence for both symmetric and asymmetric scalar DM models.

The frequentist results for symmetric scalar DM are shown in Figure 3.9. Like before, we show the contours and best-fit of under-abundant DM for comparison, in grey. Apart from the way in which the indirect detection constraints are evaded, the asymmetric fermionic DM and symmetric scalar DM models have similar phenomenology. The results are thus similar to that of asymmetric fermionic DM. As before the bullet cluster likelihood gives rise to a preference for small $m_{\rm DM}$ and large $g_{\rm DM}$. This leads to a small preference for large ϵ_R to reproduce to right relic abundance, in contrast to the asymmetric fermionic case which for large asymmetry can saturate the relic abundance for a wider range of annihilation cross-sections. These effects

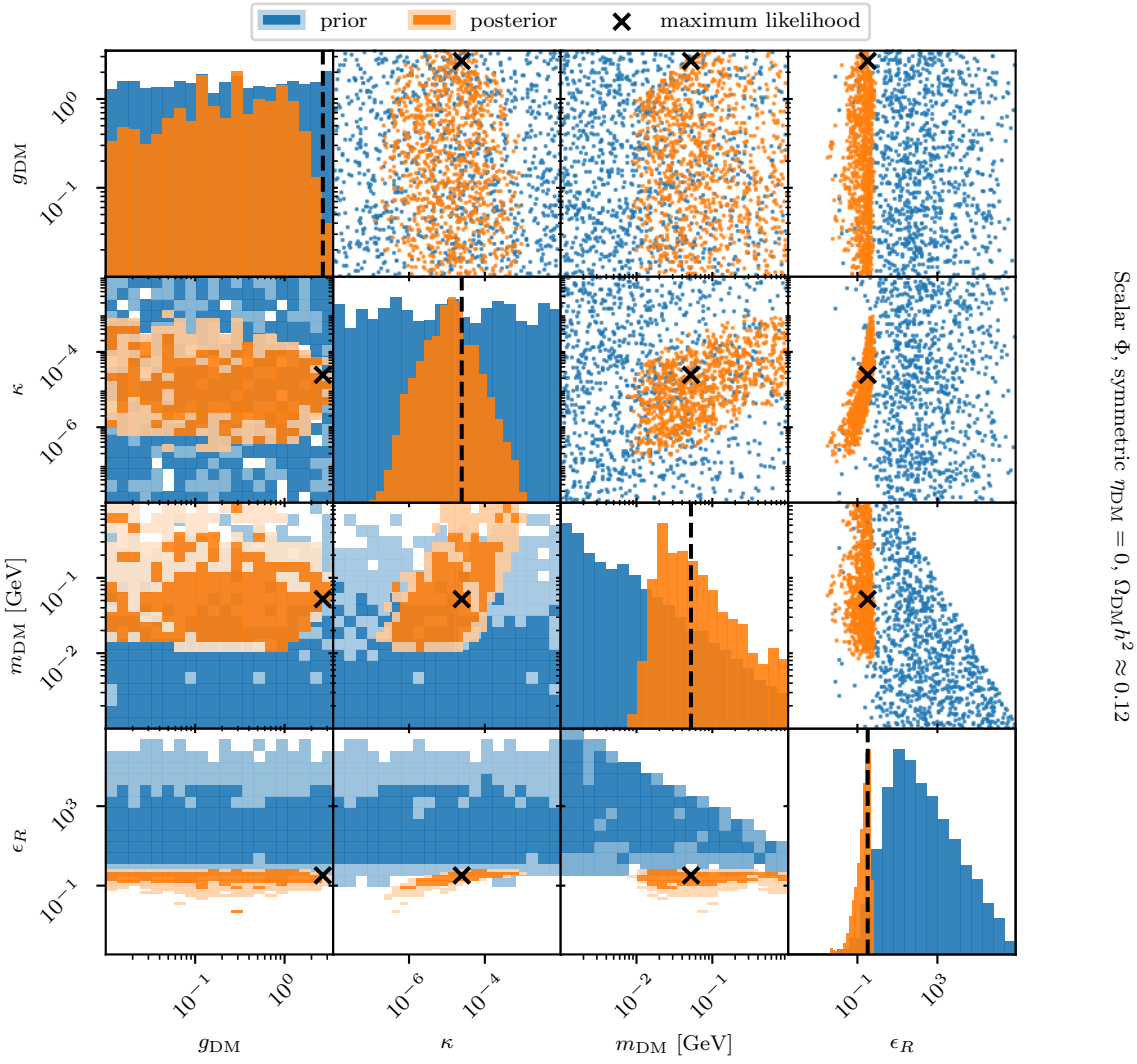

Figure 3.10.: Prior (blue) and posterior (orange) probabilities for the symmetric scalar DM model with $\Omega_{\rm DM}h^2 \approx 0.12$.

lead to exclusion of small ϵ_R for large $m_{\rm DM}$. This region leads to under-abundant DM and is hence contained within the grey contours. In addition, the under-abundant DM also includes the large $g_{\rm DM}$, small $m_{\rm DM}$ region which is excluded by the bullet cluster constraint in the $\Omega_{\rm DM}h^2 \approx 0.12$ case. For under-abundant DM, the BaBar bound can also be evaded by having simultaneously $g_{\rm DM} \approx 10^{-2}$ and $\kappa > 10^{-3}$, such that $BR_{A'} \to \chi\bar{\chi} \ll 1$. But this region would anyway be constrained by additional relevant likelihoods like searches for dark photons decaying into muon pairs at LHCb [201], which is not included in our analysis.

The Bayesian results for the symmetric scalar DM with $\Omega_{\rm DM}h^2 \approx 0.12$ shown in Figure 3.10 is similar to the Bayesian results for asymmetric fermion DM shown in Figure 3.8. Similar to asymmetric fermionic DM, confidence regions in Figure 3.9 are slightly different from the credible regions here, due to the best-fit (driven by the bullet cluster likelihood) not coinciding with posterior maxima, while the discussion about the various boundaries for different parameters remains the same as that in the frequentist case.

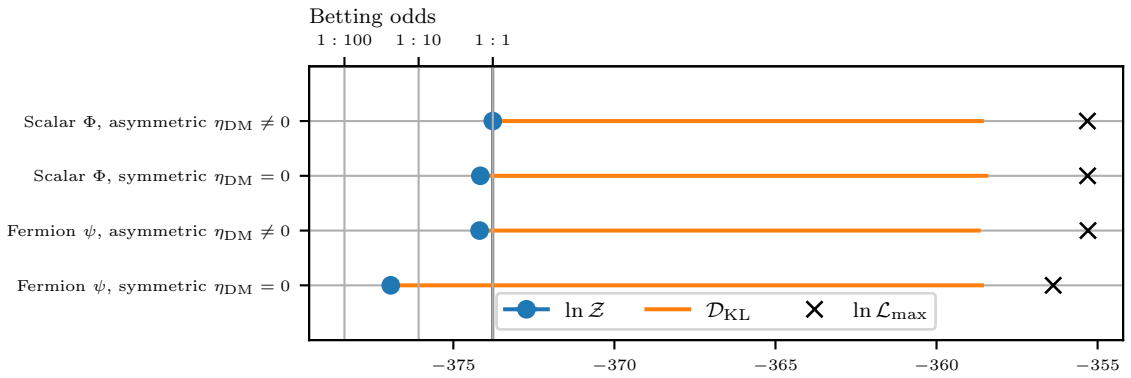

Figure 3.11.: Bayes factors for the various models considered in this work. The blue dots indicate the logarithm of the Bayesian evidence, which can be translated into betting odds relative to the most favoured model (see vertical lines and labels at the top). The orange bars show the Kullback-Leibler divergence of prior and posterior for each model, with longer bars indicating a larger fine-tuning penalty. This penalty is largest for the symmetric fermionic DM model, accounting for the smaller Bayesian evidence, whereas the log-likelihoods of the respective best-fit points (indicated by the black crosses) are similar for all models.

As expected, the asymmetric case doesn't significantly change the allowed parameter space. The Bayesian evidences given by,

$$\log \mathcal{Z}_{\rm sym} = \langle \log \mathcal{L} \rangle_{\mathcal{P}} - \mathcal{D}_{\rm KL} = -358.46 - 15.70 \ , \tag{3.9}$$

$$\log \mathcal{Z}_{\rm asym} = \langle \log \mathcal{L} \rangle_{\mathcal{P}} - \mathcal{D}_{\rm KL} = -358.60 - 15.18 \ , \tag{3.10}$$

are very similar to each other and to the asymmetric fermionic DM case and are not preferred over one another in the Bayesian framework. The Bayesian evidences of all models that saturate the relic density are shown in Figure 3.11.

3.4. Discussion

We discuss the implications of our results for future laboratory experiments.

3.4.1. Sensitivity projections

We show the sensitivities of future experiments in relevant parameter space for two of our preferred models in Figure 3.12, namely the asymmetric fermionic DM (left) and the symmetric scalar DM (right). We show sensitivity projections of the single-photon search by Belle II with 20 fb^{-1} [202] and the missing energy search by LDMX with 10^{16} electrons from an 8 GeV beam [185] in the $\kappa - m_{A'}$ plane. In the $\sigma_p - m_{\rm DM}$ plane, we show sensitivity curves from SuperCDMS [203], and the recently proposed DELight experiment [204], which plans to use superfluid helium to reach lower DM masses. In the $\sigma_e - m_{\rm DM}$ plane, we show the projections from DAMIC and SENSEI (both taken from ref. [205]).

We see that LDMX, DAMIC and SENSEI will be able to probe regions close to the best-fit point, while others still probe significant parts of the parameter space. For the corresponding Bayesian plots of observables see appendix D in B24. In the Bayesian framework, we find that LDMX will be able to probe 64% of the posterior volume.

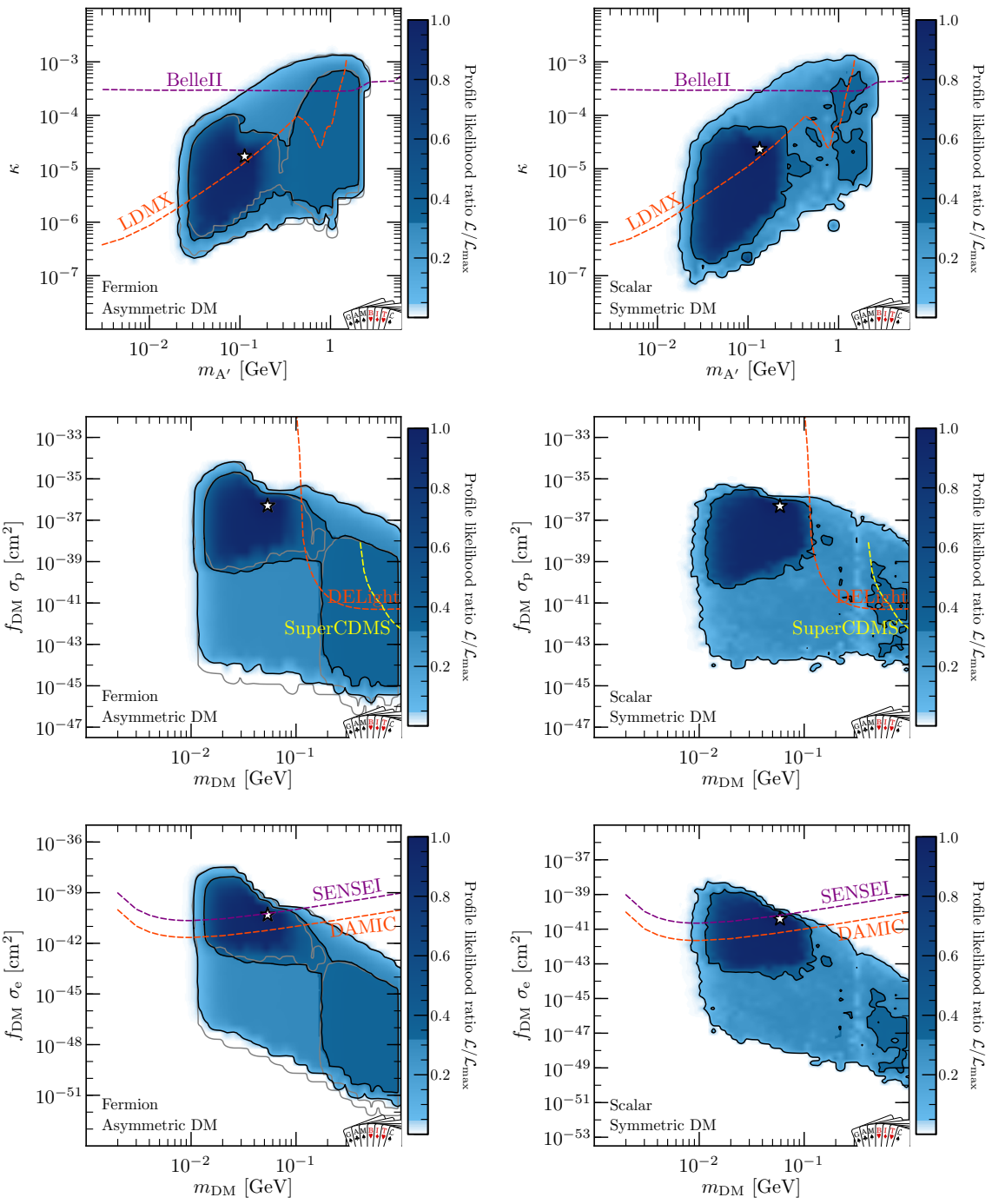

Figure 3.12.: Allowed parameter regions of the asymmetric fermionic DM model (left column) and the symmetric scalar DM model (right column) in terms of the quantities that are most directly relevant for observations: kinetic mixing versus dark photon mass (top row), effective DM-nucleon scattering cross section versus DM mass (middle row) and effective DM-electron scattering cross section versus DM mass (bottom row). In each panel we show the projected sensitivities for various near-future experiments.

3.4.2. New benchmark point

In literature, DM models coupled to a dark photon are often studied by fixing some model parameters [206–209]. It is convention to fix the dark photon mass as $m_{A'} = 3m_{\rm DM}$, which corresponds to $\epsilon_R = 5/4$. The dark sector gauge coupling, $\alpha_D = g_{\rm DM}^2/(4\pi)$ is also often fixed

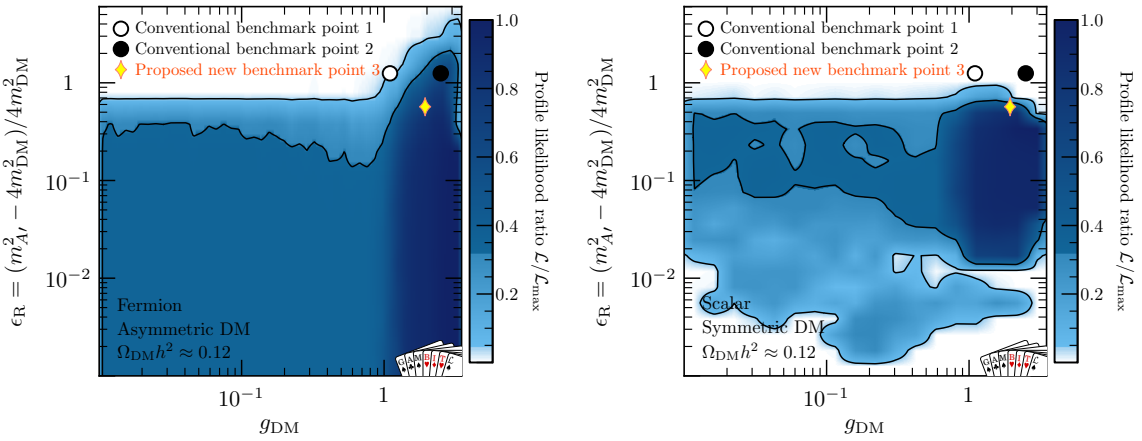

Figure 3.13.: Allowed parameter space for the asymmetric fermion DM model (left) and the symmetric scalar DM model (right) in the ϵ_R – $g_{\rm DM}$ parameter plane. The conventional benchmark points with $m_{A'}/m_{\rm DM} = 3$ and either $\alpha_D = 0.1$ (BP1) or $\alpha_D = 0.5$ (BP2) are indicated by a white and a black dot, respectively. Our proposed benchmark point with $m_{A'}/m_{\rm DM} = 2.5$ and $\alpha_D = 0.3$ (BP3) is indicated by a yellow diamond.

to 0.1 or 0.5 corresponding to $g_{\rm DM} = 1.1$ and $g_{\rm DM} = 2.5$, respectively. We plot these conventional benchmark points on the confidence regions identified from our frequentist analysis for the two preferred models, in Figure 3.13. We see that in the asymmetric fermionic DM model, the benchmark point 1 (white circle) is almost outside the 95% confidence region, while benchmark point 2 (black circle) lies within the 68% confidence region. For the symmetric scalar DM, the situation is worse as both the benchmark points lie outside the 95% confidence region. From our scans, we thus propose a new benchmark point that lies within the 68% confidence region for both asymmetric fermionic and symmetric scalar DM models,

$$\begin{aligned} m_{A'} &= \frac{5}{2} m_{\rm DM} \quad \text{or} \quad \epsilon_R = \frac{9}{16} \\ \alpha_{\rm DM} &= 0.3 \quad \text{or} \quad g_{\rm DM} = 1.94\ . \end{aligned} \tag{3.11}$$

We also show this new benchmark point (yellow diamond) in Figure 3.13. Since the new benchmark point is at large ϵ_R and large $g_{\rm DM}$ which corresponds to less resonant enhancement of annihilation cross-section, the point doesn't suffer from the uncertainty in relic density estimation mentioned in section 3.2.1. For the proposed new benchmark point, the confidence regions shrink considerably. In the case of scalar symmetric DM model, due to the relic density requirement, fixing ϵ_R and $g_{\rm DM}$ also essentially fixes κ and $m_{\rm DM}$. For the asymmetric fermionic DM model, allowing asymmetry to vary gives a region of parameter space that can reproduce the DM relic abundance. We show the allowed parameter regions for asymmetric fermionic DM model in Figure 3.14. The various constraints included in the work are shown in the panel on the left. On the right panel, we show the sensitivity projections of future experiments and we observe that this benchmark point can be completely explored in the near future.

3.4.3. Aftermath

Since this work was published, there have been a few interesting developments. In direct detection, DAMIC-M [210] published more stringent constraints compared to [190] by accumulating a larger exposure. The new DAMIC-M 90% confidence upper-limit on the DM-electron scattering cross-section as a function of $m_{\rm DM}$ is shown in maroon for the asymmetric fermionic DM in the left panel of Figure 3.15. The constraint excludes a small region

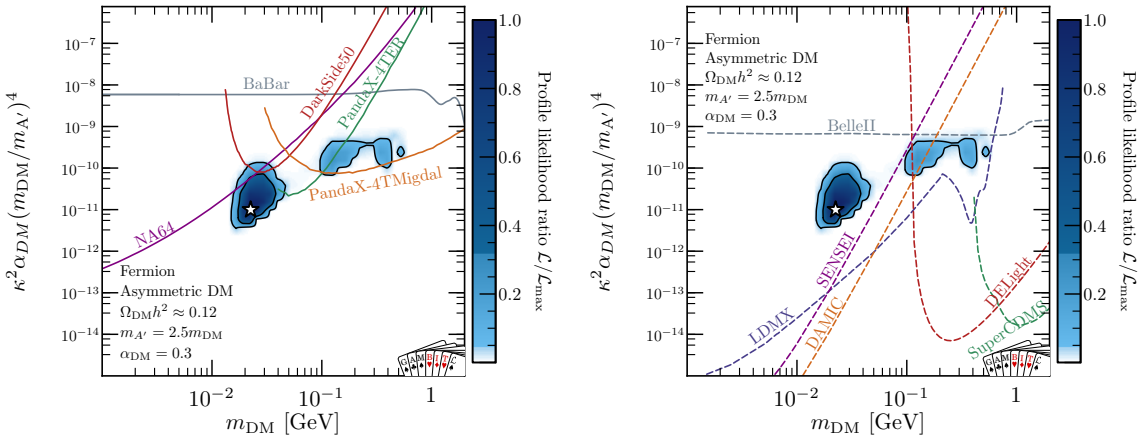

Figure 3.14.: Allowed parameter regions for asymmetric fermionic DM with fixed $\epsilon_R = 0.5625$ and $g_{\rm DM} = 1.94$ (BP3). In the left panel we show the various constraints implemented in this work, whereas the right panel shows projected sensitivities.

of parameter space at large $\sigma_{\rm e}$ and small $m_{\rm DM}$ for heavy mediators. While the improved upper-limit is extremely constraining for symmetric scalar and asymmetric fermion DM away from the resonance [211], when considered together with the relic density constraint, it does not change our findings significantly. This is because, the other constraints included in the analysis, namely, accelerator, CMB and indirect detection constraints already strongly constrain the parameter space such that both the symmetric scalar and asymmetric fermion DM are required to be close to resonance, $\epsilon \lesssim 1$ ($m_{A'}/m_{\rm DM} \lesssim 2.8$) to be viable. On the model parameter space, the only change would be a very slight shift of the 95% confidence contours to lower couplings for the smallest allowed $m_{\rm DM}$.

In indirect detection, the authors of [124] and [212] identified an error in their original analysis of the X-ray constraint form XMM-NEWTON, which is included in our global fit. The error was in the X-ray flux normalization, where the total geometric solid angle was wrongly used in place of the exposure-weighted average solid angle (which is much smaller) [213]. This gave rise to an underestimation of the X-ray fluxes observed that lead to artificially stringent constraints. The constraint was subsequently revised in the latest version of [124] and in [213]. The XMM-NEWTON constraint is now weaker than the CMB constraint in the entire DM mass range between an MeV and a GeV. Furthermore, [213] has currently determined eROSITA to be the leading player in constraining X-rays from DM annihilations, which is still weaker than the CMB s-wave annihilation constraint. But for p-wave annihilating DM for which CMB constraints become much weaker, X-ray constraint from eROSITA is currently the strongest constraint in this mass range, as DM within the galaxy today is much hotter ($v^2/c^2 \sim 10^{-3}$) than annihilating DM during recombination ($v^2/c^2 \sim 10^{-8}$).

We show the new upper bounds (95% confidence level) on $\sigma_{\rm ann}v$ as a function of $m_{\rm DM}$ from XMM-NEWTON (green) and eROSITA (maroon) in Figure 3.15 in the symmetric fermion DM model with $\Omega_{\rm DM}h^2 \lesssim 0.12$. For comparison, we still show the old XMM-NEWTON constraint (purple) with the label *X-ray*. We point out that the weakening of this constraint once again doesn't affect our results significantly because the old X-ray constraint is very close to the CMB constraint which is now the strongest constraint, in the entire mass range considered. Nothing changes in the cases of under-abundant, asymmetric or scalar DM that already evaded CMB constraints efficiently. The only change would be the shift of confidence contours to slightly higher couplings in the symmetric fermionic DM model with $\Omega_{\rm DM}h^2 \approx 0.12$.

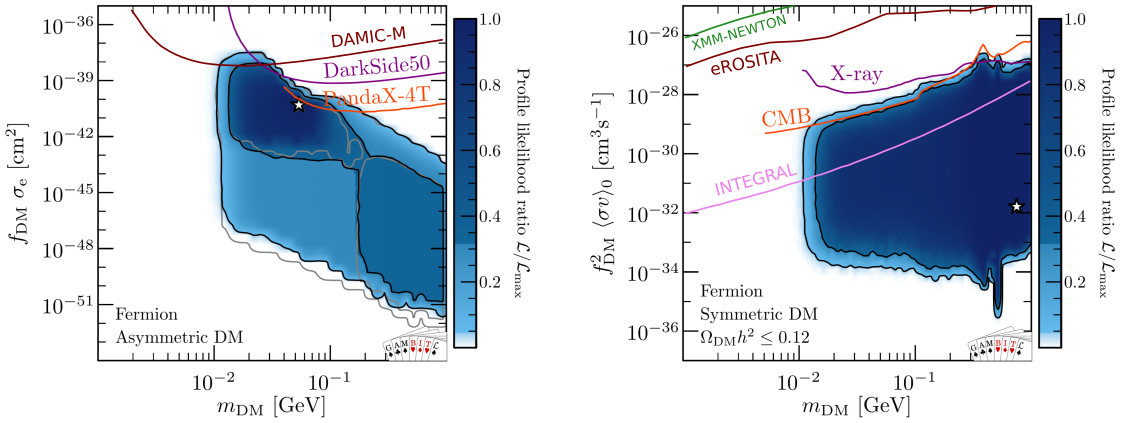

Figure 3.15.: Left panel: The new DAMIC-M 90% confidence upper bound [210] on the DM-electron scattering cross-section as a function of DM mass for the asymmetric fermionic DM model with $\Omega_{\rm DM}h^2 \approx 0.12$. **Right panel** The revised XMM-NEWTON (green) and eROSITA (maroon) upper bounds (95% confidence level) from [213] on $\sigma_{\rm ann}v$ as a function of the DM mass in the symmetric fermionic DM model with $\Omega_{\rm DM}h^2 \lesssim 0.12$.

Finally, though we chose to not include it in the analysis, we show the constraint on annihilation from the 511 keV line observed by INTEGRAL. While a clear explanation of the signal from standard astrophysical backgrounds is still lacking, the morphology of the signal has been used to place constraints on annihilating DM [212]. Even though this constraint surpasses the CMB constraint, the astrophysical uncertainties involved in modelling charged cosmic ray transport make it challenging to consistently include the constraint in a global analysis. When included in the analysis, this constraint can exclude a large part of the parameter space for symmetric fermionic DM with $\Omega_{\rm DM}h^2 \approx 0.12$, but the conclusions for our preferred models – asymmetric fermionic and symmetric scalar DM – remain unchanged.

3.5. Conclusion

In this chapter, we examined the status of sub-GeV fermionic and scalar DM coupled to a dark photon that undergoes kinetic mixing with the standard model photon. Since the thermal annihilation cross-section for the fermionic DM is excluded by CMB s-wave annihilation constraint, the DM relic density constraint cannot be simultaneously be satisfied. We explored three ways to overcome this obstacle. Firstly, we introduced resonant annihilation such that the annihilation close to freeze-out can be resonantly enhanced while it remains suppressed in the late universe. Secondly, we introduced a DM particle-antiparticle asymmetry that remains constant throughout the evolution of the universe. DM that is highly asymmetric would lead to suppressed indirect detection signals in the late universe. Asymmetric DM also requires a higher annihilation cross-section than that usually quoted as the thermal relic cross-section to reproduce the correct DM relic abundance. Thus the asymmetric DM accommodates larger couplings and is hence discoverable in current and future experiments. Finally, we also allowed our DM candidate to form only a part of the observed DM.

With the above-mentioned features, we performed global fits with `GAMBIT` in the frequentist and Bayesian framework for symmetric and asymmetric fermionic DM in both under-abundant DM and $\Omega_{\rm DM}h^2 \approx 0.12$ case. We found large allowed parameter regions for symmetric fermionic DM when allowing DM under-abundance, see Figure 3.1. For symmetric DM, when it is required to saturate the relic density, only very small couplings were allowed such that they are out of reach of current and future experiments, see Figure 3.3. Including

asymmetry reversed this situation (see Figure 3.4), making the model discoverable in future experiments, such that it didn't require suppression of various constraints from DM underabundance. Symmetric scalar DM with p-wave suppression naturally evades CMB constraint and hence is successful in fitting all available data in a large portion of the model parameter space, see Figure 3.9. From Bayesian model comparison, we found that asymmetric fermionic DM is preferred over symmetric fermionic DM, while there is no preference between asymmetric fermion and (a)symmetric scalar DM.

As a by-product of the global fits, we found that the benchmark points usually used in literature for both fermionic and scalar DM are either excluded at 95% confidence level or barely within the 68% confidence region. We thus proposed a new benchmark point as a target for future experiments that is consistent with all current constraints. We presented the sensitivities of several upcoming experiments on relevant parameter planes (see Figure 3.12) and determined that LDMX has the largest potential for discovery, probing 64% of the posterior volume. Finally, we discussed the impact of new constraints that came after our publication on our allowed parameter regions.

CHAPTER 4

Conformal dark sectors and PTAs

This chapter is based on the publication [214]. My contributions to this publication were understanding the astrophysical and cosmological constraints relevant for this model, extending the `GAMBIT` *implementation of these constraints to apply for this model, performing the global fits with* `GAMBIT`*, and producing all plots of the global fit results presented in this chapter.*

In the last chapter, we studied models of sub-GeV DM while remaining agnostic to how it obtained its mass. But, supposing the dark sector particles obtain masses from a dark Higgs mechanism, the DM phenomenology can be markedly different. The dark Higgs, apart from changing the predictions for the usual existing DM searches, can open a completely new avenue to look for signals of this model – gravitational waves (GWs). If the dark Higgs acquires a non-zero vev through a first order phase transition (FOPT), it can give rise to a stochastic gravitational wave background (SGWB) that could be detected with pulsar timing arrays (PTAs) or upcoming GW detectors.

Cosmological FOPTs that produce GWs have been studied for a long time [215, 216], motivated by open questions in the SM, mainly baryogenesis [217]. Following the discovery of the Higgs boson, with the understanding that the SM electro-weak baryogenesis only involves a second-order phase transition, studies of baryogenesis were extended with hidden/dark sectors to source the required strong FOPTs [218–223]. Later, with the first direct observation of gravitational waves, LIGO opened the gates for GW astronomy. Consequently, there was a boom of interest in using GWs as probes of DM particle properties, demanding exploration of dark sector FOPTs [224–230].

Today, the study of cosmological sources of a SGWB is especially interesting and timely in light of exciting recent developments. In 2023, the NANOGrav collaboration announced evidence for a SGWB in the nHz frequency range from the analysis of their 15-year pulsar timing dataset [231] (here after referred to as NG15). Hints of SGWB observation were already reported by NANOGrav back in 2020, in the analysis of their 12.5-year dataset [232] after years of null-results. Today (2025), the observation has been independently confirmed by the European PTA and the Indian PTA [233], the Chinese PTA [234], the Parkes PTA [235], the MeerKAT PTA [236] and the International PTA [237].

The leading astrophysical explanation for the NANOGrav signal is GWs produced in the mergers of supermassive black hole (SMBH) binaries. While this model is statistically consistent with data, it leaves room for a better statistical fit which can point to the presence of other exotic sources [238]. Such sources can include inflation [239, 240], cosmic strings [241–243], domain walls [244, 245] and FOPTs. A dark sector FOPT interpretation of the PTA signal, involving a $U(1)'$ gauge symmetry has been studied [246–248]. Similarly, models of DM within a dark sector in conjunction with nHz GW production have also been studied in [249–253]. The focus of the thesis being sub-GeV DM with a dark photon portal, in our second publication [214] (hereafter referred to as SB25), we added a dark Higgs to the dark sector. We performed global fits of this model to see if it can explain the PTA signal, produce the correct DM relic abundance while simultaneously satisfying other laboratory, astrophysical and cosmological constraints.

4.1. Supermassive black holes and SGWB

Although the physics is very different, the observational history of DM and black holes have shared parallels: both do not emit light directly and have to be inferred gravitationally. On astrophysical scales, these two candidates once competed to explain gravitational dynamics in the inner most parts of galaxies [254]. Today, they compete again, this time at cosmological time scales, to explain the PTA signal [255].

SMBHs, black holes of mass $10^6 - 10^{10}\,\mathrm{M}_\odot$ were first proposed as explanations for *quasars* (and active galactic nuclei), high-redshift objects that are much smaller than, but have luminosities exceeding that of galaxies [256]. It is now accepted that the relativistic jets from quasars are a result of accreting SMBHs and after they stop accreting, these quiet remnants must reside in the center of most galaxies [257]. Moreover, hierarchical formation of galaxies through mergers implies that the universe should be populated with SMBH binaries [258]. If the SMBH binaries manage to shrink to a separation of $\lesssim 10^{-2}\,\mathrm{pc}$, they can eventually coalesce by losing energy dominantly through the emission of nHz GWs, which could explain the observed PTA signal. Different signals including electromagnetic signatures of accreting SMBHs, along with their temporal and spectral variability have been used to identify binaries. Several such accreting SMBH binaries at sub-kpc separations have been identified [259]. Only one parsec-scale binary has been observed so far [260]. While several candidates for sub-parsec binaries have been identified, their confirmation is challenging due to limitations in the observational methods [261]. This situation is expected to improve with better data from upcoming optical surveys and more data from PTAs.

Despite the observational difficulties in resolving compact binaries, from a theoretical standpoint, it is still unclear whether environmentally driven energy loss mechanisms (by ejection of stars in the vicinity in three-body interactions) are efficient in bringing binaries to separations where GW emission would take over, between the time of binary formation and today. This is the so-called *final-parsec problem* [262]. Different solutions have been proposed, including the effects of gaseous interactions [263], rotation of non-spherical galaxies [264], a tertiary SMBH [265], and dynamical friction from self-interacting DM spikes [138]. But the subject is still not settled and is an active area of investigation. Regardless, the possibility of SGWB observation by PTAs had motivated the study of GW emission from SMBH binary mergers. The SGWB from SMBH mergers can be modeled as a power-law [266],

$$h^2\Omega_{\mathrm{gw}}^{\mathrm{BH}}(f) = \frac{2\pi^2}{3H_{100}^2} A^2 \left(\frac{f}{1\mathrm{yr}^{-1}}\right)^{5-\gamma} \mathrm{yr}^{-2}, \tag{4.1}$$

where $H_{100} \equiv H_0/h = 100\,\mathrm{km\,s^{-1}\,Mpc^{-1}}$ and $H_0 = 67.8\,\mathrm{km\,s^{-1}\,Mpc^{-1}}$ is the current day Hubble rate. The amplitude A is controlled by the astrophysical parameters involved in

details of galaxy evolution, galaxy merger rates, SMBH-host halo relationship, while the slope γ is determined mainly by the sub-parsec scale binary evolution of SMBHs. Depending on the differences in modelling, these values can range between $A \sim 10^{-18} - 10^{-14}$ and $\gamma \approx 3 - 6$, see [255] and references in their table A1. The history of binary evolution does leave imprints on its SGWB spectra, which can lead to deviations from a single power-law [267], but the single power-law is commonly in adopted in literature for simplicity.

The SMBH interpretation of the NANOGrav signal thus offers a unique opportunity to move towards a better understanding of SMBH binary evolution. The NANOGrav collaboration performed power-law fits (of just the lowest 5 frequency bins) to the free-spectrum posteriors from NG15 dataset, and found best-fit parameters $\gamma \approx 3$ and $A \sim 10^{-14}$ [255]. They also constructed the `holodeck` libraries that consist of GWB spectra from SMBH binary populations for different sets of astrophysical parameters involved in modelling of the SMBH binary population and evolution. Concretely, they include 6 parameters that govern galaxy mass function, SMBH-host galaxy mass relationship, binary evolution lifetime and power law of the SMBH orbital decay rate. By training Gaussian processes on the simulated libraries, they were able to fit their model against the free-spectrum posteriors and obtain the posterior probabilities for the SMBH binary parameters, see fig.9 in [255]. The resulting posteriors on these parameters are slightly different from typically assumed values: better fits are achieved with shorter binary hardening timescales, larger galaxy merger rates and larger normalization of SMBH-galaxy mass relation.

The findings of [255] are indicative of the fact that the amplitude of the NANOGrav signal observed is quite large compared to theoretical expectation, making it difficult to fit, which has motivated new physics interpretations of the signal [238].

4.2. Review of cosmological FOPTs

A cosmological FOPT occurs in a scenario where a field acquires a non-zero vev v, which is separated from its false vacuum by a potential barrier. In this case, the field can transition to the true vacuum by tunnelling through or fluctuating over the potential barrier, resulting in a sudden release of the energy stored in the false vacuum. The released energy goes into heating the plasma in the true vacuum, the expansion and collision of bubbles of the true vacuum, as well as the sound waves in the plasma, which subsequently source the GWs that we can observe as a stochastic background today. In the model considered in this work, the GW contribution from bubble collisions are negligible and here on we only talk about the contribution from sound waves. The spectrum of the GWs produced in this process, depends on the phase transition properties such as when it happens, how fast it happens, how much energy is released, and where the energy goes. This is determined by the temperature dependence of the effective potential of the field, which in turn depends on the particle content of the dark sector.

We focus on the evolution of a complex scalar field in a dark sector. This can be tracked by studying its effective potential, which is the sum of the tree-level potential, quantum corrections and thermal corrections. At large temperatures, the effective potential of the field starts out with a minimum at $\phi_b = 0$, where ϕ_b is the static background field. As the universe cools down below a critical temperature T_c, the effective potential develops a new minimum. The presence of a potential barrier prevents the field from gradually relaxing to the true vacuum (*cross-over* phase transition), instead the field has to tunnel through the barrier. See Figure 4.1 for an illustration of the temperature dependence of the effective potential. This introduces stochasticity in the process, and bubbles of the true vacuum randomly nucleate at different points in space.

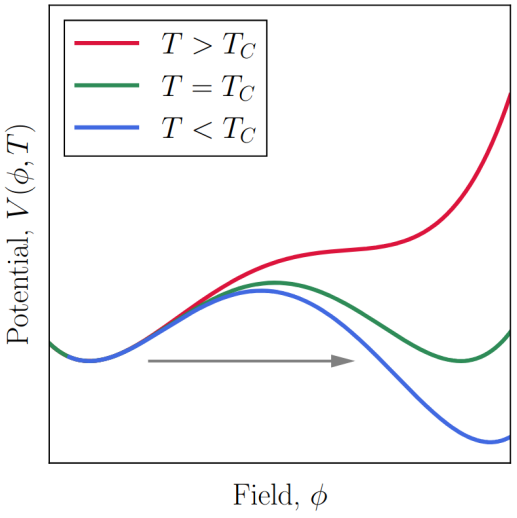

Figure 4.1.: Illustration of the temperature dependence of the effective potential $V(\phi, T)$ of a field ϕ that undergoes a first order phase transition. From [268].

The bubbles of true phase, once nucleated, start growing in size aided by the energy released in the transition to the true vacuum. As temperature decreases, more bubbles nucleate and grow in size until they fill 29% of the universe. This temperature is called the percolation temperature $T_{\rm p}$. If the bubble nucleation rate remains large compared to Hubble expansion, the rest of the universe gradually gets converted to the true vacuum. The phase transition is considered to have completed when 99% of the universe is in the true vacuum. The release of vacuum energy continually heats up the plasma until the end of the phase transition. The temperature of the plasma immediately after the end of the phase transition is called the reheating temperature $T_{\rm reh}$.

The time-scale of the phase transition from bubble nucleation to completion, depends on the bubble nucleation rate. A larger increase in bubble nucleation rate after nucleation starts means that many small bubbles fill up the universe efficiently thus quickly bringing the phase transition to its end. This can be quantified by the phase transition speed,

$$\beta/H = \frac{(8\pi)^{1/3} v_w}{R H_*} \tag{4.2}$$

where v_w is the bubble wall velocity and RH_* is the mean bubble separation at percolation, in units of Hubble length. In general, the effective potential minimum deepens as temperature decreases, and thus field transition to true vacuum at lower temperatures release more energy. This implies that slower phase transitions release more energy.

While most of the released energy goes into reheating the plasma, the fraction of energy that goes into GWs is described by the kinetic energy fraction K [269],

$$K = 0.6\,\kappa(\alpha)\frac{\alpha}{1+\alpha} \tag{4.3}$$

where κ is called the efficiency factor and α the phase transition strength. The strength is defined as $\alpha = \Delta\theta/\rho_{\rm tot}(T_{\rm p})$, where $\Delta\theta$ is the difference in the trace of the energy-momentum tensor between the true and the false vacuum, and $\rho_{\rm tot}$ the total energy density in the SM and the dark sector. For a phase transition accompanied by large vacuum energy release, $\alpha \gg 1$, $\kappa \to 1$ and hence $K \to 1$.

The phase transition speed β/H and the kinetic energy fraction K, along with a few other factors that are not important for the discussion here, set the amplitude of the GW spectrum.

As argued before, slow phase transitions lead to large vacuum energy release and strong phase transitions lead to efficient conversion of this energy to GWs. Hence, the amplitude of GWs is large for small β/H and $\alpha \gtrsim 1$. The function describing the spectral shape $\tilde{S}(f)$ is obtained from simulations and follows a doubly broken power-law [270]. Finally, in order to obtain the GW spectrum today, both the frequencies and the energy densities have to be redshifted by appropriate factors. In summary, the GW spectrum from sound-wave contribution is given by its density parameter as a function of the frequency [9],

$$h^2\Omega_{\rm GW}^{\rm PT}(f) \simeq 2.7 \cdot 10^{-5} \left(\frac{3.91}{h_{\rm reh}}\right)^{4/3} \left(\frac{g_{\rm reh}}{2}\right) \left(\frac{\beta}{H}\right)^{-2} v_w^2 \; K^2 \; \tilde{S}(f) \; , \tag{4.4}$$

where $g_{\rm reh}$ and $h_{\rm reh}$ are the total energy and entropy degrees of freedom respectively, at $T_{\rm reh}$. The second frequency break in $\tilde{S}(f)$, which is where the GW spectrum reaches its maximum amplitude is given by,

$$f_2 \simeq 2.8\,{\rm nHz} \left(\frac{\Delta_w^{-1}}{v_w}\right) \left(\frac{g_{\rm reh}}{100}\right)^{1/2} \left(\frac{100}{h_{\rm reh}}\right)^{1/3} \left(\frac{\beta}{H}\right) \left(\frac{T_{\rm reh}}{100\,{\rm MeV}}\right) \; , \tag{4.5}$$

where for relativistic bubble wall velocities, $\Delta_w^{-1}/v_w \sim \mathcal{O}(1)$. For more details, see sec. 3.2 in SB25.

4.3. Conformal dark sector models

With a general understanding of GW production from cosmological FOPTs, we can now attempt to construct a model that can fit the PTA signal. The PTA signal is observed to be a steadily increasing spectrum in the nHz frequency range with a peak amplitude of $h^2\Omega_{\rm GW}^{\rm peak} \sim 10^{-7}$. As seen from Equation 4.5, we can obtain a GW spectrum in the nHz frequency range for $T_{\rm reh} \sim \mathcal{O}(100)\,{\rm MeV}$ and $\beta/H \lesssim 100$. And from Equation 4.4, we see that we need sufficiently slow (small β/H) and strong (large α, $K \to 1$) phase transitions to achieve an amplitude as large as the observed one. Such conditions can be achieved when supercooling occurs, i.e. when the field stays in the false vacuum for a long time before converting to the true vacuum, thereby releasing a large amount of vacuum energy. This can be achieved by tuning the effective potential such that $T_{\rm p} \ll T_c$.

It has been shown that nearly conformal dark sectors can achieve strong supercooling before phase transition occurs, providing a boost to the GW signal [246]. We will thus adopt this symmetry in our model to obtain a good fit to data. We start with a complex scalar Φ with a scale-invariant tree-level potential,

$$V(\Phi) = \lambda(\Phi^*\Phi)^2 \; .$$

We consider a $U(1)'$ symmetry whose gauge boson is the dark photon A'. Note that the tree-level potential respects both the conformal and the gauge symmetry. We further introduce fermions that will act as our DM candidate. We introduce them as two left handed fermions $\chi_{1,2}$ with equal and opposite $U(1)'$ charges. We set the charge of the complex scalar to be $Q_\phi = Q_2 - Q_1 = 1$ so that the Yukawa terms are gauge-invariant. The Lagrangian is given by,

$$\mathcal{L} = |D_\mu\Phi|^2 - \frac{1}{4}F'_{\mu\nu}F'^{\mu\nu} + \bar{\chi}_1 i\not{D}\chi_1 + \bar{\chi}_2 i\not{D}\chi_2 - \Big(\frac{y_1}{2}\Phi\bar{\chi}_1^c\chi_1 + \frac{y_2}{2}\Phi^*\bar{\chi}_2^c\chi_2 + \text{ h.c. }\Big) - V(\Phi), \tag{4.6}$$

[9] This relation is valid for $\beta/H \gtrsim 3$. FOPTs that don't satisfy this condition are anyway problematic because the phase transition would be extremely slow and might not complete, leaving the universe stuck in vacuum domination.

where the gauge covariant derivative is $D_\mu = \partial_\mu + igQA'_\mu$ and χ^c denotes the charge-conjugated field. For simplicity, we assume that these fermions are mass degenerate, i.e., $y_1 = y_2 \equiv y$. After spontaneous symmetry breaking, the Majorana fermions $\chi'_{1,2} = \chi_{1,2} + \chi^c_{1,2}$ acquire masses. Since they are mass-degenerate, we can define a single Dirac fermion,

$$\chi = \frac{1}{\sqrt{2}}(\chi'_1 + i\chi'_2) \ . \tag{4.7}$$

The simplified interaction Lagrangian is then given by,

$$\mathcal{L}_{\rm int} \supset -\lambda v\phi^3 - \frac{\lambda}{4}\phi^4 + g^2 v A'_\mu A'^\mu \phi + \frac{g^2}{2}\phi^2 A'_\mu A'^\mu + \frac{g}{2}\bar{\chi}\gamma^\mu\gamma^5\chi A'_\mu - \frac{y}{2\sqrt{2}}\phi\bar{\chi}\chi \ , \tag{4.8}$$

with the fermion mass term $\mathcal{L} \supset -m_\chi\bar{\chi}\chi$. Here, we ignored the opposite $U(1)'$ charges on the Majorana fermions and simplified the interaction to a single term shown in the Lagrangian. The sign of the charges do not enter in any of the processes considered in our analysis and hence the above simplification is justified. The dark sector particle masses after symmetry breaking are given by,

$$m_\phi = \sqrt{3\lambda}v, \quad m_{A'} = gv, \quad m_\chi = \frac{yv}{\sqrt{2}} \ , \tag{4.9}$$

where λ is the quartic self-coupling which is fixed by g, y and v due to the conformal symmetry. The requirement of real m_ϕ restricts us to $y < g$ in this model, in which case the heaviest dark sector particle is the dark photon.

Let us briefly stop here and consider a dark sector with no portal to the SM. Assuming instantaneous reheating and thermalisation within the dark sector, a strong FOPT with supercooling would possibly reheat the dark sector to temperatures higher than that of the SM bath. If the dark sector is relativistic, it would add a positive contribution to $N_{\rm eff}$. If it is non-relativistic, it could lead to early matter domination. Both of these are strongly constrained by the CMB. Thus, to provide a good fit to the PTA signal while being consistent with standard cosmology, the energy density in the dark sector should be efficiently depleted after the phase transition by annihilations or decays to the SM [230].

We introduce again our kinetic mixing portal from the last chapter. This portal does not spoil the conformal symmetry of the model and we can still obtain strong supercooling[10]. This portal gives rise to an effective interaction between the dark photon and the SM fermions, see subsection 3.1.1. This allows decays of dark photons to SM fermions for dark photon masses above the MeV-scale. The portal also allows loop-induced decays of dark Higgs into SM fermions. The energy density apart from that in our DM candidate can then be dumped into the SM thermal bath through decays of the dark photons and the dark Higgs. While the dark photon decays are efficient, the dark Higgs can have lifetimes as large as 10^5 s in our model parameter space, which is strongly constrained by BBN and CMB. This brings us to two possibilities, one where the dark Higgs is coupled to electrons through some effective interaction $y_{\rm eff}\phi\bar{e}e$ which we call *coupled dark sector*. For details on other possible couplings, see sec. 2.2 and on how such an effective coupling can arise, see appendix A in SB25. The other possibility is where it can only decay through dark photon loops, which we refer to as *secluded dark sector*. We will study both cases separately in our work.

To summarize, we introduced three dark sector particles: the dark Higgs ϕ, the dark photon A' and the dirac fermion DM candidate χ. We have four model parameters: the Yukawa coupling y, the gauge coupling g, the vev v and the kinetic mixing parameter κ. Note that we do not vary $y_{\rm eff}$ freely in our theory and consider it to be some value that

[10] A Higgs mixing portal would violate the conformal symmetry of the model as the electro-weak symmetry breaking would give mass to the dark Higgs as well [271].

satisfies $y_{\rm eff} \ll \kappa$ such that dark Higgs mediated annihilations $\bar{\chi}\chi \leftrightarrow e^+e^-$ is suppressed compared to that mediated by dark photon, but still ensures efficient decays of the dark Higgs to electrons. Here on, when we mention annihilations to electron-positron pairs we only refer to dark photon mediated case.

4.4. DM production

In line with the candidates of interest in the thesis, we consider production of DM through freeze-out mechanism. In section 2.1, we came to the conclusion that, to be consistent with BBN and CMB, DM should undergo non-relativistic freeze-out and it should freeze-out before BBN. There we assumed that the DM relic density is set by freeze-out of annihilations to SM fermions which have negligible chemical potentials. As we will see later, a good fit to the PTA signal requires $g \sim \mathcal{O}(10^{-1})$, while kinetic mixing parameter $\kappa > 10^{-3}$ is excluded by laboratory experiments. Since $\kappa \ll g$ throughout the parameter space we consider, the additional annihilation channel $\bar{\chi}\chi \leftrightarrow \phi\phi$ turns out to be more efficient than annihilation to electron-positron pairs. DM production in both coupled and secluded dark sector cases thus proceeds through freeze-out out of $\bar{\chi}\chi \leftrightarrow \phi\phi$. For the range of kinetic mixing parameter values that we consider, $10^{-7} \leq \kappa \leq 10^{-3}$, DM scattering off electrons is efficient as long as electrons are relativistic. Hence we set the dark sector temperature equal to that of the SM during freeze-out. This assumption will allow us to work with the standard thermal distributions for the dark sector particles involved in the freeze-out.

4.4.1. Coupled dark sector

After the FOPT, kinetic and chemical equilibrium between the dark sector and the SM are restored by efficient annihilations $\bar{\chi}\chi \leftrightarrow e^+e^-$ and dark Higgs decays $\phi \leftrightarrow e^+e^-$. The former only maintains $\mu_{\bar{\chi}} = -\mu_\chi$, while the latter ensures $\mu_\phi = 0$ until they decay away. For DM annihilations to products with zero chemical potential, one can solve the standard Boltzmann equation we derived in section 2.2. So this is very similar to the standard freeze-out picture, with the difference that DM annihilates to dark Higgs and not SM fermions. Therefore, for χ to make up a viable DM candidate, it needs to freeze-out before BBN. When we have the mass hierarchy $m_\chi > m_\phi$, it implies $y \gtrsim 0.3$. Therefore DM particles efficiently annihilate to the dark Higgs and the DM abundance is depleted strongly before annihilations freeze out. We thus require $m_\chi < m_\phi$ where annihilations becomes forbidden at zero temperature and Boltzmann suppressed during freeze-out.

4.4.2. Secluded dark sector

At high temperatures when both $\bar{\chi}\chi \leftrightarrow e^+e^-$ and $\bar{\chi}\chi \leftrightarrow \phi\phi$ are efficient, we have $\mu_{\bar{\chi}} + \mu_\chi = 2\mu_\phi = 0$ for negligible $\mu_{e^\pm}$. The reaction $\bar{\chi}\chi \leftrightarrow e^+e^-$ drops out of equilibrium first, at a temperature $T_f^{\rm SM}$. Below this temperature, there are no other reactions to maintain the dark Higgs chemical potential at zero. We therefore cannot use Equation 2.12 and one would have to solve the coupled Boltzmann equations for χ and ϕ to obtain the DM yield at T_f^ϕ, the temperature at which $\bar{\chi}\chi \leftrightarrow \phi\phi$ freezes-out.

Instead, we estimate the relic abundances based on the following arguments. Assuming that the other number-changing processes $3\phi \to 2\phi$ and $\bar{\chi}\chi \to 3\phi$ are already inefficient at temperatures below chemical decoupling of the dark sector from the SM, the total comoving number density of DM particles, antiparticles and dark Higgs stays constant. Assuming symmetric DM $n_\chi = n_{\bar{\chi}}$, and writing in terms of yields we have,

$$Y_\chi(T_f^{\rm SM})\left(1 + \frac{Y_\phi}{2Y_\chi}(T_f^{\rm SM})\right) = Y_\chi(T_f^\phi)\left(1 + \frac{Y_\phi}{2Y_\chi}(T_f^\phi)\right) . \tag{4.10}$$

The above equation can be solved for $Y_\chi(T_f^\phi)$ once we determine $T_f^{\rm SM}$, T_f^ϕ, $Y_\chi(T_f^{\rm SM})$ and the yield ratios at both these temperatures. The DM yield after freeze-out stays constant such that the yield today is given by $Y_{\chi,0} = Y_\chi(T_f^\phi)$. The dark Higgs abundance on the other hand, gets depleted due to decays and is subject to constraints from BBN and CMB, see subsection 4.6.4.

The temperature at which the dark sector decouples from the SM $T_f^{\rm SM}$, can be obtained by solving the standard Boltzmann equation in Equation 2.12 by completely ignoring $\bar\chi\chi \leftrightarrow \phi\phi$ processes, from which we also obtain

$$\tilde\Omega_\chi h^2 = 2.755 \cdot 10^8 \left(\frac{m_\chi}{1\,\text{GeV}}\right) Y_\chi(T_f^{\rm SM}) \ .$$

At this temperature, the ratio of yields can be easily obtained from their equilibrium distributions that assume zero chemical potentials,

$$\frac{Y_\phi}{Y_\chi}(T_f^{\rm SM}) = \frac{Y_\phi^{\rm eq}}{Y_\chi^{\rm eq}} = \frac{g_\phi}{g_\chi}\,(1-\delta)^{3/2}\, e^{\delta x_f^{\rm SM}} \ , \tag{4.11}$$

where $\delta = 1 - m_\phi/m_\chi$, $x_f^{\rm SM} = m_\chi/T_f^{\rm SM}$, $g_\chi = 2$ and $g_\phi = 1$.

At $T_f^\phi < T < T_f^{\rm SM}$, detailed balance requires that

$$Y_\chi^2 \langle\sigma v\rangle_{\bar\chi\chi\to\phi\phi} = Y_\phi^2 \langle\sigma v\rangle_{\phi\phi\to\bar\chi\chi} \ , \tag{4.12}$$

from which we get $\dfrac{Y_\phi}{Y_\chi}(T_f^\phi) = \sqrt{\dfrac{\langle\sigma v\rangle_{\bar\chi\chi\to\phi\phi}}{\langle\sigma v\rangle_{\phi\phi\to\bar\chi\chi}}} = \sqrt{\bar r}$. We obtain the DM freeze-out temperature T_f^ϕ by numerically solving the freeze-condition $Y_\chi(T_f^\phi)\langle\sigma v\rangle_{\bar\chi\chi\to\phi\phi} \approx H(T_f^\phi)/s(T_f^\phi)$, which using the above results can be written as,

$$Y_\chi\left(x_f^{\rm SM}\right) \frac{1 + \frac{1}{2}\frac{g_\phi}{g_\chi}(1-\delta)^{3/2} e^{\delta x_f^{\rm SM}}}{1 + \frac{1}{2}\sqrt{\bar r(x_f^\phi)}} \langle\sigma v\rangle_{\chi\chi\to\phi\phi}(x_f^\phi) = H(x_f^\phi)/s(x_f^\phi) \ . \tag{4.13}$$

This then gives us everything we need to evaluate the current day DM abundance, $\Omega_{\rm DM}h^2 = 2\Omega_\chi h^2$ and the dark Higgs abundance that would have remained today in case it is stable $\tilde\Omega_\phi h^2$,

$$\Omega_\chi h^2 \simeq \tilde\Omega_\chi h^2 \times \frac{1 + \frac{1}{2}\frac{g_\phi}{g_\chi}(1-\delta)^{3/2} e^{\delta x_f^{\rm SM}}}{1 + \frac{1}{2}\sqrt{\bar r(x_f^\phi)}}, \tag{4.14}$$

$$Y_\phi(T_f^\phi) = \ (Y_\chi)_{x_f^{\rm SM}} \left(1 + \frac{1}{2}\frac{g_\phi}{g_\chi}(1-\delta)^{3/2} e^{\delta x_f^{\rm SM}}\right) \left(\frac{\sqrt{\bar r}}{1 + \frac{1}{2}\sqrt{\bar r}}\right)_{x_f^\phi} \ , \tag{4.15}$$

where the subscripts $x_f^{\rm SM}$ and x_f^ϕ indicate the quantities evaluated at that temperature.

For $m_\chi < m_\phi$ ($\delta < 0$), the dark Higgs efficiently annihilate to DM and most of the energy density in the dark sector ends up in DM after decoupling from SM, $\Omega_\chi h^2 \approx \tilde\Omega_\chi h^2$. In the opposite case, $m_\chi > m_\phi$ ($\delta > 0$), the dark Higgs annihilations are kinematically suppressed while DM annihilates efficiently into the dark Higgs, quickly depleting its energy density, $\Omega_\chi h^2 \ll \tilde\Omega_\chi h^2$. In both cases, the smaller the mass difference, the longer do the dark sector interactions stay in equilibrium. Thus for $\delta \to 0$, freeze-out can happen as late as $x_f^\phi \sim 10^4$, which can be during BBN for $m_\chi \sim \mathcal{O}(100\,\text{MeV})$.

4.5. GW prediction

In our model, we consider contributions to the observed SGWB from both SMBH binary mergers and the dark sector FOPT,

$$h^2\Omega_{\rm gw}(f) = h^2\Omega^{\rm BH}_{\rm gw}(f) + h^2\Omega^{\rm PT}_{\rm gw}(f). \tag{4.16}$$

For the SMBH binary contribution, we adopt the power-law in Equation 4.1 and treat A, γ as nuisance parameters. The prediction for GW spectrum from our dark sector FOPT starts with the computation of the quantum and thermal corrections to the tree-level potential. The temperature-dependent effective potential is then used to determine various thermodynamic properties of the FOPT including percolation temperature $T_{\rm p}$, mean bubble separation RH_*, kinetic energy fraction K, reheating temperature $T_{\rm reh}$. For the parameter space that we consider, we find sound-wave contribution to be the strongest and omit others assuming that they are sub-dominant. The prediction for the GW spectrum from sound waves is then determined based on the above quantities according to Equation 4.4. All these calculations starting from the effective potential to the GW signal prediction have been performed with a modified version of `TransitionListener` [272].

4.6. Constraints

In this section, we discuss the constraints included in our global fits that we perform using `GAMBIT`. We include the same accelerator constraints on dark photon decays discussed in the previous chapter in subsection 3.2.2. In our model, DM scattering off SM fermions are momentum suppressed rendering direct detection constraints irrelevant. DM annihilations to both SM fermions and dark Higgs proceed through p-wave and hence indirect detection constraints are also irrelevant for our model. We thus do not include direct and indirect detection constraints in our global fits. Additionally, we include the bullet cluster constraint discussed in subsection 2.6.2.

4.6.1. Relic density likelihood

We employ the `GAMBIT` interface to `DarkSUSY` [75] to perform the relic density calculations for both the coupled and the secluded dark sector case.

We then compare the predictions to the observation $\Omega h^2 = 0.120 \pm 0.001$ by Planck [7]. We have a sizeable theory uncertainty that is much larger than the measurement uncertainty. In the coupled dark sector case, this is due to potential early kinetic decoupling occurring in parts of the parameter space that we don't include in our calculation (see footnote from sec. 4 in SB25). For the secluded dark sector case, the main source of uncertainty is from the use of sudden freeze-out approximation of $\phi\phi \leftrightarrow \bar{\chi}\chi$ in Equation 4.13 to calculate the final DM relic abundance. We therefore conservatively include a theoretical uncertainty of a factor of 2 and implement the relic density likelihood as,

$$\log_2\left(\frac{\Omega h^2}{0.12}\right) = 0 \pm 1\ . \tag{4.17}$$

Although this likelihood seems to allow large variation in relic density, we point out that the relic density depends exponentially on model parameters in the critical regimes. This leads to modest shifts in the allowed parameter regions for a factor 2 uncertainty.

4.6.2. SMBH likelihood

We impose the following 2D Gaussian likelihood on the SMBH model parameters A and γ,

$$\mu_{(A,\gamma)} = \begin{pmatrix} -15.615 \\ 4.707 \end{pmatrix} \quad \text{and} \quad \text{cov}_{(A,\gamma)} = \begin{pmatrix} 0.279 & -0.003 \\ -0.003 & 0.124 \end{pmatrix}. \tag{4.18}$$

This distribution was obtained by [238] by fitting the free-spectrum posteriors in the NG15 dataset (first 14 frequency bins) to GWB spectra from `holodeck` libraries, simulated using standard values of astrophysical parameters from literature. These values were based on observational constraints and numerical studies of SMBH binary evolution. They also assumed purely GW-driven hardening in the sub-parsec scale binary evolution. Although realistic treatment involving environment effects could change the low-frequency spectra, the amplitude would remain unaffected. This forms the main motivation for this study.

4.6.3. PTA likelihood

We compare the GW prediction obtained from `TransitionListener` [272] to NG15 dataset and calculate the corresponding PTA likelihood using the `ceffyl` [273] backend in `PTArcade` [274]. The likelihood is then passed on to `GAMBIT` through a newly implemented interface called `ptalistener`. The `ceffyl` package calculates the PTA likelihood by comparison of predicted GW spectrum to the free-spectrum posteriors of the cross-correlated timing-residual power spectral density. This provides a speed up of $10^2 - 10^4$ [238] compared to the full likelihood of timing residuals, which is crucial in our global fitting context.

4.6.4. BBN and CMB constraints

In our model, the FOPT can influence cosmology by injecting energy into the SM thermal bath during reheating and increasing radiation density through the emission of gravitational waves. The dark sector reheating at the end of FOPT can in turn reheat the SM plasma through DM-electron scatterings, dark photon decays (as well as dark Higgs decays in the coupled dark sector model). If the reheating happens at very low temperatures, the non-thermal neutrinos from energetic $e^{\pm}$ annihilations would not have enough time to thermalise and cause changes to the primordial light element abundances. Constraints exist for low reheating scenarios, where a massive particle that dominated the energy density of the universe before radiation domination, injects energy into the SM plasma through decays. These constraints on reheating temperature have been obtained by studying the effects of neutrino spectral distortions on BBN and CMB [106],

$$T_{\text{reh}} > 3.79\,\text{MeV} \quad \text{(Planck+lensing+DESI)}, \tag{4.19}$$

$$T_{\text{reh}} > 5.96\,\text{MeV} \quad \text{(BBN+Planck+lensing+DESI)}\ . \tag{4.20}$$

These represent the most stringent constraints to date on low reheating scenarios, obtained from precise treatment of neutrino distributions and use of the latest data. Since strong supercooling implies the release of large amounts of energy, we can apply these constraints to our reheating temperatures. But the above constraints are subject to uncertainties due to choice of priors used in the analysis, hence we implement a conservative constraint of $T_{\text{reh}} > 3\,\text{MeV}$, instead of doing a detailed study of changes to BBN and CMB through neutrino spectral distortions.

The energy density in GWs can contribute to the total energy density as dark radiation and can increase N_{eff} in extreme cases. But even for the largest observed peak amplitude

$h^2\Omega_{\rm GW}^{\rm peak} \simeq 10^{-7}$, the change induced to $N_{\rm eff}$ is much smaller than the current observational bounds on $\Delta N_{\rm eff}$ and hence we neglect this contribution while calculating the $N_{\rm eff}$ likelihood.

The other main effect of this model on cosmology comes from out-of-equilibrium dark Higgs decays in the secluded dark sector model. The details of how these affect BBN and CMB have been discussed in subsection 2.3.2. Here, we will outline the implementation of constraints on decaying dark Higgs.

For decays during BBN, we study the modifications induced by using `AlterBBN` [173]. Since CMB measurement of $\eta_{\rm CMB}$ is highly constrained, we start from this value and obtain an estimate for the its initial value at the start of BBN $\eta_{\rm BBN}$. This is done in `GAMBIT` by solving the Boltzmann equation for the non-relativistic decaying dark Higgs, as well as the Friedmann equation, see [175] for details of implementation. This value of $\eta_{\rm BBN}$ is fed to the `GAMBIT` interface of `AlterBBN` which then gives predictions for light element abundances as well as the modified $N_{\rm eff}$. The modified light element abundances and $N_{\rm eff}$ are used to calculate their corresponding likelihoods.

For decays after BBN, $\tau_\phi > 10^4\,$s, strong constraints come from photodisintegration of light nuclei [275]. We study the effects of photodisintegration using `GAMBIT` interface to the public code `ACROPOLIS` [108]. It takes as input the dark Higgs abundance at the end of freeze-out as well the lifetime and outputs the final light element abundances which can be compared against observations. We find the allowed parameter regions are restricted to $\tau_\phi \ll 10^7\,$s and hence do not include the CMB constraints (see subsection 2.4.1) other than the Planck $N_{\rm eff}$ likelihood.

4.7. Results

To motivate the ranges of parameters used in the global fit, we performed a fit of GW prediction from the FOPT in our model to PTA data, as well as performed a quick scan to understand the regions of parameter space that fit all data. Let us first discuss the fit of the PTA signal to our model. The rising spectrum of the PTA signal imposes a lower bound on the peak frequency, $f_{\rm peak} \gtrsim 10^{-8}\,$Hz which implies $v \gtrsim 50\,$MeV. For larger values of v, the required large amplitudes cannot be sourced by FOPT due to a lower bound that we impose on the transition speed $\beta/H \gtrsim 10$. Small values of g correspond to slower transitions and strong supercooling and hence greater amplitudes, which can be fit by larger peak frequencies. Smaller values of g and v mean large amplitude signals with smaller peak frequencies, which overshoot the PTA signal. Large values of g and v correspond to very small amplitudes, which require an additional SMBH contribution to fit the PTA signal. Thus the PTA signal prefers band of values that are decreasing in g for increasing v (see fig. 6 in SB25). So, although the dark sector gauge coupling can vary by orders of magnitude up to the perturbativity bound, $g < \sqrt{4\pi}$, we restrict ourselves to a range $0.3 \leq g \leq 1$ that provides a good fit to the PTA signal. For the same reason we choose to vary the dark Higgs vev in the range $10\,{\rm MeV} \leq v \leq 1\,{\rm GeV}$.

The DM and dark Higgs mass ratio are tightly constrained by the relic density requirement. With g and v fixed by the PTA likelihood, this requires $0.15 \leq y \leq 0.45$ for the coupled dark sector case. This corresponds to $0.5 \lesssim m_\chi/m_\phi \lesssim 1$, i.e. the regime of forbidden annihilations. For the secluded dark sector case, we find that $m_\chi \approx m_\phi$ is required to fit the relic density requirement. To aid the sampler in exploring this highly constrained parameter space, we introduce

$$\delta = \frac{m_\chi - m_\phi}{m_\chi}\,, \tag{4.21}$$

which we vary in the range $10^{-3} \leq \delta \leq 0.1$. Values of kinetic mixing parameter above 10^{-3} are excluded by experiments, while values below 10^{-7} are irrelevant for phenomenology. We

Parameter	g	y	δ	κ	v	$m_{A'}$	m_ϕ	m_χ	T_p	T_reh	α	β/H
Unit	-	-	-	-	MeV	MeV	MeV	MeV	MeV	MeV	-	-
Point A	0.677	0.224	-0.322	2.29×10^{-6}	173	117	36.3	27.4	2.28	16.8	4.7×10^3	33.7
Point B	0.601	0.234	6.48×10^{-3}	2.7×10^{-4}	692	416	114	115	1.21	55.9	9.48×10^6	18.0

Table 4.1.: Particle masses and phase transition properties for two specific parameter points. The first corresponds to the best-fit point of the coupled dark sector scan presented in section 4.7.1. The second corresponds to the best-fit point of the secluded dark sector scan after imposing an additional requirement on the lifetime of the dark Higgs boson, see section 4.7.2. The derived parameter $\delta = (m_\chi - m_\phi)/m_\chi = 1 - \sqrt{6\lambda}/y$ quantifies the relative mass difference between the DM particle and the dark Higgs boson.

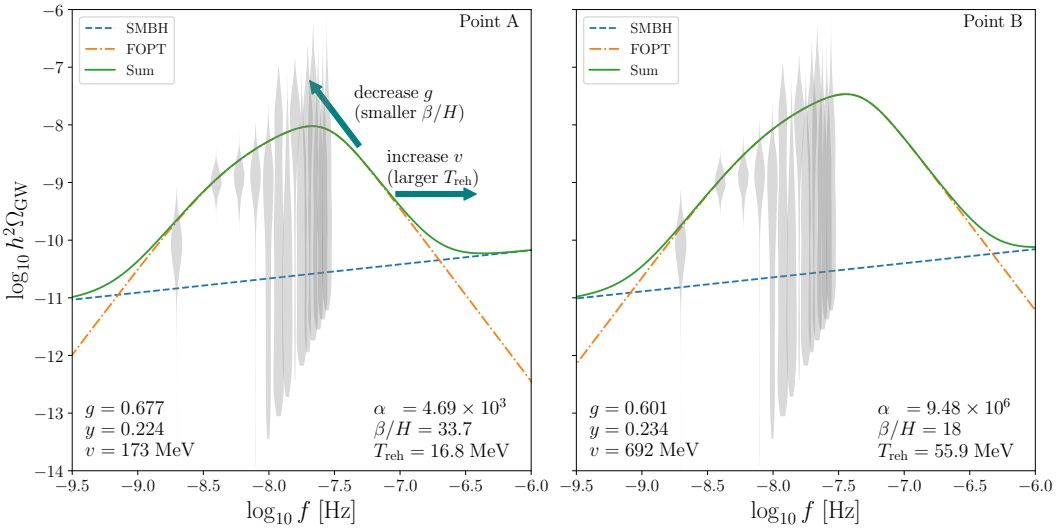

Figure 4.2.: Gravitational wave spectra and NANOGrav 15 yr spectrograms for the two parameter points given in table 4.1. The best-fit SMBH contribution to the GW signal for these parameter points is given by power laws with amplitude and slope $(\log_{10} A, \gamma) = (-15.67, 4.755)$ and $(-15.66, 4.756)$, respectively.

fix κ to this range for the coupled dark sector case. But for secluded dark sector case, we find that large values of κ are required to deplete the energy density in the dark Higgs, hence we use $10^{-5} \leq \kappa \leq 10^{-3}$.

For these parameter ranges, we performed global fits for both the coupled and secluded dark sector models, in the frequentist framework using the `Diver` [196] scanning algorithm in `GAMBIT`. We use a population size of 38000 and a convergence threshold of 10^{-5}. Full samples from the parameter scan, scan configuration files as well as example `pippi` plotting scripts are available on Zenodo [276]. Plots are made using `pippi` v2.1 [197].

We find viable regions of parameter space in both cases. The best-fit points obtained from the global fits are tabulated in Table 4.1, for both the coupled (point A) and secluded dark sector (point B) cases. For the secluded dark sector, the best-fit point is obtained after filtering the allowed parameter regions based on the condition that the freeze-out happens when dark Higgs decays are inefficient in maintaining chemical equilibrium, i.e. $T_f^\phi > T_\mathrm{decay}$. Due to this procedure and the uncertainties involved in relic density computation, we interpret these points conservatively as exemplary points in the parameter space of both models that give a good fit to all available data, and not necessarily the 'best-fit' points in the usual statistical sense. The corresponding GW spectra for the best-fits are shown in Figure 4.2. The left

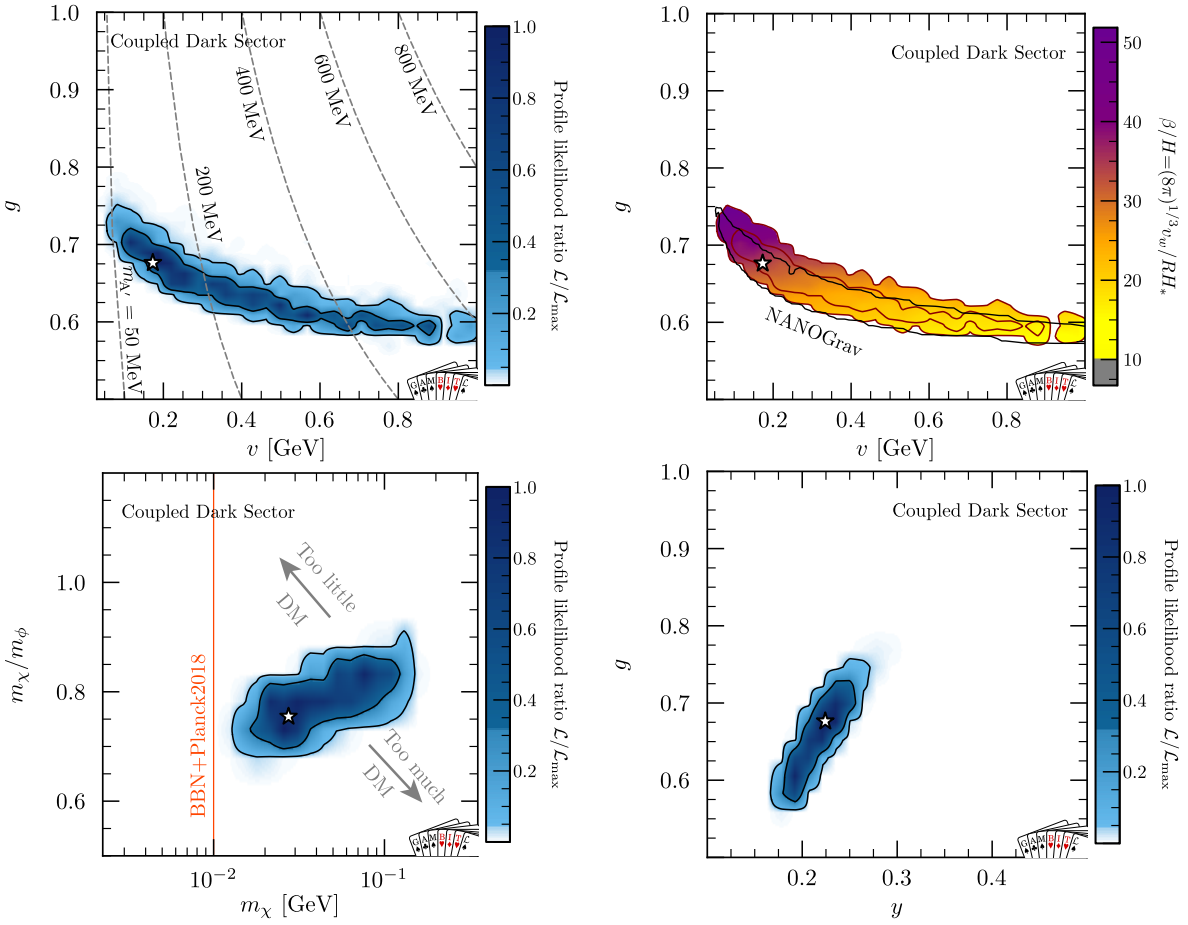

Figure 4.3.: Allowed parameter regions determined through a global analysis of the coupled dark sector scenario in terms of the profile likelihood (blue shading). In the top-left panel, dashed lines indicate constant values of the dark photon mass $m_{A'} = gv$. In the top-right panel, we instead shade the allowed parameter region according to the speed of the phase transition, parametrised by β/H. The black solid line indicates the parameter region preferred by PTA data alone when neglecting any potential SMBH contribution. In the bottom-left panel we indicate the additional constraints that define the allowed regions of parameter space.

panel shows the best-fit GW spectrum of the coupled dark sector case. For the coupled dark sector model, the global fits have been able to find a parameter point that has strong ($\alpha = 4.69 \times 10^3$) and slow ($\beta/H = 33.7$) phase transition at $T_\mathrm{p} = 2.28\,\mathrm{MeV}$, which gives a good fit to the PTA signal. In the right panel, we show GW spectrum corresponding to point B from the secluded dark sector model. As will be explained in detail in section 4.7.2, this case requires a larger vev, which in turn shifts the GW signal to a larger peak frequency. In order to still obtain a good fit, the phase transition needs to be even stronger ($\alpha = 9.48 \times 10^6$) and slower ($\beta/H = 18.0$), which is achieved by a slightly lower gauge coupling g compared to the coupled dark sector scenario. Notably, the combination of FOPT and SMBH signal give a much better fit to the GW spectrum than a single power-law contribution from SMBH binaries in both the coupled ($\Delta \log \mathcal{L}_\mathrm{PTA} = 6.8$) and secluded ($\Delta \log \mathcal{L}_\mathrm{PTA} = 6.6$) dark sector scenarios. We will now present and discuss the full viable parameter regions obtained from the global fits.

4.7.1. Coupled dark sector

The results of the global analysis is shown in Figure 4.3. In each panel we show the confidence regions corresponding to 68% (dark blue) and 95% CL (light blue), indicated by coloured regions within black contours. The white regions are excluded at 95% CL. The color shading in blue represents the profile likelihood, where the likelihood is profiled (maximized) over parameters not shown in the plot. The maximum-likelihood point is indicated by the white star.

In the top left panel, we show the profiled likelihood in $g-v$ plane. As we just mentioned, the PTA likelihood requires anti-correlated g and v to fit the PTA signal. This is because, more supercooling (small g) is required to produce the amplitude corresponding to a larger peak frequency. Unlike the sub-GeV fermionic DM model in the last chapter (subsection 3.3.1), where the indirect detection constraints played an important role in constraining symmetric DM, we are free of these stringent constraints and hence g (and therefore v) is mainly determined by the PTA likelihood. To see this more explicitly, we show the 95% CL contour of PTA likelihood (black contour) when fitting the pure FOPT GW signal to NG15 data without the SMBH contribution, in the top right panel.

Very small values of g would lead to strong supercooling, which would end up overshooting the observed PTA signal amplitude. This is strongly constrained, and hence we see that the lower boundary of the confidence region from the global analysis matches the contour from the fit to just the PTA likelihood. For larger g, even with a very small FOPT GW signal, we can obtain a good fit to NG15 data by including an additional contribution from SMBH binaries, in our global fit. We therefore see that the upper boundary extends farther than the PTA likelihood contour. In this panel, the color shading shows the phase transition speed β/H instead of the profiled likelihood ratio. We observe that slow phase transitions ($\beta/H \simeq 15-45$) could be achieved in the entire confidence region.

With g and v constrained by the PTA likelihood, the dark photon mass, given by $m_{A'} = gv$, is also restricted to the range $m_{A'} \simeq 50-600\,\mathrm{MeV}$ in the allowed regions. The dashed grey lines in the top right panel show lines of constant dark photon mass. We remind the reader about the condition $y < g$ for m_ϕ to be real. For these values, the dark Higgs mass is almost independent of y and is constrained by the PTA likelihood to be in the range $m_\phi \simeq 20-170\,\mathrm{MeV}$.

The only parameters left are the Yukawa coupling y and the kinetic mixing parameter κ. For large dark photon masses determined by the PTA likelihood, interactions mediated by the dark photon (expect for DM-electron scatterings) are suppressed. Moreover, the dark Higgs are kept in chemical equilibrium with the SM plasma through an effective coupling to electrons, until DM freezes-out. Therefore, even after $\chi\bar{\chi} \leftrightarrow e^+e^-$ drops out of equilibrium, dark Higgs is maintained at zero chemical potential and the DM relic abundance is determined by the freeze-out temperature of the process $\chi\bar{\chi} \leftrightarrow \phi\phi$. Hence, the kinetic mixing parameter does not have any effect on the phenomenology, except to keep the dark sector and SM plasma in thermal equilibrium until freeze-out.

The Yukawa coupling y is determined by the relic density likelihood. The relic density is set by $\chi\bar{\chi} \leftrightarrow \phi\phi$ such that it is sensitive to the ratio m_χ/m_ϕ. This ratio is determined mainly by y with a mild dependence on g, with large m_χ/m_ϕ for large y and large g. But $m_\chi/m_\phi > 1$ with the corresponding large y would mean that efficient annihilations strongly deplete the DM number density before freeze-out. Hence we need $m_\chi < m_\phi$, i.e. the regime of forbidden annihilations. We show the allowed parameter regions in the $m_\chi/m_\phi - m_\chi$ plane in the bottom left panel. We find that reproducing the relic density requires $m_\chi/m_\phi \simeq 0.7-0.9$. This translates to $y \approx 0.5g^2$. We therefore get a well-constrained positively correlated confidence

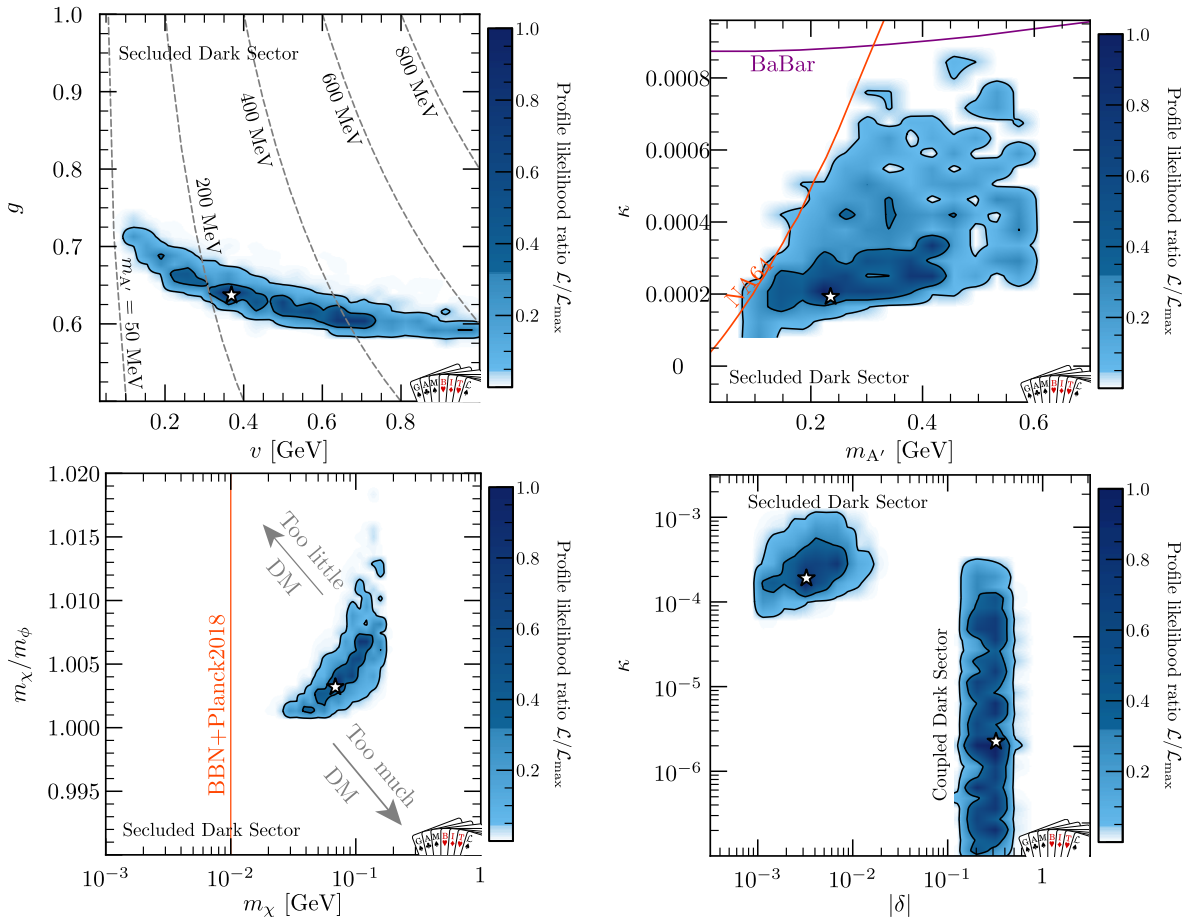

Figure 4.4.: Allowed parameter regions determined through a global analysis of the secluded dark sector scenario in terms of the profile likelihood (blue shading). In the top-left panel, dashed lines indicate constant values of the dark photon mass $m_{A'} = gv$. As in figure 4.3, we explicitly indicate relevant experimental constraints beyond those from the PTA GW signal.

region in the $g-y$ plane, shown in the bottom right panel. In this case, the lower and upper bounds on g from the PTA likelihood translate to bounds on y and hence the DM masses are constrained to $m_\chi \simeq 20 - 100\,\text{MeV}$.

We would now like to discuss the thermal history of the point A from Table 4.1 for concreteness. Once the effective potential forms a second minimum at non-zero background field value, the nucleation of bubbles of the true phase occurs at 2.8 MeV, followed by percolation at $T_\text{p} = 2.3\,\text{MeV}$. At the end of the FOPT, the combined dark sector and SM plasma is reheated to $T_\text{reh} = 16.8\,\text{MeV}$. At this temperature, the dark sector particles ($m_{A'} = 117\,\text{MeV}, m_\chi = 27\,\text{MeV}, m_\phi = 36\,\text{MeV}$) are either already Boltzmann suppressed or beginning to get suppressed, given that they have vanishing chemical potentials. DM freeze-out happens at $T_\text{f} = 1.2\,\text{MeV}$ ($x_\text{f} \approx 22$), which is close to the beginning of BBN. By this point, all dark sector particles in chemical equilibrium are strongly Boltzmann suppressed such that they leave no imprints on BBN and we find that $N_\text{eff} = 3.023$ is only slightly different from the SM prediction.

4.7.2. Secluded dark sector

We show results of the global fit for the secluded dark sector in Figure 4.4. The figure style is as before. Similar to the coupled dark sector model, as seen in the top left panel, g and

v are fixed by the PTA likelihood and the corresponding discussion remains the same. But this time, the phenomenology is sensitive to the kinetic mixing parameter.

In the top right panel, we show the confidence regions in the $\kappa - m_{A'}$ plane. The kinetic mixing parameter determines the lifetime of the dark Higgs, which should decay sufficiently early to avoid strong BBN and CMB bounds. We see that the allowed values of κ are around $10^{-4} - 10^{-5}$, and for a given $m_{A'}$ go up till the NA64 and BaBar bounds. Moreover, the total DM density in the dark sector is sensitive to the kinetic mixing parameter κ. In contrast to the coupled dark sector case, the dark sector particles start developing non-zero chemical potentials earlier, which counteracts the Boltzmann suppression. Thus we have a larger energy density in the dark sector and hence in DM, which needs to be depleted in order to not overclose the universe. For this purpose, we need a slightly larger m_χ compared to m_ϕ. But a larger mass difference between the two would exponentially suppress the DM number density and hence we are forced to be at small positive values of $\delta = 1 - m_\phi/m_\chi$.

The tight relationship between m_χ and m_ϕ required by the relic density constraints is seen in the bottom left panel. Here, we once again see that the dark matter (and dark Higgs) masses are constrained to lie in between $20 - 100\,\mathrm{MeV}$. Finally, in the bottom right panel, we show the allowed values of kinetic mixing parameter for different values of δ for both the coupled and secluded dark sector models. We observe that, while in the coupled dark sector case, κ is largely unconstrained with $\delta \approx -0.33$. For the secluded dark sector case, the kinetic mixing parameter takes the largest values allowed by accelerator experiments with $\delta \approx 10^{-3}$.

To understand the role of the decaying dark Higgs and the BBN constraints on them, we show results in relevant quantities in Figure 4.5. We show profiled likelihoods in terms of the dark Higgs lifetime τ_ϕ, the fraction of dark Higgs abundance that would have been observed today if they were stable , $f_\phi = \tilde{\Omega}/\Omega_{\mathrm{DM}}$, the kinetic mixing parameter κ and finally the combination of parameters that determines the chemical decoupling of the dark sector from the SM plasma, $\kappa^2 g^2 m_\chi^2/(m_{A'}^2 - 4m_\chi^2)^2$. In the top left panel, we see that the dark Higgs abundance is anti-correlated with the parameter combination that we just mentioned. Small values of this parameter combination corresponds to early chemical decoupling, which results in a larger dark Higgs abundance. In the top right panel, we see the expected scaling between κ and τ_ϕ. The dark Higgs lifetime goes as $\tau_\phi \propto \kappa^{-4}$ and the upper bound on κ from accelerator experiments is translated to a lower bound on τ_ϕ. Meanwhile, the lower bound on κ comes from the upper bound on τ_ϕ from stringent photo disintegration constraints. We thus see the dark Higgs lifetime constrained to $10\,\mathrm{s} \leq \tau_\phi \leq 10^4\,\mathrm{s}$ and it decays during or after BBN. This can be seen in the bottom left panel, where we observe that the dark Higgs abundance is increasingly constrained by BBN and CMB bounds for increasing lifetimes. For $\tau_\phi = 2 \cdot 10^4\,\mathrm{s}$, the bound is approximately $f_\phi \lesssim 1$. Hence BBN constraints effectively impose $\tau_\phi < 10^4\,\mathrm{s}$, which translates to the lower bound $\kappa > 10^{-4}$. For smaller lifetimes, the bounds from cosmology are much weaker, while the abundance is constrained by the limits on κ.

Let us now follow the thermal history of the secluded dark sector for the best-fit point shown in Figure 4.4 and Figure 4.5 (different from point B in Table 4.1). The dark sector forms bubbles of the true vacuum at a nucleation temperature of $2.5\,\mathrm{MeV}$ which percolate at $T_\mathrm{p} = 1.9\,\mathrm{MeV}$. At the end of the phase transition, the combined dark sector and SM bath is reheated to $T_\mathrm{reh} = 32.8\,\mathrm{MeV}$. The dark sector particles are non-relativistic below the reheating temperature ($m_{A'} = 235\,\mathrm{MeV},\ m_\chi = 68.8\,\mathrm{MeV},\ m_\phi = 68.4\,\mathrm{MeV}$). The dark sector undergoes chemical decoupling from the SM plasma at $T_f^{\mathrm{SM}} \approx 5.3\,\mathrm{MeV}$ ($x_f^{\mathrm{SM}} \approx 13$). The DM freeze-out finally occurs at a temperature of $T_f^\phi \approx 30\,\mathrm{keV}$, almost close to the end of BBN. We remind the reader that the DM freeze-out after BBN is allowed because both the DM and the dark Higgs are not in chemical equilibrium with the SM plasma and have sub-dominant

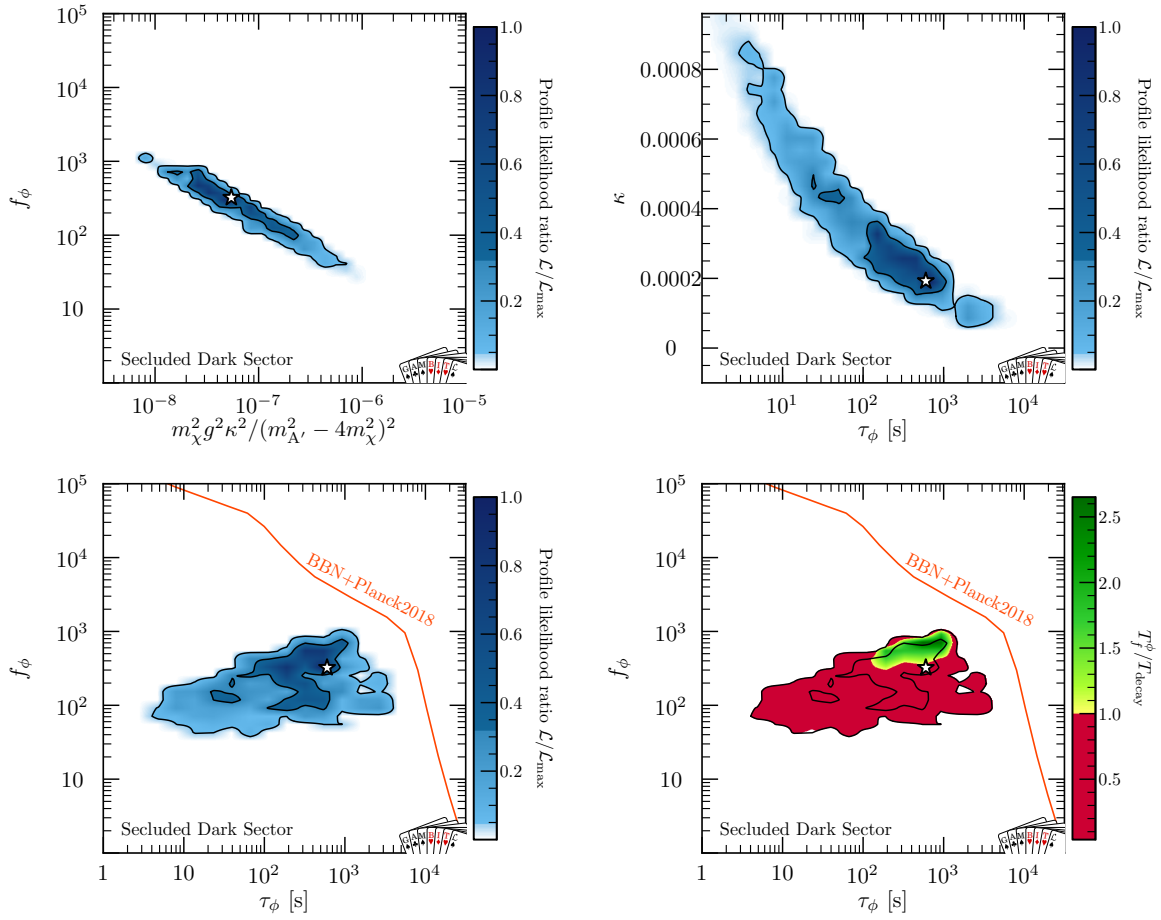

Figure 4.5.: Allowed parameter regions for the dark Higgs boson lifetime τ_ϕ and relative would-be abundance $f_\phi = \tilde{\Omega}_\phi/\Omega_{\rm DM}$ in terms of the profile likelihood (blue shading) and the largest ratio of decoupling temperature and dark Higgs decay temperature found for a given point in the $\tau_\phi - f_\phi$ plane (red to green shading). The exclusion limit shown in the bottom panels is taken from ref. [99].

energy densities compared to that of SM radiation. When they decay, the entropy injection is constrained by BBN and CMB, but it is small enough such that the dilution of relic species negligible. The dark Higgs decays start becoming relevant at $T < T_{\rm decay} \approx 60\,\text{keV}$.

Since our best-fit point has $T_f^\phi < T_{\rm decay}$, it is inconsistent with the assumption of constant total number density in the dark sector, in our relic density calculation. Although the relic density requirement can possibly be satisfied by other points in the parameter space, a precise treatment would involve solving coupled Boltzmann equations. Hence, we refrain from such a calculation which would be prohibitive in the context of global fits. Thus to understand the regions of our allowed parameter space where the relic density estimate is reliable, we show $T_f^\phi/T_{\rm decay}$ in the bottom right panel. We find that we do have allowed parameter space where relic density requirement is reliably satisfied along with other constraints included in the analysis. For a plots of the parameter space that satisfies the constraint $T_f^\phi/T_{\rm decay} > 1$, see fig.15 in SB25.

Since the secluded dark sector model is significantly constrained by the relic density requirement, if we relax the constraint and impose it as an upper bound, as expected large regions of parameter space open up. Specifically, the mass ratio of DM and dark Higgs isn't as tightly constrained and $\delta \gg 10^{-3}$ becomes possible. DM can thus efficiently annihilate to

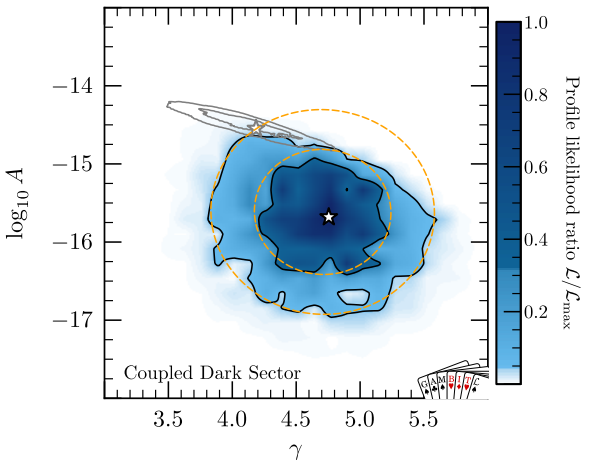

Figure 4.6.: Allowed parameter regions for the slope (γ) and amplitude (A) of the SMBH contribution to the GW signal. Description in the beginning of text in section 4.8.

dark Higgs such that its energy density is quickly depleted. The increased energy density in the dark Higgs now has to be transferred to the SM through decays. This would be possible for small lifetimes as we saw in the bottom left panel of Figure 4.5, where the CMB and BBN bounds were much weaker than that imposed by κ.

4.8. Discussion and outlook

We show in Figure 4.6 the comparison between the allowed regions for the amplitude A and slope γ of the GW signal from SMBH binaries (see section 4.1). The yellow lines indicate the priors for the parameters based on astrophysical expectations for SMBH binaries (see subsection 4.6.2). The grey contours are posteriors from the fitting a pure SMBH GW signal using the PTA likelihood described in subsection 4.6.3. The best-fit corresponding to the grey contours lies barely within the 95% CL contour of the astrophysical expectation (yellow dashed lines) indicating a tension, which agrees with the findings of [238]. The black contours with the blue shading correspond to allowed regions for the SMBH parameters in our global fits for the couple dark sector model. We find that NG15 data prefers the model where we add a FOPT contribution to the GW signal atop the one from SMBH binary mergers, compared to the model where the PTA signal is attributed to pure astrophysical origin. Moreover, the allowed regions (black contours) for the SMBH parameters in our model agree with the astrophysical expectations (yellow dashed lines), the only difference being the exclusion of large amplitudes and slopes which would overshoot the PTA signal. We arrive at the same conclusion in comparing the secluded dark sector model to the SMBH-only case. Thus the FOPT GW contribution provides the extra power observed at $f > 3\,\mathrm{nHz}$ required to fit the PTA signal.

Future updates of the PTA signal, with improved constraints on the GW spectrum, information on anisotropies as well as possible detection of individual sources of continuous GW signals can shed more light on the origin of the signal. Moreover, observations at higher frequencies can already significantly constrain our models. The coupled dark sector model allows a large range of GW signal amplitudes and peak frequencies and can hence fit future measurements as well. But the secluded dark sector case (with the constraint $T_f^\phi > T_{\mathrm{decay}}$) prefers large v and hence large peak frequencies that lie beyond the current observational range, as seen in the right panel of Figure 4.2. Thus, in case a further rise is not seen at larger frequencies in future measurements, our secluded dark sector model would be disfavoured.

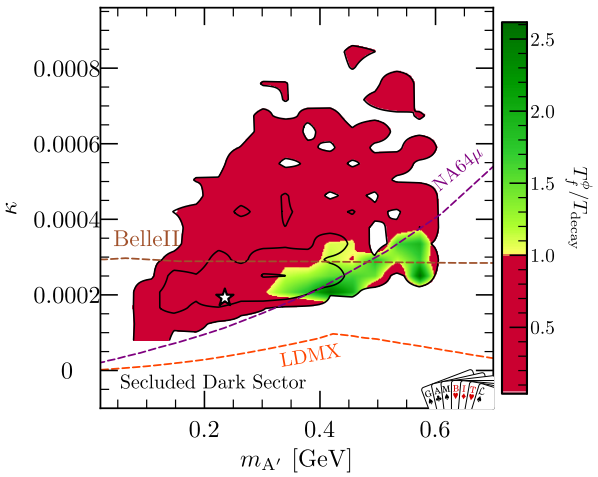

Figure 4.7.: Projected sensitivities of searches for invisibly decaying photons at Belle II, as well as for the proposed LDMX and NA64μ experiments in the $m_{A'} - \kappa$ parameter plane of the secluded dark sector model. The colour shading indicates the ratio $T_f^\phi/T_{\rm decay}$; ratios smaller than unity indicate that our relic density calculation may be unreliable.

Upcoming laboratory experiments like invisible dark photon searches at BelleII [202], NA64 experiments with muon beams [277], LDMX [208] would be able to further constrain our models, see Figure 4.7.

4.9. Conclusion

Following the announcement of evidence for observation of a stochastic gravitational wave background at nHz frequencies, by many pulsar timing arrays, we studied the implications of such a signal on the cosmology of dark sectors. The GW signal has been observed to have a large peak amplitude $h^2\Omega_{\rm GW}^{\rm peak} \simeq 10^{-8}$ compared to what is expected from the canonical explanation - gravitational waves from merging supermassive black hole binaries. Thus, we examined the additional contribution to the signal that could arise from a first order phase transition in a dark sector. The large gravitational amplitudes require strong and slow phase transitions.

We constructed dark sector models that can provide such a large GW signal, by imposing a conformal as well as a $U(1)'$ gauge symmetry on our complex scalar. We also included a fermionic particle which acts as our DM candidate. The gauge boson associated with the $U(1)'$ gauge symmetry is the dark photon, the heaviest particle in our dark sector. We introduced a portal to SM through kinetic mixing of the dark photon with the SM photon, so that the large energy density in the dark sector at the end of the phase transition can be depleted by decays and annihilations. Furthermore, based on the dark Higgs couplings to SM, we differentiated two possibilities – one where the dark Higgs is coupled to SM electrons and positrons through an effective interaction term, which we call the *coupled dark sector*; and the other where there exists no such coupling and the dark Higgs decays to SM through dark photon loops, called the *secluded dark sector*.

We performed global fits for both the coupled and secluded dark sector models, including all relevant cosmological, astrophysical, as well as accelerator constraints. We found viable parameter space in both cases. In both cases, the PTA likelihood mainly determines the allowed parameter regions for the gauge coupling g and the vev v. Additionally, in both models, DM dominantly annihilates to the dark Higgs and hence the relic density is mainly set by this annihilation channel. In the coupled dark sector case, the DM and dark Higgs are in

chemical equilibrium with the SM plasma until DM freezes-out. Thus, the DM number density is highly Boltzmann suppressed during freeze-out and in order to avoid completely depleting the DM abundance, we found that the global fits prefer the regime of forbidden annihilations, i.e. $m_\chi < m_\phi$. The relic density requirement constrains the DM and dark Higgs mass ratio, and hence the Yukawa coupling y. The dark Higgs abundance is fully depleted before DM freeze-out and hence standard cosmology is recovered. The kinetic mixing parameter remains unconstrained and can have κ as small as 10^{-7} and possibly be unobservable in upcoming experiments.

In comparison to the coupled dark sector, the secluded dark sector is more constrained and as a result more predictive. In this case, the dark sector decouples from the SM before DM freeze-out and both the DM and the dark Higgs develop non-zero chemical potentials. The large energy density in DM has to be depleted before freeze-out, and we found that the relic density constraint requires fine-tuning between the DM and dark Higgs masses, $\delta = 1 - m_\phi/m_\chi \approx 10^{-3}$. Here, the large energy density in the dark Higgs is depleted through out-of-equilibrium decays and is constrained by BBN and CMB. We found that large values of the kinetic mixing parameter $\kappa \approx 10^{-4}$ are required to be consistent with standard cosmology. This case can hence be better probed with future laboratory experiments as well as improved measurements of the PTA signal.

The upcoming third IPTA data release will help us better understand the origin of the GW signal. Even if it ultimately turns out that the main source of the signal doesn't originate from dark sector FOPTs, they will help us further our knowledge of dark sectors by constraining them and advance our understanding of supermassive black holes.

Part II.

Statistics and visualization of Global fits

CHAPTER 5

Global fits

To aid the global fitting procedures involved in the two publications discussed in the previous chapters, I developed the tool `GAMBIT UTILISeD` *for interactive visualisation of global fit results of dark matter models, obtained using GAMBIT. I present the features of this tool along with a quick start guide in section 5.7.*

In the search for DM, when experimental data becomes available, we can ask different questions depending on whether or not we observe DM signals. In the case where we observe no DM signals in the data, the relevant question is: *are there parameter regions that are consistent with constraints?* The answer to this question can tell us whether a model is fine-tuned, excluded or still viable, which would then help guide future experiments and theoretical research by identifying viable targets. If we observe a signal that could be attributed to DM, the relevant questions are: *which regions of parameter space in my model fit the data best? how well does my model fit the data? and how does it compare to a different model?* By answering these questions, we arrive at a model that comes closest to the truth, by providing a good statistical fit to the data. This is done by performing statistical analyses under frequentist or Bayesian frameworks.

Due to limitations in observations and the intrinsic quantum noise of physical systems, statistical errors enter data and propagate into the results of data analysis. Therefore, while presenting the results of statistical analyses, it is crucial to estimate the statistical errors involved. In parameter estimation, we thus quote parameters that best-fit the data as well as the errors on the estimate. In frequentist framework, these are confidence regions at some confidence level C. Furthermore, errors can also be introduced by systematics in experiments. They are defined such that, on repeating the experiment a large number of times, the constructed confidence regions cover the true values in a fraction C of the experiments. Regions that satisfy this condition are said to have proper *coverage*. In Bayesian framework, the results are presented as credible regions that have a more intuitive meaning - regions that have a probability C of containing the true values.

This chapter is organised as follows. In section 5.1, we discuss Neyman's procedure to construct confidence regions that guarantees coverage at said confidence level. In section 5.2, we

present *likelihood ratio tests*, a more economical method to construct confidence regions, albeit with coverage that might not be exact. We then discuss construction of Bayesian credible regions in section 5.3. In section 5.4, we examine the necessity for performing global fits with the help of illustrative examples. We then outline the methods for statistical model comparison in frequentist and Bayesian frameworks in section 5.6. Finally, in section 5.7 we present the tool `GAMBIT UTILISeD` developed as a part of this thesis, for interactive visualisation of global fits results obtained using `GAMBIT`.

5.1. Neyman construction

In this section, we present Neyman's procedure [278] to construct confidence levels with exact or over-coverage. Consider an experiment in which we can collect data x [11]. We construct a statistical model that says x is distributed according to some probability distribution f which depends on a set of unknown parameters θ, i.e. $x \sim f(x|\theta)$. Let us denote the unknown true values of these parameters by θ_0. On performing the experiment, we observe the data $x_{\rm obs}$. Based on the observed data, let us assume that we have constructed a set $\mathcal{C}(x_{\rm obs})$ which contains all parameter points within the confidence region. Then, coverage at confidence level C is assured when the probability that the true value is contained in $\mathcal{C}(x)$ for a given θ_0 is C,

$$P(\theta_0 \in \mathcal{C}(x)|\theta_0) = C \ . \tag{5.1}$$

Note that the set $\mathcal{C}(x)$ is the random variable here, whereas $\mathcal{C}(x_{\rm obs})$ is a specific realization of this random variable and θ_0 is an unknown fixed parameter.

The Neyman construction gives a procedure to construct $\mathcal{C}(x)$ that obeys Equation 5.1. Assuming one can simulate the experiment, the procedure begins with the simulation for a specific value of θ, i.e drawing samples from the distribution $f(x|\theta)$. Then we construct the acceptance region for the chosen value of θ, $\mathcal{A}(\theta)$, such that,

$$P(x \in \mathcal{A}(\theta)|\theta) = C \ . \tag{5.2}$$

After repeating this for all possible values of θ, we perform the actual experiment to get data $x_{\rm obs}$. There will be a fraction of the constructed acceptance regions that contain $x_{\rm obs}$. The set of all θ values whose acceptance region contains $x_{\rm obs}$ forms the confidence set $\mathcal{C}(x_{\rm obs})$.

Confidence sets constructed using this method have correct coverage, because by construction,

$$x \in \mathcal{A}_{\theta_0} \iff \theta_0 \in \mathcal{C}(x) \tag{5.3}$$

which implies

$$P(\theta_0 \in \mathcal{C}(x)) = P(x \in \mathcal{A}_{\theta_0}) = C \ . \tag{5.4}$$

If the distribution $f(x|\theta)$ is complex, it is already difficult to sample it well once. When the dimensionality of θ is large, then sampling a complex distribution for all possible values of θ becomes infeasible. So, in practice we often use the likelihood ratio test to construct confidence regions that might not have exact coverage but are usually good enough for global fits.

[11] For ease, we suppress the usual vector or boldface notation that indicates a set of paramters or quantities.

5.2. Likelihood ratio tests

In this section, we describe how to construct confidence regions with likelihood ratio tests (LRTs). Before that, we will convince ourselves that constructing confidence regions by performing a series of hypothesis tests is the same as Neyman's construction.

Consider a null hypothesis H_0, the hypothesis that we are going to test. Then choose a test statistic t, such that larger values correspond to larger incompatibility with H_0. We can derive a critical value t_c for a chosen level of type-I error α (probability of rejecting the null hypothesis when it is true) using,

$$\alpha = \int_{t_c}^{\infty} g(t|H_0)\mathrm{d}t \ , \tag{5.5}$$

where $g(t|H_0)$ is the distribution of the test statistic under the null hypothesis and α is called the *size* or *significance* of the test[12]. The hypothesis is rejected at a confidence $C = 1 - \alpha$ when $t_{\mathrm{obs}} > t_c$.

Let's go back to our experiment described in the previous section. The test statistic depends on the observables x, i.e., $t \equiv t(x)$. Let's consider the null hypothesis to be θ taking on a specific value. The acceptance region for each value of θ is given by,

$$\mathcal{A}(\theta) = \{t(x)|t(x) < t_c(\theta)\} \ . \tag{5.6}$$

If we perform a series of hypothesis tests for different values of θ, the confidence region is formed by all accepted values of θ, i.e.

$$\mathcal{C}(t(x_{\mathrm{obs}})) = \{\theta|t(x_{\mathrm{obs}}) < t_c(\theta)\} \ , \tag{5.7}$$

This procedure is thus equivalent to the Neyman construction, with slight conceptual changes. Therefore, the "accepted" regions constructed through hypothesis testing have the same properties as confidence regions constructed using the Neyman construction and have proper coverage.

The advantage in this procedure is that we can be smart about our choice of the test statistic. Consider the profiled likelihood ratio,

$$\lambda(\theta) = \frac{\mathcal{L}(x_{\mathrm{obs}}|\theta, \hat{\hat{\nu}})}{\mathcal{L}(x_{\mathrm{obs}}|\hat{\theta}, \hat{\nu})} \ , \tag{5.8}$$

where we have introduced nuisance parameters ν. In the numerator, we have the profiled likelihood, where $\hat{\hat{\nu}}$ indicates the value of ν that maximizes the likelihood for a given value of θ. The denominator is the likelihood evaluated at values $\hat{\theta}$ and $\hat{\nu}$ that maximize it. Profiling over nuisance parameters makes sure that the results of the analyses are not affected by nuisance parameters.

The profiled likelihood ratio is interesting because, under regularity conditions, *Wilk's theorem* [279] states that $-2\ln\lambda(\theta)$ follows a χ^2 distribution with degrees of freedom equal to difference in degrees of freedom between the numerator and the denominator. Thus, with the profiled likelihood ratio as the test statistic, one can forego the need for computationally expensive simulations to determine $g(t|\theta)$. Therefore, to construct the confidence region, all we have to do is find the maximum likelihood and calculate the profiled likelihood at different points in the parameter space. The confidence region is then constructed by collecting all

[12]Note that this significance is different from the one quoted for discoveries.

points with $-2\ln\lambda(\theta) < \chi^2_c$ based on the chosen confidence level. The critical χ^2 values for k degrees of freedom can be calculated as ,

$$\begin{aligned} 1 - C = \alpha = & \int_{t_c}^{\infty} \mathrm{d}x \; \frac{1}{2^{k/2}\,\Gamma(k/2)} \; x^{k/2-1} \; \mathrm{e}^{-x/2} \\ & \alpha = \mathcal{Q}(k/2, t_c/2) \\ & \implies t_c = 2\;\mathcal{P}^{-1}(k/2, C) \;, \end{aligned} \tag{5.9}$$

where $\mathcal{Q}$ and $\mathcal{P}$ are the upper and lower regularized gamma functions. For example, for $C = 0.95$, we get $t_c = 3.84$ for $k = 1$ and $t_c = 5.99$ for $k = 2$. The computational task involved in constructing confidence regions is that of optimisation and is solved with algorithms like differential evolution (e.g. see `Diver` [196]).

The relevant conditions for Wilks' theorem to apply are that the sample size should be large and the true values of the unknown parameters should lie in the interior of the parameter space. If these conditions are not met, then the assumption of χ^2 distribution for t may not be accurate, yielding confidence regions that have only approximate coverage. This is most often the case in practice, but this doesn't not really affect the qualitative conclusions we draw from such analyses, to answer the questions posed in the beginning of this chapter.

5.3. Bayesian credible regions

In the Bayesian framework, parameter inference is a lot more intuitive, because unlike in frequentist statistics, probability is interpreted as the degree of belief in an event and so is not limited to phenomena that are inherently random. Consequently, in contrast to confidence regions, credible regions of credible level C can be interpreted as regions that have a probability C of containing the true value of the unknown parameter, given the data that was observed. Credible regions are obtained from the *posterior probability distribution* of the model parameter, given the observed data. In terms of the experiment discussed in the previous sections, the posterior is the probability of θ given the observation x_{obs}, i.e. $\mathcal{P}(\theta|x_{\mathrm{obs}})$, which is connected to the likelihood $\mathcal{L}(x_{\mathrm{obs}}|\theta)$ through the Bayes theorem,

$$\mathcal{P}(\theta|x_{\mathrm{obs}}) = \frac{\mathcal{L}(x_{\mathrm{obs}}|\theta)\pi(\theta)}{P(x_{\mathrm{obs}})} \;, \tag{5.10}$$

where $\pi(\theta)$ encapsulates prior knowledge on the model parameter(s), called the *prior* and $P(x)$ can be interpreted as a normalisation factor and is called the *Bayesian evidence*.

When nuisance parameters ν are present, their effect on the posterior is removed by *marginalisation*, i.e. integrating them out,

$$\mathcal{P}(\theta|x_{\mathrm{obs}}) = \int \mathcal{P}(\theta, \nu|x_{\mathrm{obs}})\pi(\nu)\mathrm{d}\nu, \tag{5.11}$$

where $\pi(\nu)$ is the prior on the nuisance parameters. The regions of credible level C for the desired parameters can then be obtained from the marginalised posterior probability distribution by finding regions that contain a fraction C of the posterior volume. There are many regions that contain a fraction C of the volume, and hence different ways in which to draw credible regions. One common method is to draw level sets, where credible regions are given by regions within contours of highest probability that contain a fraction C of the posterior volume.

There are two computational tasks involved in Bayesian inference, finding the posterior maximum, as well as performing the integration to obtain the marginalized posteriors. For

complex high-dimensional likelihoods, this can only be done numerically and both these tasks can be tackled with efficient sampling of the posterior. Once the posterior is sampled well enough, one can trivially find where it reaches its maximum, while marginalisation can be performed using Monte Carlo integration,

$$\mathcal{P}(\theta|x_{\rm obs}) \approx \frac{\rm Vol(R)}{N} \sum_{i=1}^{N} \mathcal{P}(\theta, \nu_i|x_{\rm obs})\pi(\nu_i) \ , \tag{5.12}$$

where R is the nuisance parameter space over which the posterior is integrated. Algorithms like nested sampling (e.g. see MultiNest [280]) and Markov chain Monte Carlo (MCMC) are powerful sampling methods that are commonly used in Bayesian inference.

5.4. Global fits

With the knowledge of how to construct confidence and credible regions starting from likelihoods, we now turn to the question of which likelihood to use. In searches for new physics, we have data from different complementary experiments that utilize a large amount of human and energy resources. To make optimal use of these results that guide theory and experiments in BSM searches, one must evaluate the viability of current models based on all available data in *global fits*. Global fits pertain to using a carefully constructed likelihood, that combines data from different BSM searches, to derive confidence or credible regions. Global fits require a significant amount of efforts to understand, reproduce and implement likelihoods from various experiments. So, in what follows, we will argue why they are really necessary and how a more naive approach of a simple *overlay* of constraints doesn't really deliver the same level of scientific output.

In models with just two parameters, it is usually possible to recast all relevant constraints on the model parameter plane and thus identify allowed regions by a simple overlay of constraints. If one is satisfied with not making statistical statements about the allowed regions, then these results from overlay of constraints are often good enough to understand the model's status. The situation gets more complicated once we move beyond two parameters.

For models with more than two parameters, recasting existing constraints on observables (e.g. constraints on annihilation cross section, DM-nucleon cross-section, etc.) to model parameter spaces typically involves fixing one or more parameters. In Figure 5.1, we show examples of works that study the same fermionic DM model studied in section 3.1, by overlay of constraints. In the left panel, constraints are shown on the $\langle\sigma v\rangle - m_{\rm DM}$ plane for the symmetric fermionic DM model, taken from [281]. Allowed regions are those in white, below the upper limits from terrestrial, CMB and indirect detection experiments. Here, we see recasted terrestrial constraints on this plane, which requires fixing the ratio $m_{A'}/m_{\rm DM}$ and $g_{\rm DM}$ to specific values. In the right panel, we see constraints on the $\sigma_e - m_{\rm DM}$ plane for asymmetric fermionic DM model, taken from [211]. The small white regions are viable and can produce the correct relic density at different values of asymmetry. Here, we see recasted CMB constraints onto this plane,which requires fixing $m_{A'}/m_{\rm DM}$.

Even in such cases where we fix certain parameters, there might not always exist a single parameter plane in which all constraints relevant to the model can be overlaid. For example, in the left panel in Figure 5.1, one cannot show the self-interaction cross-section constraint on this model, since $g_{\rm DM}$ is fixed. Therefore the main drawbacks in this procedure are: (*i*) we throw away information on parameters that we keep fixed, (*ii*) the commonly used benchmark points might already be excluded by combined likelihoods, as we showed in the case of fermionic sub-GeV model studied in subsection 3.4.2. (*iii*) it is difficult to understand

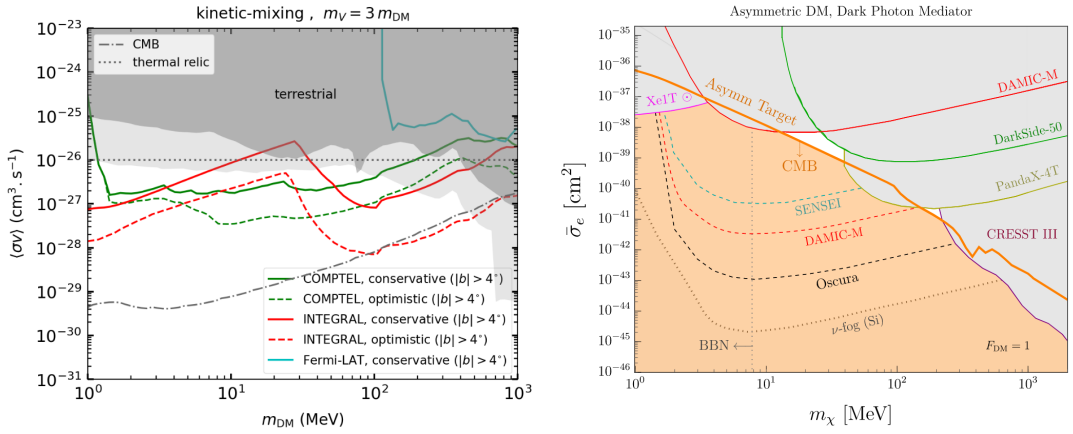

Figure 5.1.: Constraints on the fermionic DM model discussed in section 3.1 for the case of symmetric DM (left) on the $\langle\sigma v\rangle - m_{\rm DM}$ plane for $m_{A'} = 3m_{\rm DM}, g_{\rm DM} = 2.5$, from [281] and asymmetric DM (right) on the $\sigma_e - m_{\rm DM}$ plane for $m_{A'} = 3m_{\rm DM}$, from [211].

the status of a model from such plots with fixed parameters, even when making array of plots for different values of the fixed parameters.

Without fixing any of the model parameters, one can still try to combine constraints by filtering out points in the full parameter space that satisfy all constraints. For example, in Figure 5.2 taken from [166], the viable regions are obtained by filtering out allowed points by scanning over all model parameters. They allowed regions are shown in blue on the $\sigma_e - m_{\rm DM}$ plane, along with direct detection constraints (curves) and regions excluded by accelerator constraints (purple). Here, the projection on to a plane is done by maximizing over model parameters that give the maximum relic density while still being consistent with all constraints, including the relic density upper-limit $\Omega_{\rm DM}h^2 \leq 0.12$. This is a successful example of combining constraints without performing a full statistical global analysis due to two main reasons. First, the relic density provides a meaningful way to project allowed regions from the full parameter space on to 2D planes. In global fits of models without such a special observable, it might not be possible to find a similarly meaningful projection of allowed regions on to 2D planes. Secondly, this procedure works well when most constraints (on any model parameter or observable X) can be reduced to a single condition of the form $X < X_c$ or if they can be directly cast on to the parameter plane in which results are presented. If this is not the case, one would have to calculate the actual observables that experiments constrain and compare to observations. For e.g., one has to calculate quantities like event rates R and apply the condition $R < R_{\rm obs}$. Both scanning the full parameter space and performing such calculations already increase the computational complexity, such that the calculating full likelihoods in these analyses might be worthwhile.

The advantage with using likelihoods now is that we can do a proper statistical analysis. To obtain confidence regions or credible intervals in the end that are compatible with all available data, we need to use a combined likelihood. Combining the likelihoods can be non-trivial depending on how the experimental results were published. Without knowledge of the complete statistical model, assumptions will have to be made about the nuisance parameters and errors involved in the analysis. Guidelines for publishing experimental results that ensure a full record of relevant information required to reproduce or reinterpret results have been been brought forth in [282]. Combining different experiments in a global likelihood requires a full statistical model as well as the full likelihood (as opposed to profiled likelihoods or marginalized posteriors in parameter planes). A full statistical model here refers to $f(x|\theta)$ and not the likelihood which is $\mathcal{L}(\theta) = f(x_{\rm obs}|\theta)$. Another advantage in using likelihoods is

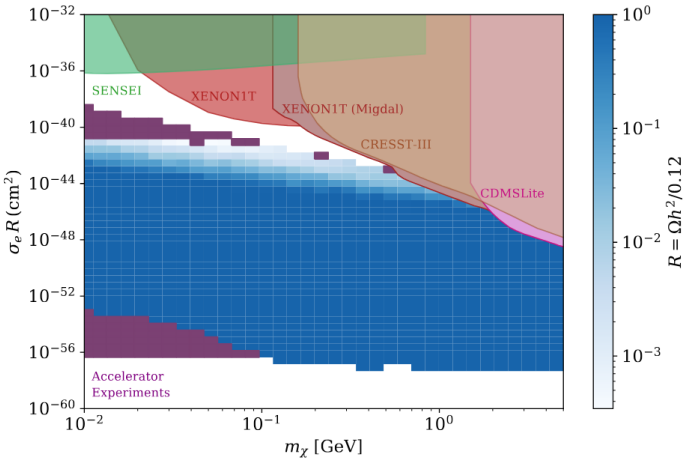

Figure 5.2.: Allowed regions (blue) and constraints on symmetric fermionic DM, taken from [166].

that the parameter space can be scanned more efficiently, by using the likelihood information, such that the scanner spends most of its time exploring regions of high likelihood.

Apart from the computational advantages they provide, global fits increase the constraining power of experiments that are sensitive to the same parameter (or observable) regions, which cannot be achieved by a simple overlay of constraints. Similarly, they can also identify excesses of low significance spread across different data sets as well as identify tensions in different datasets.

5.5. GAMBIT

Global fits involve identifying experiments relevant for the physics model of interest, interpretation of published likelihoods from these experiments, implementation of the said likelihoods, theoretical predictions for physics observables, and finally careful consideration and implementation of the statistical analysis pipeline. Even though most of these tasks are common to global analyses of different physics models, most studies are limited to one class of physics models and hence the codes produced as a part of the work are limited in scope (for eg., see SUSY focused global fitting code `SFITTER` [283]).

The global and modular BSM inference tool (`GAMBIT`) is a global fitting code developed to address the issue of redundancy in setting up pipelines for global analyses. The main design principles are modularity and flexibility which allow for seamless switching between different theory predictions, fast extension with new likelihoods, and access to different statistical tool chains. It is written in C++ and contains standardised methods to interface external codes written in `Python`, `Mathematica`, `C` and `Fortran`. It is completely open source and the latest version, `GAMBIT` v2.5 is available at https://github.com/GambitBSM/gambit_2.5 .

The code is organised into multiple modules called `Bits`. The `ScannerBit` contains the module functions and parts of code responsible for parameter sampling, prior transformation, likelihood optimisation and other relevant statistical issues. The other `Bits` are physics modules which contain module functions that calculate different physical quantities and likelihoods. For example, `DarkBit` [284] contains functions that calculate likelihoods from direct and indirect detection searches and the corresponding observables required for these likelihood calculations. `GAMBIT` also contains a database of physics models defined in terms of model parameters. Models can be implemented hierarchically, where parameter translations

between `parent model` and `child model` are defined. Similarly, parameter translations between different `friend models` can also be defined. Such a hierarchical and cross-connected model database allows for module functions written for one model to be used for another without further modification.

`GAMBIT` achieves modularity by declaring for each function a `capability`, a metadata string that describes the physical quantity that the function outputs. The required inputs are declared as `dependencies`, metadata containing the data type and the metadata string describing the input. The dependency of each module function can be satisfied by the output of other module functions, model parameters or quantities calculated by `backends` (`GAMBIT` interface to external codes). So each function is declared with a capability and dependencies which can be satisfied by other functions with a suitable capability. There can be multiple module functions with the same capability that satisfy the dependency of a different module function. For example, the function `CosmoBit::compute_BBN_LogLike` calculates the BBN log likelihood. It has the capability `BBN_LogLike` and has a dependency on theoretical predictions for primordial abundances which can be satisfied by both the functions `CosmoBit::primordial_abundances` and `CosmoBit::primordial_abundances_decayingDM` with the capability `primordial_abundances`. Both calculate primordial abundances in non-standard cosmologies, while the former calculates the abundances at the end of BBN, the latter also considers the effect of photodisintegration after the end of BBN.

The above described internal structure where the inter-dependencies of different functions are not hardcoded and instead depend on matching dependency and capability strings allows for modularity and flexibility. During runtime, the dependencies are matched to capabilities of module functions by the `dependency resolver`. It creates a directed graph of module functions called the `dependency tree`. The dependency tree starts with nodes containing the model parameters, and is followed by nodes containing module functions that calculate intermediate physical quantities and ends in nodes with module functions that calculate the requested observables or likelihoods. The graph edges in the dependency tree correspond to resolved dependencies that connect the outputs and inputs of various module functions. Once a dependency tree is generated, `GAMBIT` performs numerical calculations of requested observables and likelihoods following this tree, for each set of parameter points sampled by the statistical scanning algorithm.

The user input to `GAMBIT` is provided through a YAML file containing details on the models to be scanned, scan ranges of free parameters, values for fixed parameters, scanning algorithm to be used, and the observables and likelihoods to be calculated. In case of degeneracy in satisfying a dependency, rules explicitly specifying the module functions to be used can be added. The output consists of tables of observables and likelihoods at each sampled parameter point and can be stored in `ASCII` or `HDF5` format.

In this thesis, we exclusively used `GAMBIT` to perform global fits of all DM models considered. Once viable regions are determined through global fits with `GAMBIT`, the next question to ask is which model fits the data the best. In the next section, we briefly mention model comparison methods in frequentist and Bayesian frameworks.

5.6. Model comparison

Frequentist model comparison

In frequentist analysis, model comparison is performed with an extension of the hypothesis test described in section 5.2. Here, we additionally have an alternate hypothesis H_A and can define the type-II error (probability of accepting the null hypothesis when it is false) as,

$$\beta = \int_{-\infty}^{t_c} g(t|H_A)\mathrm{d}t \ , \tag{5.13}$$

where $g(t|H_A)$ is the distribution of the test statistic t under the alternate hypothesis H_A. The quantity $1-\beta$ is called the *power* of the hypothesis test. In searches for new physics, we take the null hypothesis to be data consistent with standard physics and the alternate hypothesis to be the presence of new physics signals. In these hypothesis tests, it is desirable to choose a test statistic that maximizes the power of the test. The *Neyman-Pearson lemma* [285] states that this can be achieved with ratio of maximum likelihoods under the two hypotheses,

$$\Lambda = \frac{\mathcal{L}_{\max}(t_{\text{obs}}|H_0)}{\mathcal{L}_{\max}(t_{\text{obs}}|H_A)} \ . \tag{5.14}$$

For nested models, where the null hypothesis corresponds to a fixed value θ_0 and for the alternate hypothesis, the value of θ is determined from the data, one can once again evoke the Wilk's theorem to determine the distribution of $-2\ln\Lambda$. When Wilks' theorem doesn't apply, the distribution of the test statistic would have to be determined through numerical simulations [286]. In hypothesis tests, one often quotes *p-values*, which is defined as the probability of an event more extreme than that observed under the null hypothesis,

$$p = \int_{t_{\text{obs}}}^{\infty} g(t|H_0)\mathrm{d}t \ . \tag{5.15}$$

The hypothesis test can also thus be stated in terms of the p-value as rejection of the null hypothesis when $p < \alpha$. In searches for new physics, a quantity that gives a more intuitive understanding of the rarity of the observed event under the null hypothesis, is the statistical significance Z. It is determined from the p-value as,

$$Z = \sqrt{2}\Phi^{-1}(1-2p) \ , \tag{5.16}$$

where Φ^{-1} is the inverse cumulative distribution function of the standard Gaussian (normal distribution around $\mu = 0$ with error $\sigma = 1$). The statistical significance corresponds to the number of Gaussian standard deviations σ away from the mean, where the upper tail with values larger than $Z\sigma$ has a cumulative probability equal to the p-value. For example, assuming that the test-statistic follows a χ^2 distribution of one degree of freedom, the null hypothesis is rejected when $p < 5.7 \times 10^{-7}$, corresponding to a 5σ significance. In particle physics, as a standard, a statistical significance of 5σ is required to claim a *discovery*.

Bayesian model comparison

The advantage in Bayesian model comparison is that non-nested models can be compared without having to rely on numerical simulations, but they require prior assumptions on the models. Consider hypotheses H_1 and H_2 with parameters θ_1 and θ_2, the Bayesian evidences for these models are calculated from the likelihood as,

$$\mathcal{Z}_{1(2)} = \int \mathcal{L}(x_{\text{obs}}|\theta_{1(2)})\pi(\theta_{1(2)})\ \mathrm{d}\theta_{1(2)} \ . \tag{5.17}$$

The ratio of evidences, $\kappa_{12} = \mathcal{Z}_1/\mathcal{Z}_2$ is called the *Bayes factor*. The model selection is then performed using the ratio of probability of the two hypotheses given the data, called *posterior odds*,

$$\frac{\mathcal{P}(H_1|x_{\text{obs}})}{\mathcal{P}(H_2|x_{\text{obs}})} = \kappa_{12}\frac{\pi(H_1)}{\pi(H_2)} \ , \tag{5.18}$$

where $\pi(H_{1(2)})$ are the priors on the two hypotheses being tested. For equal priors, the posterior odds is equal to the Bayes factor, which can be interpreted according to the *Kass-Rafftery* scale [287] as strong and very strong evidence in favour of H_1 for $\kappa_{12} > 20$ and $\kappa_{12} > 150$, respectively. The results of Bayesian model comparison are sensitive to the

choice of priors and the subjectiveness introduced by these priors is the main argument against Bayesian approach put forth by frequentists. But within the Bayesian framework, it is expected that for a reasonable choice of a prior, one should ultimately arrive at the truth by repeated update of knowledge of the model from repeated measurements. In this case, in limit of large enough data, the frequentist and Bayesian results are expected to be consistent. There exist guidelines to choosing reasonable priors in the literature, for example, see [288] and [289].

5.7. GAMBIT UTILISeD

`GAMBIT-UTILISeD`, which stands for `GAMBIT` Utility To Interpret Likelihoods In Several Dimensions, is an interactive tool for visualizing and interpreting results of global analyses of DM models with high-dimensional parameter spaces. `GAMBIT` outputs HDF5 tables containing likelihoods and observables at each sampled parameter point. These results are then presented as profiled likelihood plots or posterior histograms (see in section 3.3 and section 4.7). While tools to produce such publication-quality plots (`pippi` [197] and `anesthetic` [198]) do exist, interpretation of fit results from these plots can be non-intuitive without an understanding of the effect of individual likelihoods on different parameter planes. In addition, likelihood implementation, testing and quick parameter scans, will greatly benefit from an interactive plotting tool that can quickly make plots of likelihoods and observables for different choices of parameters, without having to rewrite code.

`GAMBIT UTILISeD`, aims to fill these gaps, by providing an interactive web-based plotting application, built using the dash python package [290]. The application is accessed via a browser and displays a dashboard that can be navigated similar to any web page by clicking on interactive elements. The dashboard contains several pages, in which users can quickly make interactive plots of different kinds for their choice of parameters and likelihoods. We provide a summary of the available plotting features with illustrative examples based on global fit results of the symmetric fermionic DM model discussed in section 3.3.

5.7.1. Interactive sample visualisation

We provide two different plots to visualise the viable sample in the full parameter space: a 3D scatter plot with sliders for extra parameters and a parallel coordinates plot. The 3D scatter plot gives the most direct visualisation of the viable sample and is color-coded according to the likelihood ratio $\mathcal{L}/\mathcal{L}_{\max}$.

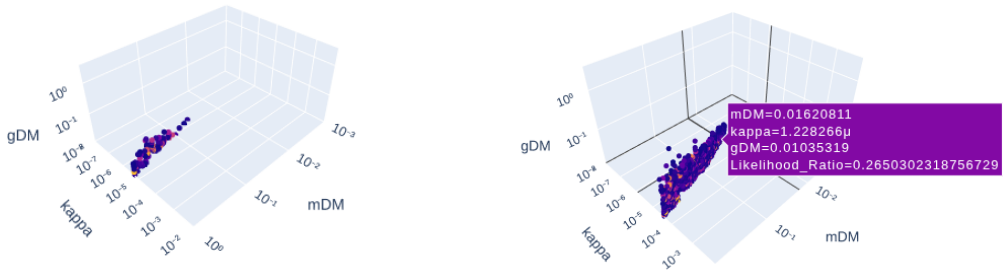

Figure 5.3.: Scatter plots of viable sample color-coded accroding to $\mathcal{L}/\mathcal{L}_{\max}$ for $\epsilon_R = 0.003$ (left) and $\epsilon_R = 0.08$ (right) with $m_{\rm DM}$, κ and $g_{\rm DM}$ on x-, y- and z-axis respectively.

Shown in Figure 5.3 is the 3D scatter plot with $m_{\rm DM}$, κ and $g_{\rm DM}$ on x-, y- and z-axis respectively, for two different values of ϵ_R, whose values can be selected using a slider. Note

that all axes labels for different parameters match parameter names in GAMBIT and are obtained automatically from HDF5 samples [13]. From these plots, we see that there is a positive correlation between κ and $m_{\rm DM}$, as well as ϵ_R. Increasing κ increases annihilation cross-section, whereas increasing $m_{\rm DM}$ and ϵ_R lead to smaller annihilation cross-sections. Hence a positive correlation between these parameters is required to achieve the thermal annihilation cross-section that produces the correct relic abundance. We also note that the likelihood does not vary smoothly with any of the parameters and the small changes seem to be driven by numerical fluctuations, leading to the flat profiled likelihoods we observed in subsection 3.3.1.

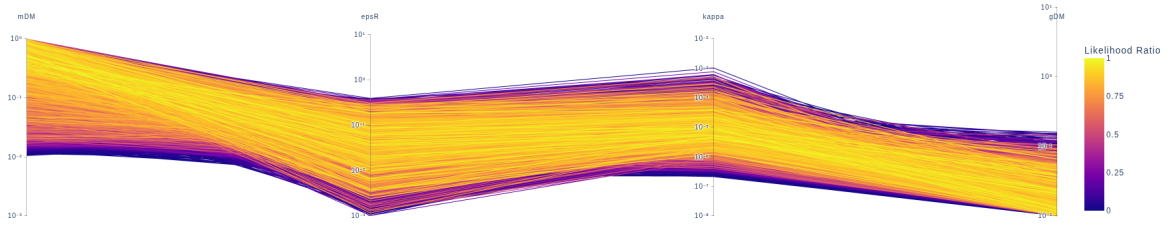

Figure 5.4.: Parallel coordinates plot of free parameters in the model showing the viable sample as lines connecting the different axes, color-coded according to $\mathcal{L}/\mathcal{L}_{\rm max}$.

We show the parallel coordinates plot in Figure 5.4. The plot displays all model parameters as vertical axes with each point in the viable sample represented by a line connecting the different axes, and color-coded according to the likelihood ratio. One can immediately determine the allowed ranges for all parameters in the scan from this plot. For instance, we see that values close to the upper and lower bound on κ as well as very small values of $m_{\rm DM}$ are excluded. Additionally, the order in which the axes are displayed can be changed interactively. This helps in understanding correlations between different parameters by placing the desired axes next to each other. One can also filter out a range of parameters to see the viable parameter space by clicking and dragging on the axes. For example, from Figure 5.5,

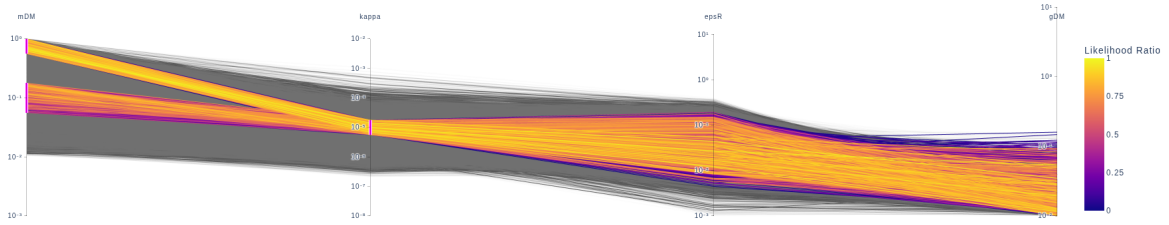

Figure 5.5.: Parallel coordinates plot as describe in Figure 5.4, with a filter applied on a range of values on $m_{\rm DM}$ and κ.

we see once again that large likelihoods can be achieved for positively correlated κ and $m_{\rm DM}$.

5.7.2. Individual likelihood visualisation

Understanding the effect of individual likelihoods on the model parameter space is important in the likelihood implementation and testing phase. Plotting individual likelihoods is also necessary to identify the most constraining likelihoods on the model parameter space. This knowledge can be useful in updates of global fits when updated individual likelihoods become available. For instance, if the original likelihood was found to be less constraining compared to others in the global analysis, one can choose to cut down on computational costs by simply postprocessing the global fit with an updated likelihood, instead of rerunning the

[13] Labels in math mode would require users to input labels for each parameter, which goes against the aim of making this tool free of redundant user input. We rather focus on functionality and quick plotting.

entire global scan. Currently, the code can automatically plot likelihoods available in `DarkBit` that are used in the global scan, but can be easily extended to other likelihoods available in `GAMBIT`. The likelihoods are grouped under different classes of experiments, each with its own page where the plots are displayed on parameter planes chosen by the user. The different pages can be accessed from the navigation bar on the top of the page.

Each page displays a grid of plots showing the individual profiled likelihood ratios for the entire sample. In every page, we also include a panel showing the total profiled likelihood ratio for reference. The plots are labelled by the `GAMBIT capability` of the corresponding likelihoods and the axes by the parameter names defined in `GAMBIT`.

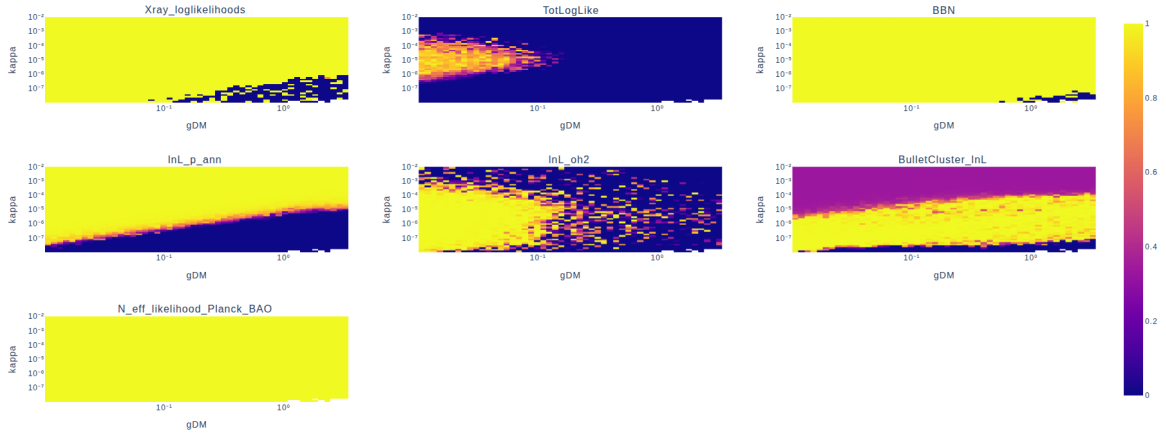

Figure 5.6.: Astrophysical and cosmological likelihoods on the $g_{\rm DM} - \kappa$ plane for the symmetric fermionic DM model, discussed in subsection 3.3.1. In every panel, we show the ratio of the profiled likelihood to the maximum likelihood, ranging from 0 to 1, indicated by the blue to yellow color-shading.

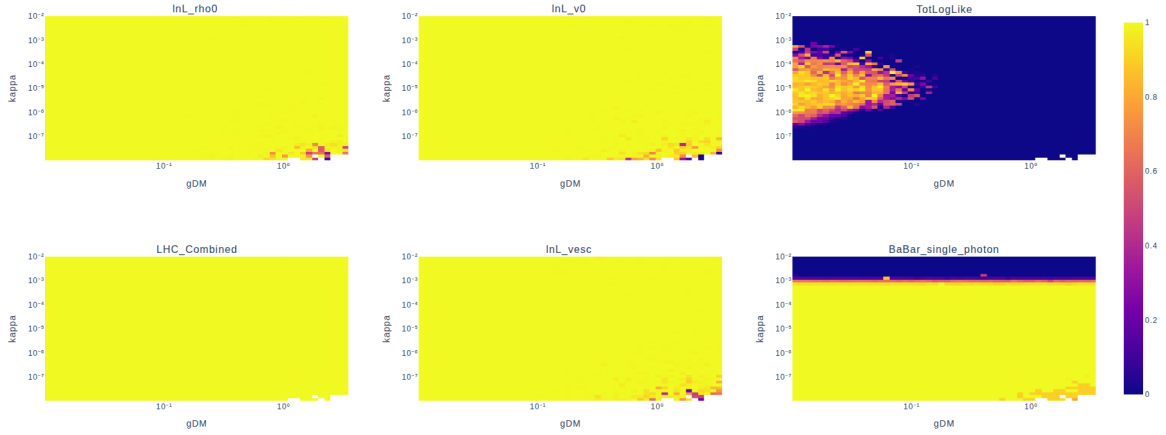

Figure 5.7.: Same as Figure 5.6, but showing collider and nuisance parameter likelihoods on the $g_{\rm DM} - \kappa$ plane.

For illustration, we now show the most relevant individual likelihoods for the symmetric fermionic DM model on the $g_{\rm DM} - \kappa$ plane. In Figure 5.6, we show a screenshot of the page containing the astrophysical and cosmological likelihoods. We see that the indirect detection (Xray_loglikelihoods) and the CMB (lnL_p_ann) likelihoods disfavor regions with large $g_{\rm DM}$ and small κ, while the relic density likelihood (lnL_oh2) constrains regions with large $g_{\rm DM}$ and κ as well, as they can lead to DM under-production. The bullet cluster likelihood (BulletCluster_lnL) prefers the region corresponding to $0.5\,\mathrm{cm}^2\,\mathrm{g}^{-1}$. The other relevant con-

straint on this parameter plane comes from BaBar (BaBar_single_photon). In Figure 5.7, we show the BaBar and combined beam-dump likelihoods (LHC_Combined), as well as the likelihoods on the nuisance parameters, namely the local DM density (lnL_rho0), the local DM velocity (lnL_v0) and the local escape velocity (lnL_vesc).

5.7.3. Total profiled likelihood visualisation

This page displays plots of the ratio of the total profiled likelihood to the maximum total likelihood in all possible model parameter planes for the entire sample. We shows these plots for the symmetric fermionic DM model in Figure 5.8, and they agree with the results presented in subsection 3.3.1.

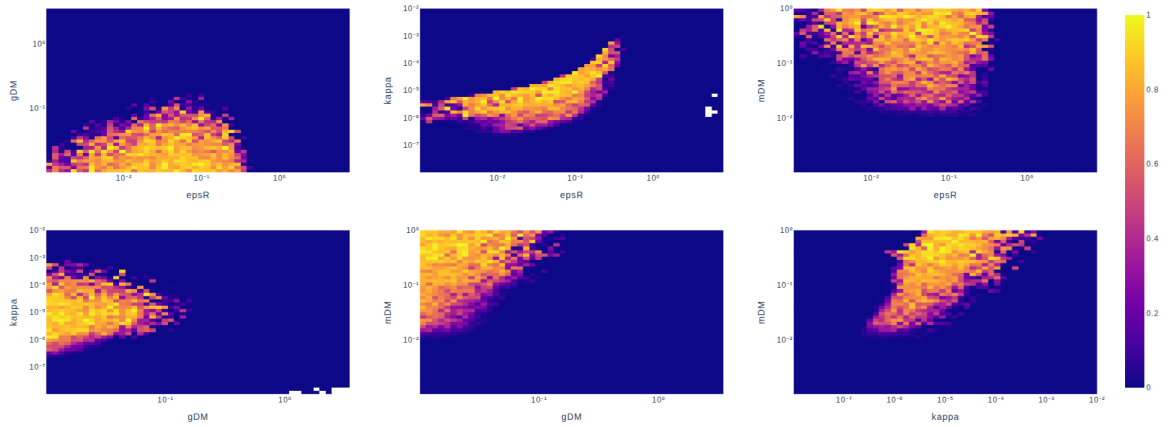

Figure 5.8.: Ratio of profiled total likelihood to maximum total likelihood in different model parameter planes.

5.7.4. Quick start guide

The code is written completely in python and uses the dash python package to set up the web-application. It is fully open source and available on github [14]. The utility functions used to load the sample, perform binning, and profiling are defined in the module `load_sample.py`. The dashboard is set up in `app.py` and the code for different pages in the dashboard are contained in separate files within the `pages/` directory. The required python packages are listed in `req.txt`. Once these are installed, the application can be run by opening a terminal and simply running the python script `app.py` by entering the command `python app.py`. The plots are made by default for the symmetric fermion DM model whose sample file is available at `samples/SubGeV_fermion_allDM_sym.hdf5`. Samples from global fits of other models studied in the thesis can be downloaded from Zenodo [200, 276]. To visualise a different sample, the last line in the `load_sample.py` file, calling the `Sample` class is to be edited with the corresponding sample file path and the group name of the HDF5 file containing the sample, see instructions provided in `load_sample.py`.

[14] https://github.com/sowmiya-balan/GAMBIT-UTILISeD.git

CHAPTER 6

Summary and outlook

The last decade has seen substantial progress in probing sub-GeV DM, both through increasingly sensitive direct detection experiments and novel methods to constrain sub-GeV DM. On the theoretical side, a wide range of sub-GeV DM models and their phenomenology have been explored. Of particular interest are models with sub-GeV DM coupled to a dark photon that has kinetic mixing with the SM photon. These dark photon portal models have a rich phenomenology and can give rise to observable signals in colliders, direct detection, indirect detection, cosmological and astrophysical observations. In light of the rapid advancements in the field, the status update of this particularly interesting class of models became necessary. In this thesis, we contribute to this effort by studying five different sub-GeV DM models across two publications.

In our first publication presented in chapter 3, we chose to study models with fermionic and scalar DM coupled to a dark photon. The fermionic DM model undergoes s-wave annihilation and is constrained by the stringent CMB energy injection bound to remain below the thermal annihilation cross-section. This prevents the model from producing the correct DM relic abundance through freeze-out. We considered three possible solutions to overcome this challenge: resonant annihilation, particle-antiparticle asymmetry and under-abundant DM. We then performed global analyses for two different cases ($\Omega_{\rm DM}h^2 \approx 0.12$ and $\Omega_{\rm DM}h^2 \lesssim 0.12$) for both symmetric and asymmetric fermionic DM. Although we found viable regions in all four analyses, in the case of symmetric fermionic DM with $\Omega_{\rm DM}h^2 \approx 0.12$, the allowed regions were strictly restricted to small values of gauge coupling and kinetic mixing parameter. Non-zero asymmetry widens the range of annihilation cross-sections that can reproduce the DM relic abundance, and also suppresses annihilation signals close to recombination and today. This allowed for larger gauge coupling and kinetic mixing parameter values making the model potentially discoverable in future experiments. In both symmetric and asymmetric fermionic DM models, we found that the model was forced to stay close to resonance, $m_{A'} \approx 2m_{\rm DM}$ to simultaneously reproduce the correct DM relic abundance and satisfy the CMB constraint.

In the case of scalar DM coupled to the dark photon, the annihilation is p-wave dominated and hence the CMB constraint is much weaker due to the velocity suppression. The most relevant constraints on this model are then the relic density, direct detection and accelerator constraints. Similar to fermionic DM, we found that allowed regions in this model are also restricted to remain close to resonance. But unlike before, they can allow large gauge

coupling and kinetic mixing parameter values without the inclusion of non-zero asymmetry. Bayesian model comparison showed that asymmetric fermionic DM was preferred over symmetric fermionic DM, while there was no preference among symmetric scalar, asymmetric scalar and asymmetric fermionic DM. The main conclusion from this work was that both asymmetric fermionic DM and scalar DM coupled to the dark photon are viable under current constraints and significant parts of their allowed regions can be probed with upcoming experiments, most notably, the LDMX experiment.

In our second publication, presented in chapter 4, we explored the connection between DM and the nano-Hertz gravitational wave background observed by several PTA collaborations. First order phase transitions around MeV temperatures in a sub-GeV dark sector can produce gravitational waves in the nHz frequency range. We hence considered a dark sector with a dark Higgs that undergoes FOPT and gives masses to the dark photon and the fermionic DM candidate. We proposed two variations of this model, one where the dark Higgs has an effective coupling to the SM electrons and can directly decay to the SM, which we called the *coupled dark sector*; and another model where no such coupling exists and the dark Higgs can only decay to the SM through dark photon loops, called the *secluded dark sector*. We performed global fits of both these models to determine if they can reproduce the correct DM relic abundance, provide a good fit to the PTA signal along with the contribution form supermassive black hole binary mergers, as well as satisfy current constraints from laboratory and astrophysical data.

The allowed regions were found to be mainly shaped by a combination of the PTA likelihood, relic density constraint, laboratory constraints on the dark photon and cosmological constraints on dark Higgs decays. While we found viable regions in both models, the kinetic mixing parameter in the coupled dark sector was relatively unconstrained leaving room for the possibility that the model remains unobservable in laboratory experiments. The secluded dark sector, on the other hand, required more fine-tuning compared to the coupled dark sector case in order to be able to fit the large PTA signal while depleting the dark Higgs abundance after DM freeze-out through decays, without significantly altering the cosmological history. The secluded dark sector case preferred larger values of the kinetic mixing parameter and can hence be probed by upcoming experiments.

Such large scale comprehensive global scans were only made possible by the modular global fitting code `GAMBIT`. In this thesis we extended and employed `GAMBIT` to perform the global fits for all the models considered. In chapter 5, we discussed the statistics and rationale of global fits. We also presented a look at the internal structure of `GAMBIT` to understand how it achieves modularity and flexibility, its core design principles. While `GAMBIT` eliminates the redundancy in production, visualization of global fit results can still involve redundant coding tasks, making interpretation and presentation of the results a time-consuming process. In order to address these issues, I developed `GAMBIT-UTILISeD`, a web-based application for fast and interactive visualization of global fits results of models with high dimensional parameter spaces. In the second part of chapter 5, I presented the features of this tool as well as a quick start guide.

The future of sub-GeV DM looks exciting as we are making progress on multiple fronts. On the direct detection side, the DAMIC-M experiment that searches for DM-induced electronic recoils using its semiconductor based prototype detector, has already exceeded expectations in sensitivity to DM-electron scatterings [210]. It has constrained considerable parts of parameter space of benchmark models using ~ 1.3 kg-day exposure. With the soon to be installed full apparatus, the DAMIC-M experiment plans to collect a kg-year exposure and expects orders of magnitude improvement in sensitivity. Other charged coupled device (CCD) detectors like SENSEI at SNOLAB [291] (running) and OSCURA [292] (upcoming) will help further

probe the thermal sub-GeV DM parameter space. Liquid noble element detectors of currently running experiments like PandaX-4T [293], XENONnT [294] and upcoming ones like DarkSide-20k [188] will increase their sensitivity to DM-electron and DM-nuclear scattering cross-sections with larger exposures. In parallel, new detector technologies and alternative target materials are also being explored (for example, see DELight experiment [204]).

On the accelerator side, the LDMX experiment [208] which is an electron beam fixed-target experiment (currently under construction), will reach unprecedented sensitivities to several benchmark thermal sub-GeV DM targets. Another upcoming experiment is the SHiP experiment [295], a recently approved fixed target experiment at the CERN SPS accelerator which will also be able to probe the thermal sub-GeV DM targets.

Several experiments have been proposed to fill the MeV gap to increase sensitivity to gamma rays in this energy range. MeV scale gamma rays can be produced in sub-GeV DM annihilations and exotic light particle decays. The COSI experiment has been approved for running and forecast studies show that it can significantly improve indirect detection constraints on both s-wave and p-wave annihilating DM [281]. For s-wave annihilating DM, when considering both prompt and secondary emission, COSI can reach sensitivities down to the CMB constraint. For p-wave annihilating DM, X-ray constraints are already stronger than CMB constraints and hence COSI will probe an unexplored part of the parameter space for these models. Other proposed experiments include GECCO, e-ASTROGRAM, AMEGO, MAST, AdEPT, PANGU and GRAMS. Sensitivity forecasts of these experiments show that they can improve indirect detection constraints for channels involving neutral pions [122]. In particular, the MAST experiment can place very strong constraints on DM annihilation cross-section for the neutral pion and photon annihilation channels.

We are also set to see substantial improvement in the $\Delta N_{\rm eff}$ constraint from the upcoming CMB-S4 project [119] which can, among others, constrain dark sector models with FOPTs that produce very large GW signals. Furthermore, better measurements of the CMB spectral shape by future missions like PIXIE [296] and Voyage 2050 [297] can improve the CMB spectral distortion constraints on energy injection from dark sectors decays and annihilations. While third IPTA release will provide conclusive evidence for the stochastic GW background, disentangling the true origin of the PTA signal will require accurate measurement of the signal shape with a high signal-to-noise ratio, more information on GW anisotropies [298] and searches for individual sources of continuous GW signals [299]. Studies of binary black hole mergers with future space based interferometers like LISA, apart from helping us understand their GW signals, will also shed light on their environments. For example, the presence of a DM spike around the black hole can leave imprints on the GW signal from the black hole mergers and precise measurements of the signal can help reconstruct the DM model parameters [300]. Hence, the study of black hole environments can help differentiate between CDM and SIDM spikes which lead to different effects on black hole mergers and accretion [138, 139].

Apart from the above mentioned GW probes of SIDM, stringent constraints on DM self-interactions from other astrophysical observations exist, see section 2.6. But the most robust constraint that is suitable to the context of global fits comes from the Bullet cluster. In subsection 2.6.2, we presented an improved version of the original bullet cluster constraint developed as a part of the thesis and included in all global fits performed in this thesis. More statistically rigorous and stronger self-interaction constraints from cluster mergers can be achieved with access to an ensemble of well observed merging cluster systems with clean data. With upcoming large scale structure surveys like Euclid [301], this situation is set to improve and we expect improved measurements of merging cluster systems with larger statistics. On smaller scales, precise measurement of the stellar velocities close to the galactic center by JWST along with physics informed simulations are expected to lead to a better determination of the

Milky Way's inner DM density profile which will help us further our understanding of DM self-interactions [302].

To conclude, in this thesis, we have made an attempt to summarize the implications of current experimental data on the sub-GeV DM model space and identified targets for future experiments. In the next decades, the vast number of currently running, soon to be launched, and planned experiments promise unprecedented experimental progress in searches for sub-GeV DM. Global fits will remain a necessary and crucial ingredient in exploiting the complementarity of these searches to understand the status of DM models and uncover the true nature of DM.

APPENDIX A

Bullet Cluster constraint

A.1. Evaporation rate

Cluster masses are dominated mainly by DM($\sim 90\%$), followed by gas($\sim 10\%$), with stars only making up a negligible fraction of mass, such that $M^{\rm main,sub} = M^{\rm main,sub}_{\rm tot} + M^{\rm main,sub}_{\rm gas}$. Here $M_{\rm tot}$ denotes the total DM mass, which can be larger than the mass of the DM candidate under consideration, $M_{\rm DM}$. We make no assumption on the symmetry of DM and consider (anti)particles to make up a fraction f_χ($f_{\bar\chi}$) of the total DM mass $M_{\rm tot}$, such that $f_\chi + f_{\bar\chi} = M_{\rm DM}/M_{\rm tot} \equiv f_{\rm DM} \leq 1$.

Self-interactions between $\chi\chi$, $\bar\chi\bar\chi$ and $\chi\bar\chi$ contribute to the mass loss in the cluster merger. Kahlhoefer et. al derived evaporation rates of a smaller cluster in unequal mass mergers [156]. I will quickly discuss how these rates are calculated before returning to mass loss derivation. Whether or not a particle is expelled from the subcluster, or at least kicked to an outer orbit, depends on the amount of energy transferred in the collision. Occasionally, enough energy can be transferred to a subcluster particle in just one interaction. This is called *immediate* evaporation. The opposite case called *cumulative* evaporation is the one in which a subcluster particle gets expelled by accumulating energy from multiple interactions. We have to consider both types of evaporation when calculating the mass loss. The rates for immediate and cumulative evaporation are given by [156]:

$$R_{\rm imd} = \frac{\bar\rho_{\rm main}}{m_{\rm DM}} v_0 \sigma_{\rm imd} \equiv \frac{\bar\rho_{\rm main}}{m_{\rm DM}}\ v_0 \int {\rm d}\phi \int_{2\bar v^2_{\rm esc,sub}/v_0^2 - 1}^{1-2\bar v^2_{\rm esc,sub}/v_0^2} {\rm d}\cos\theta \frac{{\rm d}\sigma}{{\rm d}\Omega} \tag{A.1}$$

$$R_{\rm cml} = \frac{\bar\rho_{\rm main}}{m_{\rm DM}} v_0 \sigma_T \equiv \frac{\bar\rho_{\rm main}}{m_{\rm DM}} v_0 \int {\rm d}\phi \int_{-1}^{1} {\rm d}\cos\theta\ (1 - |\cos\theta|) \frac{{\rm d}\sigma}{{\rm d}\Omega}\,, \tag{A.2}$$

where $\bar\rho_{\rm main} = 2.955 \cdot 10^6\,{\rm M_\odot kpc^{-3}}$ is the average DM density within 150 kpc of the main cluster, $m_{\rm DM}$ is the DM mass, $\bar v_{\rm esc,sub} = 2408$ km/s is the average escape velocity within 150 kpc of the subcluster, $v_0 = 3900$ km/s is the constant collision velocity and σ_T is the (corrected) momentum-transfer cross section (cluster and merger parameters obtained from

ref. [151]). The total evaporation for a (anti)particle is calculated as the sum of cumulative and immediate evaporation rates,

$$\Gamma_\chi = \frac{\bar{\rho}_{\rm main}}{m_{\rm DM}} v_0 \ [f_\chi(\sigma_{{\rm imd},\chi\chi} + \sigma_{T,\chi\chi}) + f_{\bar{\chi}}(\sigma_{{\rm imd},\chi\bar{\chi}} + \sigma_{T,\chi\bar{\chi}})] = \frac{\bar{\rho}_{\rm main}}{m_{\rm DM}} \ v_0 \ \sigma_{{\rm eff},\chi} \tag{A.3}$$

$$\Gamma_{\bar{\chi}} = \frac{\bar{\rho}_{\rm main}}{m_{\rm DM}} v_0 \ [f_{\bar{\chi}}(\sigma_{{\rm imd},\bar{\chi}\bar{\chi}} + \sigma_{T,\bar{\chi}\bar{\chi}}) + f_\chi(\sigma_{{\rm imd},\chi\bar{\chi}} + \sigma_{T,\chi\bar{\chi}})] = \frac{\bar{\rho}_{\rm main}}{m_{\rm DM}} \ v_0 \ \sigma_{{\rm eff},\bar{\chi}}. \tag{A.4}$$

Using these rates for particle and antiparticle evaporation, the DM mass loss is given by,

$$M^{\rm sub}_{\rm DM}(t) - M^{\rm sub}_{\rm DM}(0) = -M^{\rm sub}_{\rm tot} \left[f_\chi \left(1 - \exp^{-\int {\rm d}t \, \Gamma_\chi} \right) + f_{\bar{\chi}} \left(1 - \exp^{-\int {\rm d}t \, \Gamma_{\bar{\chi}}} \right) \right] . \tag{A.5}$$

Since we use MLR measurements within 150 kpc of the total mass peak, we calculate the mass loss within a radius of 150 kpc from the center of the sublucster. We then make the following simplifying assumptions: (i) Evaporative collisions occur only after pericenter passage, (ii) a particle takes time $\Delta t = 150\,{\rm kpc}/\bar{v}_{\rm esc,sub}$ to leave the central region of the subcluster when ejected with velocity $\bar{v}_{\rm esc,sub}$. The relative mass loss $\Delta_{\rm DM} \equiv (M^{\rm sub}_{\rm DM,i} - M^{\rm sub}_{\rm DM,f})/M^{\rm sub}_{\rm tot,i}$ (with subscript i (f) denoting the initial (final) value) can be determined as

$$\Delta_{\rm DM} = (f_{\rm DM} - f_{\bar{\chi}}) \left(1 - \exp\left(-\bar{\Sigma}_{\rm main} \frac{\sigma_{{\rm eff},\chi}}{m_{\rm DM}} \right) \right) + f_{\bar{\chi}} \left(1 - \exp\left(-\bar{\Sigma}_{\rm main} \frac{\sigma_{{\rm eff},\bar{\chi}}}{m_{\rm DM}} \right) \right) \tag{A.6}$$

where

$$\bar{\Sigma}_{\rm main} = \bar{\rho}_{\rm main} \, (Z - v_0 \Delta t) = 1.41 \cdot 10^9 {\rm M}_\odot {\rm kpc}^{-2} \tag{A.7}$$

and $Z = 720$kpc is the observed separation between the two clusters. This is the prediction for the fractional DM mass lost by the subcluster. But in major mergers, a subcluster can also lose a fraction of its gas mass. Thus, the measured total mass loss $\Delta_{\rm M} = (M^{\rm sub}_{\rm f} - M^{\rm sub}_{\rm i})/M^{\rm sub}_{\rm i}$ will include a contribution from gas. The DM mass loss and the total mass loss are related by,

$$\Delta_{\rm M} = \Delta_{\rm DM}(1 - R^{\rm sub}_i) + R^{\rm sub}_i (1 - x) \tag{A.8}$$

where $R^{\rm sub}_i = M^{\rm sub}_{\rm gas,i}/M^{\rm sub}_{\rm i}$ is the initial ratio of gas mass to total cluster mass and $x = M^{\rm sub}_{\rm gas,f}/M^{\rm sub}_{\rm gas,i}$, such that $(1-x)$ is the fraction of gas lost during the collision. While $R^{\rm sub}_{\rm f}$ can be obtained from observations, we approximate $R^{\rm sub}_{\rm i}$ by the observed value from the main cluster after the collision, i.e. we set $R^{\rm sub}_{\rm i} = R^{\rm main}_{\rm f} == R^{\rm main}_{\rm obs}$. We then have

$$x = \left(\frac{R^{\rm sub}_{\rm f}}{1 - R^{\rm sub}_{\rm f}} \right) \left(\frac{1 - R^{\rm main}_{\rm f}}{R^{\rm main}_{\rm f}} \right) (1 - \Delta_{\rm DM}) \, . \tag{A.9}$$

We use $R^{\rm main}_{\rm f} = 0.09 \pm 0.01$ and $R^{\rm sub}_{\rm f} = 0.04 \pm 0.01$ from ref. [148].

A.2. Measuring mass loss

In plain sight, measuring mass loss looks relatively simple - determine the mass observationally, assume an initial mass and find the difference. But there are some technicalities to be considered. In practice, halo mass[15] can be estimated from observables like total luminosities of the member galaxies, the number of the member galaxies, the X-ray emission from hot gas, the gravitational lensing signals, the Sunyaev- Zeldovich effect, the galaxy velocity dispersion, etc. But such halo mass estimates suffer from systematics involved in modeling of observable-mass relationships. In comparison, lensing provides a relatively direct probe of

[15] Defining boundaries of a cluster such that the mass of a cluster is that enclosed within this boundary is already non-trivial. See, for example, [303].

mass, but still has systematics. Lensing mass reconstructions for the subcluster and main cluster based on HST data are available in [304, 305].

To then assume a reasonable initial mass for the subcluster, one would have to construct a sample of cluster mass measurements and fit it to a distribution. Self-interactions have the most noticeable effect in the inner parts of the cluster and a measurement of mass within 250 kpc of the subcluster is available from lensing mass reconstruction [305]. Thus, to study mass lost by inner parts, one would have to compare it to the distribution of cluster masses at this radius which suffers from relatively large uncertainties and comparison to full halo masses would lead to very weak constraints; whereas MLRs, being the ratio of two measurements, might have smaller errors in comparison. Moreover, compared to mass profiles, MLR values increase more slowly with radius before plateauing around 300 kpc. Comparing the MLR value at a smaller radius to values measured at larger radii would then lead to mass loss estimates that are larger than those predicted. Hence, prior with $\gamma_i(200\,\mathrm{kpc})$ from [154] gives us conservative constraints. As mentioned in the main text, MLR measurements at 200 kpc for a sample of clusters are available in literature [154]. The data was found to be well described by a log-normal distribution in both i and b-bands.

Moreover, MLR in both these bands depends only mildly on the luminosity. This points to the fact that larger halos are not necessarily increasingly efficient at forming galaxies; i.e. richness doesn't scale with mass and that galaxy clusters are dominated by DM. Thus, in the context of mergers, a decrease in MLR can be attributed mainly to DM mass loss. But every merger would lead to significant stripping of gas and non-negligible gas loss. Therefore, attributing the whole of the observed mass loss solely to DM loss leads to artificially stringent constraints. On the other hand, an increase in MLR immediately points to a loss in luminosity.

The i-band (near-infrared wavelengths), has the least contamination from gas. This band still has luminosity contributions from galaxies and dust. But galaxies are considered collisionless and dust forms a vanishingly small fraction of the galaxy clusters. The b-band (blue wavelengths) has contributions from hot gas, young stars and galaxies. Old galaxy clusters would thus have large MLRs in b-band compared to larger wavelengths. In mergers, one can therefore expect decrease in i-band MLRs and increase in b-band MLRs (if the cluster did have blue gas prior to collision). This is consistent with observed bullet cluster values in comparison to MLR means extracted from [154]. It is easier to include a gas mass loss than to determine the change in gas luminosity, we thus choose to work with only the i-band.

Acknowledgements (Danksagungen)

I have had the pleasure of crossing paths with a number of wonderful people during my time in Germany who have enriched both my academic and personal life. I am deeply grateful for the support, encouragement, and friendship I have received, and I would like to especially thank a few of them here. To begin, I express my heartfelt gratitude to my supervisor Prof. Dr. Felix Kahlhöfer for his sincerity, for always welcoming my questions, no matter how simple and for his expert guidance. Our meetings have always left me inspired and in good spirits and I truly appreciate the kindness and encouragement I received when I needed it.

A special thanks to my GAMBIT collaborators, Tomas Gonzalo, Taylor Gray, Torsten Bringmann, Carlo Tasillo, Jonas Matuszak, Michael Korsmeier, Kathrin Nippel and Silvia Manconi for the highly enjoyable scientific collaboration and stimulating conversations. I am also sincerely grateful to Felix Kahlhöfer, Torsten Bringmann, Silvia Manconi, and Tomas Gonzalo for their invaluable support during my postdoc applications. I would also like to thank my second supervisor, Prof. Dr. Thomas Schwetz-Mangold, for the insightful discussions during journal club sessions and elsewhere.

The global fits in this thesis were performed using the computing resources provided by the Cambridge Service for Data Driven Discovery (CSD3), part of which is operated by the University of Cambridge Research Computing on behalf of the STFC DiRAC HPC Facility (www.dirac.ac.uk). The DiRAC component of CSD3 was funded by BEIS capital funding via STFC capital grants ST/P002307/1 and ST/R002452/1 and STFC operations grant ST/R00689X/1. DiRAC is part of the National e-Infrastructure.

I acknowledge the support by the Doctoral School 'Karlsruhe School of Elementary and Astroparticle Physics: Science and Technology'. I would also like to thank the KSETA doctoral school for supporting me with travel funds. I especially thank the organizers of Dark Matter 2023 (Santander), Light Dark World 2023 (Karlsruhe), ISAPP School 2024 (Bad Liebenzell) and DM & Neutrinos 2025 (Paris) for curating a highly engaging scientific program and creating opportunities for young scientists to connect and collaborate. I am thankful to Miguel Escudero for his inspiring lectures and delightful discussions during the ISAPP summer school.

I am grateful to my fellow TTP IT admins Manuel Egner, Jonas Matuszak, and Dominik Grau, as well as the ITP admins, for their support, patience, and camaraderie throughout my time as an admin. I thank my current and past colleagues Tomas Gonzalo, Alessandro Morandini, Cristina Benso, Nicoline Hemme, Jonas Matuszak, Henda Mansour, Giovani Dalla Valle Garcia, Kierthika Chathirathas, Sabya Chatterjee, Kiran Sharma, Thomas Rink, Maksym Ovchynnikov, and the Bachelor and Master students over the years for the making the journal clubs lively and engaging. Thanks to Tim Kretz and Maksym Riabokon for all

the memes, internet humour, animal pictures, and earnest conversations. Your company was the only thing that made the office bearable during the hottest days. Jonas, thank you for always stopping by to check in on me in the mornings and for all the times we reassured each other by sharing our stupid mistakes. Cristina, thank you for always offering help when needed despite your busy schedule and for the delightful conversations. Henda, I cherish getting to know you, our shared love of cooking, our warm conversations, and all those times of sharing food with each other. Giovani, thank you for always keeping the conversation going and putting a smile on the faces of those around you.

A sincere thanks to Jonas, Sabarish and Kierthi for proof reading parts of the thesis and for your valuable feedback.

A very special thanks to Nicoline and Kierthi for your friendship, for encouraging me to try new things, for all the wonderful experiences, and for your emotional support and well wishes throughout my PhD. My journey would have been vastly different without you two, and I am truly grateful to have had the opportunity to spend this time with you.

I thank Sabarish for always being by my side, for making me believe in myself, for nurturing my love for physics, for always being ready to discuss physics, and for everything else you've given me over the years. Thanks to Sabarish, Ajith and Bala for keeping me sane during thesis writing, for the countless hours on zoom and for giving me weekends to look forward to.

Finally, I would not have made it here without the emotional and financial support from my family during my Masters in Germany. Thanks to my mom for always believing in me and being an unwavering supporter in my career decisions, and to my sister and brother-in-law for taking care of everything back home, allowing me to pursue my dreams away from home.

References

[1] S. Smith, "The Mass of the Virgo Cluster," *The Astrophysical Journal* **83** (Jan., 1936) 23.

[2] F. Zwicky, "On the Masses of Nebulae and of Clusters of Nebulae," *The Astrophysical Journal* **86** (Oct., 1937) 217.

[3] K. Lundmark, "Über die Bestimmung der Entfernungen, Dimensionen, Massen und Dichtigkeit fur die nächstgelegenen anagalacktischen Sternsysteme.," *Meddelanden fran Lunds Astronomiska Observatorium Serie I* **125** (Jan., 1930) 1–13.

[4] V. C. Rubin and W. K. Ford, Jr., "Rotation of the Andromeda Nebula from a Spectroscopic Survey of Emission Regions," *The Astrophysical Journal* **159** (Feb., 1970) 379.

[5] H. Reeves, J. Audouze, W. A. Fowler, and D. N. Schramm, "On the Origin of Light Elements," *The Astrophysical Journal* **179** (Feb., 1973) 909–930.

[6] N. A. Bahcall, L. M. Lubin, and V. Dorman, "Where is the Dark Matter?," *Astrophysical Journal Letters* **447** (July, 1995) L81, `arXiv:astro-ph/9506041 [astro-ph]`.

[7] **Planck** Collaboration, N. Aghanim *et al.*, "Planck 2018 results. VI. Cosmological parameters," *Astron. Astrophys.* **641** (2020) A6, `arXiv:1807.06209 [astro-ph.CO]`. [Erratum: Astron.Astrophys. 652, C4 (2021)].

[8] W. Hu, "Lecture Notes on CMB Theory: From Nucleosynthesis to Recombination," `arXiv:0802.3688 [astro-ph]`.

[9] **Boomerang** Collaboration, C. B. Netterfield *et al.*, "A measurement by Boomerang of multiple peaks in the angular power spectrum of the cosmic microwave background," *Astrophys. J.* **571** (2002) 604–614, `arXiv:astro-ph/0104460`.

[10] S. Hanany *et al.*, "MAXIMA-1: A Measurement of the cosmic microwave background anisotropy on angular scales of 10 arcminutes to 5 degrees," *Astrophys. J. Lett.* **545** (2000) L5, `arXiv:astro-ph/0005123`.

[11] **WMAP** Collaboration, C. L. Bennett *et al.*, "First year Wilkinson Microwave Anisotropy Probe (WMAP) observations: Preliminary maps and basic results," *Astrophys. J. Suppl.* **148** (2003) 1–27, `arXiv:astro-ph/0302207`.

[12] **2dFGRS** Collaboration, W. J. Percival *et al.*, "The 2dF Galaxy Redshift Survey: The Power spectrum and the matter content of the Universe," *Mon. Not. Roy. Astron. Soc.* **327** (2001) 1297, `arXiv:astro-ph/0105252`.

[13] **DESI** Collaboration, M. Abdul Karim *et al.*, "DESI DR2 Results II: Measurements of Baryon Acoustic Oscillations and Cosmological Constraints," `arXiv:2503.14738 [astro-ph.CO]`.

[14] W. Tucker, P. Blanco, S. Rappoport, L. David, D. Fabricant, E. E. Falco, W. Forman, A. Dressler, and M. Ramella, "1E0657-56: A Contender for the Hottest Known Cluster of Galaxies," Jan., 1998. http://arxiv.org/abs/astro-ph/9801120. arXiv:astro-ph/9801120.

[15] M. Markevitch, A. H. Gonzalez, L. David, A. Vikhlinin, S. Murray, W. Forman, C. Jones, and W. Tucker, "A TEXTBOOK EXAMPLE OF A BOW SHOCK IN THE MERGING GALAXY CLUSTER 1E 0657-56,".

[16] D. Clowe, A. Gonzalez, and M. Markevitch, "Weak lensing mass reconstruction of the interacting cluster 1E0657-558: Direct evidence for the existence of dark matter," *The Astrophysical Journal* **604** no. 2, (Apr., 2004) 596–603. http://arxiv.org/abs/astro-ph/0312273. arXiv:astro-ph/0312273.

[17] D. Clowe, M. Bradac, A. H. Gonzalez, M. Markevitch, S. W. Randall, C. Jones, and D. Zaritsky, "A direct empirical proof of the existence of dark matter," *The Astrophysical Journal* **648** no. 2, (Sept., 2006) L109–L113. http://arxiv.org/abs/astro-ph/0608407. arXiv:astro-ph/0608407.

[18] E. Hubble, "A relation between distance and radial velocity among extra-galactic nebulae," *Proc. Nat. Acad. Sci.* **15** (1929) 168–173.

[19] P. J. E. Peebles, *The large-scale structure of the universe*. 1980.

[20] **Supernova Search Team** Collaboration, A. G. Riess *et al.*, "Observational evidence from supernovae for an accelerating universe and a cosmological constant," *Astron. J.* **116** (1998) 1009–1038, arXiv:astro-ph/9805201.

[21] **Supernova Cosmology Project** Collaboration, S. Perlmutter *et al.*, "Measurements of Ω and Λ from 42 High Redshift Supernovae," *Astrophys. J.* **517** (1999) 565–586, arXiv:astro-ph/9812133.

[22] **Boomerang** Collaboration, P. de Bernardis *et al.*, "A Flat universe from high resolution maps of the cosmic microwave background radiation," *Nature* **404** (2000) 955–959, arXiv:astro-ph/0004404.

[23] J. F. Navarro, C. S. Frenk, and S. D. M. White, "The Structure of cold dark matter halos," *Astrophys. J.* **462** (1996) 563–575, arXiv:astro-ph/9508025.

[24] J. S. Bullock and M. Boylan-Kolchin, "Small-Scale Challenges to the ΛCDM Paradigm," *Ann. Rev. Astron. Astrophys.* **55** (2017) 343–387, arXiv:1707.04256 [astro-ph.CO].

[25] K. A. Oman *et al.*, "The unexpected diversity of dwarf galaxy rotation curves," *Mon. Not. Roy. Astron. Soc.* **452** no. 4, (2015) 3650–3665, arXiv:1504.01437 [astro-ph.GA].

[26] A. Klypin, I. Karachentsev, D. Makarov, and O. Nasonova, "Abundance of Field Galaxies," *Mon. Not. Roy. Astron. Soc.* **454** no. 2, (2015) 1798–1810, arXiv:1405.4523 [astro-ph.CO].

[27] B. Moore, S. Ghigna, F. Governato, G. Lake, T. R. Quinn, J. Stadel, and P. Tozzi, "Dark matter substructure within galactic halos," *Astrophys. J. Lett.* **524** (1999) L19–L22, arXiv:astro-ph/9907411.

[28] M. Boylan-Kolchin, J. S. Bullock, and M. Kaplinghat, "The Milky Way's bright satellites as an apparent failure of ΛCDM," *MNRAS* **422** no. 2, (May, 2012) 1203–1218, arXiv:1111.2048 [astro-ph.CO].

[29] D. N. Spergel and P. J. Steinhardt, "Observational evidence for selfinteracting cold dark matter," *Phys. Rev. Lett.* **84** (2000) 3760–3763, arXiv:astro-ph/9909386.

[30] S. Adhikari *et al.*, "Astrophysical Tests of Dark Matter Self-Interactions," arXiv:2207.10638 [astro-ph.CO].

[31] A. G. Riess *et al.*, "A Comprehensive Measurement of the Local Value of the Hubble Constant with 1 km s^{-1} Mpc^{-1} Uncertainty from the Hubble Space Telescope and the SH0ES Team," *Astrophys. J. Lett.* **934** no. 1, (2022) L7, arXiv:2112.04510 [astro-ph.CO].

[32] W. L. Freedman and B. F. Madore, "Progress in direct measurements of the Hubble constant," *JCAP* **11** (2023) 050, arXiv:2309.05618 [astro-ph.CO].

[33] N. Schöneberg, G. Franco Abellán, A. Pérez Sánchez, S. J. Witte, V. Poulin, and J. Lesgourgues, "The H0 Olympics: A fair ranking of proposed models," *Phys. Rept.* **984** (2022) 1–55, arXiv:2107.10291 [astro-ph.CO].

[34] L. Perivolaropoulos and F. Skara, "Challenges for ΛCDM: An update," *New Astron. Rev.* **95** (2022) 101659, arXiv:2105.05208 [astro-ph.CO].

[35] S. Shankaranarayanan and J. P. Johnson, "Modified theories of gravity: Why, how and what?," *Gen. Rel. Grav.* **54** no. 5, (2022) 44, arXiv:2204.06533 [gr-qc].

[36] J. D. Bekenstein, "Relativistic gravitation theory for the MOND paradigm," *Phys. Rev. D* **70** (2004) 083509, arXiv:astro-ph/0403694. [Erratum: Phys.Rev.D 71, 069901 (2005)].

[37] C. Skordis, "Generalizing tensor-vector-scalar cosmology," *Phys. Rev. D* **77** (2008) 123502, arXiv:0801.1985 [astro-ph].

[38] C. Skordis and T. Złośnik, "Gravitational alternatives to dark matter with tensor mode speed equaling the speed of light," *Phys. Rev. D* **100** no. 10, (2019) 104013, arXiv:1905.09465 [gr-qc].

[39] C. Skordis and T. Zlosnik, "New Relativistic Theory for Modified Newtonian Dynamics," *Phys. Rev. Lett.* **127** no. 16, (2021) 161302, arXiv:2007.00082 [astro-ph.CO].

[40] M. Viel, G. D. Becker, J. S. Bolton, and M. G. Haehnelt, "Warm dark matter as a solution to the small scale crisis: New constraints from high redshift Lyman-α forest data," *Phys. Rev. D* **88** (2013) 043502, arXiv:1306.2314 [astro-ph.CO].

[41] G. Arcadi, D. Cabo-Almeida, M. Dutra, P. Ghosh, M. Lindner, Y. Mambrini, J. P. Neto, M. Pierre, S. Profumo, and F. S. Queiroz, "The Waning of the WIMP: Endgame?," *Eur. Phys. J. C* **85** no. 2, (2025) 152, arXiv:2403.15860 [hep-ph].

[42] K. Choi, S. H. Im, and C. Sub Shin, "Recent Progress in the Physics of Axions and Axion-Like Particles," *Ann. Rev. Nucl. Part. Sci.* **71** (2021) 225–252, arXiv:2012.05029 [hep-ph].

[43] K. N. Abazajian, "Sterile neutrinos in cosmology," *Phys. Rept.* **711-712** (2017) 1–28, arXiv:1705.01837 [hep-ph].

[44] C. M. Vogel, H. García Escudero, J. Froustey, and K. N. Abazajian, "Return of the Lepton Number: Sterile Neutrino Dark Matter Production and the Revival of the Shi-Fuller Mechanism," arXiv:2507.18752 [hep-ph].

[45] **LZ** Collaboration, J. Aalbers *et al.*, "Dark Matter Search Results from 4.2 Tonne-Years of Exposure of the LUX-ZEPLIN (LZ) Experiment," *Phys. Rev. Lett.* **135** no. 1, (2025) 011802, arXiv:2410.17036 [hep-ex].

[46] M. Ibe, W. Nakano, Y. Shoji, and K. Suzuki, "Migdal Effect in Dark Matter Direct Detection Experiments," *JHEP* **03** (2018) 194, arXiv:1707.07258 [hep-ph].

[47] D. Hooper and L. Goodenough, "Dark Matter Annihilation in The Galactic Center As Seen by the Fermi Gamma Ray Space Telescope," *Phys. Lett. B* **697** (2011) 412–428, arXiv:1010.2752 [hep-ph].

[48] **PAMELA** Collaboration, O. Adriani *et al.*, "An anomalous positron abundance in cosmic rays with energies 1.5-100 GeV," *Nature* **458** (2009) 607–609, arXiv:0810.4995 [astro-ph].

[49] A. Cuoco, M. Krämer, and M. Korsmeier, "Novel Dark Matter Constraints from Antiprotons in Light of AMS-02," *Phys. Rev. Lett.* **118** no. 19, (2017) 191102, arXiv:1610.03071 [astro-ph.HE].

[50] S. Murgia, "The Fermi–LAT Galactic Center Excess: Evidence of Annihilating Dark Matter?," *Ann. Rev. Nucl. Part. Sci.* **70** (2020) 455–483.

[51] J. Heisig, M. Korsmeier, and M. W. Winkler, "Dark matter or correlated errors: Systematics of the AMS-02 antiproton excess," *Phys. Rev. Res.* **2** no. 4, (2020) 043017, arXiv:2005.04237 [astro-ph.HE].

[52] S. Balan, F. Kahlhoefer, M. Korsmeier, S. Manconi, and K. Nippel, "Fast and accurate AMS-02 antiproton likelihoods for global dark matter fits," *JCAP* **08** (2023) 052, arXiv:2303.07362 [hep-ph].

[53] I. Cholis, T. Linden, and D. Hooper, "A Robust Excess in the Cosmic-Ray Antiproton Spectrum: Implications for Annihilating Dark Matter," *Phys. Rev. D* **99** no. 10, (2019) 103026, arXiv:1903.02549 [astro-ph.HE].

[54] A. McDaniel, M. Ajello, C. M. Karwin, M. Di Mauro, A. Drlica-Wagner, and M. A. Sánchez-Conde, "Legacy analysis of dark matter annihilation from the Milky Way dwarf spheroidal galaxies with 14 years of Fermi-LAT data," *Phys. Rev. D* **109** no. 6, (2024) 063024, arXiv:2311.04982 [astro-ph.HE].

[55] CMS Collaboration, "Summary plots from cms public results: Exo searches at $\sqrt{s} = 13$ tev." Presented at the 2024 Moriond Conference, CMS TWiki. https://twiki.cern.ch/twiki/bin/view/CMSPublic/SummaryPlotsEXO13TeV.

[56] **XENON** Collaboration, E. Aprile *et al.*, "First Indication of Solar B8 Neutrinos via Coherent Elastic Neutrino-Nucleus Scattering with XENONnT," *Phys. Rev. Lett.* **133** no. 19, (2024) 191002, arXiv:2408.02877 [nucl-ex].

[57] **XENON** Collaboration, E. Aprile *et al.*, "First Search for Light Dark Matter in the Neutrino Fog with XENONnT," *Phys. Rev. Lett.* **134** no. 11, (2025) 111802, arXiv:2409.17868 [hep-ex].

[58] **PANDA-X, PandaX** Collaboration, A. Abdukerim *et al.*, "PandaX-xT—A deep underground multi-ten-tonne liquid xenon observatory," *Sci. China Phys. Mech. Astron.* **68** no. 2, (2025) 221011, arXiv:2402.03596 [hep-ex].

[59] **XLZD** Collaboration, J. Aalbers *et al.*, "The XLZD Design Book: Towards the Next-Generation Liquid Xenon Observatory for Dark Matter and Neutrino Physics," arXiv:2410.17137 [hep-ex].

[60] **CTA Consortium** Collaboration, B. S. Acharya *et al.*, *Science with the Cherenkov Telescope Array*. WSP, 11, 2018. arXiv:1709.07997 [astro-ph.IM].

[61] L. J. Hall, K. Jedamzik, J. March-Russell, and S. M. West, "Freeze-In Production of FIMP Dark Matter," *JHEP* **03** (2010) 080, arXiv:0911.1120 [hep-ph].

[62] K. M. Zurek, "Multi-Component Dark Matter," *Phys. Rev. D* **79** (2009) 115002, arXiv:0811.4429 [hep-ph].

[63] K. Petraki and R. R. Volkas, "Review of asymmetric dark matter," *Int. J. Mod. Phys. A* **28** (2013) 1330028, arXiv:1305.4939 [hep-ph].

[64] M. Pospelov, A. Ritz, and M. B. Voloshin, "Secluded WIMP Dark Matter," *Phys. Lett. B* **662** (2008) 53–61, arXiv:0711.4866 [hep-ph].

[65] J. Edsjo and P. Gondolo, "Neutralino relic density including coannihilations," *Phys. Rev. D* **56** (1997) 1879–1894, arXiv:hep-ph/9704361.

[66] D. Tucker-Smith and N. Weiner, "Inelastic dark matter," *Phys. Rev. D* **64** (2001) 043502, arXiv:hep-ph/0101138.

[67] P. Asadi, T. R. Slatyer, and J. Smirnov, "WIMPs without weakness: Generalized mass window with entropy injection," *Phys. Rev. D* **106** no. 1, (2022) 015012, arXiv:2111.11444 [hep-ph].

[68] S. Hamdan and J. Unwin, "Dark Matter Freeze-out During Matter Domination," *Mod. Phys. Lett. A* **33** no. 29, (2018) 1850181, arXiv:1710.03758 [hep-ph].

[69] H. Davoudiasl, D. Hooper, and S. D. McDermott, "Inflatable Dark Matter," *Phys. Rev. Lett.* **116** no. 3, (2016) 031303, arXiv:1507.08660 [hep-ph].

[70] **GAMBIT** Collaboration, P. Athron *et al.*, "GAMBIT: The Global and Modular Beyond-the-Standard-Model Inference Tool," *Eur. Phys. J. C* **77** no. 11, (2017) 784, arXiv:1705.07908 [hep-ph]. [Addendum: Eur.Phys.J.C 78, 98 (2018)].

[71] I. Baldes and R. Jinno, "Acoustically driven dark matter freeze-out," arXiv:2506.11884 [hep-ph].

[72] S. Dodelson, *Modern Cosmology*. Academic Press, Amsterdam, 2003.

[73] P. Gondolo and G. Gelmini, "Cosmic abundances of stable particles: Improved analysis," *Nucl. Phys. B* **360** (1991) 145–179.

[74] M. Drees, F. Hajkarim, and E. R. Schmitz, "The Effects of QCD Equation of State on the Relic Density of WIMP Dark Matter," *JCAP* **06** (2015) 025, arXiv:1503.03513 [hep-ph].

[75] T. Bringmann, J. Edsjö, P. Gondolo, P. Ullio, and L. Bergström, "DarkSUSY 6 : An Advanced Tool to Compute Dark Matter Properties Numerically," *JCAP* **07** (2018) 033, arXiv:1802.03399 [hep-ph].

[76] G. Alguero, G. Belanger, F. Boudjema, S. Chakraborti, A. Goudelis, S. Kraml, A. Mjallal, and A. Pukhov, "micrOMEGAs 6.0: N-component dark matter," *Comput. Phys. Commun.* **299** (2024) 109133, arXiv:2312.14894 [hep-ph].

[77] R. A. Alpher, H. Bethe, and G. Gamow, "The origin of chemical elements," *Phys. Rev.* **73** (1948) 803–804.

[78] A.-K. Burns, T. M. P. Tait, and M. Valli, "PRyMordial: the first three minutes, within and beyond the standard model," *Eur. Phys. J. C* **84** no. 1, (2024) 86, arXiv:2307.07061 [hep-ph].

[79] C. Giovanetti, M. Lisanti, H. Liu, S. Mishra-Sharma, and J. T. Ruderman, "LINX: A Fast, Differentiable, and Extensible Big Bang Nucleosynthesis Package," arXiv:2408.14538 [astro-ph.CO].

[80] C. Pitrou, A. Coc, J.-P. Uzan, and E. Vangioni, "Precision big bang nucleosynthesis with improved Helium-4 predictions," *Phys. Rept.* **754** (2018) 1–66, arXiv:1801.08023 [astro-ph.CO].

[81] T. Chowdhury and S. Ipek, "Neutron lifetime anomaly and Big Bang nucleosynthesis," *Can. J. Phys.* **102** no. 2, (2024) 96–99, arXiv:2210.12031 [hep-ph].

[82] J. Froustey, C. Pitrou, and M. C. Volpe, "Neutrino decoupling including flavour oscillations and primordial nucleosynthesis," *JCAP* **12** (2020) 015, arXiv:2008.01074 [hep-ph].

[83] J. J. Bennett, G. Buldgen, P. F. De Salas, M. Drewes, S. Gariazzo, S. Pastor, and Y. Y. Y. Wong, "Towards a precision calculation of $N_{\rm eff}$ in the Standard Model II: Neutrino decoupling in the presence of flavour oscillations and finite-temperature QED," *JCAP* **04** (2021) 073, arXiv:2012.02726 [hep-ph].

[84] M. Drewes, Y. Georis, M. Klasen, L. P. Wiggering, and Y. Y. Y. Wong, "Towards a precision calculation of N $_{eff}$ in the Standard Model. Part III. Improved estimate of NLO contributions to the collision integral," *JCAP* **06** (2024) 032, arXiv:2402.18481 [hep-ph].

[85] M. Escudero, "Neutrino decoupling beyond the Standard Model: CMB constraints on the Dark Matter mass with a fast and precise $N_{\rm eff}$ evaluation," *JCAP* **02** (2019) 007, arXiv:1812.05605 [hep-ph].

[86] M. Escudero Abenza, "Precision early universe thermodynamics made simple: $N_{\rm eff}$ and neutrino decoupling in the Standard Model and beyond," *JCAP* **05** (2020) 048, arXiv:2001.04466 [hep-ph].

[87] S. Gariazzo, P. F. de Salas, O. Pisanti, and R. Consiglio, "PArthENoPE revolutions," *Computer Physics Communications* **271** (Feb., 2022) 108205, arXiv:2103.05027 [astro-ph.IM].

[88] Y. Xu, K. Takahashi, S. Goriely, M. Arnould, M. Ohta, and H. Utsunomiya, "NACRE II: an update of the NACRE compilation of charged-particle-induced thermonuclear reaction rates for nuclei with mass number $A < 16$," *Nucl. Phys. A* **918** (2013) 61–169, arXiv:1310.7099 [nucl-th].

[89] T.-H. Yeh, K. A. Olive, and B. D. Fields, "The impact of new $d(p,\gamma)3$ rates on Big Bang Nucleosynthesis," *JCAP* **03** (2021) 046, arXiv:2011.13874 [astro-ph.CO].

[90] O. Pisanti, G. Mangano, G. Miele, and P. Mazzella, "Primordial Deuterium after LUNA: concordances and error budget," *JCAP* **04** (2021) 020, arXiv:2011.11537 [astro-ph.CO].

[91] C. Pitrou, A. Coc, J.-P. Uzan, and E. Vangioni, "A new tension in the cosmological model from primordial deuterium?," *Mon. Not. Roy. Astron. Soc.* **502** no. 2, (2021) 2474–2481, arXiv:2011.11320 [astro-ph.CO].

[92] V. Mossa *et al.*, "The baryon density of the Universe from an improved rate of deuterium burning," *Nature* **587** no. 7833, (2020) 210–213.

[93] **Particle Data Group** Collaboration, S. Navas *et al.*, "Review of particle physics," *Phys. Rev. D* **110** no. 3, (2024) 030001.

[94] P. F. Depta, M. Hufnagel, K. Schmidt-Hoberg, and S. Wild, "BBN constraints on the annihilation of MeV-scale dark matter," *JCAP* **04** (2019) 029, arXiv:1901.06944 [hep-ph].

[95] N. Sabti, J. Alvey, M. Escudero, M. Fairbairn, and D. Blas, "Refined Bounds on MeV-scale Thermal Dark Sectors from BBN and the CMB," *JCAP* **01** (2020) 004, arXiv:1910.01649 [hep-ph].

[96] C. Giovanetti, M. Lisanti, H. Liu, and J. T. Ruderman, "Joint Cosmic Microwave Background and Big Bang Nucleosynthesis Constraints on Light Dark Sectors with Dark Radiation," *Phys. Rev. Lett.* **129** no. 2, (2022) 021302, arXiv:2109.03246 [hep-ph].

[97] B. D. Fields, K. A. Olive, T.-H. Yeh, and C. Young, "Big-Bang Nucleosynthesis after Planck," *JCAP* **03** (2020) 010, arXiv:1912.01132 [astro-ph.CO]. [Erratum: JCAP 11, E02 (2020)].

[98] M. Hufnagel, K. Schmidt-Hoberg, and S. Wild, "BBN constraints on MeV-scale dark sectors. Part I. Sterile decays," *JCAP* **02** (2018) 044, arXiv:1712.03972 [hep-ph].

[99] M. Hufnagel, K. Schmidt-Hoberg, and S. Wild, "BBN constraints on MeV-scale dark sectors. Part II. Electromagnetic decays," *JCAP* **11** (2018) 032, arXiv:1808.09324 [hep-ph].

[100] T.-H. Yeh, K. A. Olive, and B. D. Fields, "Limits on non-relativistic matter during Big-bang nucleosynthesis," *JCAP* **07** (2024) 016, arXiv:2401.08795 [astro-ph.CO].

[101] K. Akita, G. Baur, M. Ovchynnikov, T. Schwetz, and V. Syvolap, "Dynamics of metastable standard model particles from long-lived particle decays in the MeV primordial plasma," *Phys. Rev. D* **111** no. 6, (2025) 063542, arXiv:2411.00931 [hep-ph].

[102] A. Boyarsky, M. Ovchynnikov, N. Sabti, and V. Syvolap, "When feebly interacting massive particles decay into neutrinos: The Neff story," *Phys. Rev. D* **104** no. 3, (2021) 035006, arXiv:2103.09831 [hep-ph].

[103] M. Kawasaki, K. Kohri, T. Moroi, and Y. Takaesu, "Revisiting Big-Bang Nucleosynthesis Constraints on Long-Lived Decaying Particles," *Phys. Rev. D* **97** no. 2, (2018) 023502, arXiv:1709.01211 [hep-ph].

[104] A. Boyarsky, M. Ovchynnikov, O. Ruchayskiy, and V. Syvolap, "Improved big bang nucleosynthesis constraints on heavy neutral leptons," *Phys. Rev. D* **104** no. 2, (2021) 023517, arXiv:2008.00749 [hep-ph].

[105] T. Hasegawa, N. Hiroshima, K. Kohri, R. S. L. Hansen, T. Tram, and S. Hannestad, "MeV-scale reheating temperature and thermalization of oscillating neutrinos by radiative and hadronic decays of massive particles," *JCAP* **12** (2019) 012, arXiv:1908.10189 [hep-ph].

[106] N. Barbieri, T. Brinckmann, S. Gariazzo, M. Lattanzi, S. Pastor, and O. Pisanti, "Current constraints on cosmological scenarios with very low reheating temperatures," arXiv:2501.01369 [astro-ph.CO].

[107] M. Kawasaki and T. Moroi, "Electromagnetic cascade in the early universe and its application to the big bang nucleosynthesis," *Astrophys. J.* **452** (1995) 506, arXiv:astro-ph/9412055.

[108] P. F. Depta, M. Hufnagel, and K. Schmidt-Hoberg, "ACROPOLIS: A generiC fRamework fOr Photodisintegration Of LIght elementS," *JCAP* **03** (2021) 061, arXiv:2011.06518 [hep-ph].

[109] M. Kawasaki, K. Kohri, and T. Moroi, "Big-Bang nucleosynthesis and hadronic decay of long-lived massive particles," *Phys. Rev. D* **71** (2005) 083502, arXiv:astro-ph/0408426.

[110] S. Bianco, P. F. Depta, J. Frerick, T. Hambye, M. Hufnagel, and K. Schmidt-Hoberg, "Photo- and Hadrodisintegration constraints on massive relics decaying into neutrinos," arXiv:2505.01492 [hep-ph].

[111] R. Allahverdi *et al.*, "The First Three Seconds: a Review of Possible Expansion Histories of the Early Universe," *Open J. Astrophys.* **4** (2021) astro.2006.16182, arXiv:2006.16182 [astro-ph.CO].

[112] D. S. Gorbunov and V. A. Rubakov, *Introduction to the theory of the early universe: Cosmological perturbations and inflationary theory.* 2011.

[113] N. Lee and Y. Ali-Haïmoud, "HYREC-2: a highly accurate sub-millisecond recombination code," *Phys. Rev. D* **102** no. 8, (2020) 083517, arXiv:2007.14114 [astro-ph.CO].

[114] A. Lewis, A. Challinor, and A. Lasenby, "Efficient computation of CMB anisotropies in closed FRW models," *Astrophys. J.* **538** (2000) 473–476, arXiv:astro-ph/9911177.

[115] J. Lesgourgues, "The Cosmic Linear Anisotropy Solving System (CLASS) I: Overview," arXiv:1104.2932 [astro-ph.IM].

[116] D. J. Fixsen, E. S. Cheng, J. M. Gales, J. C. Mather, R. A. Shafer, and E. L. Wright, "The Cosmic Microwave Background spectrum from the full COBE FIRAS data set," *Astrophys. J.* **473** (1996) 576, arXiv:astro-ph/9605054.

[117] A. Kogut *et al.*, "The Primordial Inflation Explorer (PIXIE): mission design and science goals," *JCAP* **04** (2025) 020, arXiv:2405.20403 [astro-ph.CO].

[118] T. R. Slatyer, "Indirect Dark Matter Signatures in the Cosmic Dark Ages II. Ionization, Heating and Photon Production from Arbitrary Energy Injections," *Phys. Rev. D* **93** no. 2, (2016) 023521, arXiv:1506.03812 [astro-ph.CO].

[119] **CMB-S4** Collaboration, K. Abazajian *et al.*, "Snowmass 2021 CMB-S4 White Paper," arXiv:2203.08024 [astro-ph.CO].

[120] R. Bartels, D. Gaggero, and C. Weniger, "Prospects for indirect dark matter searches with MeV photons," *JCAP* **05** (2017) 001, arXiv:1703.02546 [astro-ph.HE].

[121] R. Essig, E. Kuflik, S. D. McDermott, T. Volansky, and K. M. Zurek, "Constraining Light Dark Matter with Diffuse X-Ray and Gamma-Ray Observations," *JHEP* **11** (2013) 193, arXiv:1309.4091 [hep-ph].

[122] K. E. O'Donnell and T. R. Slatyer, "Constraints on dark matter with future MeV gamma-ray telescopes," *Phys. Rev. D* **111** no. 8, (2025) 083037, arXiv:2411.00087 [hep-ph].

[123] M. Boudaud, J. Lavalle, and P. Salati, "Novel cosmic-ray electron and positron constraints on MeV dark matter particles," *Phys. Rev. Lett.* **119** no. 2, (2017) 021103, arXiv:1612.07698 [astro-ph.HE].

[124] M. Cirelli, N. Fornengo, J. Koechler, E. Pinetti, and B. M. Roach, "Putting all the X in one basket: Updated X-ray constraints on sub-GeV Dark Matter," *JCAP* **07** (2023) 026, arXiv:2303.08854 [hep-ph].

[125] P. De la Torre Luque, S. Balaji, M. Fairbairn, F. Sala, and J. Silk, "511 keV Galactic Photons from a Dark Matter Spike," arXiv:2410.16379 [astro-ph.HE].

[126] T. Siegert, "The Positron Puzzle," 3, 2023. arXiv:2303.15582 [astro-ph.HE].

[127] P. De la Torre Luque, S. Balaji, and J. Silk, "New 511 keV Line Data Provide Strongest sub-GeV Dark Matter Constraints," *Astrophys. J. Lett.* **973** no. 1, (2024) L6, arXiv:2312.04907 [hep-ph].

[128] M. Cirelli, A. Strumia, and J. Zupan, "Dark Matter," arXiv:2406.01705 [hep-ph].

[129] T. R. Slatyer, "Indirect dark matter signatures in the cosmic dark ages. I. Generalizing the bound on s-wave dark matter annihilation from Planck results," *Phys. Rev. D* **93** no. 2, (2016) 023527, arXiv:1506.03811 [hep-ph].

[130] T. R. Slatyer and C.-L. Wu, "General Constraints on Dark Matter Decay from the Cosmic Microwave Background," *Phys. Rev. D* **95** no. 2, (2017) 023010, arXiv:1610.06933 [astro-ph.CO].

[131] E. O. Nadler, D. Kong, D. Yang, and H.-B. Yu, "SIDM Concerto: Compilation and Data Release of Self-interacting Dark Matter Zoom-in Simulations," arXiv:2503.10748 [astro-ph.CO].

[132] Z. C. Zeng, A. H. G. Peter, X. Du, A. Benson, S. Kim, F. Jiang, F.-Y. Cyr-Racine, and M. Vogelsberger, "Core-collapse, evaporation, and tidal effects: the life story of a self-interacting dark matter subhalo," *Mon. Not. Roy. Astron. Soc.* **513** no. 4, (2022) 4845–4868, arXiv:2110.00259 [astro-ph.CO].

[133] G. Despali, L. G. Walls, S. Vegetti, M. Sparre, M. Vogelsberger, and J. Zavala, "Constraining SIDM with halo shapes: Revisited predictions from realistic simulations of early-type galaxies," *Mon. Not. Roy. Astron. Soc.* **516** no. 3, (2022) 4543–4559, arXiv:2204.12502 [astro-ph.CO].

[134] A. Robertson, E. Huff, and K. Markovic, "Why weak lensing cluster shapes are insensitive to self-interacting dark matter," *Mon. Not. Roy. Astron. Soc.* **521** no. 2, (2023) 3172–3185, arXiv:2210.13474 [astro-ph.CO].

[135] V. M. Sabarish, M. Brüggen, K. Schmidt-Hoberg, M. S. Fischer, and F. Kahlhoefer, "Simulations of galaxy cluster mergers with velocity-dependent, rare, and frequent self-interactions," *Mon. Not. Roy. Astron. Soc.* **529** no. 3, (2024) 2032–2046, arXiv:2310.07769 [astro-ph.CO].

[136] E. L. Sirks, D. Harvey, R. Massey, K. A. Oman, A. Robertson, C. Frenk, S. Everett, A. S. Gill, D. Lagattuta, and J. McCleary, "Hydrodynamical simulations of merging galaxy clusters: giant dark matter particle colliders, powered by gravity," *Mon. Not. Roy. Astron. Soc.* **530** no. 3, (2024) 3160–3170, arXiv:2405.00140 [astro-ph.CO].

[137] E. O. Nadler, R. An, D. Yang, H.-B. Yu, A. Benson, and V. Gluscevic, "COZMIC. III. Cosmological Zoom-in Simulations of Self-interacting Dark Matter with Suppressed Initial Conditions," *Astrophys. J.* **986** (2025) 129, arXiv:2412.13065 [astro-ph.CO].

[138] G. Alonso-Álvarez, J. M. Cline, and C. Dewar, "Self-Interacting Dark Matter Solves the Final Parsec Problem of Supermassive Black Hole Mergers," *Phys. Rev. Lett.* **133** no. 2, (2024) 021401, arXiv:2401.14450 [astro-ph.CO].

[139] V. M. Sabarish, M. Brüggen, K. Schmidt-Hoberg, and M. S. Fischer, "Accretion of self-interacting dark matter onto supermassive black holes," arXiv:2505.14779 [astro-ph.CO].

[140] M. G. Roberts, L. Braff, A. Garg, S. Profumo, and T. Jeltema, "Little Red Dots from Ultra-Strongly Self-Interacting Dark Matter," *arXiv e-prints* (July, 2025) arXiv:2507.03230, arXiv:2507.03230 [astro-ph.GA].

[141] C. A. Correa, "Constraining velocity-dependent self-interacting dark matter with the Milky Way's dwarf spheroidal galaxies," *MNRAS* **503** no. 1, (May, 2021) 920–937, arXiv:2007.02958 [astro-ph.GA].

[142] L. Sagunski, S. Gad-Nasr, B. Colquhoun, A. Robertson, and S. Tulin, "Velocity-dependent Self-interacting Dark Matter from Groups and Clusters of Galaxies," *JCAP* **01** (2021) 024, arXiv:2006.12515 [astro-ph.CO].

[143] S. Y. Kim, A. H. G. Peter, and D. Wittman, "In the Wake of Dark Giants: New Signatures of Dark Matter Self Interactions in Equal Mass Mergers of Galaxy Clusters," *Mon. Not. Roy. Astron. Soc.* **469** no. 2, (2017) 1414–1444, arXiv:1608.08630 [astro-ph.CO].

[144] M. S. Fischer, N.-H. Durke, K. Hollingshausen, C. Hammer, M. Brüggen, and K. Dolag, "The role of baryons in self-interacting dark matter mergers," *Mon. Not. Roy. Astron. Soc.* **523** no. 4, (2023) 5915–5933, arXiv:2302.07882 [astro-ph.CO].

[145] D. Harvey, R. Massey, T. Kitching, A. Taylor, and E. Tittley, "The non-gravitational interactions of dark matter in colliding galaxy clusters," *Science* **347** (2015) 1462–1465, arXiv:1503.07675 [astro-ph.CO].

[146] D. Wittman, N. Golovich, and W. A. Dawson, "The Mismeasure of Mergers: Revised Limits on Self-interacting Dark Matter in Merging Galaxy Clusters," *Astrophys. J.* **869** no. 2, (2018) 104, arXiv:1701.05877 [astro-ph.CO].

[147] M. Markevitch, A. H. Gonzalez, L. David, A. Vikhlinin, S. Murray, W. Forman, C. Jones, and W. Tucker, "A Textbook example of a bow shock in the merging galaxy cluster 1E0657-56," *Astrophys. J. Lett.* **567** (2002) L27, arXiv:astro-ph/0110468.

[148] M. Bradac, D. Clowe, A. H. Gonzalez, P. Marshall, W. Forman, C. Jones, M. Markevitch, S. Randall, T. Schrabback, and D. Zaritsky, "Strong and weak lensing united. 3. Measuring the mass distribution of the merging galaxy cluster 1E0657-56," *Astrophys. J.* **652** (2006) 937–947, arXiv:astro-ph/0608408.

[149] M. Markevitch, A. H. Gonzalez, D. Clowe, A. Vikhlinin, L. David, W. Forman, C. Jones, S. Murray, and W. Tucker, "Direct constraints on the dark matter self-interaction cross-section from the merging galaxy cluster 1E0657-56," *Astrophys. J.* **606** (2004) 819–824, arXiv:astro-ph/0309303.

[150] S. W. Randall, M. Markevitch, D. Clowe, A. H. Gonzalez, and M. Bradac, "Constraints on the Self-Interaction Cross-Section of Dark Matter from Numerical Simulations of the Merging Galaxy Cluster 1E 0657-56," *Astrophys. J.* **679** (2008) 1173–1180, arXiv:0704.0261 [astro-ph].

[151] A. Robertson, R. Massey, and V. Eke, "What does the Bullet Cluster tell us about self-interacting dark matter?," *Mon. Not. Roy. Astron. Soc.* **465** no. 1, (2017) 569–587, arXiv:1605.04307 [astro-ph.CO].

[152] J. G. Holland, H. Böhringer, G. Chon, and D. Pierini, "Optical and X-ray profiles in the REXCESS sample of galaxy clusters," *Mon. Not. Roy. Astron. Soc.* **448** no. 3, (2015) 2644–2664, arXiv:1501.04286 [astro-ph.GA].

[153] P. Popesso, A. Biviano, H. Bohringer, and M. Romaniello, "RASS-SDSS Galaxy Cluster Survey. 7. On the Cluster Mass to Light ratio and the Halo Occupation Distribution," *Astron. Astrophys.* **464** (2007) 451, arXiv:astro-ph/0606260.

[154] R. N. Proctor, C. Mendes de Oliveira, L. Azanha, R. Dupke, and R. Overzier, "A derivation of masses and total luminosities of galaxy groups and clusters in the maxBCG catalogue," *Mon. Not. Roy. Astron. Soc.* **449** no. 3, (2015) 2345–2352, arXiv:1503.00975 [astro-ph.CO].

[155] E. Tempel, T. Tuvikene, R. Kipper, and N. I. Libeskind, "Merging groups and clusters of galaxies from the SDSS data. The catalogue of groups and potentially merging systems," *Astron. Astrophys.* **602** (2017) A100, arXiv:1704.04477 [astro-ph.CO].

[156] F. Kahlhoefer, K. Schmidt-Hoberg, M. T. Frandsen, and S. Sarkar, "Colliding clusters and dark matter self-interactions," *Mon. Not. Roy. Astron. Soc.* **437** no. 3, (2014) 2865–2881, arXiv:1308.3419 [astro-ph.CO].

[157] S. Balan *et al.*, "Resonant or asymmetric: the status of sub-GeV dark matter," *JCAP* **01** (2025) 053, arXiv:2405.17548 [hep-ph].

[158] P. Bechtle *et al.*, "How alive is constrained SUSY really?," *Nucl. Part. Phys. Proc.* **273-275** (2016) 589–594, arXiv:1410.6035 [hep-ph].

[159] **GAMBIT** Collaboration, P. Athron *et al.*, "Status of the scalar singlet dark matter model," *Eur. Phys. J. C* **77** no. 8, (2017) 568, arXiv:1705.07931 [hep-ph].

[160] A. Caputo, A. J. Millar, C. A. J. O'Hare, and E. Vitagliano, "Dark photon limits: A handbook," *Phys. Rev. D* **104** no. 9, (2021) 095029, arXiv:2105.04565 [hep-ph].

[161] A. Boyarsky, M. Drewes, T. Lasserre, S. Mertens, and O. Ruchayskiy, "Sterile neutrino Dark Matter," *Prog. Part. Nucl. Phys.* **104** (2019) 1–45, arXiv:1807.07938 [hep-ph].

[162] G. Arcadi, A. Djouadi, and M. Raidal, "Dark Matter through the Higgs portal," *Phys. Rept.* **842** (2020) 1–180, arXiv:1903.03616 [hep-ph].

[163] C. Chang, P. Scott, T. E. Gonzalo, F. Kahlhoefer, A. Kvellestad, and M. White, "Global fits of simplified models for dark matter with GAMBIT: I. Scalar and fermionic models with s-channel vector mediators," *Eur. Phys. J. C* **83** no. 3, (2023) 249, arXiv:2209.13266 [hep-ph].

[164] C. Chang, P. Scott, T. E. Gonzalo, F. Kahlhoefer, and M. White, "Global fits of simplified models for dark matter with GAMBIT: II. Vector dark matter with an s-channel vector mediator," *Eur. Phys. J. C* **83** no. 8, (2023) 692, arXiv:2303.08351 [hep-ph]. [Erratum: Eur.Phys.J.C 83, 768 (2023)].

[165] M. Blennow, E. Fernandez-Martinez, A. Olivares-Del Campo, S. Pascoli, S. Rosauro-Alcaraz, and A. V. Titov, "Neutrino Portals to Dark Matter," *Eur. Phys. J. C* **79** no. 7, (2019) 555, arXiv:1903.00006 [hep-ph].

[166] E. Bernreuther, S. Heeba, and F. Kahlhoefer, "Resonant sub-GeV Dirac dark matter," *JCAP* **03** (2021) 040, arXiv:2010.14522 [hep-ph].

[167] N. Brahma, S. Heeba, and K. Schutz, "Resonant pseudo-Dirac dark matter as a sub-GeV thermal target," *Phys. Rev. D* **109** no. 3, (2024) 035006, arXiv:2308.01960 [hep-ph].

[168] B. Holdom, "Two U(1)'s and Epsilon Charge Shifts," *Phys. Lett. B* **166** (1986) 196–198.

[169] R. Barkana, N. J. Outmezguine, D. Redigolo, and T. Volansky, "Strong constraints on light dark matter interpretation of the EDGES signal," *Phys. Rev. D* **98** no. 10, (2018) 103005, arXiv:1803.03091 [hep-ph].

[170] W. L. Xu, C. Dvorkin, and A. Chael, "Probing sub-GeV Dark Matter-Baryon Scattering with Cosmological Observables," *Phys. Rev. D* **97** no. 10, (2018) 103530, arXiv:1802.06788 [astro-ph.CO].

[171] E. C. G. Stueckelberg, "Interaction forces in electrodynamics and in the field theory of nuclear forces," *Helv. Phys. Acta* **11** (1938) 299–328.

[172] T. Binder, T. Bringmann, M. Gustafsson, and A. Hryczuk, "Early kinetic decoupling of dark matter: when the standard way of calculating the thermal relic density fails," *Phys. Rev. D* **96** no. 11, (2017) 115010, arXiv:1706.07433 [astro-ph.CO]. [Erratum: Phys.Rev.D 101, 099901 (2020)].

[173] A. Arbey, J. Auffinger, K. P. Hickerson, and E. S. Jenssen, "AlterBBN v2: A public code for calculating Big-Bang nucleosynthesis constraints in alternative cosmologies," *Comput. Phys. Commun.* **248** (2020) 106982, arXiv:1806.11095 [astro-ph.CO].

[174] **GAMBIT Cosmology Workgroup** Collaboration, J. J. Renk *et al.*, "CosmoBit: A GAMBIT module for computing cosmological observables and likelihoods," *JCAP* **02** (2021) 022, arXiv:2009.03286 [astro-ph.CO].

[175] C. Balázs *et al.*, "Cosmological constraints on decaying axion-like particles: a global analysis," *JCAP* **12** (2022) 027, arXiv:2205.13549 [astro-ph.CO].

[176] P. Stöcker, M. Krämer, J. Lesgourgues, and V. Poulin, "Exotic energy injection with ExoCLASS: Application to the Higgs portal model and evaporating black holes," *JCAP* **03** (2018) 018, arXiv:1801.01871 [astro-ph.CO].

[177] A. Coogan, L. Morrison, and S. Profumo, "Hazma: A Python Toolkit for Studying Indirect Detection of Sub-GeV Dark Matter," *JCAP* **01** (2020) 056, arXiv:1907.11846 [hep-ph].

[178] A. Coogan, L. Morrison, T. Plehn, S. Profumo, and P. Reimitz, "Hazma meets HERWIG4DM: precision gamma-ray, neutrino, and positron spectra for light dark matter," *JCAP* **11** (2022) 033, arXiv:2207.07634 [hep-ph].

[179] **GAMBIT** Collaboration, P. Athron *et al.*, "Thermal WIMPs and the scale of new physics: global fits of Dirac dark matter effective field theories," *Eur. Phys. J. C* **81** no. 11, (2021) 992, arXiv:2106.02056 [hep-ph].

[180] **LSND** Collaboration, L. B. Auerbach *et al.*, "Measurement of electron - neutrino - electron elastic scattering," *Phys. Rev. D* **63** (2001) 112001, arXiv:hep-ex/0101039.

[181] P. deNiverville, M. Pospelov, and A. Ritz, "Observing a light dark matter beam with neutrino experiments," *Phys. Rev. D* **84** (2011) 075020, arXiv:1107.4580 [hep-ph].

[182] **MiniBooNE DM** Collaboration, A. A. Aguilar-Arevalo *et al.*, "Dark Matter Search in Nucleon, Pion, and Electron Channels from a Proton Beam Dump with MiniBooNE," *Phys. Rev. D* **98** no. 11, (2018) 112004, arXiv:1807.06137 [hep-ex].

[183] **NA64** Collaboration, Y. M. Andreev *et al.*, "Search for Light Dark Matter with NA64 at CERN," *Phys. Rev. Lett.* **131** no. 16, (2023) 161801, arXiv:2307.02404 [hep-ex].

[184] **BaBar** Collaboration, J. P. Lees *et al.*, "Search for Invisible Decays of a Dark Photon Produced in e^+e^- Collisions at BaBar," *Phys. Rev. Lett.* **119** no. 13, (2017) 131804, arXiv:1702.03327 [hep-ex].

[185] T. Åkesson *et al.*, "Current Status and Future Prospects for the Light Dark Matter eXperiment," in *Snowmass 2021*. 3, 2022. arXiv:2203.08192 [hep-ex].

[186] **XENON** Collaboration, E. Aprile *et al.*, "Light Dark Matter Search with Ionization Signals in XENON1T," *Phys. Rev. Lett.* **123** no. 25, (2019) 251801, arXiv:1907.11485 [hep-ex].

[187] **SENSEI** Collaboration, L. Barak *et al.*, "SENSEI: Direct-Detection Results on sub-GeV Dark Matter from a New Skipper-CCD," *Phys. Rev. Lett.* **125** no. 17, (2020) 171802, arXiv:2004.11378 [astro-ph.CO].

[188] **DarkSide** Collaboration, P. Agnes *et al.*, "Search for Dark Matter Particle Interactions with Electron Final States with DarkSide-50," *Phys. Rev. Lett.* **130** no. 10, (2023) 101002, arXiv:2207.11968 [hep-ex].

[189] **PandaX** Collaboration, D. Huang *et al.*, "Search for Dark-Matter–Nucleon Interactions with a Dark Mediator in PandaX-4T," *Phys. Rev. Lett.* **131** no. 19, (2023) 191002, arXiv:2308.01540 [hep-ex].

[190] **DAMIC-M** Collaboration, I. Arnquist *et al.*, "First Constraints from DAMIC-M on Sub-GeV Dark-Matter Particles Interacting with Electrons," *Phys. Rev. Lett.* **130** no. 17, (2023) 171003, arXiv:2302.02372 [hep-ex].

[191] **SuperCDMS** Collaboration, D. W. Amaral *et al.*, "Constraints on low-mass, relic dark matter candidates from a surface-operated SuperCDMS single-charge sensitive detector," *Phys. Rev. D* **102** no. 9, (2020) 091101, arXiv:2005.14067 [hep-ex].

[192] **LZ** Collaboration, J. Aalbers *et al.*, "Search for new physics in low-energy electron recoils from the first LZ exposure," *Phys. Rev. D* **108** no. 7, (2023) 072006, arXiv:2307.15753 [hep-ex].

[193] T. Emken, "obscura: A modular c++ tool and library for the direct detection of (sub-gev) dark matter via nuclear and electron recoils," *Journal of Open Source Software* **6** no. 68, (2021) 3725. https://doi.org/10.21105/joss.03725.

[194] **CRESST** Collaboration, A. H. Abdelhameed *et al.*, "First results from the CRESST-III low-mass dark matter program," *Phys. Rev. D* **100** no. 10, (2019) 102002, arXiv:1904.00498 [astro-ph.CO].

[195] **GAMBIT** Collaboration, P. Athron *et al.*, "Global analyses of Higgs portal singlet dark matter models using GAMBIT," *Eur. Phys. J. C* **79** no. 1, (2019) 38, arXiv:1808.10465 [hep-ph].

[196] **GAMBIT** Collaboration, G. D. Martinez, J. McKay, B. Farmer, P. Scott, E. Roebber, A. Putze, and J. Conrad, "Comparison of statistical sampling methods with ScannerBit, the GAMBIT scanning module," *Eur. Phys. J. C* **77** no. 11, (2017) 761, arXiv:1705.07959 [hep-ph].

[197] P. Scott, "Pippi - painless parsing, post-processing and plotting of posterior and likelihood samples," *Eur. Phys. J. Plus* **127** (2012) 138, arXiv:1206.2245 [physics.data-an].

[198] W. J. Handley, M. P. Hobson, and A. N. Lasenby, "PolyChord: nested sampling for cosmology," *Mon. Not. Roy. Astron. Soc.* **450** no. 1, (2015) L61–L65, arXiv:1502.01856 [astro-ph.CO].

[199] W. Handley, "anesthetic: nested sampling visualisation," *The Journal of Open Source Software* **4** no. 37, (Jun, 2019) 1414. http://dx.doi.org/10.21105/joss.01414.

[200] S. Balan, C. Balazs, T. Bringmann, C. Cappiello, R. Catena, T. Emken, T. E. Gonzalo, T. R. Gray, W. Handley, Q. Huynh, F. Kahlhoefer, and A. C. Vincent, "Supplementary data for "resonant or asymmetric: The status of sub-gev dark matter"," May, 2024. https://doi.org/10.5281/zenodo.11232712.

[201] **LHCb** Collaboration, R. Aaij *et al.*, "Search for $A' \to \mu^+\mu^-$ Decays," *Phys. Rev. Lett.* **124** no. 4, (2020) 041801, arXiv:1910.06926 [hep-ex].

[202] **Belle-II** Collaboration, W. Altmannshofer *et al.*, "The Belle II Physics Book," *PTEP* **2019** no. 12, (2019) 123C01, arXiv:1808.10567 [hep-ex]. [Erratum: PTEP 2020, 029201 (2020)].

[203] **SuperCDMS** Collaboration, R. Agnese *et al.*, "Projected Sensitivity of the SuperCDMS SNOLAB experiment," *Phys. Rev. D* **95** no. 8, (2017) 082002, arXiv:1610.00006 [physics.ins-det].

[204] B. von Krosigk *et al.*, "DELight: A Direct search Experiment for Light dark matter with superfluid helium," *SciPost Phys. Proc.* **12** (2023) 016, arXiv:2209.10950 [hep-ex].

[205] R. Essig, M. Fernandez-Serra, J. Mardon, A. Soto, T. Volansky, and T.-T. Yu, "Direct Detection of sub-GeV Dark Matter with Semiconductor Targets," *JHEP* **05** (2016) 046, arXiv:1509.01598 [hep-ph].

[206] E. Izaguirre, G. Krnjaic, P. Schuster, and N. Toro, "Analyzing the Discovery Potential for Light Dark Matter," *Phys. Rev. Lett.* **115** no. 25, (2015) 251301, arXiv:1505.00011 [hep-ph].

[207] J. Alexander *et al.*, "Dark Sectors 2016 Workshop: Community Report," 8, 2016. arXiv:1608.08632 [hep-ph].

[208] A. Berlin, N. Blinov, G. Krnjaic, P. Schuster, and N. Toro, "Dark Matter, Millicharges, Axion and Scalar Particles, Gauge Bosons, and Other New Physics with LDMX," *Phys. Rev. D* **99** no. 7, (2019) 075001, arXiv:1807.01730 [hep-ph].

[209] J. Beacham *et al.*, "Physics Beyond Colliders at CERN: Beyond the Standard Model Working Group Report," *J. Phys. G* **47** no. 1, (2020) 010501, arXiv:1901.09966 [hep-ex].

[210] **DAMIC-M** Collaboration, K. Aggarwal *et al.*, "Probing Benchmark Models of Hidden-Sector Dark Matter with DAMIC-M," *Phys. Rev. Lett.* **135** no. 7, (2025) 071002, arXiv:2503.14617 [hep-ex].

[211] G. Krnjaic, "Testing Thermal-Relic Dark Matter with a Dark Photon Mediator," arXiv:2505.04626 [hep-ph].

[212] P. De la Torre Luque, S. Balaji, and J. Koechler, "Importance of Cosmic-Ray Propagation on Sub-GeV Dark Matter Constraints," *Astrophys. J.* **968** no. 1, (2024) 46, arXiv:2311.04979 [hep-ph].

[213] S. Balaji, D. Cleaver, P. De la Torre Luque, and M. Michailidis, "Dark Matter in X-rays: Revised XMM-Newton Limits and New Constraints from eROSITA," arXiv:2506.02310 [hep-ph].

[214] S. Balan, T. Bringmann, F. Kahlhoefer, J. Matuszak, and C. Tasillo, "Sub-GeV dark matter and nano-Hertz gravitational waves from a classically conformal dark sector," *JCAP* **08** (2025) 062, arXiv:2502.19478 [hep-ph].

[215] A. Kosowsky, M. S. Turner, and R. Watkins, "Gravitational waves from first order cosmological phase transitions," *Phys. Rev. Lett.* **69** (1992) 2026–2029.

[216] M. Kamionkowski, A. Kosowsky, and M. S. Turner, "Gravitational radiation from first order phase transitions," *Phys. Rev. D* **49** (1994) 2837–2851, arXiv:astro-ph/9310044.

[217] V. A. Kuzmin, V. A. Rubakov, and M. E. Shaposhnikov, "On the Anomalous Electroweak Baryon Number Nonconservation in the Early Universe," *Phys. Lett. B* **155** (1985) 36.

[218] W.-Z. Feng, P. Nath, and G. Peim, "Cosmic Coincidence and Asymmetric Dark Matter in a Stueckelberg Extension," *Phys. Rev. D* **85** (2012) 115016, arXiv:1204.5752 [hep-ph].

[219] D. Borah and J. M. Cline, "Inert Doublet Dark Matter with Strong Electroweak Phase Transition," *Phys. Rev. D* **86** (2012) 055001, arXiv:1204.4722 [hep-ph].

[220] G. Gil, P. Chankowski, and M. Krawczyk, "Inert Dark Matter and Strong Electroweak Phase Transition," *Phys. Lett. B* **717** (2012) 396–402, arXiv:1207.0084 [hep-ph].

[221] J. M. Cline and K. Kainulainen, "Electroweak baryogenesis and dark matter from a singlet Higgs," *JCAP* **01** (2013) 012, arXiv:1210.4196 [hep-ph].

[222] T. Alanne, K. Tuominen, and V. Vaskonen, "Strong phase transition, dark matter and vacuum stability from simple hidden sectors," *Nucl. Phys. B* **889** (2014) 692–711, arXiv:1407.0688 [hep-ph].

[223] M. Chala, G. Nardini, and I. Sobolev, "Unified explanation for dark matter and electroweak baryogenesis with direct detection and gravitational wave signatures," *Phys. Rev. D* **94** no. 5, (2016) 055006, arXiv:1605.08663 [hep-ph].

[224] P. Schwaller, "Gravitational Waves from a Dark Phase Transition," *Phys. Rev. Lett.* **115** no. 18, (2015) 181101, arXiv:1504.07263 [hep-ph].

[225] J. Jaeckel, V. V. Khoze, and M. Spannowsky, "Hearing the signal of dark sectors with gravitational wave detectors," *Phys. Rev. D* **94** no. 10, (2016) 103519, arXiv:1602.03901 [hep-ph].

[226] A. Addazi and A. Marciano, "Gravitational waves from dark first order phase transitions and dark photons," *Chin. Phys. C* **42** no. 2, (2018) 023107, arXiv:1703.03248 [hep-ph].

[227] M. Breitbach, J. Kopp, E. Madge, T. Opferkuch, and P. Schwaller, "Dark, Cold, and Noisy: Constraining Secluded Hidden Sectors with Gravitational Waves," *JCAP* **07** (2019) 007, arXiv:1811.11175 [hep-ph].

[228] D. Croon, V. Sanz, and G. White, "Model Discrimination in Gravitational Wave spectra from Dark Phase Transitions," *JHEP* **08** (2018) 203, arXiv:1806.02332 [hep-ph].

[229] T. Bringmann, T. E. Gonzalo, F. Kahlhoefer, J. Matuszak, and C. Tasillo, "Hunting WIMPs with LISA: correlating dark matter and gravitational wave signals," *JCAP* **05** (2024) 065, arXiv:2311.06346 [astro-ph.CO].

[230] T. Bringmann, P. F. Depta, T. Konstandin, K. Schmidt-Hoberg, and C. Tasillo, "Does NANOGrav observe a dark sector phase transition?," *JCAP* **11** (2023) 053, arXiv:2306.09411 [astro-ph.CO].

[231] **NANOGrav** Collaboration, G. Agazie *et al.*, "The NANOGrav 15 yr Data Set: Evidence for a Gravitational-wave Background," *Astrophys. J. Lett.* **951** no. 1, (2023) L8, arXiv:2306.16213 [astro-ph.HE].

[232] **NANOGrav** Collaboration, Z. Arzoumanian *et al.*, "The NANOGrav 12.5 yr Data Set: Search for an Isotropic Stochastic Gravitational-wave Background," *Astrophys. J. Lett.* **905** no. 2, (2020) L34, arXiv:2009.04496 [astro-ph.HE].

[233] **EPTA, InPTA:** Collaboration, J. Antoniadis *et al.*, "The second data release from the European Pulsar Timing Array - III. Search for gravitational wave signals," *Astron. Astrophys.* **678** (2023) A50, arXiv:2306.16214 [astro-ph.HE].

[234] H. Xu *et al.*, "Searching for the Nano-Hertz Stochastic Gravitational Wave Background with the Chinese Pulsar Timing Array Data Release I," *Res. Astron. Astrophys.* **23** no. 7, (2023) 075024, arXiv:2306.16216 [astro-ph.HE].

[235] D. J. Reardon *et al.*, "Search for an Isotropic Gravitational-wave Background with the Parkes Pulsar Timing Array," *Astrophys. J. Lett.* **951** no. 1, (2023) L6, arXiv:2306.16215 [astro-ph.HE].

[236] M. T. Miles *et al.*, "The MeerKAT Pulsar Timing Array: the first search for gravitational waves with the MeerKAT radio telescope," *Mon. Not. Roy. Astron. Soc.* **536** no. 2, (2024) 1489–1500, arXiv:2412.01153 [astro-ph.HE].

[237] J. Antoniadis *et al.*, "The International Pulsar Timing Array second data release: Search for an isotropic gravitational wave background," *Mon. Not. Roy. Astron. Soc.* **510** no. 4, (2022) 4873–4887, arXiv:2201.03980 [astro-ph.HE].

[238] **NANOGrav** Collaboration, A. Afzal *et al.*, "The NANOGrav 15 yr Data Set: Search for Signals from New Physics," *Astrophys. J. Lett.* **951** no. 1, (2023) L11, arXiv:2306.16219 [astro-ph.HE]. [Erratum: Astrophys.J.Lett. 971, L27 (2024), Erratum: Astrophys.J. 971, L27 (2024)].

[239] S. Vagnozzi, "Inflationary interpretation of the stochastic gravitational wave background signal detected by pulsar timing array experiments," *JHEAp* **39** (2023) 81–98, arXiv:2306.16912 [astro-ph.CO].

[240] A. Ashoorioon, K. Rezazadeh, and A. Rostami, "NANOGrav signal from the end of inflation and the LIGO mass and heavier primordial black holes," *Phys. Lett. B* **835** (2022) 137542, arXiv:2202.01131 [astro-ph.CO].

[241] J. Ellis, M. Lewicki, C. Lin, and V. Vaskonen, "Cosmic superstrings revisited in light of NANOGrav 15-year data," *Phys. Rev. D* **108** no. 10, (2023) 103511, arXiv:2306.17147 [astro-ph.CO].

[242] W. Buchmuller, V. Domcke, and K. Schmitz, "Metastable cosmic strings," *JCAP* **11** (2023) 020, arXiv:2307.04691 [hep-ph].

[243] S. Blasi, V. Brdar, and K. Schmitz, "Has NANOGrav found first evidence for cosmic strings?," *Phys. Rev. Lett.* **126** no. 4, (2021) 041305, arXiv:2009.06607 [astro-ph.CO].

[244] Y. Gouttenoire and E. Vitagliano, "Domain wall interpretation of the PTA signal confronting black hole overproduction," *Phys. Rev. D* **110** no. 6, (2024) L061306, arXiv:2306.17841 [gr-qc].

[245] N. Kitajima, J. Lee, K. Murai, F. Takahashi, and W. Yin, "Gravitational waves from domain wall collapse, and application to nanohertz signals with QCD-coupled axions," *Phys. Lett. B* **851** (2024) 138586, arXiv:2306.17146 [hep-ph].

[246] J. Gonçalves, D. Marfatia, A. P. Morais, and R. Pasechnik, "Supercooled phase transitions in conformal dark sectors explain NANOGrav data," arXiv:2501.11619 [hep-ph].

[247] F. Costa, J. Hoefken Zink, M. Lucente, S. Pascoli, and S. Rosauro-Alcaraz, "Supercooled dark scalar phase transitions explanation of NANOGrav data," *Phys. Lett. B* **868** (2025) 139634, arXiv:2501.15649 [hep-ph].

[248] J. Li and P. Nath, "Supercooled phase transitions: Why thermal history of hidden sector matters in analysis of pulsar timing array signals," *Phys. Rev. D* **111** no. 12, (2025) 123007, arXiv:2501.14986 [hep-ph].

[249] C. Han, K.-P. Xie, J. M. Yang, and M. Zhang, "Self-interacting dark matter implied by nano-Hertz gravitational waves," *Phys. Rev. D* **109** no. 11, (2024) 115025, arXiv:2306.16966 [hep-ph].

[250] S. Jiang, A. Yang, J. Ma, and F. P. Huang, "Implication of nano-Hertz stochastic gravitational wave on dynamical dark matter through a dark first-order phase transition," *Class. Quant. Grav.* **41** no. 6, (2024) 065009, arXiv:2306.17827 [hep-ph].

[251] D. Borah, S. Jyoti Das, and R. Samanta, "Imprint of inflationary gravitational waves and WIMP dark matter in pulsar timing array data," *JCAP* **03** (2024) 031, arXiv:2307.00537 [hep-ph].

[252] K. Fujikura, S. Girmohanta, Y. Nakai, and Z. Zhang, "Cold darkogenesis: Dark matter and baryon asymmetry in light of the PTA signal," *Phys. Lett. B* **858** (2024) 139045, arXiv:2406.12956 [hep-ph].

[253] A. Adhikary, D. Borah, S. Mahapatra, I. Saha, N. Sahu, and V. S. Thounaojam, "New realisation of light thermal dark matter with enhanced detection prospects," *JCAP* **12** (2024) 043, arXiv:2405.17564 [hep-ph].

[254] G. H. Xu and J. P. Ostriker, "Dynamics of massive black holes as a possible candidate of Galactic dark matter," *Astrophys. J.* **437** (1994) 184–193.

[255] **NANOGrav** Collaboration, G. Agazie *et al.*, "The NANOGrav 15 yr Data Set: Constraints on Supermassive Black Hole Binaries from the Gravitational-wave Background," *Astrophys. J. Lett.* **952** no. 2, (2023) L37, arXiv:2306.16220 [astro-ph.HE].

[256] D. Lynden-Bell and M. J. Rees, "On quasars, dust and the galactic centre," *MNRAS* **152** (Jan., 1971) 461.

[257] J. Kormendy and L. C. Ho, "Coevolution (Or Not) of Supermassive Black Holes and Host Galaxies," *Ann. Rev. Astron. Astrophys.* **51** (2013) 511–653, arXiv:1304.7762 [astro-ph.CO].

[258] M. C. Begelman, R. D. Blandford, and M. J. Rees, "Massive black hole binaries in active galactic nuclei," *Nature* **287** (1980) 307–309.

[259] Y.-C. Chen, H.-C. Hwang, Y. Shen, X. Liu, N. L. Zakamska, Q. Yang, and J. I. Li, "Varstrometry for Off-nucleus and Dual Subkiloparsec AGN (VODKA): Hubble Space Telescope Discovers Double Quasars," *Astrophys. J.* **925** no. 2, (2022) 162, arXiv:2108.01672 [astro-ph.HE].

[260] P. Breiding, S. Burke-Spolaor, M. Eracleous, T. Bogdanović, T. J. W. Lazio, J. Runnoe, and S. Sigurdsson, "The Search for Binary Supermassive Black Holes

among Quasars with Offset Broad Lines Using the Very Long Baseline Array," *Astrophys. J.* **914** no. 1, (2021) 37, arXiv:2103.14176 [astro-ph.GA].

[261] L. Z. Kelley, Z. Haiman, A. Sesana, and L. Hernquist, "Massive BH Binaries as Periodically-Variable AGN," *Mon. Not. Roy. Astron. Soc.* **485** no. 2, (2019) 1579–1594, arXiv:1809.02138 [astro-ph.HE].

[262] M. Milosavljevic and D. Merritt, "The Final parsec problem," *AIP Conf. Proc.* **686** no. 1, (2003) 201–210, arXiv:astro-ph/0212270.

[263] M. Siwek, R. Weinberger, and L. Hernquist, "Orbital evolution of binaries in circumbinary discs," *Mon. Not. Roy. Astron. Soc.* **522** no. 2, (2023) 2707–2717, arXiv:2302.01785 [astro-ph.HE].

[264] K. Holley-Bockelmann and F. M. Khan, "Galaxy Rotation and Rapid Supermassive Binary Coalescence," *Astrophys. J.* **810** no. 2, (2015) 139, arXiv:1505.06203 [astro-ph.GA].

[265] M. Bonetti, F. Haardt, A. Sesana, and E. Barausse, "Post-Newtonian evolution of massive black hole triplets in galactic nuclei – II. Survey of the parameter space," *Mon. Not. Roy. Astron. Soc.* **477** no. 3, (2018) 3910–3926, arXiv:1709.06088 [astro-ph.GA].

[266] F. A. Jenet, G. B. Hobbs, W. van Straten, R. N. Manchester, M. Bailes, J. P. W. Verbiest, R. T. Edwards, A. W. Hotan, J. M. Sarkissian, and S. M. Ord, "Upper bounds on the low-frequency stochastic gravitational wave background from pulsar timing observations: Current limits and future prospects," *Astrophys. J.* **653** (2006) 1571–1576, arXiv:astro-ph/0609013.

[267] B. Kocsis and A. Sesana, "Gas driven massive black hole binaries: signatures in the nHz gravitational wave background," *Mon. Not. Roy. Astron. Soc.* **411** (2011) 1467, arXiv:1002.0584 [astro-ph.CO].

[268] P. Athron, C. Balázs, A. Fowlie, L. Morris, and L. Wu, "Cosmological phase transitions: From perturbative particle physics to gravitational waves," *Prog. Part. Nucl. Phys.* **135** (2024) 104094, arXiv:2305.02357 [hep-ph].

[269] R. Jinno, T. Konstandin, H. Rubira, and I. Stomberg, "Higgsless simulations of cosmological phase transitions and gravitational waves," *JCAP* **02** (2023) 011, arXiv:2209.04369 [astro-ph.CO].

[270] **LISA Cosmology Working Group** Collaboration, C. Caprini, R. Jinno, M. Lewicki, E. Madge, M. Merchand, G. Nardini, M. Pieroni, A. Roper Pol, and V. Vaskonen, "Gravitational waves from first-order phase transitions in LISA: reconstruction pipeline and physics interpretation," *JCAP* **10** (2024) 020, arXiv:2403.03723 [astro-ph.CO].

[271] E. Madge, E. Morgante, C. Puchades-Ibáñez, N. Ramberg, W. Ratzinger, S. Schenk, and P. Schwaller, "Primordial gravitational waves in the nano-Hertz regime and PTA data — towards solving the GW inverse problem," *JHEP* **10** (2023) 171, arXiv:2306.14856 [hep-ph].

[272] F. Ertas, F. Kahlhoefer, and C. Tasillo, "Turn up the volume: listening to phase transitions in hot dark sectors," *JCAP* **02** no. 02, (2022) 014, arXiv:2109.06208 [astro-ph.CO].

[273] W. G. Lamb, S. R. Taylor, and R. van Haasteren, "Rapid refitting techniques for Bayesian spectral characterization of the gravitational wave background using pulsar

timing arrays," *Phys. Rev. D* **108** no. 10, (2023) 103019, arXiv:2303.15442 [astro-ph.HE].

[274] A. Mitridate, D. Wright, R. von Eckardstein, T. Schröder, J. Nay, K. Olum, K. Schmitz, and T. Trickle, "PTArcade," arXiv:2306.16377 [hep-ph].

[275] P. F. Depta, M. Hufnagel, and K. Schmidt-Hoberg, "Updated BBN constraints on electromagnetic decays of MeV-scale particles," *JCAP* **04** (2021) 011, arXiv:2011.06519 [hep-ph].

[276] S. Balan, T. Bringmann, F. Kahlhoefer, J. Matuszak, and C. Tasillo, "Sub-gev dark matter and nano-hertz gravitational waves from a classically conformal dark sector," July, 2025. https://doi.org/10.5281/zenodo.15863201.

[277] **NA64** Collaboration, S. Gninenko, " Proposal for an experiment to search for dark sector particles weakly coupled to muon at the SPS," Tech. Rep. CERN-SPSC-2019-002, SPSC-P-359, CERN, Geneva, Jan, 2019. http://cds.cern.ch/record/2653581.

[278] J. Neyman, "Outline of a theory of statistical estimation based on the classical theory of probability," *Philosophical Transactions of the Royal Society of London. Series A, Mathematical and Physical Sciences* **236** no. 767, (1937) 333–380. http://www.jstor.org/stable/91337.

[279] S. S. Wilks, "The Large-Sample Distribution of the Likelihood Ratio for Testing Composite Hypotheses," *Annals Math. Statist.* **9** no. 1, (1938) 60–62.

[280] F. Feroz, M. P. Hobson, and M. Bridges, "MultiNest: an efficient and robust Bayesian inference tool for cosmology and particle physics," *Mon. Not. Roy. Astron. Soc.* **398** (2009) 1601–1614, arXiv:0809.3437 [astro-ph].

[281] M. Cirelli, A. Kar, and H. Shaikh, "Indirect searches for realistic sub-GeV Dark Matter models," arXiv:2508.03819 [hep-ph].

[282] K. Cranmer *et al.*, "Publishing statistical models: Getting the most out of particle physics experiments," *SciPost Phys.* **12** no. 1, (2022) 037, arXiv:2109.04981 [hep-ph].

[283] R. Lafaye, T. Plehn, and D. Zerwas, "SFITTER: SUSY parameter analysis at LHC and LC," arXiv:hep-ph/0404282.

[284] **GAMBIT Dark Matter Workgroup** Collaboration, T. Bringmann *et al.*, "DarkBit: A GAMBIT module for computing dark matter observables and likelihoods," *Eur. Phys. J. C* **77** no. 12, (2017) 831, arXiv:1705.07920 [hep-ph].

[285] J. Neyman and E. S. Pearson, "Ix. on the problem of the most efficient tests of statistical hypotheses," *Philosophical Transactions of the Royal Society of London. Series A, Containing Papers of a Mathematical or Physical Character* **231** no. 694-706, (1933) 289–337, https://royalsocietypublishing.org/doi/pdf/10.1098/rsta.1933.0009.

[286] S. Algeri, J. Aalbers, K. Dundas Morå, and J. Conrad, "Searching for new phenomena with profile likelihood ratio tests," *Nature Rev. Phys.* **2** no. 5, (2020) 245–252, arXiv:1911.10237 [physics.data-an].

[287] R. E. Kass and A. E. Raftery, "Bayes Factors," *J. Am. Statist. Assoc.* **90** no. 430, (1995) 773–795.

[288] H. Jeffreys, "An Invariant Form for the Prior Probability in Estimation Problems," *Proceedings of the Royal Society of London Series A* **186** no. 1007, (Sept., 1946) 453–461.

[289] L. Demortier, S. Jain, and H. B. Prosper, "Reference priors for high energy physics," *Phys. Rev. D* **82** (2010) 034002, arXiv:1002.1111 [stat.AP].

[290] P. T. Inc., "Dash: Analytical web applications for python," 2025. https://dash.plotly.com.

[291] **SENSEI** Collaboration, P. Adari *et al.*, "First Direct-Detection Results on Sub-GeV Dark Matter Using the SENSEI Detector at SNOLAB," *Phys. Rev. Lett.* **134** no. 1, (2025) 011804, arXiv:2312.13342 [astro-ph.CO].

[292] A. Aguilar-Arevalo *et al.*, "The Oscura Experiment," *arXiv e-prints* (Feb., 2022) arXiv:2202.10518, arXiv:2202.10518 [astro-ph.IM].

[293] **PandaX** Collaboration, S. Li *et al.*, "Search for Light Dark Matter with Ionization Signals in the PandaX-4T Experiment," *Phys. Rev. Lett.* **130** no. 26, (2023) 261001, arXiv:2212.10067 [hep-ex].

[294] **XENON** Collaboration, E. Aprile *et al.*, "Search for Light Dark Matter in Low-Energy Ionization Signals from XENONnT," *Phys. Rev. Lett.* **134** no. 16, (2025) 161004, arXiv:2411.15289 [hep-ex].

[295] **SHiP** Collaboration, C. Ahdida *et al.*, "Sensitivity of the SHiP experiment to light dark matter," *JHEP* **04** (2021) 199, arXiv:2010.11057 [hep-ex].

[296] A. Kogut *et al.*, "The Primordial Inflation Explorer (PIXIE): a nulling polarimeter for cosmic microwave background observations," **2011** no. 7, (July, 2011) 025, arXiv:1105.2044 [astro-ph.CO].

[297] J. Chluba *et al.*, "New horizons in cosmology with spectral distortions of the cosmic microwave background," *Exper. Astron.* **51** no. 3, (2021) 1515–1554, arXiv:1909.01593 [astro-ph.CO].

[298] S. R. Taylor, R. van Haasteren, and A. Sesana, "From Bright Binaries To Bumpy Backgrounds: Mapping Realistic Gravitational Wave Skies With Pulsar-Timing Arrays," *Phys. Rev. D* **102** no. 8, (2020) 084039, arXiv:2006.04810 [astro-ph.IM].

[299] **IPTA** Collaboration, M. Falxa *et al.*, "Searching for continuous Gravitational Waves in the second data release of the International Pulsar Timing Array," *Mon. Not. Roy. Astron. Soc.* **521** no. 4, (2023) 5077–5086, arXiv:2303.10767 [gr-qc].

[300] P. S. Cole *et al.*, "Distinguishing environmental effects on binary black hole gravitational waveforms," *Nature Astron.* **7** no. 8, (2023) 943–950, arXiv:2211.01362 [gr-qc].

[301] R. Laureijs *et al.*, "Euclid Definition Study Report," *arXiv e-prints* (Oct., 2011) arXiv:1110.3193, arXiv:1110.3193 [astro-ph.CO].

[302] A. Hussein, L. Necib, M. Kaplinghat, S. Y. Kim, A. Wetzel, J. I. Read, M. P. Rey, and O. Agertz, "Theoretical Predictions for the Inner Dark Matter Distribution in the Milky Way Informed by Simulations," arXiv:2501.14868 [hep-ph].

[303] H. Miyatake, "Cosmology with Galaxy Clusters," arXiv:2505.07697 [astro-ph.CO].

[304] D. Paraficz, J. P. Kneib, J. Richard, A. Morandi, M. Limousin, E. Jullo, and J. Martinez, "The Bullet cluster at its best: weighing stars, gas, and dark matter," *Astronomy & Astrophysics* **594** (2016) A121, arXiv:1209.0384 [astro-ph.CO].

[305] S. Cha, B. Y. Cho, H. Joo, W. Lee, K. HyeongHan, Z. P. Scofield, K. Finner, and M. J. Jee, "A High-Caliber View of the Bullet Cluster through JWST Strong and Weak Lensing Analyses," *Astrophys. J. Lett.* **987** no. 1, (2025) L15.